Study of photonic crystals on thin film lithium niobate for sensing applications - design, fabrication and characterization

Wentao Qiu

SPIM

Thèse de Doctorat

école doctorale **sciences pour l'ingénieur et microtechniques**

UFC UNIVERSITÉ DE FRANCHE-COMTÉ

Study of photonic crystals on thin film lithium niobate for sensing applications

design, fabrication and characterization

WENTAO QIU

SPIM

Thèse de Doctorat

école doctorale **sciences pour l'ingénieur et microtechniques**

UFC UNIVERSITÉ DE FRANCHE-COMTÉ

THÈSE présentée par

WENTAO QIU

pour obtenir le

Grade de Docteur de
l'Université de Franche-Comté

Spécialité : **Optics and photonics**

Study of photonic crystals on thin film lithium niobate for sensing applications

design, fabrication and characterization

Soutenue publiquement le 21 June 2016 devant le Jury composé de :

HERVÉ MAILLOTTE	President	Directeur de Recherche,Institut FEMTO-ST
SÉGOLÈNE CALLARD	Reviewer	Professor - École Centrale de Lyon
YAN PENNEC	Reviewer	Professor - Université de Lille 1
ABDERRAHMANE BELKHIR	Examinateur	Professor - Université Mouloud Mammeri, Tizi Ouzou, Algeria
MARIA-PILAR BERNAL	Examinateur	Directrice de Recherche, Institut FEMTO-ST
FADI ISSAM BAIDA	Examinateur	Professor - Université de Franche-Comté

Acronym list

E-field	Electric field
T-sensor	Temperature sensor
EMI	Electromagnetic interference
EMC	Electromagnetic compatibility
EEG	Electroencephalogram
ECG	Electrocardiography
FBG	Fiber Bragg grating
M-Z	Mach-Zehnder
EO	Electro optic
GRIN	Gradient-index
RF	Radio frequency
PDLC	Polymer-dispersed liquid crystals
LC	Liquid crystals
SOI	Silicon on insulator
VCSEL	Vertical-cavity surface-emitting laser
LPFG	Long period fiber grating
HiBi-FLM	High birefringence fiber-loop mirrors
PhC	Photonic crystals
PCF	Photonic crystals fiber
GR	Guided resonance
RIE	Reative ion etching
FIB	Focus ion beam
LN	Lithium niobate
F-P	Fabry-Perot
Si	Silicon
$BaTiO_3$	Barium titanate
BCB	Benzocyclobutene
HF	Hydrogen fluoride
PECVD	Plasma-enhanced chemical vapor deposition
CMP	Chemical mechanical polishing
CIS	Crystals ion slicing
PPLN	Periodically poled lithium niobate
ER	Extinction ratio
EM	Electromagnetic
WG	Waveguide
FDFD	Finite difference frequency domain

FD-BPM	Finite difference- Beam propagation method
2D-FDTD	Two dimensional - finite difference time domain
3D-FDTD	Three dimensional - finite difference time domain
PWE	Plane wave expansion
FT	Fourier transform
CW	Continuous wave
FD	Finite difference
TMM	Transfer matrix method
FEM	Finite element method
PML	Perfectly matched layer
PBC	Periodic boundary condition
CFL	Courant-Friedrichs-Lewy
FFT	Fast Fourier transform
NA	Numerical aperture
FoM	Figure of merits
WDM	Wavelength division multiplexer
PE	Proton exchanged
APE	Annealed proton exchanged
SEM	Scanning electron microscope
TE	Transverse electric
TM	Transverse magnetic
PBG	Photonic bandgap
DI	Deionized water
SBM	Slow Bloch mode
SPL	Suzuki phase lattice
BS	Beam splitter
OSA	Optical spectrum analyzer

TABLE DES FIGURES

LISTE DES TABLES

SOMMAIRE

I

CONTENTS

1

INTRODUCTION

1.1/ RESEARCH BACKGROUND

Photonic technology, which employs light as a medium, has been proved as a viable solution to ever increasing demands for faster communication and large amounts of data. Optical fiber technology which constitutes the backbone of high speed communications systems bringing easy access to Internet from anywhere around the world has great impact on the whole society [11, 12, 13, 14, 15]. Another impressive application of photonic technology is the harvesting of solar energy. Solar cells which exploit the photovoltaic effect of the material enables renewable clean energy source from the sun. Commercial solar cells for generating photovoltaic energy have already been conveniently available thanks to the advancement of photovoltaic related research [16, 17, 18, 19, 20]. Besides revolutionary change in high speed fiber optic communications and cleaner energy harvesting, photonics have shaped a new landscape in many domains such as higher data rate optical interconnection in electronic chips, new generation of compact and highly sensitive sensors etc.

Photonic sensors are in a growing demand in many areas ranging from gas and oil industry, automotive, avionic, military, geophysical, environmental and to biomedical applications [21, 22, 23, 24, 25]. Looking at the scientific literature, it clearly appears that in the past few decades there has been an increasing number of journals and magazines dealing with the subject of sensors, with large room dedicated to photonic based devices. Light is incredibly versatile for measuring all kinds of physical quantities : temperature, electric field

(E-field), displacement, strain etc. Photonic sensors are promising candidates for the new generation of sensors developments due to their virtues of high sensitivity, large dynamic range, compact size etc. In addition, a growing number of industrial applications are also being demonstrated, which spans from a better process control, safety and security improvement, transportation, environment, structural health monitoring, health care and to food quality. Sensors are also expected to significantly contribute to intelligent information systems in stationary and mobile applications by connecting to the fiber based networks such as those on fiber sensors. The nanotechnologies that integrate sensors in nanoscale size will revolutionize probe designs in health care, climate control, physical parameter measurement and detection of toxic substances [21, 23] etc thanks to its ability to provide higher spatial resolution and more compact size. Two types of photonic sensors are explored in this thesis : E-field sensors and temperature sensors (T-sensors).

E-field sensors with high sensitivity are in increasing demand as the need for EMI (electromagnetic interference), EMC (electromagnetic compatibility) testing on integrated circuit is growing due to the fact that the electronic industry has scaled down to sub 10-nm or smaller [21, 25, 26, 27, 28]. In addition, the monitoring of electromagnetic phenomena is critical for power utilities, process control, medical apparatuses, ballistic control etc. Further more, the effects of the presence of E-field (in particular of medium and high-intensity E-field) on human health and the precautionary principle needs to be evaluated to determine the maximum permissible E-field exposure levels. To verify and respect the E-field exposure limits, it is obviously necessary to develop high sensitivity E-field sensors [21]. Moreover, E-field measurement and diagnostic techniques can serve as powerful tools in the design and analysis of high frequency antennas or circuits where the knowledge of the complete field patterns and polarization characterizations would be beneficial. The common E-field sensors employs antenna design and receivers that are linked by cables to the measuring electronics and very often such configurations distort the field to be detected making it very difficult to know the original state of the signal. In particular, if the sensor is placed under the electric field emitter to be tested, electrical coupling oc-

curs and radio waves other than the free space propagating signal arise. In addition, since the antenna size is related to the wavelength of the signal, the electric field detectors are relatively large (especially at lower frequencies) so that compact detectors and arrays are not possible. Guided or radiated E-fields are usually characterized by using metallic probes or dipole antennas respectively which present important limitations : a relatively narrow frequency bandwidth, a quite low spatial resolution and a significant disturbance of the signal to be measured [29, 30].

Photonic E-field sensors made of almost dielectric material are particularly attractive, being able to offer high electrical insulation and total immunity to electromagnetic interference, thus minimizing the perturbation that they induce on the signal to be measured and to reach a greater spatial resolution and a wider frequency bandwidth. Photonic based sensors have several advantages over metallic sensing probes. The bandwidth of dielectric materials is significantly larger than that of metals. It is intrinsically broad band operation due to its free of metal or small metallic element of nano antenna which helps to avoid degradation such as RF loss and limited conductivity. In addition, the optical fiber connection of photonic based sensors provides optical isolation to the instrumentation in order to protect it from possible overload conditions. In biomedical sensor applications, high spatial resolution (small physical size of the probe) photonic E-field sensor can be an excellent candidate in applications such as probe of monitoring EEG (electroencephalogram), ECG (electrocardiogram) signals for personal health care as those are shown in Fig.1.1 since the monitoring of ECG or EEG signals can be regarded as a device recording the sum of all the electrical impulse activity in the heart or brain. Designing these kinds of probes as a compact hand-held device with high sensitivity would have significant impact on personal health care [31, 32, 33, 34, 35].

Another type of sensor being explored in this thesis is temperature sensor. Most of the variables, for instance humidity, pressure, flow, stress and gas concentration, measured in scientific investigations or engineering applications depend, by varying degrees, on temperature. This necessitates the simultaneous measurement of temperature along with the variable of interest in order to perform high

fidelity temperature compensated measurements. A high precision T-sensor would yield better characterization of the physical quantities that are temperature dependent [23]. Traditional T-sensors are based on fiber Bragg grating (FBG) structures [36, 37, 38, 39] where long interaction lengths are needed in order to obtain important sensitivities and measurement range. In this thesis, focuses are put on developing T-sensors with compact size and high sensitivity.

1.2/ PHOTONIC BASED E-FIELD SENSORS AND T-SENSORS

1.2.1/ STATE OF THE ART ON E-FIELD SENSORS

As the electronic circuits shrink down as small as sub 10-nm, specification of the malfunctioning electronic circuit elements and measurement of the EMI induced electric field become necessary for detailed evaluation of EMI and an appropriate countermeasure. However, with conventional measuring instruments, it is impossible to separately measure the electric field to be detected since the utilization of metallic cables introduce interference to the measuring probe. Consequently, photonic based E-field sensors mostly composed of non-metallic materials are highly suitable for these applications. Some advantages of photonic based sensors compared with

(a) (b)

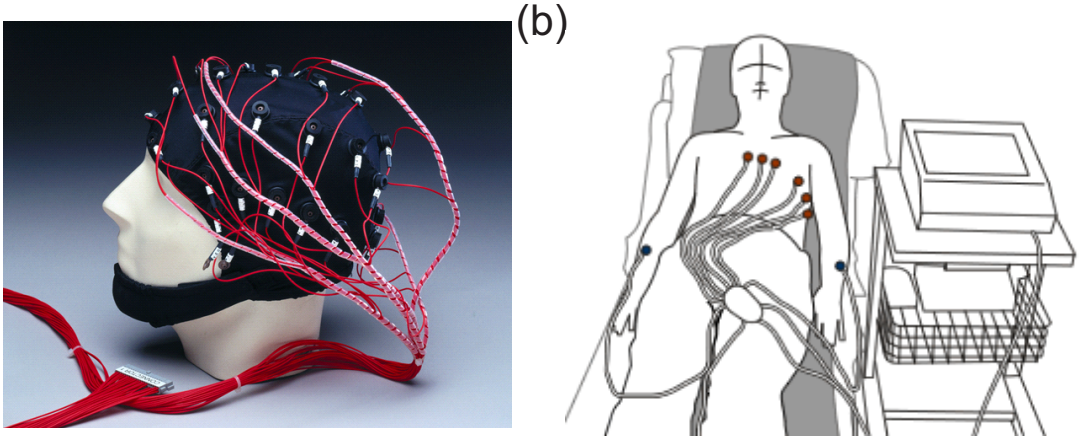

FIGURE 1.1 – Measurements of electrical signals generated by (a) brain with EEG probe, (b) heart with ECG probe.

traditional metallic based sensors are summarized as follows :

— Non-electrical method of operation, which is explosion-proof

and offers intrinsic immunity to radio frequency and, more generally, to any kind of electromagnetic interference ;
— Small size/weight and great flexibility that allow access to otherwise restricted areas ;
— Capability of resisting to chemically aggressive and ionizing environments ;
— Easy interface with optical data communication systems and secure data transmission.

Fiber based and integrated E-field sensors are the common two types of photonic E-field sensors. Interferometric architectures are often applied in integrated sensors. Among them, an E-field sensor using M-Z (Mach-Zehnder)interferometer has been commonly adopted. Traditionally metal electrodes have been placed near the sensing waveguides of the M-Z arms, acting as an antenna to collect the field and applying it to the proper region of the EO crystal such as $LiNbO_3$ material. Other interferometric configuration such as four-ports coupler and three-ports coupler interferometric configurations (Fig. 1.2) have also been proposed to realize electric field sensors [1, 21].

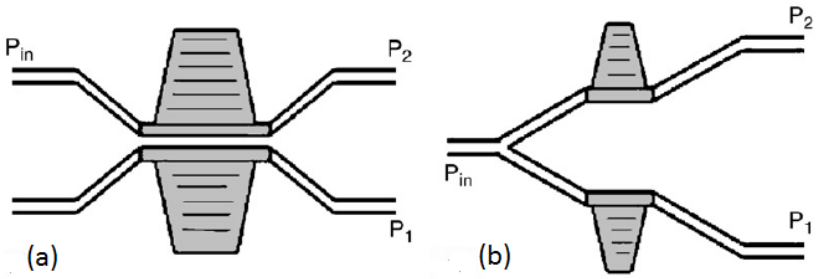

FIGURE 1.2 – E-field sensors made of (a) four-ports coupler interferometric configuration, (b) three-ports coupler interferometric configuration [1].

Even though these interferometric configuration based E-field sensor have the advantages of easy to design and to implement, they have limited spatial resolution due to the fact that a long interaction length is needed to encode the measurand into the output optical signal. Moreover, the biasing point drift is problematic for highly sensitive measurement requirement.

On the other hand, fiber based sensors combining the use of different materials proliferate in literature which present advantages of

performing remote sensing by using only a fiber optic connection, obviating required auxiliary electrical connections [40]. This maintains the safety of the operator and the integrity of any signal processing components in the rest of the system.

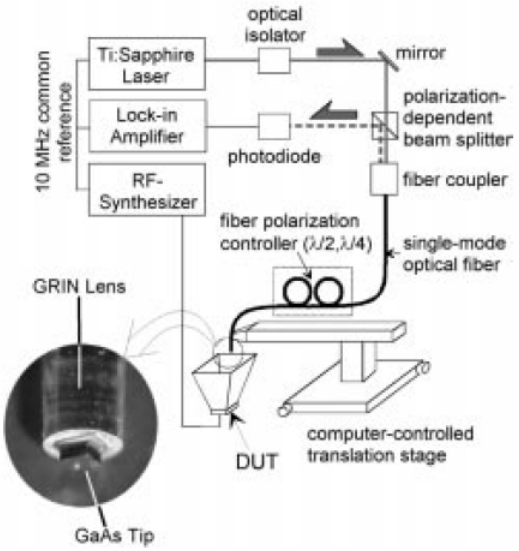

FIGURE 1.3 – Fiber-based EO-field-mapping system schematic. The input and output (signal) beams are displayed with solid and dashed gray lines, respectively. A magnified photo of the GaAs probe tip including the GRIN lens is shown [2].

Fiber tip sensors employing other EO crystal are presented for microwave-integrated circuits testing [2] as shown in Fig. 1.3. The sensor which consists of a gradient-index (GRIN) lens with diameter of 1 mm and length of 5 mm is mounted at the end face of the fiber to focus the beam onto the surface of a micro machined GaAs crystal. The crystal is attached to the GRIN lens using transparent cement. The optical beam reflected from the probe is phase modulated by the RF electric field. This signal is sent to the photo diode by a beam splitter which also converts the phase shift into an intensity modulation. In order to obtain high sensitivity, a bulky crystal and complicated interrogation system are needed thus limiting its spatial resolutions and sensitivity.

E-field optical fiber sensors can be realized by coating the optical fiber with materials whose optical properties change proportionally to an applied electric field. One of these materials is polymer-dispersed liquid crystals (PDLC), a class of materials with EO applications, which employs a mixture of liquid crystals (LC) and polymer

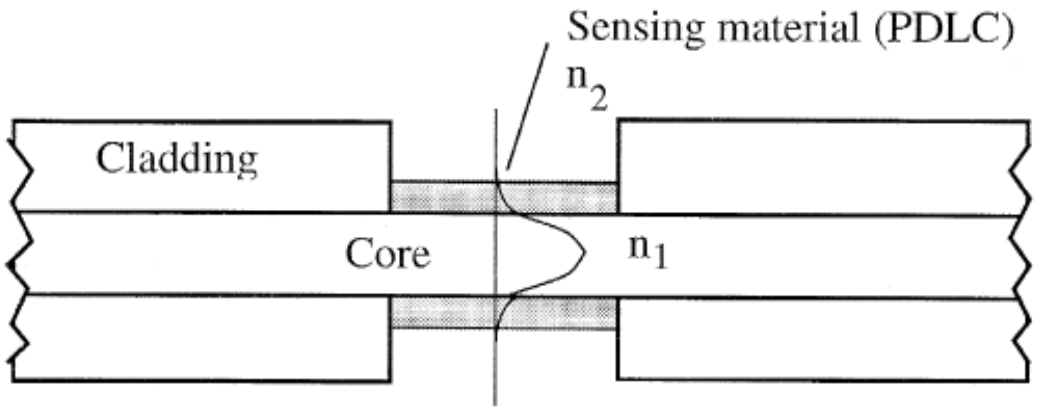

FIGURE 1.4 – E-field sensor applying PDLC [3].

using phase-separation techniques that forms micron-size droplets of LCs in the polymer matrix [41, 42]. The director within the LC domains is randomly oriented while the applied electric field causes orientation of the director change to the preferred direction, and therefore changing the PDLC refractive indexes. An evanescent field-based sensors applying PDLC as E-field sensor is shown in Fig. 1.4. This kind of E-field sensors presents low sensitivity due to the weak interaction between the evanescent field and LC droplets. Moreover, they show a long response time (around 3 min) which is determined by the electrical time constant of the device (equal to the inverse of the product of electrical resistance and capacitance of the device) [3, 43]. Other materials that have been used as E-field sensors are electrochromic materials [44]. The sensor response time is in the order of hundreds of seconds thus it can only be used for low frequency measurements.

There are also E-field fiber sensors employing piezoelectric or electrostrictive transducers to generate a phase shift in the optical signal propagating in the optical fiber. The phase shift is due to the strain produced by the interaction between the applied electric field and the piezoelectric or electrostrictive material. Koo et al. presented a polyvinylidene fluoride piezoelectrical transducer which obtained a sensitivity of 90 V/m/$(Hz)^{1/2}$ at 10 Hz [45].

Integrated optical E-field sensors based on electroabsorption modulators are also investigated in order to improve the sensitivity

and the bandwidth. They exploit the electroabsoprtion phenomenon (change of absorption coefficient of an optical material when a voltage is applied across it) to modulate the intensity of an optical signal [12]. By adopting a traveling-wave configuration for the metallic electrodes, an electroabsorption modulator can be also used as an E-fiel sensor with bandwidth of 50 GHz [46]. The best electroabsorbant sensor proposed up to date has shown a minimum detectable E-field of 0.1 V/m and a bandwidth of 6 GHz [47].

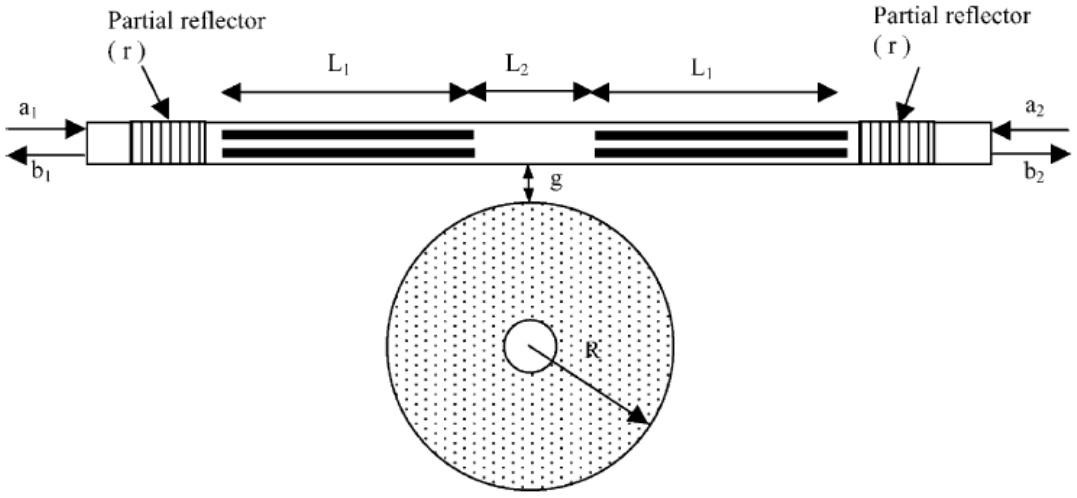

FIGURE 1.5 – Schematic of whispering gallery mode resonator coupling with Fabry Perot cavity [4].

E-field sensors employing a resonance frequency shift of high light confinement cavities are also investigated. As shown in Fig.1.5, the antenna picks up the electric field which then produce variations in the resonance frequency of the system constituted by a Fabry Perot cavity and a disk resonator [4, 48]. The estimation of the external electric field is performed by either monitoring the resonance frequency shift of the coupled cavities or by measuring the change of light intensity at the output of the system at a given wavelength. The sensor has been designed to be realized using silicon-on-insulator (SOI) technology. Simulations of its behavior show a minimum detectable voltage applied to the sensor electrodes of 0.06 V. Sensor bandwidth has been estimated around 500 MHz.

An active electrical field sensor is also investigated where the signal is picked up from the antenna and modulated directly the optical signal generated by a laser source. In the sensor proposed by Mann

et al. [49] an optical signal generated by a VCSEL is modulating by the electric signal that arrives from a dipole antenna. This sensor exhibits a sensitivity of 50 μV/m/(Hz)$^{1/2}$ (at 1 Hz) and a bandwidth of 1 GHz.

The pursue of developing high sensitivity and high resolution E-field sensors is still needed which can potentially bring significant impact on E-field measurement such as in health care applications. When it is designed in a compact size, one can imagine an array of sensors for the E-field measurement such as monitoring EEG, ECG signal to map out the images of the heart or brain electrical activity as schematically shown in Fig. 1.1. Photonic based EEG, ECG probe can be highly sensitive, since they made of almost all dielectric component, no source to interfere the weak electrical signal to be detected. In order to obtain high sensitivity and high spatial resolution, a probe that combines all dielectric material and miniaturized structure is essential. A photonic crystal fabricated in a electro-optic dielectric material with high light confinement is one promising candidate of this miniaturized structure.

1.2.2/ STATE OF THE ART ON PHOTONIC T-SENSORS

There are a variety of techniques employed for temperature sensing which utilize diverse physical phenomenon like thermal expansion [50], thermoelectricity [51], fluorescence [52, 53] etc. Selection of any of these techniques depend upon specific requirements or constraints. Among different types of T-sensors, photonics sensors enjoy an increased acceptance as well as a widespread use for structural sensing and monitoring applications in civil engineering, aerospace, marine, oil and gas, composites, smart structures, bio-medical devices, electric power industry and many others [54, 55, 56, 57].

In particular fiber optic T-sensors are the most widely used. One of the most popular fiber based T-sensor configurations are the fiber Bragg gratings based sensors as shown in Fig. 1.6. The periodic perturbation of the core index of refraction gives rise to successive coherent scattering for a narrow band of the incident light. The gra-

ting thus effectively acts as a stop-band filter, reflecting light with wavelengths close to the Bragg wavelength, and transmitting wavelengths sufficiently different from the resonance condition. Theoretical formulations based on coupled mode theory have been developed to analyze fiber grating spectra by Erdogan et al [58, 59].

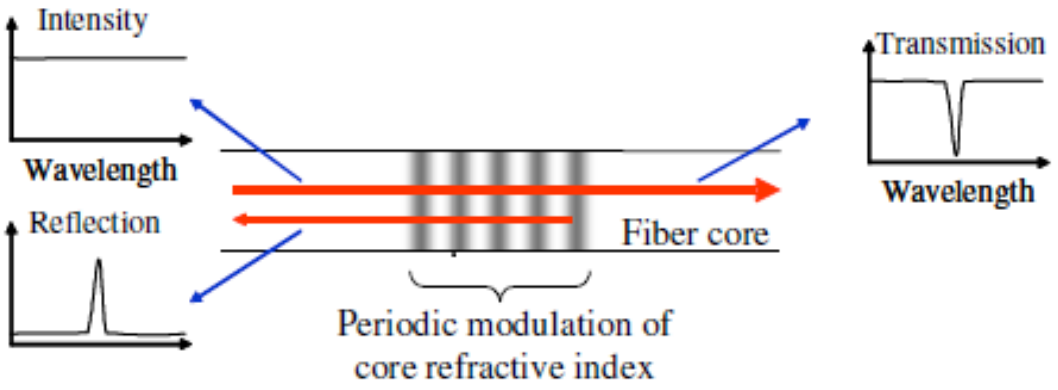

FIGURE 1.6 – Operation principle of FBGs.

However, FBG inscribed by intense UV lasers cannot withstand temperatures higher than 200^oC because the index modulated pattern in the fiber core will lose contrast [36, 37]. A typical obtained sensitivity for FBG is only on the order of $10\ pm/^oC$, while the sensitivity is about $20\ pm/^oC$ by employing a LPFG (Long Period Fiber Grating) structure. T-sensor based on FBG needs long interaction lengths in order to obtain a relative high temperature sensitivity. Moreover they also suffer several drawbacks as follows :

— Limited integratability with other functional components and limited spatial resolution due to its long interaction length and bulky device ;
— Complex interrogation techniques are required in order to detect the measured physical quantity variations ;

There are a lot of publications dealing with the performance improvement of FBG based sensors. For example, FBG sensor fabricated by other methods such as FIB can possess sensitivities up to $20\ pm/^oC$ with a fiber probe tapered to a point [38]. It has been demonstrated that by using long-period gratings the sensitivity can reach $0.6\ nm/^oC$ for a length of 1 mm [39]. Other approach such as high birefringence fiber-loop mirrors (HiBi-FLM) design is also pro-

posed which yields a higher temperature sensitivity ($0.9435\ nm/^oC$) with a long active length (720 mm) [60]. In addition, PhC (photonic crystal) has been integrated with the traditional fiber based sensors to improve its sensitivity. For instance photonic crystal fiber (PCF) based temperature sensors have been proposed showing a high sensitivity ($6.6\ nm/^oC$) but still requiring a PCF length of 6.1 cm [61].

With the advancement in micro-fabrication technology, requirements for smaller size, lower power consumption, wider temperature ranges and on chip sensor-electronics integration have challenged the conventional temperature measurement techniques. To fulfill these requirements, Si based temperature sensors have been widely studied due to its compatibility with CMOS technology and the possibility to monolithically integrate with micro-electronics.

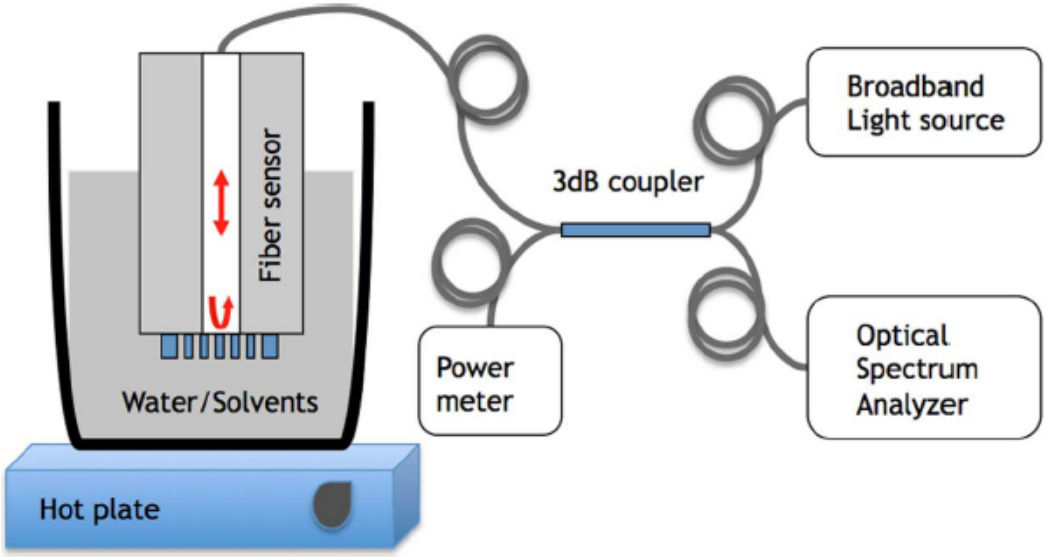

FIGURE 1.7 – Diagram of the PhC fiber tip T-sensor and the experimental setup for temperature sensing. A broadband light source is coupled into a 3 dB coupler, which sends light to the PhC end of the fiber immersed in a solution. The reflected light from the PhC is collected at the OSA [5].

The realization of a PhC fiber tip temperature sensor was proposed by Solgaards group, based on guided resonance (GR) on silicon PhC structure [5] as schematically shown in Fig. 1.7. The PhC slab was firstly fabricated by reactive ion etching (RIE) on standard wafers in a Si foundry, and successively released, transferred and bonded to the facet of a single-mode fiber by using a micromani-

pulator and focused ion beam (FIB) tool. The realized PhC fiber tip sensor demonstrated a sensitivity of $0.06\ nm/^oC$ as measured by the experimental set up in Fig. 1.7. The relatively low sensitivity is due to the small obtained refractive index variation since the thermal optics effect is small.

In this thesis, efforts are made in designing sensors that have a miniaturized size and simple interrogation technique requirement. The working principle of the most photonic sensors is to change the optical path length. This can be implemented for example in M-Z interferometer configurations with two arms to carry the measured signal. One arm of the M-Z interferometer is exposed to the measurand that can generate different phase shift than the reference arm. Henceforth, when the signals from the two arms are combined together, the variation of the measurand can be encoded in the output signal strength. Even though M-Z configuration is an efficient way to

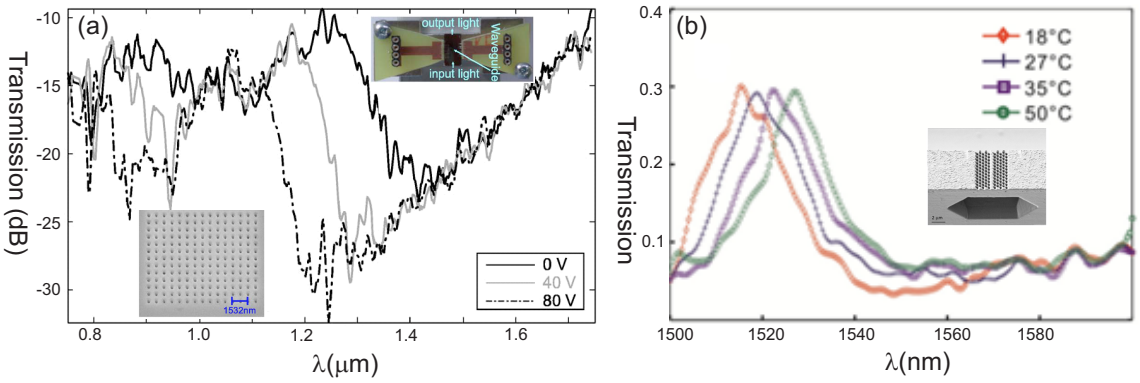

FIGURE 1.8 – (a) EO modulator fabricated on square lattice PhC by tuning the band gap edge. Left bottom inset shows the SEM image of the fabricated structure while the upper right inset shows the EO modulator device [6]. (b) PhC F-P cavity based temperature sensor. The inset shows the SEM image of the fabricated structure [7].

transform the measurand into optical signals, they suffer from long interaction length due to the small index change. If the refractive index increases by 10^{-5}, for example, it requires an optical wave propagating a distance of 10^5 wavelengths in order to experience an additional phase shift of 2π. Thus M-Z structures oftentimes have centimeter length.

Our group has been trying (10 years until now) to improve the device's overall performance (in terms of sensitivity and shrink down device size) by searching appropriate nano-patterned photonic cry-

tal structures on lithium niobate (LN) and some achievements have been made. For example, a LN PhC modulator has been realized by tuning the band gap position [6, 62] as shown in Fig. 1.8(a) with an enhancement of 312 times compared to the intrinsic EO effect of LN. An even more compact temperature sensor PhC by F-P (Fabry-Perot) (shown in Fig. 1.8(b)) cavity with an interaction length as small as 6 μm has been achieved by Huihui Lu et al [63]. By engineering the PhC dispersion properties in order to operate at slow group velocity regime, an experimental tunability of 0.359 nm/^{o}C has been achieved. Based on the accumulated experience in LN PhC designs, this thesis focuses on LN PhC high Q cavity structure for sensing applications. As it will be elaborated later, a structure that posses both high ER and Q can be achieved in guided resonance configurations and it will be exploited for sensing applications.

1.3/ THIN FILM LITHIUM NIOBATE

1.3.1/ LN PROPERTIES

Choosing a material that has a high EO coefficient is essential in order to obtain a high sensitivity performance. Silicon (Si) or related semiconductor material based photonics enjoy prosperous development in various applications due to its compatibility via Si complementary metal oxide semiconductor (CMOS) technology, which can make fabrication less costly by sharing the microelectronic industry foundry facilities. However, due to the inversion symmetry properties of Si crystal, it lacks linear EO effect [64, 65]. It is safe to say that for the moment no single material takes over the whole photonics industry as a dominant one. Most of the devices are developed in heterogeneous material system where fabrication technique such as bonding and direct thin film growth are required [66].

In applications of exploiting highly sensitive EO based sensors, materials with high intrinsic EO effect are a much more attractive choice. Despite numerous developments in EO novel materials such as graphene [67, 68, 69], electrooptical polymers [70, 71, 72, 73, 74] and barium titanate ($BaTiO_3$) [8, 75, 76, 77, 78, 79], LN conti-

nues to be the common material chosen for the fabrication of EO based modulators or sensors due to its combination of high EO coefficients and high transparency in the infrared wavelength regime [80, 81, 82, 83, 84, 85]. In addition, it also possesses many other interesting characteristics such as ferroelectricity, piezoelectricity, large acousto-optic coefficient, a broad transmission band, and high nonlinear optical coefficient at the same time, which makes it incredibly versatile to be exploited as a substrate for integrated optics [9, 65, 86]. By tailoring its properties, various useful devices which satisfy the future full optical linear and nonlinear signal processing can be made from LN. In this thesis, LN is chosen as the material to exploit its EO effect in sensing applications.

Let us first introduce some properties of LN. It is a solid synthetic crystal that is chemically very stable at room temperature. The most extended method to grow single crystals of this compound are the Czochralski method and its variants [65]. Fabrication of very homogeneous crystal in diameters of three inches can be easily achieved. A summary of its main crystal properties are presented in Table. 1.1 [9].

The pure material is transparent from the band gap edge absorption at about 320 nm (3.9 eV) up to the first infrared vibrational absorptions at a wavelength of about 5 μm (0.25 eV), covering all the visible and near infrared spectral regions. This provides a wide spectral window for LN to be exploited in various photonic applications.

Crystal composition or stoichiometry has a relevant influence on the values of many material coefficients. LN exists in a wide composition range of Li/Nb ratio. Czochralski growth from a series of melts with composition ranging from 47 mol% to 49 mol% Li_2O [65]. The congruent composition contains 48.45 mol% Li_2O and 51.55 mol% Nb_2O_5. Because of the fast growth and good homogeneity that can be achieved when growing from a melt of congruent composition, it is the most commonly used melt composition. The LN utilized in this thesis is congruent LN. The lattice constants a and c, unit cell volume and density of congruent LN at temperature of 25^o are shown in table. 1.2 [65].

TABLE 1.1 – Summary of basic properties of lithium niobate crystals

general properties :	
melting point :	$\sim$ 1260 ^{o}C
crystal symmetry :	trigonal, point group 3 m
method for single crystal growth :	Czochralski, large crystals
hardness	$\sim$ 5 Mohs
stoichiometry :	nonstoichiometric,$\sim$6% Li deficiency
	easy to dope in high concentration
ferroelectricity	Curie temperature TC = 1150^{o}C
	spontaneous polarization
	P_s(RT) $\sim$96 C/m^2
	180^o domains
piezoelectric	
pyroelectric	
optical related properties :	
transparency region :	VIS/NearIR ($\sim$350 nm - $\sim 5\mu$m)
optical anisotropy :	uniaxial, c-axis
refractive indices :	n_o = 2.286, n_e = 2.203. (at 632.8 nm)
optical homogeneity	$\Delta n \sim 5 \times 10^5$
optical effects :	acoustooptic
	electrooptic
	second order nonlinearity
	bulk photovoltaic effect
	optical damage photorefractive effect

TABLE 1.2 – Unite cell parameters (a, c, V) and density (d) for congruent LN

parameters	a (A^O)	c (A^O)	V (A^{O3})	d (g cm^{-3})
	5.15052(6)	13.86496(3)	318.513	4.646

Since many properties in LN are axis dependent, one needs to pay attention to the orientation when nano patterning are structured on it. Growth is most easily initiated along the Z axis, but other orientations can also be grown by providing a seed of the correct orientation [65]. The conventional choice of coordinate system for lithium niobate is a right-handed system with the X-axis along one of the hexagonal a_H axes, the Z-axis along the c_H axis, and the Y-axis along the direction given by the vector product $Z \times X$. The polarity of Z and Y are defined such that the piezoelectric tensor coefficients d_{33} and d_{22} are positive. The polarity of $+X$ follows from the choice of a right handed system. All the crystal properties have to satisfy the symmetry relationships of point group 3m. There is a three-fold symmetry axis (a 120^o rotation maps each atom onto an atom of the

same type), and three mirror planes perpendicular to the three equivalent X-axes. Commercially, they are three cuts of wafer in three inches that can be easily available which are schematically shown in Fig. 1.9.

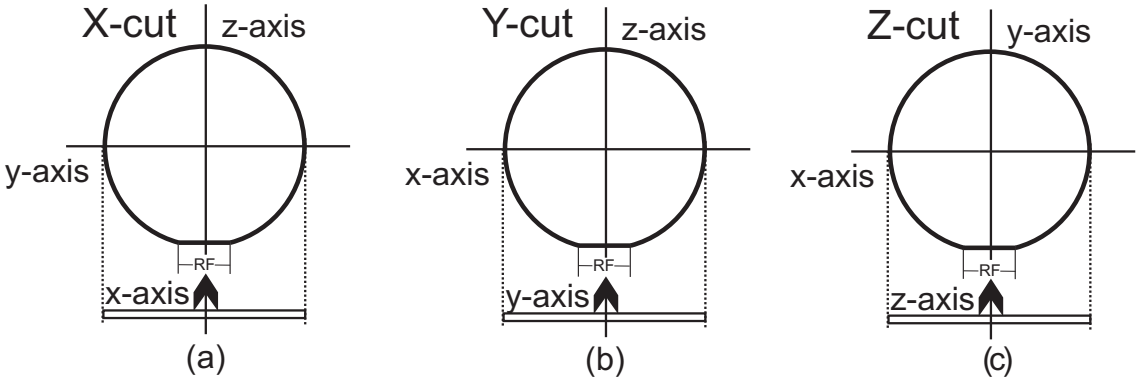

FIGURE 1.9 – Schematic of different cuts in LN. RF : reference flat. (a) X-cut, (b) Y-cut, (c) Z-cut.

Vector properties such as spontaneous polarization and pyroelectricity can exist only along the Z-axis [65]. Symmetric second order tensors, such as dielectric constant, thermal expansion etc, have two independent elements. One along the polar axis and the other perpendicular to it. Third order tensors such as the ones describing the electro-optic, piezo-electric or non-linear optic effect have four independent elements.

The crystalline structure of this material at room temperature corresponds to the trigonal 3m point group as shown in its crystallographic configuration of Fig. 1.10. This makes the crystal to be optically uniaxial, with ordinary refractive index n_o (electric field polarized normal to the c axis) and extraordinary refractive index n_e (electric field polarized along the c axis).

These refractive indices are dependent on the wavelength of the incident electromagnetic wave and the crystal temperature. The Sellmeier equation used to describe this dependence within the transparency range of lithium niobate is given by :

$$n_o^2(\lambda) = 4.9048 + \frac{0.1177}{\lambda^2 - 0.0475} - 0.0272\lambda^2$$

$$n_e^2(\lambda) = 4.5820 + \frac{0.0992}{\lambda^2 - 0.0444} - 0.0219\lambda^2 \qquad (1.1)$$

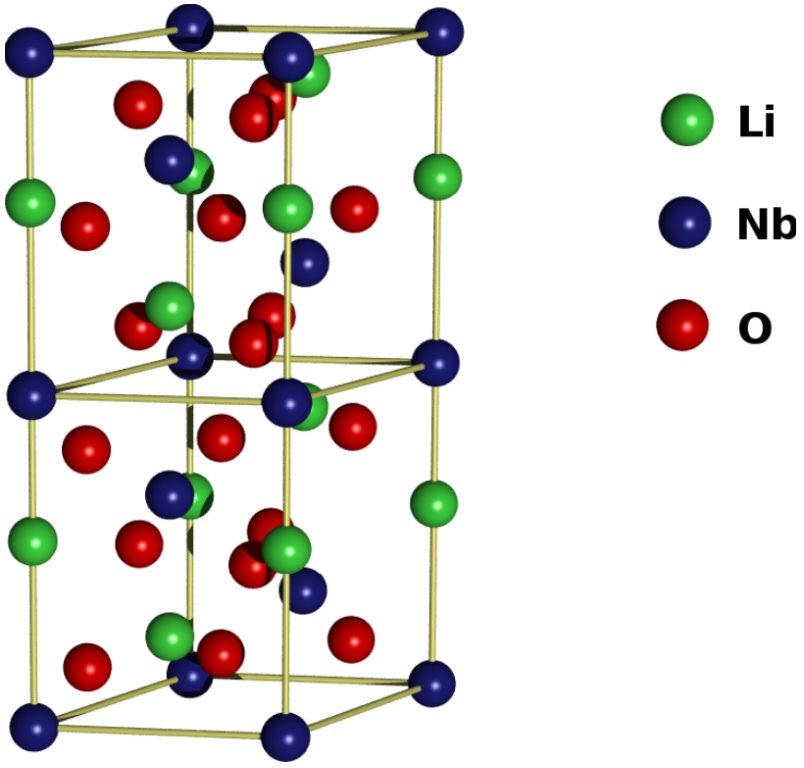

FIGURE 1.10 – Crystallographic configuration of LN.

Specifically, at the telecommunication wavelength 1.55 μm, LN has an index of $n_o = 2.210$ and $n_e = 2.138$. The phase velocity in anisotropic medium is dependent of the direction of polarization. Consider, for example, a wave propagating along y. If its electric field is paralleled to z, it will induce only P_z and will consequently 'see' an electric permeability ϵ_{33}. Its phase velocity will thus be $c_z = (\mu\epsilon_{33})^{-1/2}$. In general, the optical properties of an anisotropic medium are characterized by a geometric construction called the index ellipsoid expressed as follows :

$$\sum_{ij} \eta_{ij} x_i x_j = 1, \quad i, j = 1, 2, 3, \tag{1.2}$$

Where $\eta_{ij} = \eta_{ji}$ are elements of the impermeability tensor $\eta = \epsilon_0 \epsilon^{-1}$. As shown in Fig. 1.11 the ellipsoid principal axes are the optical principal axes of the medium. Its principal dimensions along these axes are the principal refractive indices n_1, n_2, n_3. The index ellipsoid may be used to determine the polarizations and refractive indices of the two normal modes of a wave traveling in an arbitrary direction. This is accomplished by drawing a plane perpendicular to the direction of propagation $\vec{k}$ and passing through the center of the ellipsoid. Its in-

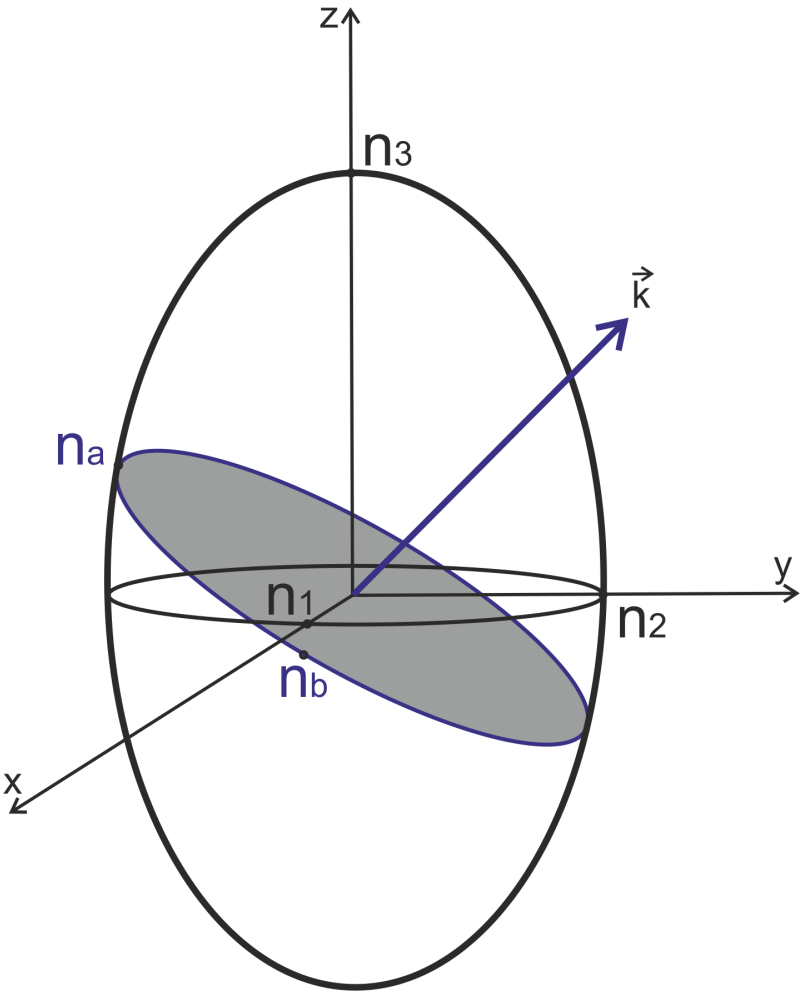

FIGURE 1.11 – The index ellipsoid. The coordinates (x, y, z) are the principal axes and n_1, n_2, n_3 are the principal refractive indices. The refractive indices of the normal modes of a wave traveling in the direction **k** are n_a and n_b.

tersection with the ellipsoid is an ellipse as shown in the gray ellipse in Fig. 1.11 whose major and minor axes have half lengths equal to n_a and n_b.

The dependence of the refractive index on the applied electric field takes one of two forms : the linear EO effect (Pockels effect) and quadratic EO effect (Kerr effect). The Pockels effect in which refractive index changes in proportion to the applied electric field, is the most exploited property in LN for EO based application such as modulators and sensors. Specifically, with the external field along the crystal z-axis, the principal axes of the indicatrix coincide with the

crystallographic axes and are given by :

$$\begin{aligned} n_x = n_y &= n_o + n_o^3 r_{13} E_x/2 \\ n_z &= n_e + n_e^3 r_{33} E_z/2 \end{aligned} \tag{1.3}$$

with the field along the x-axis, to the first order, the indicatrix axes become :

$$\begin{aligned} n_x &= n_o + n_o^3 r_{22} E_x/2 \\ n_y &= n_o - n_o^3 r_{22} E_x/2 \\ n_z &= n_e \end{aligned} \tag{1.4}$$

LN is an uniaxial birefringent crystal, the relationship between electric flux density D and electric field E is linear and can be written as $D = \epsilon E$, where ϵ is the second-rank permittivity tensor. In tensor component format, this relationship may be expressed as :

$$D_i = \sum_j \epsilon_{ij} E_j \tag{1.5}$$

where $i,\ j = \ x,\ y$, or z. Only the diagonal elements of the permittivity tensor are non-zero for non-gyrotopic material which can be shown through a thermodynamic conservation of energy argument. Furthermore, since the LN crystal is symmetric about the c-axis, the permittivity tensor can be represented by the 3×3 matrix with two distinctive values :

$$\epsilon_{ij} = \begin{bmatrix} \epsilon_{11} & 0 & 0 \\ 0 & \epsilon_{11} & 0 \\ 0 & 0 & \epsilon_{33} \end{bmatrix} \tag{1.6}$$

where $\epsilon_{11} = \epsilon_0(1 + \chi_{11})$, $\epsilon_{22} = \epsilon_0(1 + \chi_{22})$, $\epsilon_{33} = \epsilon_0(1 + \chi_{33})$.

The RF dielectric constants of lithium niobate fall into two general categories, low frequency (unclamped/constant stress) and high frequency (clamped/constant strain). At electrical frequencies below approximately 100 kHz, the crystal strain follows the electric field changes, and the constant-stress dielectric constant is labeled ϵ_{ii}^T. The subscript refers to the direction of the force and response : i = 1,2,3 for the x, y and z directions.

Constant-strain dielectric constants ϵ_{ii}^S are obtained at frequencies above approximately 10 MHz where the strain is unable to follow the

TABLE 1.3 – Dielectric constants of $LiNbO_3$

Frequency	ϵ_{11}	ϵ_{33}	Ref
Low(100 kHz)	84.6	29.1	[87, 88, 89, 90]
High(10 MHz)	44.3	27.6	[87, 88, 89, 90]
0.1 GHz	44.1	23	[91]
1.0 GHz	43.9	23.7	[91]
9.0 GHz	42.5	26	[92]
IR	41.5	44	[93]
Raman	26.0	29	[94]

fields. As can be seen from Table. 1.3 clamped dielectric constant ϵ_{11}^S is approximately half as large as the free dielectric constant ϵ_{11}^T. In contrast to ϵ_{11}, there is only a slight difference between ϵ_{33}^T and ϵ_{33}^S. Henceforth, when in RF analysis, one should pay attention to this dielectric constant frequency dependency.

1.3.1.1/ TFLN (THIN FILM LITHIUM NIOBATE) PRODUCTION

A few years ago, TFLN technology was still in its infancy. It was difficult to implement on chip compact devices such as air bridged based micro-cavities to enhance nonlinear optical processes on bulk LN as those demonstrated in other materials. Today high quality wafer scale TFLN has already been commercially available which opens the door to a new generation of upgrading traditional bulk LN based devices [95, 96, 97]. In this section, the production of TFLN is briefly introduced.

Many techniques have been studied to produce TFLN, such as chemical vapor deposition [98], RF sputtering [99], molecular beam epitaxy [100], sol-gel [101], and pulsed laser deposition [102]. However, these techniques have difficulty in producing high crystalline quality materials which exhibit properties that can be compared with bulk LN. For example, the values of the spontaneous ferroelectric polarization [103] and the EO coefficients [104] in sputtered LN are both reported to be about $\leq 1/10$ the value found in bulk single crystals. Moreover, grain boundaries in polycrystalline films generally lead to light scattering and large optical losses in devices fabricated from these films. Epitaxial growth often suffers from lattice mismatching constraints from producing high quality thin films.

Crystal ion slicing technique, which is known under the name of ”smart cut”, in combination with wafer bonding techniques is the most promising way to produce TFLN of high quality. This method was originally discovered and applied for the fabrication of SOI wafers [105, 106] and the process was disclosed in 1995 [107]. It uses high-dose implantations of H^+ and/or He^+ ions (dose D= $10^{16}10^{17}/cm^2$) for cleaving films from a bulk material. Smart cut have advantages of being able to produce a high refractive index contrast single crystalline TFLN on LN substrate or other exotic substrate material such as silicon.

The prevalent configurations of TFLN are a few hundred nanometers thick thin film crystal-bonded to a SiO_2/LN substrate [97]. Compared to the early studies where the buffer layer is benzocyclobutene (BCB) [108, 109], SiO_2 as insulator enables annealing at much higher temperatures which can minimize ion-implantation induced material damage and help to recover EO and nonlinear optical properties of the cleaved LN film. In addition, high temperature annealing contributes significantly in reducing the surface roughness of ion beam etched thin film.

The TFLN on SiO_2/LN substrate fabrication process is schematically shown in Fig. 1.12. First, a handle wafer is processed with He^+ implantation as shown in Fig. 1.12 (a). He^+ implantation is chosen as a suitable ion source for slicing LN thin film which is based on a high dose ion implantation and epitaxial lift-off. In the implanted layer, He^+ forms gaseous bubbles, also referred to as blisters. Basically, thin film exfoliation or lift-off from an implanted LN crystal can be achieved either by HF (hydrofluoric) wet-etching [110] or thermal treatment. Etching exfoliation of thin film will introduce continually and gradually varies in thickness [111], being thicker in the center and thinner towards the edges, where the exposure to HF was longer in wet etching process [112]. Henceforth, thermal treatment is often chosen as way to produce a more uniform sub-micrometer thin LN films. The energy of the implantation can be adjusted to select the film thickness.

Another LN handle sample as shown in Fig. 1.12 (b) is coated by a SiO_2 layer by plasma enhanced chemical vapor deposition

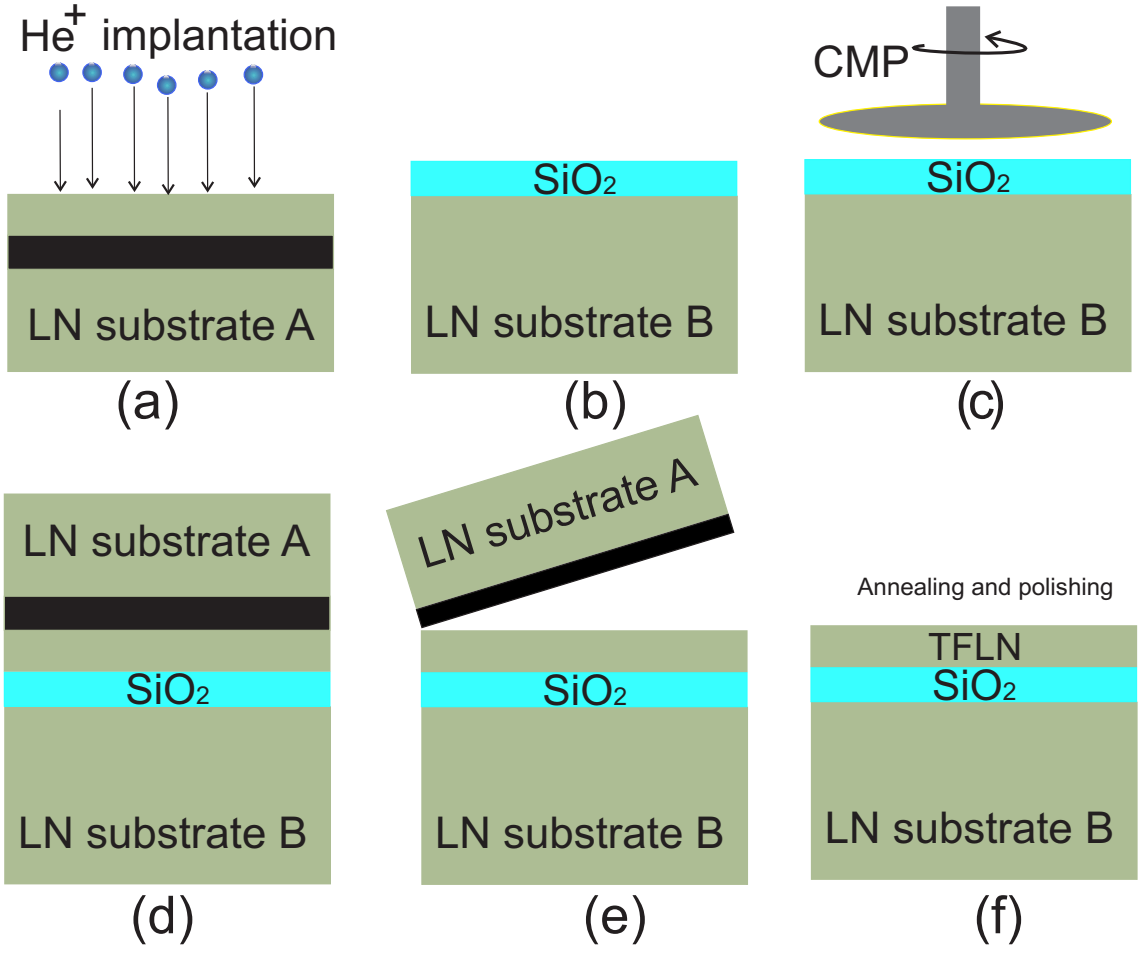

FIGURE 1.12 – (a) He-ions implantation to form an amorphous layer. (b) PECVD of silica-layer as insulator between ion sliced thin film and LN substrate. (c) CMP to reduce surface roughness down to 0.3 nm enabling direct bonding. (d) Wafer bonding. (e) Thermally annealing to induce exfoliation of the thin film (f) Annealing treatment to recover EO and nonlinear properties of the thin film and CMP process to form uniform sub-micrometer LN thin film.

(PECVD). Annealing is performed to drive off the gases trapped in the oxide layer. Subsequently as shown in Fig. 1.12 (c), the deposited silica will go through a chemical mechanical polishing (CMP) process to reduce the surface roughness down to 0.3 nm or even smaller as 0.1 nm facilitating direct wafer bonding processing as shown in Fig. 1.12 (d). Special annealing process is necessary to exfoliate thin film layer and to recover the EO and nonlinear properties of the bonded thin films as shown in Fig. 1.12 (e). CMP and subsequent surface cleaning at the end of the bonded pair is of key importance to achieve the required surfaces with low roughness. Thin films on LN substrate or silicon substrate with silica as insula-

tor layer have been achieved in wafer scale in different crystalline orientations.

Early works on investigating properties of CIS (crystal ion slicing) TFLN are done on the scale of 10 μm, which is much thicker than the films employed in this thesis. However, since they shared similar thin film production technique, the properties of the TF would expect to be the same. A variety of devices had been investigated on TFLN configurations and proved that these ion-sliced thin films are monocrystalline and thus retain their bulk optical, dielectric, magnetic, electro-optical and crystallographic properties.

The pioneering work of producing CIS of 9 μm thick films are described in [96], in which experiments are carried out to show single-crystal films have the same room-temperature dielectric, pyroelectric characteristics and ferroelectric transition temperature as single-crystal bulk LN. A stronger high-temperature pyroelectric response is found in these CIS films. CIS films suffer no degradation to the optical properties of the bulk material, such as formation of artificial birefringence. Various devices have been investigated in these type of films. It has been used to create functional optical devices such as TE-TM converters and wave plates [113] etc. CIS thin film was heterogeneously integrated onto glass substrate to investigate second harmonic generation efficiency, where the phase matching condition is provided by tuning the waveguide dispersion and implantation induced shifts in the refractive indices [114]. It is found that these thin films have a comparable nonlinear response as that of the bulk. A low loss ridge WG on CIS z-cut TFLN bonded to silica/LN substrate with vertical electrodes was fabricated and demonstrated as a phase modulator with $V_\pi L$ of 15 Vcm at 1.55 μm which yielded an estimated EO coefficient of TFLN r_{33}=31 pm/V [115].

Using benzocyclobutene as cladding layer, $LiNbO_3$ films of several cm^2 size were realized and an EO tunable micro-ring resonators was reported to show the possibilities for the use of lithium niobate in chip-scale integrated optical devices and nonlinear optical microcavities [108].

Up to now, direct electric field poling of TFLN samples was not yet successful. Probably it is due to small defects in the LN layer or in

the LN channel leading to electrical breakdown before domain inversion can be achieved. The alternative strategy to develop QPM nonlinear optical interactions is to poled the sample before the CIS in order to create buried sacrificial layer. Thin single-crystal films fabricated by ion exfoliation of a bulk periodically pole LN (PPLN) crystal are fabricated and it is shown that a reduced tuning voltages for electro-optically tunable harmonic generation in thin PPLN devices [116] can be obtained.

Experiments are conducted to directly measure the optical and EO properties of the thin film [117] which includes AFM to characterize the surface morphology of the thin film and prism coupling method to measure the refractive index and EO coefficient of the thin film. These experiments demonstrate the high quality of the thin film which have optical properties that are comparable to bulk material. Experiments of X-ray diffraction and Rutherford back-scattering spectrum are conducted in [118] to show that TFLN bonded to a substrate with silica cladding have a good crystal lattice arrangement and have optical properties similar to that of bulk LN [118].

Despite the fact that numerous works have been investigated on the TFLN based devices such as second harmonic generation, EO modulation and low loss photonic wire etc, there are only few works on LN thin film based photonic sensors exploiting the EO effect. With the high quality LN thin films, this thesis is devoted to exploit the EO based sensors on LN thin film in hope of further scaling down the device into a integratable compact size sensor with high sensitivity.

1.4/ PHOTONIC CRYSTALS : GENERALITIES

Photonic crystals (PhC) as that shown in Fig. 1.13(a) are artificial structures that have a periodic dielectric constant which are designed to control photons in the same way that crystals in solids control electrons [119, 120, 121]. They are promising artificial crystals for the miniaturization of integrated optics and for the enhancement of light-matter interactions. The periodic modulation of the refractive index in a PhC provides great freedom on the optical dispersion relation engineering. Particularly interesting is the existence

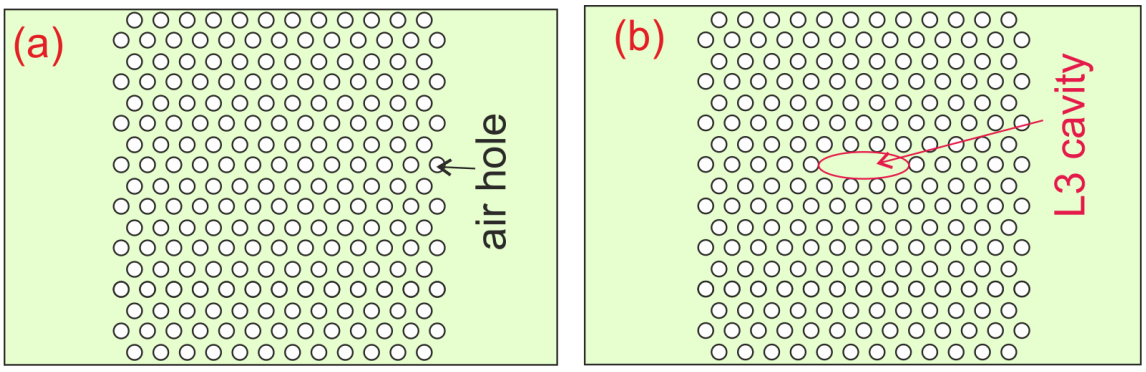

FIGURE 1.13 – (a) Schematic of triangular lattice air holes PhC in a homogeneous medium. (b) Schematic of a L3 cavity in a triangular PhC lattice.

of a photonic bandgap : a range of optical frequencies that are forbidden to propagate in the material [122, 123, 124]. If a waveguide is embedded in a PhC [125, 126], light cannot escape the waveguide through the PhC. This phenomenon can be used to create sharp waveguide bends and high-Q cavities [127, 128]. In this way, a photonic bandgap can be exploited for the fabrication of integrated optical devices at micron-meter scale. Several important properties of PhC are outlined as follows :

— Nanostructuring PhC is wavelength-independent, i.e. it can be adjusted to any wavelength of interest within the transparency window of the material ;
— PhC is material independent, it can be fabricated on almost any kind of material with the aid of modern nano fabrication technique.
— Multi-functional devices can be carved out in different PhC structures. Light propagation can be completely guided along a path of the linear defects that is introduced in PhC, in what is called a PhC WG, even when it largely bends. Sensors, filters, switches can be designed based on PhC cavity structures.
— Highly dispersive properties in PhC allow for example slow light propagation, which can be exploited in the enhancement of nonlinear phase sensitivity ;

PhC cavities such as a L3 (removing three air holes in a line) cavity shown in Fig. 1.13(b), which trap light within a finite volume, are an essential component of many important optical devices and effects, ranging from lasers [129, 130, 131, 132, 133, 134, 135], filters [136],

single photon sources [137] and sensors [138] etc. The most distinguishing feature of cavities is that they provide extraordinarily small mode volumes and very sharp resonances, resulting in high optical Q-factors up to such as 10^{14} in Si photonics [12, 14] which allows for various nonlinear effects operating at rather low light intensities thresholds. This, in turn, opens the possibilities to conveniently investigate nonlinear optical effects at power levels of the order of milliwatts, which is practically impossible with bulk optical objects.

There are many types of PhC cavities. We can obtain them by creating defect inside the PBG [134, 139] or by band engineering in order to select a mode that lies at the band-edge and possesses slow group velocity [140, 141]. Thanks to the potentials offered by PhC, a considerable size reduction can be achieved in order to realize extremely compact optical integrated devices such as micro and nanoscale switches, modulators, sensors etc that can exhibit enhanced nonlinearities [142, 143].

Enhanced nonlinear effects in PhC can be understood as a result of the compression of the local energy density in a cavity that operates at slow group velocity regime. It has been demonstrated by Soljacic et al [142] that the phase sensitivity linked to the induced change of the refraction index can be drastically enhanced if it operates in the regime of slow group velocities which occur quite commonly in PhC structures. According to perturbation theory, the induced shift in the optical frequency of a photonic band mode at a fix k which is due to a small δn is given by $\delta\omega(k)/w = -\sigma(\delta n/n)$. Where σ specifies the fraction of the total energy of the mode stored in the region where δn is being applied. The induced phase shift $\delta\phi = L * \delta k$, while δk is liked to group velocity by $V_g = d\omega/dk$. Henceforth, we have :

$$\delta\phi \approx L * \delta\omega/(dw/dk) \Rightarrow \delta\phi \approx L\omega\sigma\delta n/nV_g \tag{1.7}$$

Let the phase shift $\delta\phi = \pi$, we have

$$\frac{L}{\lambda_{air}} \approx \frac{1}{2\sigma}\left(\frac{n}{\delta n}\right)\left(\frac{V_g}{c}\right) \tag{1.8}$$

Eq. 1.8 indicates that for a given δn, the size of the device scales linearly with V_g. Moreover, for an electro-optical device that is smaller in length by a factor of V_g/c and it also requires V_g/c less power to

operate. Thus for EO based devices such as modulator, switch and sensors, the enhancement is a factor of $\left(c/V_g\right)^2$.

Slow group velocity mode combined with a highly flexible dispersion engineering structure, together with high confinement of light makes PhC a promising candidate in developing sensors with unprecedented sensitivities. Henceforth, this thesis explores PhC cavity based EO sensors on TFLN.

Cavity based sensors operate with the principle that the optical properties can be modified by an external physical signal such as an electric or magnetic field, temperature and strain etc. In order to achieve high sensitivity in a compact size, efforts were made in finding cavities with high quality factor Q, high extinction ratio (ER) characteristics and high light confinement.

1.5/ OUTLINE OF THIS THESIS

Beside this introduction chapter where the theme of studying PhC in sensing application on TFLN PhC is presented, this thesis is composed of three more chapters.

Chapter 2 presents the numerical calculation method employed in this work which include waveguide mode calculations, PhC dispersion relationship modeling, FDTD methods to simulate 2D and 3D structure through transmission/reflection investigations etc.

In chapter 3, different WG configurations (ridge WG, strip loaded WG, slot WG and double slot WG) are studied on TFLN. Defect mode in the band gap formed by PhC mirror based Fabry-Perot cavity are designed in slot WG and strip loaded WG. Fabrications attempts of slot WG and strip loaded are also presented.

Chapter 4 describes the design of guided resonance based cavities on TFLN. Systematic simulations are performed to find a suitable configuration for sensing applications. The sensitivity of the proposed structure employed as E-field sensor is theoretically estimated. These in-depth GR structure studies can be a promising candidate to build on-fiber end sensor where the PhC structure are attached

to the fiber end face.

The last chapter summarizes the results obtained from this work and gives a perspective for the future research on this related topics.

2

NUMERICAL SIMULATION TOOLS

In order to accurately study light propagation and resonance phenomenon in nano PhC devices, one needs to solve the Maxwell equations which represent one of the most elegant and concise way to state the fundamentals of electricity and magnetism. The macroscopic derivative form of the Maxwell equation is described as follows :

$$\nabla \cdot \mathbf{B} = 0 \quad Gauss' \ Law \ for \ magnetism \tag{2.1}$$

$$\nabla \cdot \mathbf{D} = \rho \quad Gauss' \ Law \ for \ electricity \tag{2.2}$$

$$\nabla \times \mathbf{H} = \frac{\partial \mathbf{D}}{\partial t} + \mathbf{J} \quad Ampere - Maxwell \ Law \tag{2.3}$$

$$\nabla \times \mathbf{E} = -\frac{\partial \mathbf{B}}{\partial t} \quad Faraday's \ Law \ of \ induction \tag{2.4}$$

Where **E** is the electric field vector, **D** is the displacement field vector, **H** is the magnetic field vector, **B** is the magnetic flux density vector, **J** is the electric current density vector and ρ is the free charge density. Both Eq. 2.1 and Eq. 2.2 are derived from Gauss's law. Equation 2.1 indicates that there is no magnetic source and the total magnetic flux piercing a closed surface is zero. Equation 2.3 is derived from Ampère's law, which indicates that electrical current (both the conductive current **J** and the displacement current $\frac{\partial \mathbf{D}}{\partial t}$) induces the magnetic field. Equation 2.4 is derived from Farady's laws, which indicates that the temporal variation of the magnetic field induces an electrical field [144, 145, 146].

In addition to these four equations, constitutive equations which describe the response of the medium to the electromagnetic field are essential to solve the electromagnetic (EM) problems. In general, the components D_i of the displacement field **D** are related to the components E_i of the electric field **E** via a complicated power series, as in Bloembergen [147] :

$$D_i/\epsilon_0 = \sum_j \epsilon_{ij} E_j + \sum_{j,k} \chi_{ijk} E_j E_k + O(\mathbf{E}^3) \tag{2.5}$$

Where $\epsilon_0 \approx 8.854 \times 10^{-12}$ F/m (farads per meter) is the vacuum permittivity. We will restrict ourselves to linear, lossless materials (non-dispersive material). Usually we consider a situation with no free charges or currents, i.e there are no sources of light, thus we can set $\rho = 0$ and $\mathbf{J} = \vec{0}$. Without specific additional statement, we ignore any explicit frequency dependence of the dielectric function $\epsilon(\mathbf{r}, \omega)$ which is also called the relative permittivity. Instead, we simply choose the value of the dielectric constant appropriate to the frequency range of the physical system that we are considering. This is fully valid when we deal with non-metallic dielectric materials. Henceforth we can formulate the constitutive relations as $\mathbf{D}(\mathbf{r}) = \epsilon(\mathbf{r})\mathbf{E}(\mathbf{r})$. The relative magnetic permeability $\mu(\mathbf{r})$ of most dielectric materials of interest is very close to unity and we may set $\mathbf{B} = \mu_0 \mathbf{H}$ for simplicity, where $\mu_0 = 4\pi \times 10^{-7}$ Henry/m is the vacuum permeability. For all but the most simple structures, the Maxwell equations cannot be solved analytically. Consequently it is essential to apply numerical modeling tools for the study and design of optical components and devices etc.

For better understanding of different numerical calculation methods that will be described later, we expand the Maxwell equations in the form of different components explicitly expressing the nabla symbol ∇ as three-dimensional gradient operator in Cartesian coordinates [148]. The curl operator $\nabla\times$ expressed in Cartesian coordinates is as follows :

$$\nabla \times \mathbf{E} \Rightarrow \begin{vmatrix} x & y & z \\ \frac{\partial}{\partial x} & \frac{\partial}{\partial y} & \frac{\partial}{\partial z} \\ \mathbf{E}_x & \mathbf{E}_y & \mathbf{E}_z \end{vmatrix}$$

Thus, **E** component in Eq. 2.3 yields the following equations in the

form of different components :

$$\frac{\partial \mathbf{E}_x}{\partial t} = \frac{1}{\epsilon}(\frac{\partial \mathbf{H}_z}{\partial y} - \frac{\partial \mathbf{H}_y}{\partial z})$$

$$\frac{\partial \mathbf{E}_y}{\partial t} = \frac{1}{\epsilon}(\frac{\partial \mathbf{H}_x}{\partial z} - \frac{\partial \mathbf{H}_z}{\partial x})$$

$$\frac{\partial \mathbf{E}_z}{\partial t} = \frac{1}{\epsilon}(\frac{\partial \mathbf{H}_y}{\partial x} - \frac{\partial \mathbf{H}_x}{\partial y}) \tag{2.6}$$

Likewise for **H** we have :

$$\frac{\partial \mathbf{H}_x}{\partial t} = \frac{1}{\mu_0}(\frac{\partial \mathbf{E}_y}{\partial z} - \frac{\partial \mathbf{E}_z}{\partial y})$$

$$\frac{\partial \mathbf{H}_y}{\partial t} = \frac{1}{\mu_0}(\frac{\partial \mathbf{E}_z}{\partial x} - \frac{\partial \mathbf{E}_x}{\partial z})$$

$$\frac{\partial \mathbf{H}_z}{\partial t} = \frac{1}{\mu_0}(\frac{\partial \mathbf{E}_x}{\partial y} - \frac{\partial \mathbf{E}_y}{\partial x}) \tag{2.7}$$

The numerical modeling methods involved in this thesis are mostly based on finite difference methods in which finite differences approximate the derivatives. They are implemented either in Fortran or Matlab languages. They can be categorized as follows according to what is calculated :

- Optical waveguide (WG) mode calculations by FDTD (finite diference time domain) [149, 150], FDFD (finite diference frequency domain) [151] methods and FD-BPM (finite diference-beam propagation method) [152].
- PhC dispersion diagram calculations by frequency-domain PWE (plane wave expansion) method [122].
- Optical transmission and/or reflection calculations by 2D-FDTD and 3D-FDTD [150].

The principle of these numerical methods will be elaborated in detail in the following sections.

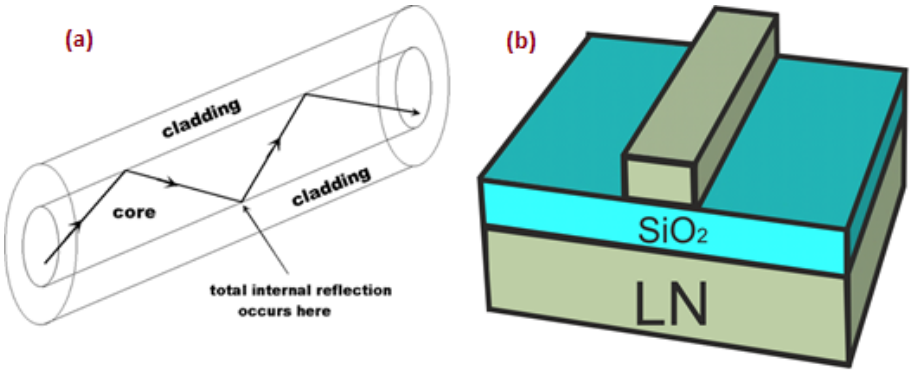

FIGURE 2.1 – (a) Optical fiber. (b) Ridge WG.

2.1/ OPTICAL MODE CALCULATION METHODS : FDTD, FDFD, BPM

Optical WGs are used to transfer electromagnetic power in optical frequency from one point to another. Usually, a WG guides light in high refractive index material by total internal refraction such as optical fiber and ridge WGs shown in Fig. 2.1. Optical WGs typically maintain a constant cross-section along their direction of propagation (except WGs such as segmented WGs with 1D patterning and PhC WGs with 2D or 3D patterning). Henceforth, one can obtain the WG mode field distribution confined in the vicinity of the guiding structure via solutions of Maxwell's equations. Three mode solver methods, FDTD, FDFD and BPM, are employed to model suitable WG configurations on TFLN. Among them, FDFD and FDTD are implemented by home-made codes which are methods based on the solution of Maxwell equations, while BPM methods introduce some approximations. The WG operating wavelength is set at 1.55 μm.

FDFD method calculates the mode effective index and mode field distribution at a fixed wavelength by expressing Maxwell equations in frequency domain. Mode solving through FDTD method needs two steps : first input a propagation vector constant to calculate the mode frequency which is represented as a peak in energy density spectrum ; then re-run a second calculation at the supported mode frequency wavelength at continuous wave excitation to obtain the mode field distributions.

Finite difference BPM is implemented in the commercial software

(RSOFT). It introduces some approximations on calculating the mode field distribution yielding an efficient computational speed. BPM mode solver is employed to perform a systematical WG mode studies due to its calculation efficiency. The principle of these mode solver methods will be described in detail in the following subsections respectively.

2.1.1/ FINITE DIFFERENCE TIME DOMAIN

Let us introduce the FDTD mode solver method by writing the EM field along a z propagation WG as follows :

$$\begin{aligned}\mathbf{E}(x,y,z,t) &= \mathbf{E}(x,y,t)exp(ik_z z)\\ \mathbf{H}(x,y,z,t) &= \mathbf{H}(x,y,t)exp(ik_z z)\end{aligned} \tag{2.8}$$

Substituting Eq. 2.8 into Eq. 2.6 and Eq. 2.7 and replacing the z dependent partial differential terms by ik_z, one gets the following equations for updating EM fields in the FDTD mode calculations :

$$\begin{aligned}\frac{\partial \mathbf{H}_x}{\partial t} &= \frac{1}{\mu_0}\left(ik_z\mathbf{E}_y - \frac{\partial \mathbf{E}_z}{\partial y}\right)\\ \frac{\partial \mathbf{H}_y}{\partial t} &= \frac{1}{\mu_0}(\frac{\partial \mathbf{E}_z}{\partial x} - ik_z\mathbf{E}_x)\\ \frac{\partial \mathbf{H}_z}{\partial t} &= \frac{1}{\mu_0}(\frac{\partial \mathbf{E}_x}{\partial y} - \frac{\partial \mathbf{E}_y}{\partial x})\\ \frac{\partial \mathbf{E}_x}{\partial t} &= \frac{1}{\epsilon}(\frac{\partial \mathbf{H}_z}{\partial y} - ik_z\mathbf{H}_y)\\ \frac{\partial \mathbf{E}_y}{\partial t} &= \frac{1}{\epsilon}(ik_z\mathbf{H}_x - \frac{\partial \mathbf{H}_z}{\partial x})\\ \frac{\partial \mathbf{E}_z}{\partial t} &= \frac{1}{\epsilon}(\frac{\partial \mathbf{H}_y}{\partial x} - \frac{\partial \mathbf{H}_x}{\partial y})\end{aligned} \tag{2.9}$$

In order to update the EM fields sequentially according to the above equations, one need to set an initial field. Initial conditions include

material distribution as the one shown in Fig. 2.2(a), an input propagation vector constant k_z and initial field distribution. Since a WG is considered as invariant along the z propagation direction, only xy cross section of the material properties $\epsilon(x, y)$ is needed for medium descriptions. Initial field can be a Gaussian source with the field amplitude in the form of $exp(-x^2/2{\sigma_x}^2 - y^2/2{\sigma_y}^2)$ where σ_x can be chosen as the width of the WG and σ_y be the height of the WG. As far as the output is concerned, one can record the related EM

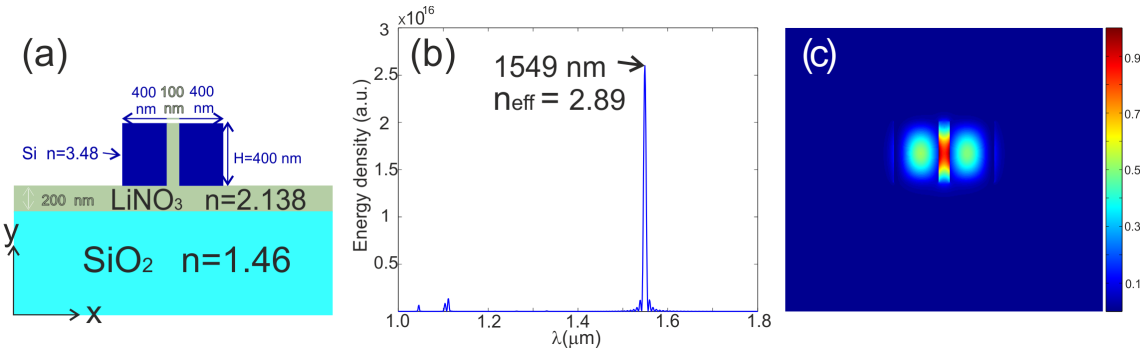

FIGURE 2.2 – (a) Schematic cross-section of the slot WG considered in the FDTD mode calculation window. The calculation window size is 590×490 in the xy cross section, and a uniform meshing of d_x= d_y= 5 nm is employed. (b) Energy density spectrum. (c) Normalized electric field amplitude x component of the calculated mode profile.

fields to extract the calculation results. At some randomly sample points in the calculation window, the time domain EM fields are recorded at each time step (or a few time steps to decrease memory requirement but attention should be paid to ensure satisfying the Nyquist sampling frequency relationship). These time sequential fields are then processed through Fourier transformations (FT) in order to obtain the frequency response [153]. Energy density spectrum in frequency domain is calculated through FT signals where the peak in the energy density spectrum ($W = \frac{1}{2}(\vec{E} \cdot \vec{D} + \vec{H} \cdot \vec{B})$) corresponds to the supported eigen-frequency of the given propagation vector constant k_z as the one located at 1549 nm shown in Fig. 2.2(b). This peak corresponds to a optical mode with effective index of 2.89. We should notice that this method can also be easily employed to determine the dispersion properties of the WG since k_z and WG modes frequency can be easily deduced from the energy density spectrum as that is shown in Fig. 2.2(b).

In order to obtain the WG mode profile, a second calculation with

continuous wave (CW) excitation at the previous calculated eigen-frequency position is performed to obtain the EM field distributions. The mode field distributions of the structure in Fig. 2.2(a) is shown in Fig. 2.2(b). It is obtained by CW simulation at the wavelength of 1549 nm corresponds to the peak wavelength in Fig. 2.2(b). Since the preferable WG mode frequency is at 1.55 μm, one needs to scan over different propagation constants in order to put the WG operation wavelength at the desired values. Nevertheless, the FDTD mode calculation method is the exact solution of Maxwell's equations yielding the most reliable results among all the methods.

2.1.2/ FINITE DIFFERENCE FREQUENCY DOMAIN

FDFD represents one of the complementary tools for better understanding optical and EM phenomena. The term "FDFD" was first used in 1989 by Ling [151]. It is a finite difference method on frequency domain to solve the Maxwell's equations. This kind of frequency-domain equations is crucial to study steady states and treats the dispersive materials accurately. Here we apply FDFD method in solving WG modes.

The method works by transforming partial differential equations (in our case Maxwell's equations) at a constant frequency into matrix form $Ax = b$. The matrix A is derived from the wave equation operator. The column vector x contains the field components and the column vector b describes the source [154, 155, 156, 157, 158]. Here we present the FDFD method for finding the modes of a structure in the absence of sources. In this case the frequency ω is itself a variable and we obtain an eigen problem in the form of $Ax = \lambda x$ (usually, the eigenvalue λ is ω^2). Note that the Gauss law for electric and magnetic inductions are implicit in the FDFD algorithm. From source free Maxwell's curl equations ($\nabla \times \mathbf{E} = -\partial \mathbf{B}/\partial t, \nabla \times \mathbf{H} = -\partial \mathbf{D}/\partial t$) and assuming the fields have the dependence of $exp[i(\beta z - \omega t)]$, we have :

$$i\omega\mu \mathbf{H}_x = \partial \mathbf{E}_z/\partial y - i\beta \mathbf{E}_y$$

$$i\omega\mu\mathbf{H}_y = i\beta\mathbf{E}_x - \partial\mathbf{E}_z/\partial x$$

$$i\omega\mu\mathbf{H}_z = \partial\mathbf{E}_y/\partial x - \partial\mathbf{E}_x/\partial y$$

$$i\omega\epsilon\mathbf{E}_x = \partial\mathbf{H}_z/\partial y - i\beta\mathbf{H}_y$$

$$i\omega\epsilon\mathbf{E}_y = i\beta\mathbf{H}_x - \partial\mathbf{H}_z/\partial x$$

$$i\omega\epsilon\mathbf{E}_z = \partial\mathbf{H}_y/\partial x - \partial\mathbf{H}_x/\partial y \tag{2.10}$$

By denoting the derivation in Eq. 2.10 with finite central difference on Yee-mesh and some algebra, we can have the following matrix form of equations in frequency domain [156] :

$$i\omega\mu\begin{bmatrix}\mathbf{H}_x\\ \mathbf{H}_y\\ \mathbf{H}_z\end{bmatrix} = \begin{bmatrix}0 & -i\beta\mathbf{I} & \mathbf{U}_y\\ i\beta\mathbf{I} & 0 & -\mathbf{U}_x\\ -\mathbf{U}_y & \mathbf{U}_x & 0\end{bmatrix}\begin{bmatrix}\mathbf{E}_x\\ \mathbf{E}_y\\ \mathbf{E}_z\end{bmatrix} \tag{2.11}$$

$$i\omega\epsilon\begin{bmatrix}\epsilon_{rx} & 0 & 0\\ 0 & \epsilon_{ry} & 0\\ 0 & 0 & \epsilon_{rz}\end{bmatrix}\begin{bmatrix}\mathbf{E}_x\\ \mathbf{E}_y\\ \mathbf{E}_z\end{bmatrix} = \begin{bmatrix}0 & -i\beta\mathbf{I} & \mathbf{V}_y\\ i\beta\mathbf{I} & 0 & -\mathbf{V}_x\\ -\mathbf{V}_y & \mathbf{V}_x & 0\end{bmatrix}\begin{bmatrix}\mathbf{H}_x\\ \mathbf{H}_y\\ \mathbf{H}_z\end{bmatrix} \tag{2.12}$$

Where $\mathbf{I}$ is a square identity matrix. $\mathbf{U}_x$, $\mathbf{U}_y$, $\mathbf{V}_x$, $\mathbf{V}_y$ are square matrices and depend on boundary conditions of the rectangular computational window. ϵ_{rx}, ϵ_{ry}, ϵ_{rz} are diagonal matrices related to the material distribution of the structure as described in [156]. After some algebra with Eq. 2.11 and 2.12, we can obtain an eigenvalue equations in terms of the transverse electric field :

$$\mathbf{P}\begin{bmatrix}\mathbf{E}_x\\ \mathbf{E}_y\end{bmatrix} = \beta^2\begin{bmatrix}\mathbf{E}_x\\ \mathbf{E}_y\end{bmatrix} \tag{2.13}$$

Alternatively, the eigenvalue equation in terms of transverse magnetic field is as follows :

$$\mathbf{Q}\begin{bmatrix}\mathbf{H}_x\\ \mathbf{H}_y\end{bmatrix} = \beta^2\begin{bmatrix}\mathbf{H}_x\\ \mathbf{H}_y\end{bmatrix} \tag{2.14}$$

where **P** and **Q** are coefficient matrix derived from Eq. 2.11 and 2.12 which contains the material permittivity distribution and the frequency information etc. Thus Eq. 2.13 and 2.14 transform the mode solving problem into an eigenvalue problem where the eigenvalue β contains the mode effective index information and the eigen vector contains the mode field distribution. This FDFD mode solving technique has been implemented in Matlab code by employing the built-in eigenvalue function in Matlab to solve Eq. 2.13 and 2.14. A mode solving example of strip loaded WG on $BaTiO_3$ is shown in Fig. 2.3. The structure (Fig. 2.3(a)) is modeled by a calculation win-

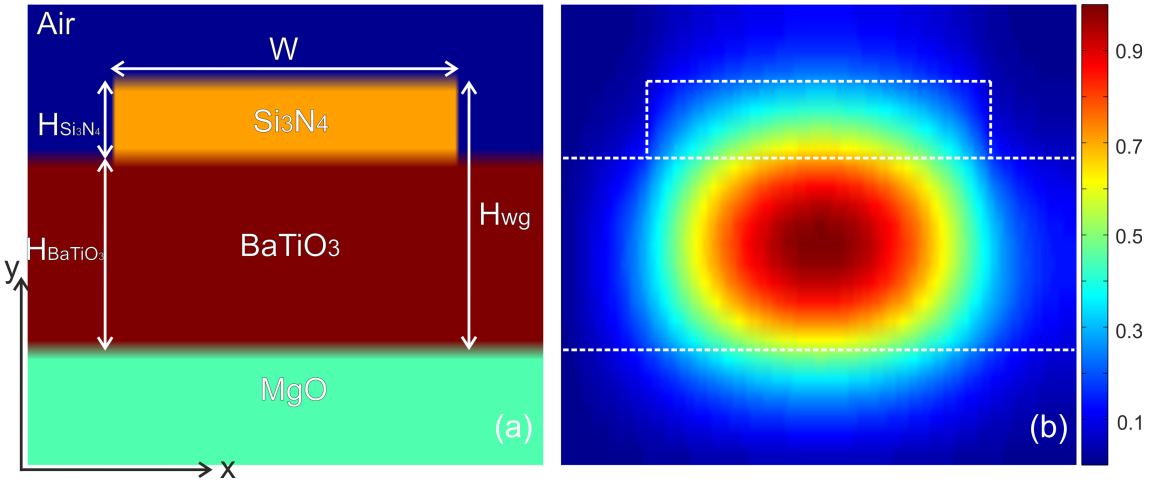

FIGURE 2.3 – (a) Schematic drawing of $BaTiO_3$ WG with Si_3N_4 strip loaded structure considered in FDFD simulation. The WG consists of three regions : the Si_3N_4 (n= 2.01, $W_{Si_3N_4}$= 4 μm, $H_{Si_3N_4}$= 0.2 μm) layer, $BaTiO_3$ (n=2.3, H_{BaTiO_3}= 0.5 μm) layer, and MgO (n=1.7) substrate respectively [8]. The meshing size d_x= d_y= 50 nm. The calculation window size in xy plane is 120×24. (b) Calculated x-polarized mode profile of electric field x component distribution of the strip loaded WG with a mode effective index of 2.12. The dashed white lines show the geometry of the WG.

dow of 120×24 which leads to a size of 120×24 by 120×24 square matrices of $\mathbf{U}_x$, $\mathbf{U}_y$, $\mathbf{V}_x$, $\mathbf{V}_y$. The coefficient matrices **P** and **Q** are square matrices with a size of 120×24×2 by 120×24×2. The calculation time took about 3.5 hours in a work station of 16 cores. This long calculation time leads to only a coarse meshing of 50 nm is utilized in order to obtain the results in a cost-effect way. Notice that, upon solving the Eq. 2.13 and 2.14, the mode effective index in a fixed frequency can be easily obtained. Henceforth, it is oftentimes combined with FDTD mode solving technique to calculate the mode field distributions.

2.1.3/ BEAM PROPAGATION METHOD

BPM is the most widely used propagation technique for modeling integrated and fiber optic photonic devices and most commercial software for such modeling is based on it. It is conceptually straightforward. We will first illustrate the principle of FD (finite difference)-BPM methods and then describe the mode solver technique through BPM calculations [159, 160, 161, 162].

FD-BPM employs finite difference methods to solve the well known parabolic or paraxial approximation of the Helmholtz equation. The basic approach is illustrated by formulating the problem under the restrictions of a scalar field (i.e. neglecting polarization effects) and paraxiality (i.e. propagation restricted to a narrow range of angles). The scalar field assumption which yields to the well-known Helmholtz equation for monochromatic waves as follows :

$$\frac{\partial^2\phi}{\partial^2 x} + \frac{\partial^2\phi}{\partial^2 y} + \frac{\partial^2\phi}{\partial^2 z} + k^2(x,y,z)\phi = 0 \tag{2.15}$$

where the scalar electric field has been written as $E(x,y,z,t) = \phi(x,y,z)e^{-\omega t}$, and $k(x,y,z) = k_0 n(x,y,z)$ is the spatially dependent wavenumber. $k_0 = 2\pi/\lambda$ being the wavenumber in free space. In a guided wave problem, assuming the propagation direction along z direction, the most rapid variation in the field ϕ is the phase variation along z. It is beneficial to factor this rapid variation out of the problem by introducing a so called slowly varying field u via the ansatz :

$$\phi(x,y,z) = u(x,y,z)e^{i\bar{k}z}$$

where $\bar{k}$ is a constant number which represents the average phase variation of the field ϕ and is refered to as the reference wavenumber. The Helmholtz equation under slowly varying field assumption yields :

$$\frac{\partial^2 u}{\partial z^2} + 2i\bar{k}\frac{\partial u}{\partial z} + \frac{\partial^2 u}{\partial x^2} + \frac{\partial^2 u}{\partial y^2} + (k^2 - \bar{k}^2)u = 0 \tag{2.16}$$

It is now assumed that the variation of u with z is sufficiently slow so that the first second order derivation term above can be neglected. This is the familiar slowly varying envelope approximation and here it is also referred to as the paraxial or parabolic approximation. With

this assumption and after slight rearrangement, the above equation reduces to :

$$\frac{\partial u}{\partial z} = \frac{i}{2\bar{k}}[(\frac{\partial^2 u}{\partial x^2}) + \frac{\partial^2 u}{\partial y^2} + (k^2 - \bar{k}^2)u] \tag{2.17}$$

This is the basic BPM equation in three dimensions. Given an input field, $u(x, y, z = 0)$ the above equation determines the evolution of the field in the space $z > 0$. Due to the paraxial and scalar field assumption, the basic BPM has limited applications. Fortunately, there are ways to relax all these constraints. Next, we will discuss about the extending of basic BPM to full-vectorial and wide angle FD-BPM methods by adding effects such as vector nature of EM field and wide angle propagation into the algorithms.

Vectorial BPM

The electromagnetic field is essentially vectorial and the vector nature is very important for us in order to obtain the correct results. Here we discuss the vectorial BPM methods. Polarization effects can be included in BPM by recognizing that the electric field **E** is a vector, and starting the derivation from the vector wave equation rather than the scalar Helmholtz equation as in Eq. 2.15.

In one approach, the equations are formulated in terms of the transverse components of the field ($\mathbf{E}_x$ and $\mathbf{E}_y$), and result in the following set of coupled equations for the corresponding slowly varying fields (u_x and u_y) :

$$\frac{\partial u_x}{\partial z} = A_{xx}u_x + A_{xy}u_y$$

$$\frac{\partial u_y}{\partial z} = A_{yx}u_x + A_{yy}u_y \tag{2.18}$$

The A_{ij} are complex differential operators, more details of the vector FD-BPM can be found in ref [152, 160, 163]. The Eqs. 2.18 are generally referred to as describing a full-vectorial BPM.

Wide-angle BPM

The fundamental physical limitation of the above methods from the parabolic approximation to the Helmholtz equation, is that it implies a paraxiality condition on the primary direction of propagation. Due to the fact that $\partial^2 u/\partial z^2$ term was neglected in the derivation of the basic BPM, it leads to the limitation of BPM to paraxiality restriction. Numerous approaches vary in the method and degree of approximation achieved in deducing the wide-angle BPM. A simple approach for deriving a wide-angle BPM equation is to consider the Helmholtz wave equation written in terms of the slowly varying field (Eq. 2.16), but before making the slowly varying envelope approximation by neglecting the $\partial^2 u/\partial z^2$ term. If **D** denotes $\partial/\partial z$ in this equation, then $\partial/\partial z^2$ is represented by $\mathbf{D}^2$. Putting aside the fact that **D** is a differential operator, the equation can now be viewed as a quadratic equation to be solved for **D**, yielding the following formal solution for a first order equation in z :

$$\frac{\partial u}{\partial z} = i\bar{k}(\sqrt{1+P}-1)u \tag{2.19}$$

$$where\ P \equiv \frac{1}{\bar{k}^2}\left(\frac{\partial^2}{\partial x^2} + \frac{\partial^2}{\partial y^2} + (k^2 + \bar{k}^2)\right)$$

Differential operator P can be evaluated through Taylor expansion or Padé approximation [164]. Thus now we had already shown the formulation of wide-angle full-vectorial BPM method. The boundary conditions can be chosen as transparent boundary conditions, which is generally very effective in allowing radiation to freely escape the computational domain. The physical propagation problem requires two key pieces of information : 1) the refractive index distribution, $n(x, y, z)$ and 2) the input wave field, $u(x, y, z = 0)$. From these information, the physics dictates the wave field throughout the rest of the domain $u(x, y, z > 0)$. BPM methods are efficient and straight forward when they are applied to study the propagation of EM field along a structure that is invariant along propagation directions. Thus, it is oftentimes applied to study direction coupler, taper design, WG propagation loss etc.

BPM mode solver

Mode solving through BPM is obtained though correlation method or imaginary distance BPM. The latter is generally significantly faster [163]. Here we will briefly illustrate the principle of imaginary distance BPM based mode solver which is the method employed in the WG modes studies in Chapter 3.

Considering 2D propagation of a scalar field for simplicity, the incident field $\phi_{in}(x)$ can be expanded with the modes of the structure as follows :

$$\phi_{in}(x) = \sum_m c_m \phi_m(x) \tag{2.20}$$

The summation in Eq.2.20 should of course consists of a true summation over guided modes and integration over radiation modes over the calculation window. Propagation through the structure can then be expressed as follows :

$$\phi(x,z) = \sum_m c_m \phi_m(x) e^{i\beta_m z} \tag{2.21}$$

Imaginary distance BPM replaces the longitudinal coordinate z by $z' = iz$, so that propagation along this imaginary axis should be as follows :

$$\phi(x,z') = \sum_m c_m \phi_m(x) e^{\beta_m z'} \tag{2.22}$$

The propagation implied by the exponential term in Eq. 2.21 has become exponential growth in Eq. 2.22, with the growth rate of each mode being equal to its real propagation constant. Since the fundamental mode ($m = 0$) has by definition the highest propagation constant, its contribution to the field will have the highest growth rate and will dominate all other modes after a certain distance, leaving only the field pattern $\phi_0(x)$, The propagation constant can then be obtained by the following variational-type expression :

$$\beta^2 = \frac{\int \phi^* (\frac{\partial^2 \phi}{\partial x^2} + k^2 \phi) dx}{\int \phi^* \phi dx} \tag{2.23}$$

Higher order modes can be obtained by using an orthogonalization procedure to subtract contributions from lower order modes while performing the propagation [165].

2.2/ PHOTONIC CRYSTAL DISPERSION CURVE MODELING METHODS : PWE

Computation of the dispersion diagram of the PhC requires electromagnetic wave propagation in the infinite space, tiled with identical cells in the xy plane. The solution of Maxwell equations must satisfy Bloch periodic boundary conditions in periodic structures. Various methods can be applied to calculate the band diagram of PhC structures such as plane wave expansion method [122, 166, 167, 168, 169, 170, 171], the transfer matrix method (TMM) [172], the finite-difference time-domain (FDTD) method [173, 174, 175], and the finite element method (FEM) [176, 177, 178] etc.

FDTD methods for band diagram calculations are obtained through Fourier-transform of the time-varying response of the system, and the peaks in the resulting spectrum correspond to the eigenfrequencies which is similar to the principle of the above introduced FDTD mode solver methods. It is an order-N method which can effectively reduce computation burden in 3D structure dispersion calculation case. It solves the Maxwell equations within the unit cell in time domain by applying an initial field that covers all the possible symmetry properties of the structure. However, care must be taken to ensure that the input source is not accidentally near orthogonal to an eigenmode. In order to compute the associated fields, one re-runs a second simulation with a narrow-band filter for each state.

TMM method expresses at a fixed frequency, and computes the transfer matrix relating field amplitudes at one end of a unit cell with those at the other end (via finite difference, analytical or other methods). This method yields the transmission spectrum directly, and mode wave vectors via the eigenvalues of the matrix. This method is a hybrid in time and frequency domain.

PWE is probably the most popular method due to its calculation efficiency. The band diagrams investigated in this thesis are performed by PWE method. Specifically, we investigate in-plane wave propagation dispersion relationship in PWE. Notice that, PWE can be also employed to calculate dispersion diagram of 3D structure by imposing a third dimensional periodicity through introducing a periodic

sequence of slabs separated by a sufficient amount of background region to ensure electromagnetic isolation as what it is implemented in the supercell technique [171]. The PWE is able to provide complete and accurate information of the PhC dispersion relationship via solving the Maxwell equations as an eigenproblem.

Let us discuss about the detail of PWE method by considering lossless and dispersionless linear materials, $\epsilon(x) > 0$ and $\mu(x) > 0$. For time-harmonic fields ($e^{-i\omega t}$) in the absence of current sources, Maxwell equations become $\nabla \times \mathbf{E} = i\omega\mu\mathbf{H}$ and $\nabla \times \mathbf{H} = -i\omega\epsilon\mathbf{E}$. After some algebra, we can decouple these equations to an equation entirely in $\mathbf{H}$:

$$\nabla \times \left(\frac{1}{\epsilon(r)} \nabla \times \mathbf{H}(r) \right) = \left(\frac{\omega}{c} \right)^2 \mathbf{H}(r) \tag{2.24}$$

This complicated differential equation is called vectorial Helmholtz equation for $\mathbf{H}(r)$, which in PhC literature it is referred as master equation [179]. The content of Eq. 2.24 is this : perform a series of operations on a function $\mathbf{H}(r)$, and if $\mathbf{H}(r)$ is really an allowable EM mode, the result will just be a constant times the original function $\mathbf{H}(r)$. If the result of an operation on a function is just the function itself, multiplied by some constant, then the function is called eigenfunction of that operator. The multiplicative constant is called the eigenvalue. The differential operator is oftentimes denoted as in Eq.2.24 as :

$$\Theta \equiv \nabla \times \left(\frac{1}{\epsilon(r)} \nabla \times \right) \tag{2.25}$$

For PhC structures, $\epsilon(r)$ is a highly discontinuous function, and $\mathbf{E}$ will be also discontinuous. Consequently $\mathbf{E}$ is not proper as a variable for calculation of the supported modes by PhC. If $\mathbf{H}$ is chosen as a variable, once $\mathbf{H}$ is calculated, $\mathbf{E}$ can be obtained by the following relation :

$$\mathbf{E}(r) = \frac{1}{i\omega\epsilon_0\epsilon(r)} \nabla \times \mathbf{H}(r) \tag{2.26}$$

According to J. D. Joannopoulos [179], Eq. 2.24 has some important features such as operator Θ is a linear Hermitian operator that makes $\mathbf{H}(r)$ a more preferable variable than $\mathbf{E}(r)$ for solving PhC eigenmodes. Particularly we want to point out the scaling properties in non-dispersive medium here, which enables the PhC design to

be extended to any frequency region. Suppose we replace the index distribution by a scaled copy $\epsilon_2(x) = \epsilon(x/\sigma)$. Thus $\epsilon_2(x)$ has the same shape as the original distribution but is expanded by a factor σ. Then by a rescaling of the position variables, it is possible to recover the original Helmholtz equation with a rescaling of the frequency to $\omega_2 = \omega/\sigma$. Thus no genuinely new solutions are obtained by rescaling the refractive index distribution. Therefore, there is normally no reason to change the variable of period which controls the size of a lattice, and no reason to perform scans over the variable of period. Oftentimes the variable in the frequency axis of dispersion curve is $\omega a/2\pi c$, i.e. a/λ. It is referred to as normalized frequency. In addition to solve the master equation, one should also need to force the transversality of the two divergence equations ($\nabla\cdot\mathbf{H} = \nabla\cdot\mathbf{D} = 0$). That is to say, **H** and **D** are built up of transverse plane waves, each of the plane wave is perpendicular to its **k**-vector, i.e. $\mathbf{k}\cdot\mathbf{H} = 0$ and $\mathbf{k}\cdot\mathbf{D} = 0$.

Periodic dielectric function

A number of standard concepts in solid-state physics related to periodic structures such as lattice vectors, primitive lattices, unit cells and reciprocal lattices etc are introduced here [180]. One, two and three dimensional periodic refractive index distribution $\epsilon(r)$ can be pictured schematically for instance like in Fig. 2.4. To describe the

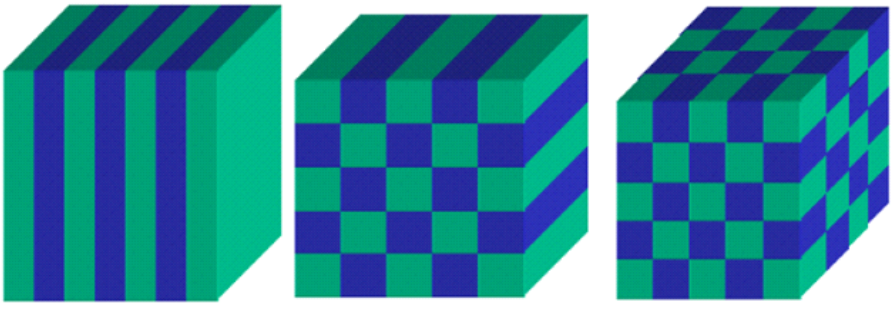

FIGURE 2.4 – Sketch of 1D, 2D and 3D dimensional PhC

periodicity, every crystalline structure is associated with direct and reciprocal lattices. Direct lattice can be represented as :

$$\mathbf{R} = l\mathbf{a}_1 + m\mathbf{a}_2 + n\mathbf{a}_3 \tag{2.27}$$

where l, m, n are integers and **R** is known as the lattice vectors. The

basis vectors $\mathbf{a}_1$, $\mathbf{a}_2$, $\mathbf{a}_3$ are termed primitive lattice vectors. Due to

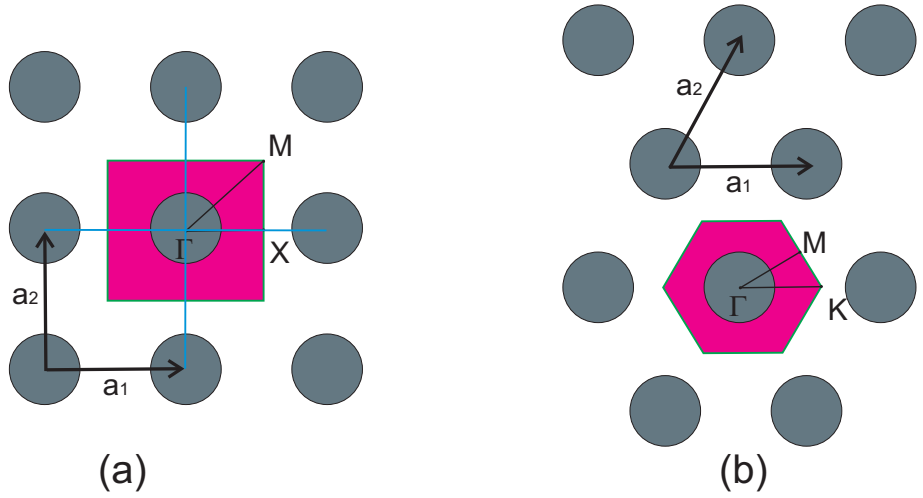

FIGURE 2.5 – Sketch of representation of primitive lattice vectors (a_1 and a_2), unit cell (Magenta regions), first Brillouin zone (regions delimited with Γ, M and K/X) in (a) 2D square lattice, (b) 2D hexagonal lattice structure.

the difficulty of realizing regular and well-controlled 3D structures at the nanometer scale, lower dimension PhC 1D or 2D PhC that exhibit many properties of the 3D structure analogs seemed promising candidates for real applications. Note that in 1D or 2D problems, we naturally need only one or two primitive lattice vectors. As an example, primitive lattice vectors associated to 2D square lattice and triangular lattice structures are shown in the Fig. 2.5.

The connection between the continuous periodic function $\epsilon(r)$ and the discrete lattice is provided by the unit cell. A unit cell is any region of space which, when translated by every lattice vector in the lattice, maps out the entire refractive index distribution function. Specifically, any unit cell which has the minimum possible volume are called primitive unit cell. One can construct the unit cell by Wigner-Seitz cell method. The cell may be chosen by first picking a lattice point, then lines are drawn to all nearby closest lattice points such as those blue lines in Fig. 2.5. At the midpoint of each line, another line is drawn normal to each of the first set of lines as those green lines in Fig. 2.5. The unit cell can reproduce the entire index distribution when translated through all the lattice vectors. One can represent a periodic structure only by their primitive lattice vector and unit cell.

A second lattice associated with every lattice in the reciprocal space

is termed the reciprocal lattice. The vectors of the reciprocal lattice are defined by the vector equations :

$$\mathbf{r}_1 = 2\pi \frac{\mathbf{a}_2 \times \mathbf{a}_3}{\mathbf{a}_1 \cdot \mathbf{a}_2 \times \mathbf{a}_3}$$

$$\mathbf{r}_2 = 2\pi \frac{\mathbf{a}_3 \times \mathbf{a}_1}{\mathbf{a}_1 \cdot \mathbf{a}_2 \times \mathbf{a}_3}$$

$$\mathbf{r}_3 = 2\pi \frac{\mathbf{a}_1 \times \mathbf{a}_2}{\mathbf{a}_1 \cdot \mathbf{a}_2 \times \mathbf{a}_3} \tag{2.28}$$

The lattice and reciprocal lattice are related by the equation

$$\mathbf{a}_i \cdot \mathbf{b}_j = 2\pi\delta_{ij} \tag{2.29}$$

Where $\delta_{ij} = 1$, if $i = j$, and 0 otherwise, $\mathbf{a}_1 \cdot (\mathbf{a}_2 \times \mathbf{a}_3)$ is the the volume of the unite cell. The lattice and reciprocal lattice are thus essentially inverse of each other. Since the lattice vectors have the dimensions of length, the reciprocal lattice vectors have dimensions of inverse length and span the reciprocal space. The reciprocal lattice vectors therefore provide a natural basis for optical wavevectors and play a central role in the PWE method. The general reciprocal lattice vector $\vec{G}$ can be denoted as :

$$\vec{G} = v_1\mathbf{r}_1 + v_2\mathbf{r}_3 + v_3\mathbf{r}_3 \tag{2.30}$$

where v_1, v_2, v_3 are integers. The Wigner-Seitz cell in the reciprocal space is known as the first Brillouin zone. The boundaries of this cell are given by planes related to points on the reciprocal lattice. The importance of the Brillouin zone stems from the Bloch wave description of waves in a periodic medium, in which it is found that the solutions can be completely characterized by their behavior in a single Brillouin zone. The considerations of symmetry of the structure allow one to restrict the reciprocal space to the reduced Brillouin zone which corresponds to the delimited region by the high symmetric points (Γ, M, X or K). Reduced Brillouin zone and symmetry points associated to the square lattice and hexagonal lattice structure are shown in Fig. 2.5. These high symmetric points are defined as follows :

— Square lattice $\Gamma = (0, 0), X = (\frac{\pi}{a}, 0)$ and $M = (\frac{\pi}{a}, \frac{\pi}{a})$.

— Hexagonal lattice $\Gamma = (0,0), K = (\frac{4\pi}{3a}, 0)$ and $M = (\frac{\pi}{a}, \frac{\pi}{\sqrt{3}a}, 0)$.

Floquet-Bloch theorem and deduction of PWE method

One can have the full view of the band diagram of the structure by solving the master equation (Eq. 2.24) with the propagation vector $\vec{k}$ along the boundaries of reduced Brillouin zone. The modes of the photonic crystal are then the solutions of Maxwell equations in eigenproblem form. The possible form of the solutions is restricted by the considerations of the geometry symmetry. In particular, the modes must satisfy the appropriate translation symmetry. According to Floquet-Bloch theorem, a plane wave in a periodic structure will be modulated by the periodicity of the PhC structure. Therefore, the complex-valued magnetic field **H** can be expressed as :

$$\mathbf{H}(r) = e^{i\vec{k}\cdot\vec{r}} h(\vec{r}) \hat{e}_k$$

where $h(\vec{r}) = h(\vec{r} + \vec{R})$ is a periodic function with periodicity of that in the PhC structure. Likewise, we can also expand the periodic refractive index distribution and magnetic field function using Fourier series in reciprocal space as follows :

$$\epsilon(r) = \sum_{\vec{G}_i} \epsilon(\vec{G}_i) e^{i\vec{G}\cdot\vec{r}} \tag{2.31}$$

$$\frac{1}{\epsilon(r)} = \sum_{\vec{G}_i} \epsilon^{-1}(\vec{G}_i) e^{i\vec{G}\cdot\vec{r}} \tag{2.32}$$

and

$$h(r) = \sum_{G_i} h(G_i) e^{i\vec{G}_i\cdot\vec{r}} \tag{2.33}$$

So,

$$\vec{H}(r) = \hat{e}_k e^{i\vec{k}\cdot\vec{r}} \sum_{G_i} h(G_i) e^{i\vec{G}_i\cdot\vec{r}} = \sum_{G_i,\lambda} h(G_i, \lambda) e^{i(\vec{k}+\vec{G}_i)\cdot\vec{r}} \hat{e}_{\lambda,\vec{k}+\vec{G}_i} \tag{2.34}$$

In Eq. 2.34, the transverse property is used to decompose the wave into the sum of a set of plane waves, which is the heart of PWE method. $\hat{e}_{\lambda,\vec{k}+\vec{G}_i}$ $(\lambda = 1, 2)$ denotes two unit vectors such that $\{\hat{e}_{1,\vec{k}+\vec{G}_i}, \hat{e}_{2,\vec{k}+\vec{G}_i}, \vec{k}+\vec{G}_i\}$ forms a Cartesian triad. $\vec{G}_i$ is the frequency component. λ represents the two axes in the perpendicular plane which

is perpendicular to $(\vec{k}+\vec{G}_i)$ and $\vec{k} = k_x\hat{x} + k_y\hat{y}$ is the in-plane wave vector. All the $\vec{G}_i$ forms the reciprocal lattice. For any plane wave $e^{i(\vec{k}+\vec{G}_i)\cdot r}$ with a propagation wave vector $\vec{k}+\vec{G}_i$, the electromagnetic fields can be expressed as a superposition of two arbitrary orthogonal components that lie in a plane perpendicular to the wave vector $\vec{k}+\vec{G}_i$.

Substituting Eqs. 2.32 and 2.34 into the master equation, Eq. 2.24, with some algebra and curl operator identities properties, we obtain the following equation as eigenvalue problem :

$$\sum_{G',\lambda'} \left[(\vec{k}+\vec{G})\times\hat{e}_\lambda\right]\cdot\left[(\vec{k}+\vec{G'})\times\hat{e}'_\lambda\right]\epsilon^{-1}(\vec{G}-\vec{G'})h(\vec{G'},\lambda) = \frac{\omega^2}{c^2}h(\vec{G},\lambda) \tag{2.35}$$

where $\lambda' = 1, 2$, and G is any reciprocal lattice vector [170].

This is an eigenproblem, which can be implemented by numerical method. However, one cannot use infinite number of $\vec{G}$ vectors and instead the use of finite number of them will lead to the truncation of high frequency components as that in signal processing. If the number of the plane wave is large enough, we can approach the true signal very well. Here we confine the discussion in 2D in-plane wave propagation case. $\vec{k}$ and $\vec{G}$ are in the same xy plane. One of the unit vectors can be constantly set to : $\hat{e}_{2,k+G} = \hat{z}$, the other unit vector $\hat{e}_{1,k+G}$ is also in the xy plane.

In the 2D structure case, Eq. 2.35 can be decoupled into two equation groups : the TE and TM. One group only contains **H** components along $\hat{e}_1$, no components along $\hat{e}_2 = \hat{z}$ so it is called TM wave. The other group only contains **H** component along $\hat{e}_2 = \hat{z}$, and **E** only have the in-plane component and it is called TE wave. The two polarization of PWE methods can be written as follows :

— TE : $\sum_{G'} \mid \vec{k}+\vec{G} \parallel \vec{k}+\vec{G'} \mid \epsilon^{-1}(\vec{G}-\vec{G'})h_1(\vec{G'}) = \frac{\omega^2}{c^2}h_1(\vec{G})$

— TM : $\sum_{G'}(\vec{k}+\vec{G})\cdot(\vec{k}+\vec{G'})\epsilon^{-1}(\vec{G}-\vec{G'})h_2(\vec{G'}) = \frac{\omega^2}{c^2}h_2(\vec{G})$

Where, h_1 is the component of the magnetic field along the z direction while h_2 is the perpendicular magnetic field component in the xy plane.

2.3/ 2D-FDTD AND 3D-FDTD ALGORITHMS

2.3.1/ FDTD IN GENERAL

Maxwell curl equations (Eq. 2.3 and 2.4) describe a situation in which the temporal change in the **E** field is dependent upon the spatial variation of the **H** field, and vice versa. FDTD in the Yee algorithm is performed by replacing the derivatives in Maxwell equations by central difference schema [149, 150]. The spatial discretization for Yee algorithm in Cartesian coordinates is shown in Fig. 2.6. This kind of discretization implicitly satisfies the zero divergence conditions to avoid spurious solutions and it naturally handles physical boundary conditions. In addition it provides a very elegant and compact way of approximating the curl equations with finite differences.

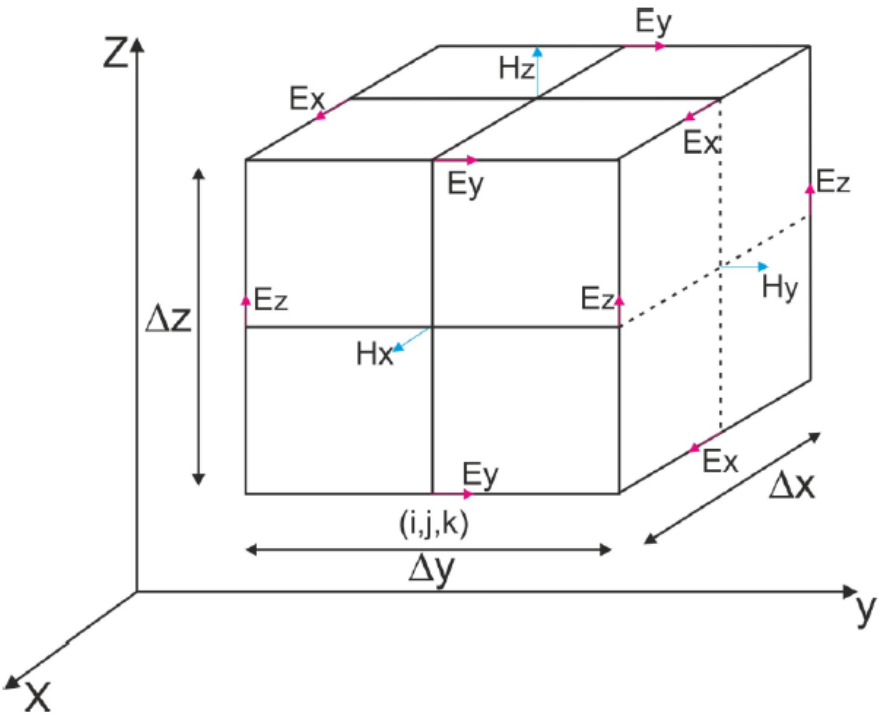

FIGURE 2.6 – A Yee elemental cell, note how the **H** field is computed at points shifted one-half grid spacing from the **E** field grid points.

Yee algorithm computes **E** and **H** field components in a leapfrog arrangement as schematically shown in Fig. 2.7, alternating between computing the **E** and **H** fields at subsequent $\Delta t/2$ intervals. **E** is calculated at time step $t = 0, \Delta t, 2\Delta t, ...$ while **H** is calculated at time steps $t = 0.5\Delta t, 1.5\Delta t, 2.5\Delta t, ...$ **E** and **H** components are also dis-

played by a half step separation in space as shown in Fig. 2.7. Let

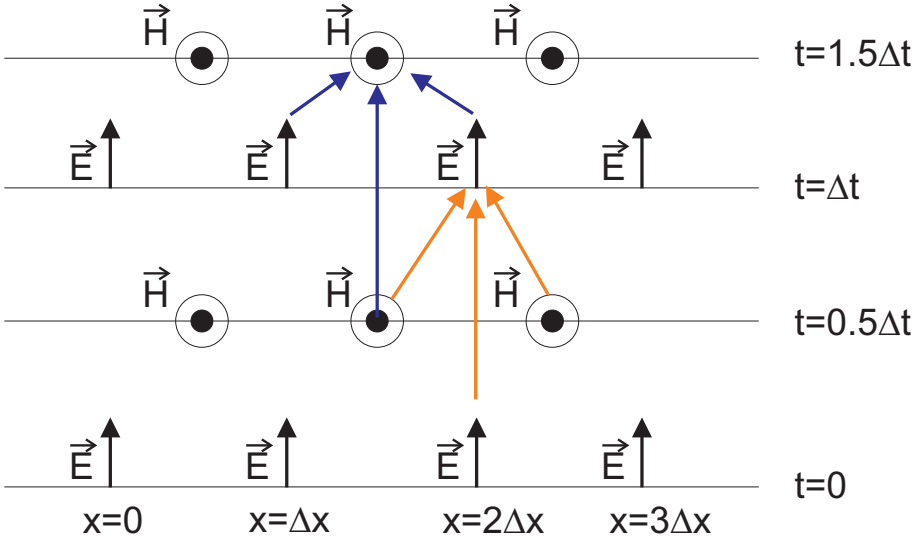

FIGURE 2.7 – Space time chart of the Yee algorithm for a 1D wave propagation example showing the use of central differences for space derivatives and leapfrog for the time.

$u(x, y, z)$ denotes any of the six field components and a grid point in space is denoted by : $(i\Delta x, j\Delta y, k\Delta z) \equiv (i, j, k)$ and a time instant $t = n\Delta t$, where i, j, k and n are integers. Then

$$u(i\Delta x, j\Delta y, k\Delta z, n\Delta t) = u^n(i, j, k)$$

By replacing the derivations in Eq. 2.6 and 2.7 with central finite difference and confining only to non-dispersive material, we obtain the explicit updating EM field equations in FDTD algorithm :

$$E_x^{n+1}(i, j, k) = E_x^n(i, j, k) + \frac{\Delta t}{\epsilon(i,j,k)}\left[\frac{H_z^{(n+1/2)}(i,j+1/2,k) - H_z^{(n+1/2)}(i,j-1/2,k)}{\Delta y}\right.$$

$$\left. - \frac{H_y^{(n+1/2)}(i,j,k+1/2) - H_y^{(n+1/2)}(i,j,k-1/2)}{\Delta z}\right]$$

$$E_y^{n+1}(i, j, k) = E_y^n(i, j, k) + \frac{\Delta t}{\epsilon(i,j,k)}\left[\frac{H_x^{(n+1/2)}(i,j,k+1/2) - H_x^{(n+1/2)}(i,j,k-1/2)}{\Delta y}\right.$$

$$\left. - \frac{H_z^{(n+1/2)}(i+1/2,j,k) - H_z^{(n+1/2)}(i-1/2,j,k)}{\Delta z}\right]$$

$$
\begin{aligned}
E_z^{n+1}(i,j,k) = \; & E_z^n(i,j,k) + \frac{\Delta t}{\epsilon(i,j,k)}\Big[\frac{H_y^{(n+1/2)}(i+1/2,j,k) - H_y^{(n+1/2)}(i-1/2,j,k)}{\Delta x} \\
& - \frac{H_x^{(n+1/2)}(i,j+1/2,k) - H_x^{(n+1/2)}(i,j-1/2,k)}{\Delta y}\Big] \\
H_x^{n+1/2}(i,j,k) = \; & H_x^{n-1/2}(i,j,k) + \frac{\Delta t}{\mu(i,j,k)}\Big[\frac{E_y^n(i,j,k+1/2) - E_y^n(i,j,k-1/2)}{\Delta z} \\
& - \frac{E_z^n(i,j+1/2,k) - E_z^n(i,j-1/2,k)}{\Delta y}\Big] \\
H_y^{n+1/2}(i,j,k) = \; & H_y^{n-1/2}(i,j,k) + \frac{\Delta t}{\mu(i,j,k)}\Big[\frac{E_z^n(i,j,k+1/2) - E_z^n(i,j,k-1/2)}{\Delta x} \\
& - \frac{E_x^n(i,j+1/2,k) - E_x^n(i,j-1/2,k)}{\Delta z}\Big] \\
H_z^{n+1/2}(i,j,k) = \; & H_z^{n-1/2}(i,j,k) + \frac{\Delta t}{\mu(i,j,k)}\Big[\frac{E_x^n(i,j,k+1/2) - E_x^n(i,j,k-1/2)}{\Delta y} \\
& - \frac{E_y^n(i,j+1/2,k) - E_y^n(i,j-1/2,k)}{\Delta x}\Big]
\end{aligned}
\tag{2.36}
$$

Electromagnetic field excitation

In order to perform the simulation, an initial launch condition ϕ_L at time $t = 0$ is needed, as well as a driving function in time. This consists of both a spatial and temporal excitation, such as

$$\phi_L(\mathbf{r}, t) = f(\mathbf{r}_0)g(t)$$

where $f(\mathbf{r}_0)$ is the spatial excitation at the launch plane and $g(t)$ is its temporal behavior. According to what it is calculated, one can launch different types of initial field profiles $f(\mathbf{r}_0)$. For example, in 2D WG structure with PhC transmission calculation, one can launch the WG mode cross section profile as the initial field. In 3D PhC on WG simulations, one can take the whole WG mode field distribution as the launch conditions. In more general cases, a simple Gaussian initial field is chosen as the launch conditions. As to temporal excitation

type $g(t)$, in a large band spectrum calculations, one should choose a short temporal pulse to excite all the frequency components. In general, a Gaussian field profile short pulse linearly polarized in xy plane is frequently utilized and the major electric field amplitude can be denoted as follows :

$$E = cos(\theta) \cdot exp(-\frac{(x-x_0)^2}{w_x^2} - \frac{(y-y_0)^2}{w_y^2}) \cdot exp(-\frac{(t-t_0)^2}{2\sigma^2}) \cdot exp(-i\frac{2\pi}{\lambda_0}ct) \tag{2.37}$$

where $cos(\theta)$ is included in Eq. 2.37 to facilitate orientating the linearly polarized light along an arbitrary direction in the launch field xy plane. The first exponential term in Eq. 2.37 denotes the spatial Gaussian field profile. The parameters x_0 and y_0 represent the center of the incident beam. The parameters w_x and w_y are the deviation of a Gaussian function, which determines the span width of an input field. The second exponential term denotes a short pulse centered at time t_0, with a standard deviation of σ that defines the spectrum range. The last exponential term specifies the centering wavelength λ_0 of the short pulse.

In continuous wave simulation in order to calculate steady states for example the field distribution at the resonance wavelength, one should choose a monochromatic wave excitation with a ramp rise time in the temporal profile. To that aim, one can change the second exponential term in Eq. 2.37 into $1 - exp(-\frac{t^2}{2\sigma^2})$, which yields a continuous wave excitation at wavelength of λ_0.

Boundary conditions

The boundary conditions at the spatial edges of the computational domain must be carefully considered. Many simulations employ an absorbing boundary condition that eliminates any outward propagating energy that impinges on the domain boundaries. The PML (perfected matched layer) , proposed by Berenger [181], consists of an absorbing boundary layer in which both electric and magnetic conductivities are introduced in such a way that the wave impedance remains constant, absorbing the energy without inducing reflections. It is one of the most powerful ways to absorb waves of any frequency

and any angle of incidence. Mathematically speaking, the PML is simply a domain that has an anisotropic and complex-valued permittivity and permeability as those gray planes denoted in Fig.2.8. This technique is based on impedance matching principle having the same refractive index at the interface between two medium. These layers are absorbent and have nonzero electric conductivity σ^e and magnetic conductivity σ^m.

Although PMLs are theoretically non-reflecting, they do exhibit some reflection due to the numerical discretization. To minimize this reflection, one can use a mesh in the PML that aligns with the anisotropy of the material properties. The feature of the PML is that it absorbs the propagating wave. Thus from a physical point of view, the PML truly can be thought of as a material with almost perfect absorption. It is an important technique to minimize the problem of calculation size using efficient boundary conditions. Truncating the geometry without introducing large errors is one of the great challenges in modeling. Empirically speaking, a size of $\lambda/6$ (λ is the smallest evaluated wavelength) PML would be enough to get a good boundary condition nearly without reflection back to the main calculation window (normally the reflection coefficient $R < 10^{-10}$).

Periodic boundary conditions (PBC) are also important because of their applicability to periodic structures such as PhC. The PBC are chosen such that the simulation is equivalent to an infinite structure which composed of only the basic computational domain and repeated endlessly in the directions of PBC. PBC can be deduced from the Floquet Bloch theorem, which states that the fields at one side of the computational cell are related to the fields at the other side plus a phase term as follows :

$$\begin{aligned}
\mathbf{E}(x = p, y, t) &= \mathbf{E}(x = 0, y, t)e^{ik_x \cdot p} \\
\mathbf{E}(x, y = p, t) &= \mathbf{E}(x, y = 0, t)e^{ik_y \cdot p} \\
\mathbf{H}(x = p, y, t) &= \mathbf{H}(x = 0, y, t)e^{ik_x \cdot p} \\
\mathbf{H}(x, y = p, t) &= \mathbf{H}(x, y = 0, t)e^{ik_y \cdot p}
\end{aligned} \tag{2.38}$$

However, in the case of arbitrary incident angle, the phase shift term is frequency dependent and it will be difficult to integrate

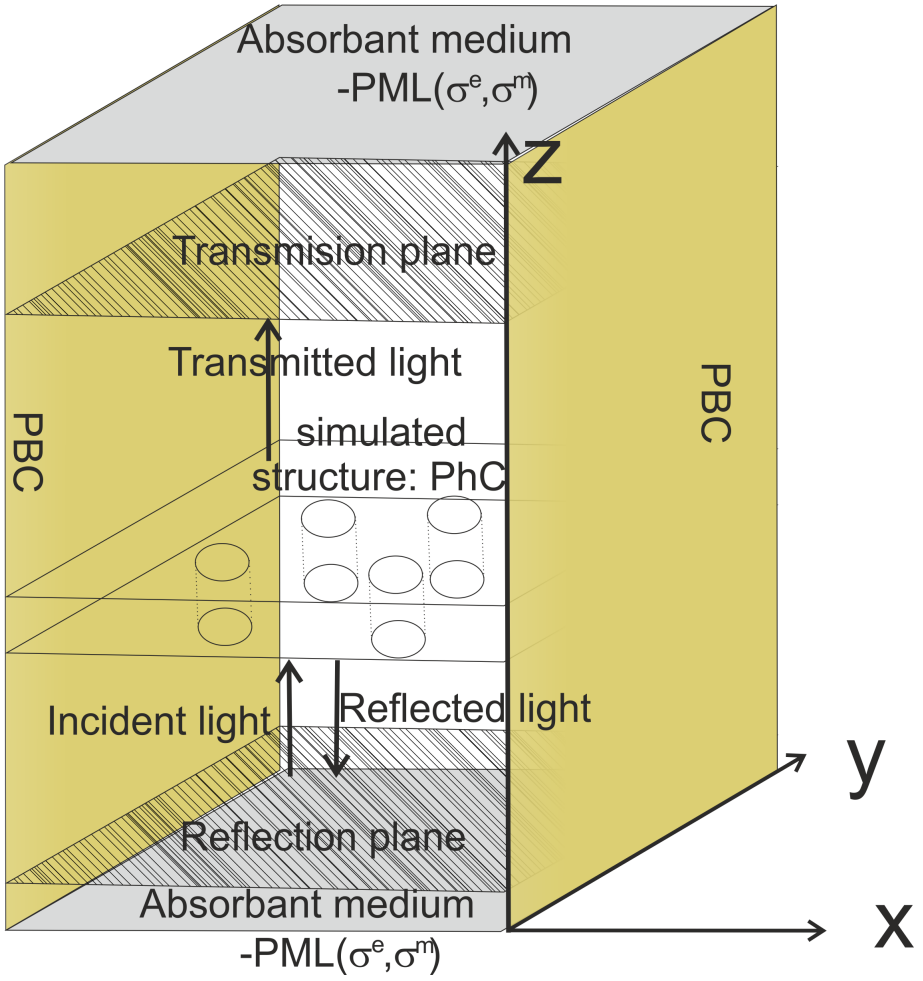

FIGURE 2.8 – PML and PBC positions in the FDTD calculations.

this boundary condition into the FDTD algorithm which is time dependent. Fortunately in normal incident case, the phase shift becomes zero, thus it can be easily implemented in the FDTD algorithm. Henceforth, we only deal with the case of normal incident condition in the 3D-FDTD calculations with PBC condition. In order to calculate the transmission and/or the reflection, a detector is usually placed at the output side, as the black lines hatched planes shown in Fig. 2.8. Through Fourier transform (FT) of the time varying EM fields recorded in the detector one can obtain the normalized transmission/reflection spectra in the frequency domain where the normalization is performed with respect to the incident signal. Note that reflection spectrum is obtained through the FT of the signal reflected by the PhC structure. If there is only one field component (**E** or **H**) such as those in Eq. 2.37 is injected on

the calculation window, then there are both forward and backward propagations of incident field. Thus, a reflection plane detector, as shown in Fig. 2.8, records both the signal reflected by PhC and the back propagation of the incident field. Henceforth, in order to obtain the reflection spectrum one needs to subtract the back propagation incident signal before performing the FT calculation.

The spatial and temporal grid

In order to obtain a simulation with enough accuracy, the spatial grid must be small enough to resolve the smallest feature of the field to be simulated. From continuous Maxwell equations to the discretized equations, numerical dispersion will occur which is an artifact resulting from the discrete spatial sampling of the FDTD mesh. This means that for a coarse mesh, the speed of light on the FDTD mesh may depart slightly from the exact value of the speed of light in the material being simulated. Furthermore, the speed of light becomes slightly anisotropic, and it depends on the direction of propagation of the light relative to the mesh. The critical parameter that affects numerical dispersion is $N = \lambda_0/(n * D)$, where λ_0 is the free space wavelength, n is the refractive index and D is the FDTD mesh cell size. N represents the number of mesh cells per wavelength, and the numerical dispersion artifact becomes negligible as N becomes large. If the refractive index n is complex, then both the real and imaginary parts are considered to ensure that it has enough points per wavelength and enough points per decay length for accurate modeling.

The non-uniform mesh makes it possible to take into account more precise geometric location of different material interfaces. It employs fine mesh cells in regions where the interfaces are important and large mesh cells in bulk regions where there are homogeneous material distributions and no important interfaces. In this thesis, both uniform and non-uniform spatial grid are employed according to the simulated geometrical structure. Typically, a spatial grid spacing smaller than $\lambda/16$, where λ is not the free space wavelength but rather the wavelength in the materials, is suggested to ensure an

accurate and convergent simulations.

On the other hand, any finite difference based numerically partial differential equations solver must satisfy Courant-Friedrichs-Lewy (CFL) condition to ensure convergence results. It arises in the numerical analysis of explicit time integration schemes. As a consequence, the time step must be less than a certain time in many explicit time-marching computer simulations, otherwise the simulation will produce incorrect results. Specifically, we list three types of stability conditions in different calculation conditions :

— 2D-FDTD mode solver case

$$\Delta t \leq \frac{1}{v_{max} \cdot \sqrt{\frac{1}{\Delta x^2} + \frac{1}{\Delta y^2} + \frac{k_z^2}{2}}}$$

— 2D-FDTD transmission and/or reflection studies case

$$\Delta t \leq \frac{1}{v_{max} \cdot \sqrt{\frac{1}{\Delta x^2} + \frac{1}{\Delta y^2}}}$$

— 3D-FDTD transmission and/or reflection studies case

$$\Delta t \leq \frac{1}{v_{max} \cdot \sqrt{\frac{1}{\Delta x^2} + \frac{1}{\Delta y^2} + \frac{1}{\Delta z^2}}}$$

Where v_{max} is the maximum propagation speed of light in the studied system. In general, this corresponds to the speed of light in the vacuum. These conditions behave quite intuitively : the numerical time must not be shorter than the necessary real needed time for the wave propagation from one cell to another which ensure the stability of the simulations. One must be careful to take into account the above mentioned stability criteria in the simulations.

A typical use of FDTD simulations is to inject an incident electromagnetic pulse into a problem geometry to perform the FT of the desired response (for example the transmitted, reflected, or scattered fields). Then by computing the corresponding power or energy at each frequency thereby to obtain the entire spectrum of the response (for instance a transmission or absorption spectrum)

in a single simulation. For a field $f(t)$ in response to the exciting pulse, one computes the FT $\hat{f}(\omega)$. Generally FT is approximated by a discrete-time Fourier transform (DTFT) of the discrete-time field, $f(n\Delta t)$:

$$\hat{f}(\omega) = \frac{1}{\sqrt{2\pi}} \int_{-\infty}^{\infty} f(t) e^{i\omega t} dt \approx \frac{\Delta t}{\sqrt{2\pi}} \sum_{n=-\infty}^{\infty} f(n\Delta t) e^{i\omega n\Delta t} \tag{2.39}$$

where, for a pulsed field, the sum over n can be truncated when f becomes sufficiently small. This computation would be performed for a set of frequencies covering the desired bandwidth. To compute the flux through some surface S, one would apply the accumulation of the $\hat{f}$ summations as the FDTD simulation progresses procedure to obtain $\hat{E}(r,\omega)$ and $\hat{H}(r,\omega)$ for $r \in S$, and then compute the flux spectrum, $P(\omega) = \frac{1}{2} Re \iint_S (\hat{E}^*(r,t) \times \hat{H}(r,t)) \cdot dS$.

2.3.2/ 2D-FDTD

Due to the large computational burden of 3D-FDTD in the design of an optical device, one can perform a 2D simulation as the starting step of the design instead. We can divide the 2D calculation into two polarizations i.e. TE ($\mathbf{E}_x, \mathbf{E}_y, \mathbf{H}_z$) and TM ($\mathbf{H}_x, \mathbf{H}_y, \mathbf{E}_z$). In the TE case, we need to solve the following partial differential equations :

$$\begin{aligned} \frac{\partial \mathbf{E}_x}{\partial t} &= \frac{1}{\epsilon} \frac{\partial \mathbf{H}_y}{\partial y} \\ \frac{\partial \mathbf{E}_y}{\partial t} &= -\frac{1}{\epsilon} \frac{\partial \mathbf{H}_z}{\partial x} \\ \frac{\partial \mathbf{H}_z}{\partial t} &= \frac{1}{\mu} \left(\frac{\partial \mathbf{E}_x}{\partial y} - \frac{\partial \mathbf{E}_y}{\partial x} \right) \end{aligned} \tag{2.40}$$

Correspondingly, in TM case, we need to solve the following partial differential equations :

$$\begin{aligned} \frac{\partial \mathbf{H}_x}{\partial t} &= -\frac{1}{\mu} \frac{\partial \mathbf{E}_z}{\partial y} \\ \frac{\partial \mathbf{H}_y}{\partial t} &= \frac{1}{\mu} \frac{\partial \mathbf{E}_z}{\partial x} \end{aligned}$$

$$\frac{\partial \mathbf{E}_z}{\partial t} = \frac{1}{\epsilon}\left(\frac{\partial \mathbf{H}_y}{\partial x} - \frac{\partial \mathbf{H}_x}{\partial y}\right) \tag{2.41}$$

In 2D calculations, a side view or a top view cross section of the 3D structure is considered to study the light propagation in a much computation efficient way. As it will be elaborated in the later chapters, this can yield results very close to that obtain from 3D calculations if proper approximated structure is chosen in 2D simulations.

2.3.3/ 3D-FDTD

In 3D-FDTD simulations, the realistic structure is exactly defined in the algorithm thus yielding the most reliable result that can mimic to the real experimental measurements. Non-uniform mesh is oftentimes employed in 3D-FDTD calculations which enables less memory requirement and decreasing computation time than an otherwise corresponding uniform mesh. There are two ways that the non-uniform mesh improves accuracy : 1) through reducing numerical dispersion 2) through improving the spatial description of interfaces. There are six EM components involved in 3D-FDTD calculation through solving Eq. 2.6 and 2.7.

There are two kinds of 3D-FDTD utilized within this thesis according to the boundary condition types. One is the 3D-FDTD with PML on z direction to simulate finite thickness of slab while PBC is implemented on the PhC xy plane, meaning infinite size of PhC as shown in Fig. 2.8. In infinite structure study case, since only a unit cell of the structure is considered. Hence the structure is oftentimes illuminated by a pulsed plane wave in the case of spectrum response study. A detector plane is placed above the PhC as shown in black lines hatched planes above and below the PhC structure as shown in Fig. 2.8. The specular transmission (also called zero order transmission) can be calculated through FFT of the time varying spatial averaged EM fields recorded in the detectors. The normalization of the transmission is performed through the incident signal which is the zeroth order transmission calculations in the incidence medium.

Another type of 3D simulation is the real 3D-FDTD in which the finite structure is realistically simulated and the structures are surrounded

by PML conditions on both the three directions. 3D-FDTD with PML simulations is essential especially in the case of studying the effect of illumination beam size, transmission collection with different numerical apertures (NA) conditions etc. The detail of these studies will be elaborated in the corresponding following chapters.

3

DEFECT MODE BASED CAVITY ON TFLN

In this chapter, sensor designs employing defect modes based cavity on TFLN structures are presented. Different waveguide (WG) configurations (ridge WG, strip loaded WG, slot and double slot WG) on TFLN have been systematically studied by mode solver techniques introduced in chapter 2. A figure of merit (FoM) is introduced to compare the light confinement ability in different configurations.

Then PhC designs on slot WG, strip loaded WG are presented. PhC design is studied by first investigating the PBG properties in order to narrow down the structure parameters to a small range. Then 2D and 3D-FDTD calculations through transmission investigations are employed to fine tune the suitable parameters. A Fabry-Perot (F-P) interferometer configuration based on PhC mirrors is employed to design E-field sensors. Their performances in sensing applications are theoretically analyzed. In the last section, fabrication trials on strip loaded WG and nano-meter scale LN slot WG are presented.

3.1/ WAVEGUIDES ON TFLN

Optical WGs are basic elements for confinement and transmission of light over various distances, ranging from tens or hundreds of micrometer in integrated photonics to hundreds or thousands of kilometer in long-distance fiber-optic transmission. They are fundamental elements that interconnect the various devices in an photonic integrated circuit, just as a metallic strip does in an electrical integra-

ted circuit. Metal interconnections became the limiting factor for the performance of electronic systems as transistors continue to shrink in size. Replacing them by optical interconnections at different levels, ranging from rack-to-rack down to chip-to-chip and intra-chip interconnections, could provide low power dissipation, low latency and high bandwidths WG transmission [12, 13, 15, 182]. The implementation of optical interconnections rely on the development of micro-optical devices that can be integrated with the microelectronics on chips.

Optical WGs perform not only guiding, but also coupling, switching, splitting, multiplexing, and demultiplexing of optical signals [183]. For example, in order to build highly compact wavelength-division-multiplexer (WDM) for on-chip high-bandwidth applications, devices with channel spacing down to 0.4 nm is required which can be only realized through tight confined WG mode in a decreased geometrical dimension [184]. In addition, tuning WG GVD (group velocity dispersion) properties yielding multi-number zero dispersion points can be employed as on chip supercontinuum generation and harmonic generation devices etc [185, 186].

In order to meet the demand for higher data bandwidth with reduced power consumption, it is crucial to reduce the energy required to create, transmit and detect the optical information. This demand requires reducing physical component sizes down beyond the diffraction limit of light while still providing integrated functionalities and tolerable losses. Nanoscale WGs hold enormous potential for on-chip photonic applications such as intra-chip optical communications, nanolasers, optical modulators and highly sensitive sensors.

The traditional technique for WG fabrication on LN is summarized in Fig. 3.1. Most often, traditional WGs fabricated on LN are obtained by annealed proton exchange (APE) or Ti in-diffusion techniques which present extremely low propagation losses (down to 0.03 dB/cm at 1550 nm) at the price of having a spatially broad guided mode. The large mode size provides limited ability to confine light with high intensity, thus oftentimes yielding a negligible nonlinear effect. Figure 3.1 also shows that only small induced index change is obtained in PE or indiffusion technique WG fabrications

which lead to the weak light confinement and a large mode size. This small index contrast hinders the bending of WGs with a radius of curvature less than a few millimeter is not possible because the light will leak out. Consequently these WG configurations are not a suitable option for high density photonic integrated circuit applications.

type of guide	treatment / temperature	indices change	profile	cut	particular characteristics
Ti^{3+} in-diffusion (Ti)	900 – 1150 °C diffusion + 400 °C annealing in O_2	$\Delta n_e \sim 0.03$ $\Delta n_0 \sim 0.01$	Gaussian ~4 μm	X, Y, Z	optical damage
proton exchange (PE)	180 – 250 °C exchange + 400 °C annealing	$\Delta n_e \sim 0.1$ $\Delta n_0 \sim -0.04$	steplike and gaussian	X, Z	mainly benzoic acid+ Li benzoate, Several structural phases
TiPE	1100 °C (Ti) + annealing in O_2 at 400 °C + 220 °C exchange (H^+)	$\Delta n_e \sim 0.1$ $\Delta n_0 \sim 0.005$	steplike, up to 10μm	X, Y, Z	prevents Y-cut surface damage with exchange
Zn in-diffusion	550 °C in Zn vapor + 800 °C diffusion in air	$\Delta n_e, \Delta n_0 \sim 0.004$	exponential ~2 μm	X, Y, Z	good optical quality <0.5 dB/cm losses, high optical damage resistance
Ion implantation He^+	2 MeV, 2×10^{16} ions/cm^2	$\Delta n_e \sim -0.08$ $\Delta n_0 \sim -0.04$	Opt. barrier ~5 μm	Z	same nonlinear coefficients as in bulk material
Ion implantation H^+	1.5 MeV, 4×10^{16} ions/cm^2	$\Delta n_e \sim -0.04$ $\Delta n_0 \sim -0.04$	Opt. barrier ~15 μm	Z	same nonlinear coefficients as in bulk material
Ion implantation Si^+ and heavy ions	3 MeV, 4×10^{14} ions/cm^2	$\Delta n_e \sim 0.008$ $\Delta n_0 \sim -0.006$	~5 μm	X, Z	optical barrier only for n_0

FIGURE 3.1 – Summary of properties of most common optical waveguides produced on lithium niobate [9].

As a typical example, LN optical modulators are $4 - 5\ cm$ long and hundreds of micrometers wide [187]. Also, for nonlinear applications, due to the low intensity of the pump source in the large cross-sectional optical waveguides, the devices must be few centimeters long in order to achieve efficient conversion [188, 189].

LN PhC has been combined with traditional APE or Ti-indiffussion WG to pursue more compact functional devices, but the poor interaction between WG mode and the PhC structure adds penalties to the expected improvements. For example, there is only a small overlap integral between the buried APE WG mode (since the modes lie at several microns meters underneath the LN surface) and the

shallow air hole PhC pattern leading to the degradation of the expected PhC performance. The shallow air holes on LN comes from the redeposition problem of etching LN [190]. Since the well known etching-resist nature of LN, the PhC milled on it oftentimes presents conical shape of holes which produces a limited aspect ratio (the ratio of the height to the radius of the cylinder holes) as shown in Fig. 3.2 (a).

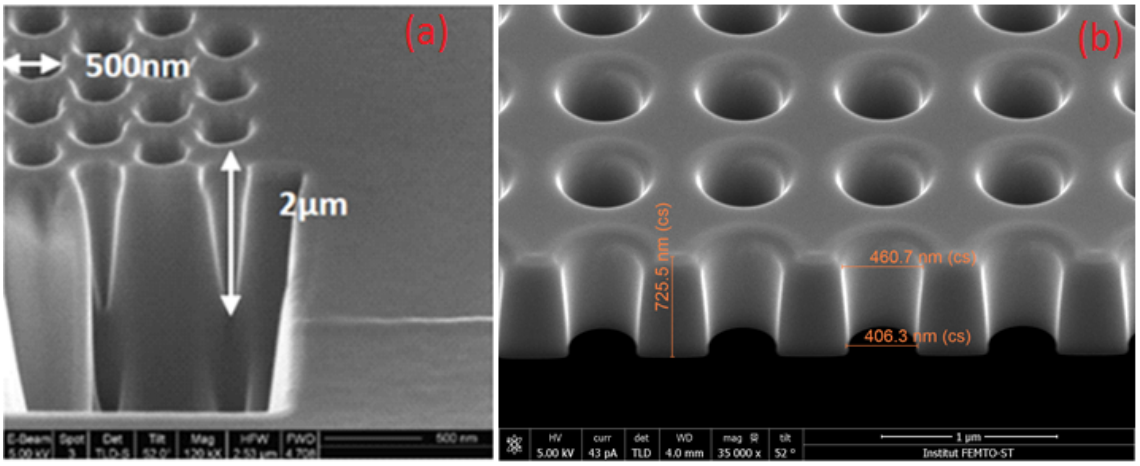

FIGURE 3.2 – (a) SEM images of FIB milled hexagonal lattice PhC of air holes arrays etched in bulk LN. The diameter of hole is 500 nm, the depth of the hole is 2μm. (b) SEM images of FIB milled square lattice PhC of air holes arrays etched in TFLN where the diameter of hole is 460 nm (top plane hole diameter) and the depth of the hole is 725 nm.

Thanks to the recent commercially available TFLN as thin as 200 nm, the effect of conical air holes shape will be alleviated since the nano structure is only patterned on such a small thickness of film. One SEM image of nano-patterning on TFLN is shown in Fig.3.2 (b), where the thickness of the film is only 725 nm.

To make the most advantage of the thin film technology in LN, we set out to find suitable WG configurations that will host the PhC. Due to their high index contrast of $\Delta n \approx 0.7$ ($n_{LN} \approx 2.138$, $n_{SiO_2} \approx 1.45$ at 1550 nm), TFLN samples are already planar WGs with sub-micrometer thickness of the core layer. As such they are ideally suitable for micro-metric size ultra compact WGs compared to that of the traditional APE or Ti-in-diffusion WGs. These ultra compact WGs can be designed as active devices exhibiting enhanced nonlinear optical properties due to the high light confinement in nano-metrical volume [191], which will open up the way to create fully integrated

multi-functional optical circuits.

A systematical WG study, based on three different mode solver techniques described in Chapter 2, is performed by varying the geometrical parameters of different WG configurations and by calculating a dimensionless FoM that quantifies the light confinement inside the WG.

WG confinement factor definition

In order to compare different WG geometries, a FoM is defined in order to quantify how light is confined inside the WG, which is also referred to as confinement factor Γ_e. Here, we define Γ_e factor as the ratio of largest (or major) electric field component amplitude integration over the LN waveguiding part divided by the same quantity integrated all over the space as follows :

$$\Gamma_e = \frac{\iint_{WG_{LN}} |E|_{major} dxdy}{\iint_{-\infty}^{+\infty} |E|_{major} dxdy} \tag{3.1}$$

Consequently, Γ_e value is between 0 and 1. The larger Γ_e is, the more confined the light is inside the active material (LN for instance). The integration region is only considered in the LN part since we assume that LN is the major active material for our applications. The choice of only considering the major electric field component is motivated by the fact that most of the nonlinear effects are generally proportional to optical susceptibilities of the material (thus proportional to the electric field amplitude). One can efficiently exploit the nonlinear effects by appropriately orienting the optical axis along the major electric field component of the guided mode. Henceforth, a larger amplitude in the major electric field might yield to larger nonlinear effects.

Notice that, different confinement factors are utilized in the literature to quantify the light confinement. For example, a confinement factor denoted as Γ which is defined as the ratio of propagating power inside the WG core to the total power of the guiding mode, is

calculated as follows :

$$\Gamma = \frac{\int_{wg\ core} Re(\mathbf{E} \times \mathbf{H}^*) dr}{\int_{wg\ mode} Re(\mathbf{E} \times \mathbf{H}^*) dr} \tag{3.2}$$

There is also confinement factor that takes into account the modal volume of the WG which is defined as follows :

$$\mathbf{V}_{eff} = \frac{\int \epsilon(r) \mid \mathbf{E}(r) \mid^2 dr}{\epsilon_{r_{max}} max(\mid \mathbf{E}(r) \mid^2)} \tag{3.3}$$

where r_{max} is the location of the maximum electric field intensity. The smaller the $\mathbf{V}_{eff}$, the higher confinement ability the WG has.

All the confinement factors introduced above can be applied to quantify light confinement ability of the WG which are strongly dependent on the design parameters such as WG height and width. They can help to target a range of suitable geometrical parameters which is suitable for applications that require high light confinement. However, it is difficult to tell one FoM is superior than the other since the final performance of the devices depend on plenty of factors. Usually, one needs to combine some more other criteria to fine tune the parameters for a specific application.

Wafer specifications

Let us first introduce the available TFLN specifications that will host the WGs. At the beginning of this work, there were two kinds of TFLN wafers/samples available which are schematically shown in Fig. 3.3 :

— (a) TFLN/SiO_2/LN substrate.
— (b) TFLN/SiO_2/Si substrate.

The available thickness *t* of the TFLN samples that are bonded onto silica buffer layer can be as thin as 200 nm, while a 700 nm is the most common thickness that is employed throughout this thesis. Since etching silica material is a well-known technique, one can fabricate photonic components on a membrane out of these TFLN samples. In the sample of TFLN bonded onto silicon substrate, one

can imagine an air-bridged type structure where TFLN is self suspended in the air if the silicon substrate is etched away. In all the

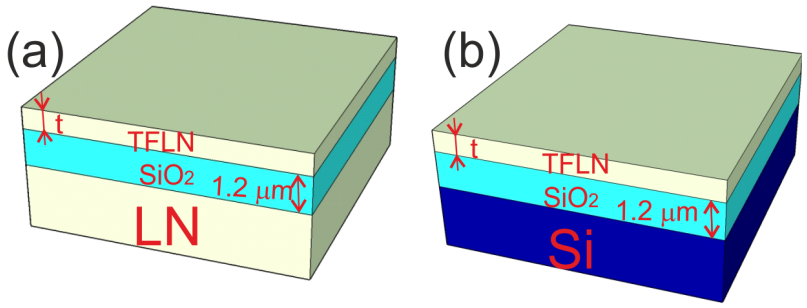

FIGURE 3.3 – (a) TFLN bonded on silica buffer layer on LN substrate. (b) TFLN bonded on silica buffer layer on Si substrate.

following simulations, focus will be put on WG mode that lies at telecom-wavelength of $\lambda = 1.55\ \mu$m.

3.1.1/ RIDGE WAVEGUIDE

Ridge WG has been investigated due to its ability of high light confinement. Examples can be found in ref. [80] where a modulator on ridge WG is designed from bulk LN. An EO polarization modulator fabricated on submicron thin films of lithium niobate ridge WG showing an $V_\pi L$ of 15 V·cm at λ=1.55 μm is presented in ref. [115]. Nevertheless, the fabrication of ridge WG is extremely difficult on a bulk LN. The advent of TFLN will make the fabrication easier since the etching is performed only on a few hundred nanometers thin film.

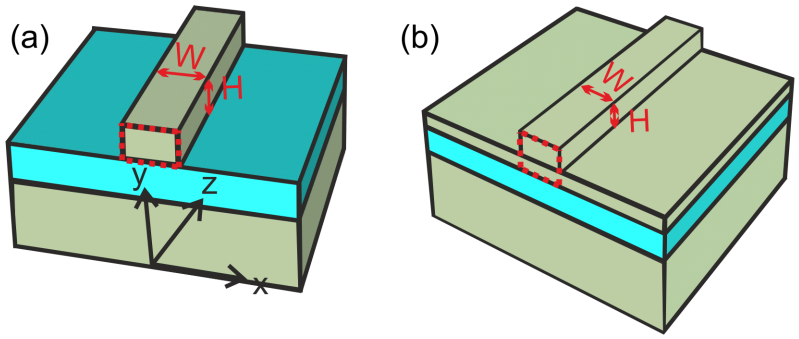

FIGURE 3.4 – The red dashed rectangles show the integration region of calculating confinement factor (a) of ridge WG with etching depth equal to the thickness of TFLN. (b) of ridge WG with etching depth smaller than the thickness of TFLN.

A ridge WG on 0.7 μm thick TFLN, as shown in Fig. 3.4, is firstly studied by varying the WG width W and the ridge height H. It is a step-index structure, usually fabricated from a planar WG that has been patterned and etched to leave a ridge. Total internal reflections take place at the lateral sides of the guide, as well as the top and bottom faces.

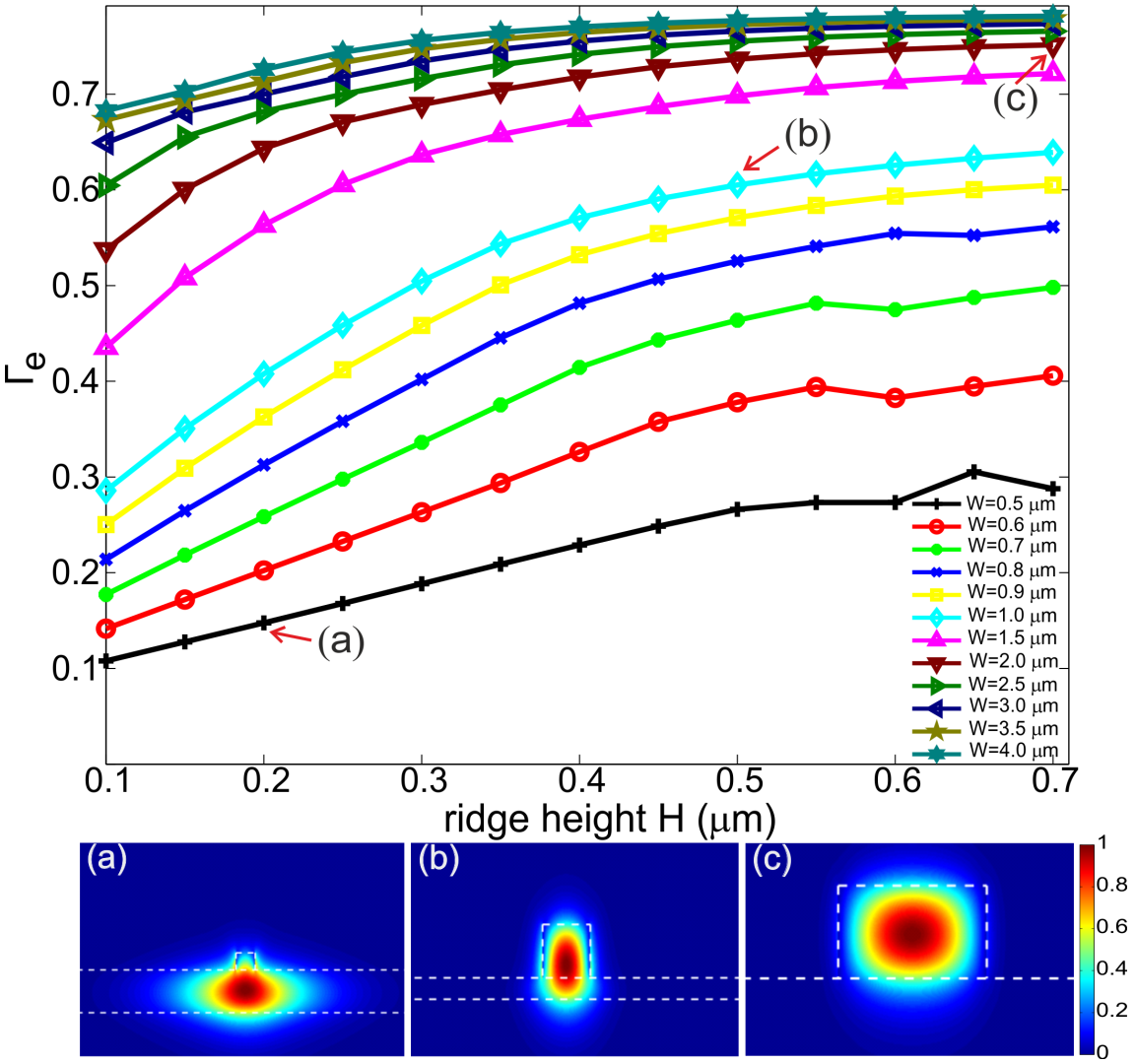

FIGURE 3.5 – Confinement factor Γ_e for TE polarization (x-polarized) mode as a function of the ridge height (H) and different values of the ridge width (W). Mode profiles (amplitude of the main electric field component i.e. $|E_x|$) for three distinct cases are shown (a) W = 0.5 μm, H= 0.2 μm, (b) W=1 μm, H= 0.5 μm, and (c) W= 2.5 μm and H= 0.7 μm.

Both x-polarized (TE) and y-polarized (TM) modes are considered and the calculated Γ_e are respectively shown in Fig. 3.5 and 3.6. In this geometry, the integration region in the numerator of Eq. 3.1 includes the LN ridge and the corresponding area under the ridge in

the LN thin film layer part that has not been etched (also known as rib WG in some of the literature, here it is referred to as ridge WG with different etching depth) as shown in the red dashed rectangles in Fig. 3.4 (b).

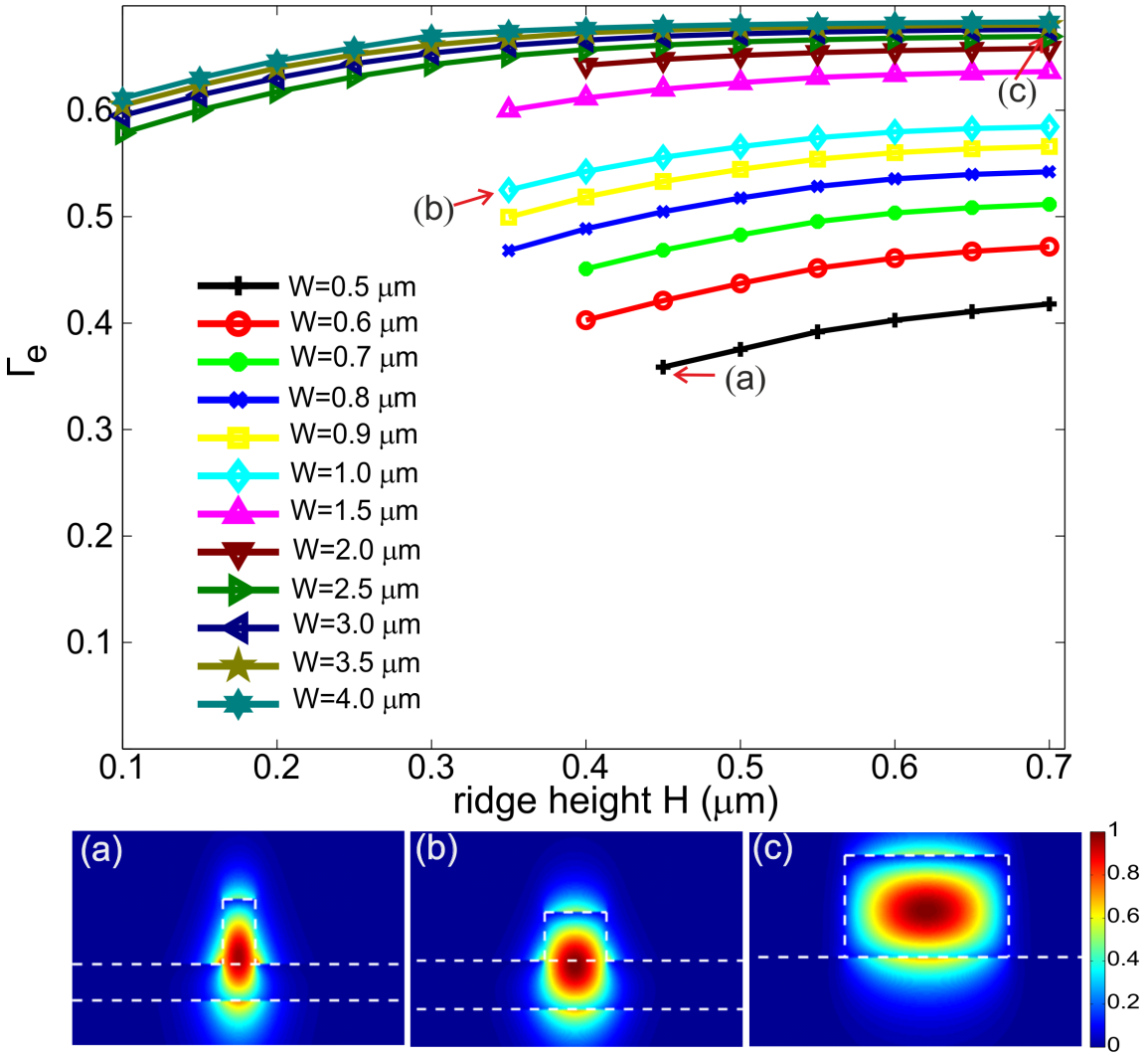

FIGURE 3.6 – Confinement factor Γ_e for TM polarization (y-polarized) mode as a function of the ridge height (H) and different values of the ridge width (W). Mode profiles (amplitude of the main electric field component i.e. $|E_y|$) for three distinct cases are shown (a) W = 0.5 μm, H= 0.45 μm, (b) for W= 1 μm, H= 0.35 μm, (c) W= 2.5 μm and H= 0.7 μm.

Regarding the confinement factor as a function of the height H, we can observe that, for both polarizations, Γ_e monotonously increases as the ridge height H increases. In the case of x-polarized light (Fig. 3.5) the slope of the curves is steeper for ridge width values between 0.5 and 1 μm. Waveguiding is more difficult for y-polarization as it can be noted in Fig. 3.6. In fact, it exists a critical value (lower

bound) of H to support y-polarized mode. This is shown in Fig. 3.6 where a big blank part (no modal solution) appears in the lower-left portion of the curves. However, one can find a set of geometrical parameters for which both polarizations are well guided in the ridge. They correspond to ridges that are 0.7 μm of height and around 2.5 μm of width. The confinement factor in this case is of 0.76 and 0.67 for x- and y-polarizations respectively.

3.1.2/ STRIP LOADED WAVEGUIDE

In a strip loaded WG, a planar WG has a strip of slightly lower index material which defines the waveguiding path. The refractive index relation between the three different layers generally satisfies $n_1 < n_3 < n_2$ as shown in Fig. 3.7(a). The refractive index relationship of $n_1 < n_2$ makes n_2 layer a planar WG. The WG is formed by a loading strip material with refractive index of n_3 ($n_3 < n_2$) as shown in Fig. 3.7(a). In the strip loaded WG, most of the energy is confined in the planar WG (the thin film). Therefore, requirements on the edge quality (side walls roughness and verticality) should not be as severe as in the case of a ridge WG. As a consequence they may be easier to fabricate and present small propagation losses [192, 193, 194].

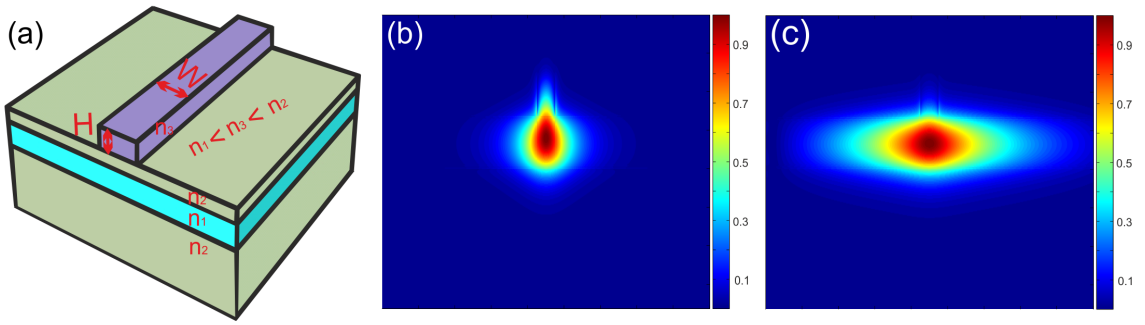

FIGURE 3.7 – (a) Sketch of strip loaded WG, where the refractive index relationship of different layers are shown. (b) Mode profile of Si_3N_4 strip loaded WG with loaded width W = 1.5 μm, loaded height H = 0.5 μm. (c) Mode profile of SiO_2 strip loaded WG with loaded width and height the same as in (b).

Studies are carried out on different loaded materials including Si_3N_4 (n= 2.01 at $\lambda = 1.55$ μm) and SiO_2 (n= 1.46 at $\lambda = 1.55$ μm) by varying the loading width and height. Among different loaded ma-

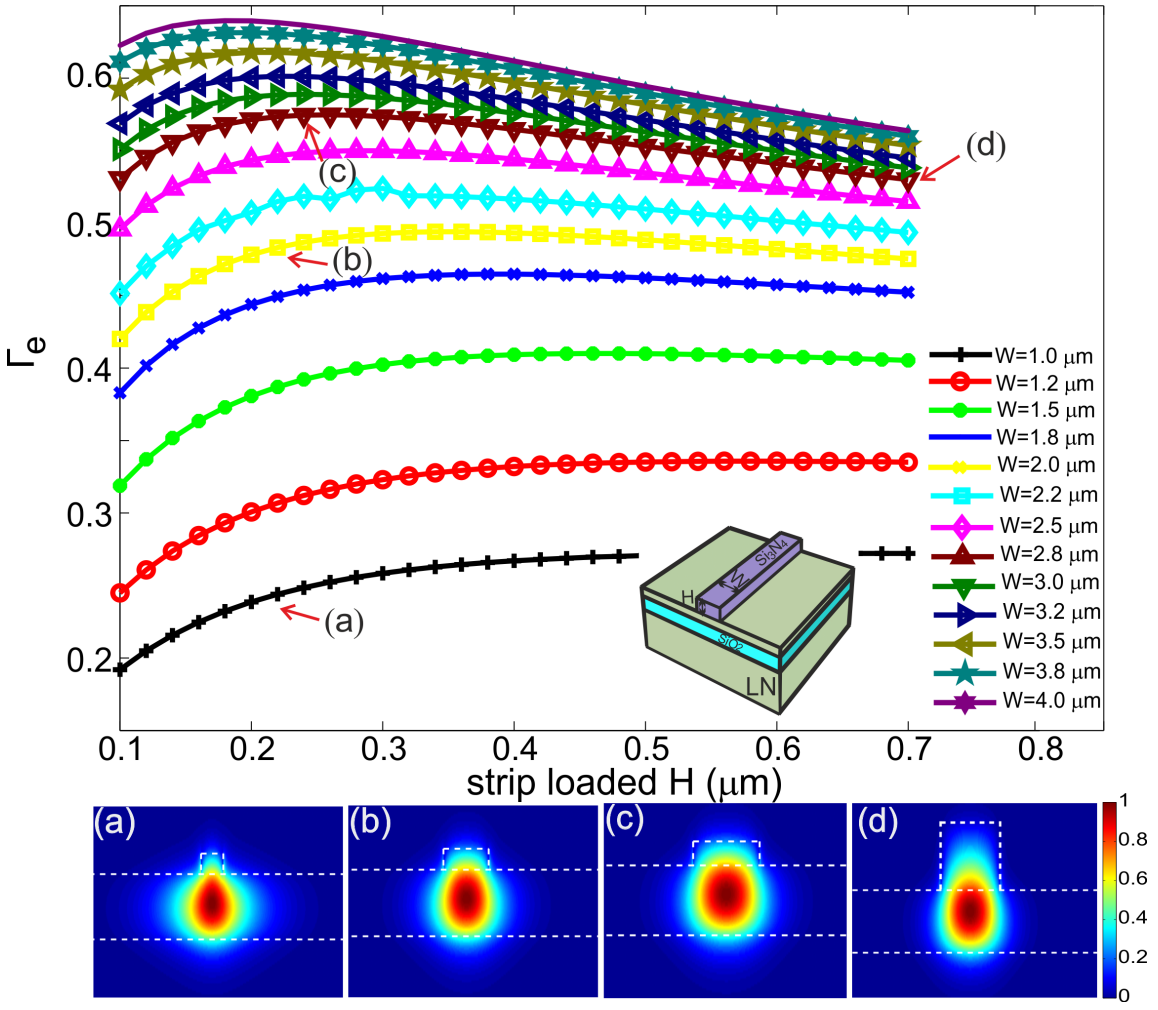

FIGURE 3.8 – Confinement factor Γ_e as a function of strip loaded height (H) in the case of x-polarization (TE). The different curves correspond to different strip loaded widths. Fig. (a), (b), (c) and (d) show the mode profiles (amplitude of the main electric field component i.e. $|E_x|$) for four distinct positions in the confinement factor curves (a) W = 1 μm, H = 0.22 μm, (b) W = 2 μm, H = 0.22 μm, (c) W = 2.8 μm, H = 0.24 μm, and (d) W = 2.8 μm, H = 0.7 μm.

terials studied, we found that a smaller refractive index difference between the loaded material and LN yields a better confined mode. As an example, mode profiles of strip loaded WG with the same loaded width (1.5 μm) and height (0.5 μm) on Si_3N_4 and SiO_2 are shown in Fig. 3.7 (b) and (c) respectively. It is evident to see that Si_3N_4 loaded WG yields a more confined mode while SiO_2 loaded WG gives a broad lateral mode distributions. In fact, the strip loaded WG guiding principle can be considered as similar to that of rib WG, where light is confined laterally by the rib width but the mode lies in the planar WG under the loaded strip. If there is a large refractive

index difference between the loaded material and the guiding core material, then it will lead to a poor defined lateral guiding path (case of a lower refractive index in the loaded material as that in Fig. 3.7 (c)) or the light totally guides up to the loaded material instead of the planar WG layer (case of higher refractive index in the loaded material). Due to the small refractive index difference with respect to LN, Si_3N_4 is considered as the most suitable material to create the load.

Both x-polarized (TE) and y-polarized (TM) modes are considered. The calculated Γ_e is respectively shown in Fig. 3.8 and 3.9. We can see that for loaded heights larger than 0.2 μm, the optical mode is well guided and confined in the lithium niobate thin film. However, as the loaded height increases, the effective index of the mode increases since light encounters more with Si_3N_4 material than air. The confinement factor in the lithium niobate is therefore smaller since, as shown in Fig. 3.8 (d), part of the energy is confined in the Si_3N_4 strip loaded region. This behavior is observed for both polarizations, as it can also be seen in Fig. 3.8 and 3.9 where negative slop of the curves are obtained for large values of H.

Concerning the light confinement with respect to the strip loaded width W, we can see that after a critical value of around 2.5 μm, light is always well confined and larger width values do not significantly increase the confinement factor. Fig. 3.9 shows that y-polarized modes are not as well guided as x-polarized ones. Indeed, if we design loaded widths smaller than 1.5 μm, light is not guided at all for this polarization. Even when the loaded width is bigger than this critical width value, there exists a critical loaded height (lower bound) in order to support y-polarized modes.

Let us now study the robustness of the strip loaded waveguides with respect to fabrication imperfections on the strip. We have numerically analyzed the case of Fig. 3.8 (c) corresponding to x-polarized mode with W= 2.8 μm, H = 0.24 μm by varying the loaded side walls from perfectly perpendicular ($\alpha = 90^o$) to some sidewall angles ($\alpha = 60^o$, 40^o, and 20^o). Fig. 3.10 shows the mode profile ($|E_x|$) for the three sidewall angles.

As we can see, light is always well confined within the LN thin film

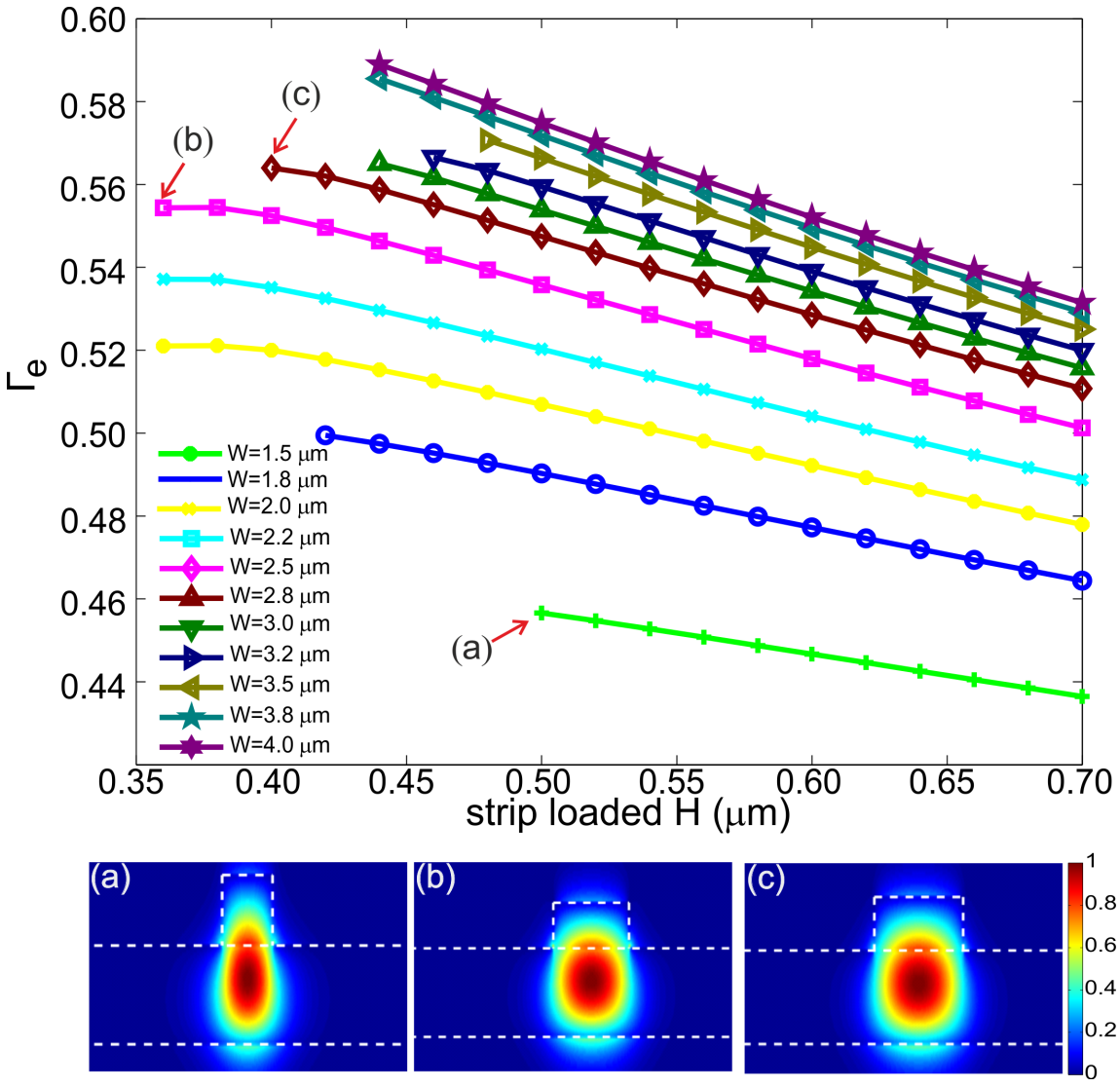

FIGURE 3.9 – Confinement factor Γ_e as a function of strip loaded height H in the case of y-polarization (TM). The different curves correspond to different strip loaded widths. Fig. (a), (b) and (c) show the mode profiles (amplitude of the main electric field component i.e. $|E_y|$) for four different positions in the confinement factor curves (a) W = 1.5 μm, H = 0.5 μm, (b) W = 2.5 μm, H = 0.36 μm, and (c) W = 2.8 μm, H = 0.4 μm.

and there is only a slight mode broadening in the x direction that is due to the fact that the lower base of Si_3N_4 trapezoid dimension increases when α decreases. The confinement factors Γ_e of 90^o, 60^o, 40^o and 20^o sidewall angles strip are 0.59, 0.56, 0.55 and 0.53 respectively, which further shows the robustness with respect to fabrication imperfections.

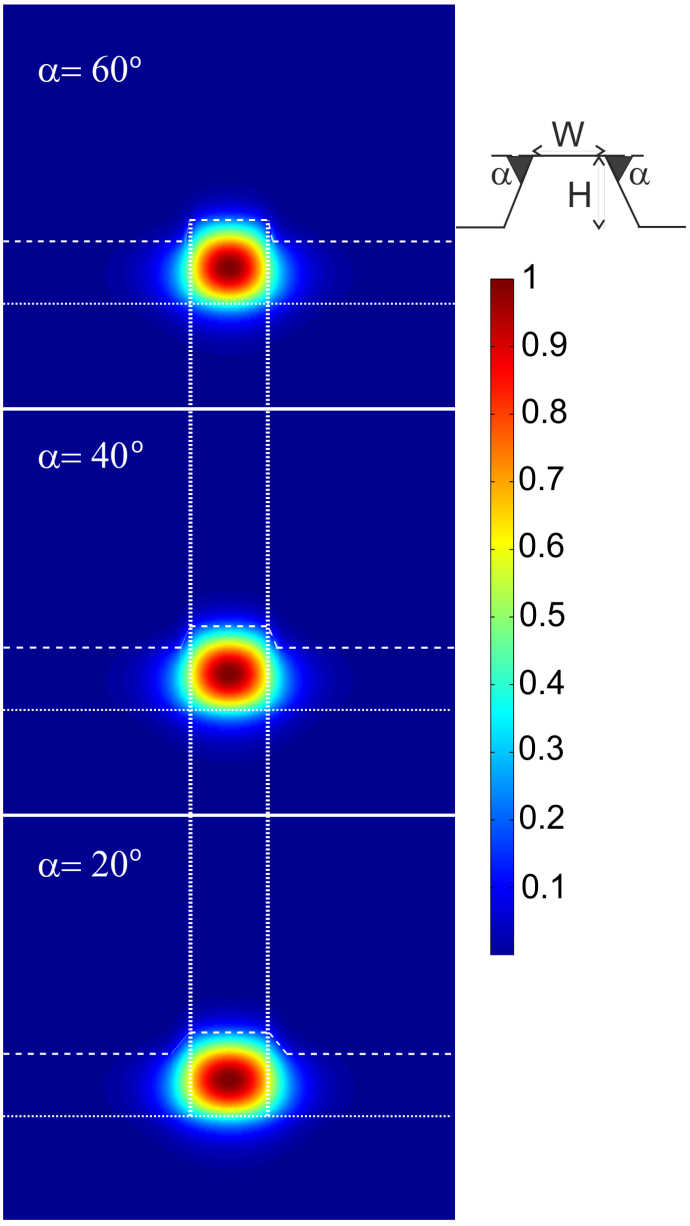

FIGURE 3.10 – Mode profiles (amplitude of the main electric field component i.e. $|E_x|$) for the strip loaded waveguide with width W = 2.8 μm and height H = 0.24 μm in which different side wall angles have been considered (α= 60^o, 40^o, and 20^o respectively).

3.1.3/ HORIZONTAL AND VERTICAL SLOT WAVEGUIDES

The guiding mechanism of a slot WG was introduced by the group of M. Lipson [195]. It takes advantage of the discontinuity of the electric field at a high-index-contrast interface to strongly enhance and confine light in a nano-scale region of low index material. A slot WG consists of two strips or slabs of high-refractive-index (n_h) materials separated by a subwavelength-scale low-refractive-index (n_l) slot re-

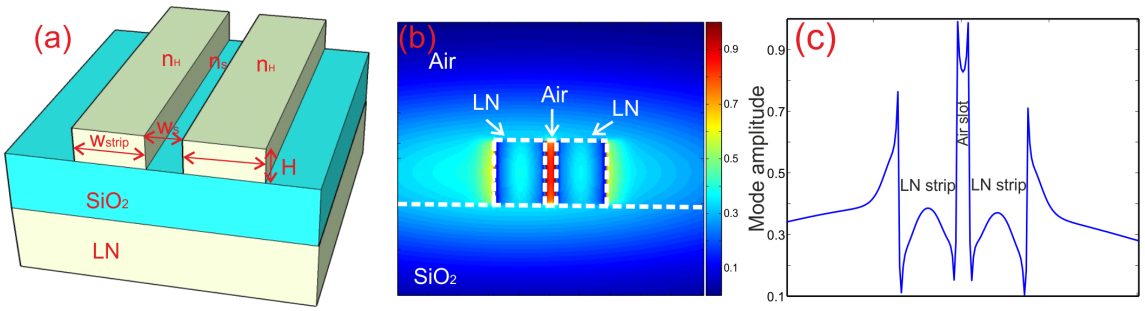

FIGURE 3.11 – (a) Slot WG configure with two LN strips and air slot on TFLN. (b) Mode profile of the LN air slot WG, with parameters of W_{strip}= 160 nm, W_s=40 nm and H= 700 nm. (c) Mode amplitude profile along the middle of the slot mode in (b).

gion. One can form air slot WG in lithium niobate as schematically shown in Fig. 3.11 (a).

The operation principle of a slot WG is based on the discontinuity of the electric field (E-field) at high-refractive-index-contrast interfaces. Maxwell's equations state that, to satisfy the continuity of the normal component of the electric displacement field **D** at an interface, the corresponding E-field must undergo a discontinuity with higher amplitude in the low-refractive-index side. That is, at an interface between two regions of dielectric constants ϵ_l and ϵ_h, respectively :

$$\begin{aligned} \mathbf{D}_l^N &= \mathbf{D}_h^N \\ \epsilon_l \mathbf{E}_l^N &= \epsilon_h \mathbf{E}_h^N \\ n_l^2 \mathbf{E}_l^N &= n_h^2 \mathbf{E}_h^N \end{aligned}$$

Where the superscript N indicates the normal components of **D** and **E** vector fields. Thus, if $n_l \ll n_h$, then $\mathbf{E}_l^N \gg \mathbf{E}_h^N$. Given that the slot critical dimension is comparable to the characteristic decay length of fundamental eigenmode of the guided-wave in high refractive index strip structure, the resulting E-field normal to the high-index-contrast interfaces is enhanced in the slot and remains high across it. Since wave propagation is due to total internal reflection, there is no interference effect involved and the slot-structure exhibits very low wavelength sensitivity. The mode profile of LN air slot WG is shown in Fig. 3.11 (b). Light intensity is increased in the nano slot region as can be seen from the WG mode cross section plot in Fig. 3.11 (c).

Since the pioneering works by researchers in Lipson's group, numerous guided-wave configurations based on the slot WG concept have been proposed and demonstrated for various applications. High field enhancement in the slot WG has been investigated by combining with high EO coefficients slot material to develop low drive voltage and high speed modulators. For instance in the team of Hochberg (University of Washington) silicon slot WGs combined with electro-optic polymers had been investigated in order to obtain exceptionally low drive voltage modulators as low as 0.25 V with a segmented WG design in which a periodic set of small arms touches both WG arms facilitating the electrical contacts [196]. Various methods have been developed to make electrical contact to the slot WG arms that can allow low optical propagation loss including segmented slot WG with an optical propagation loss of 4 dB/cm [197], a (symmetric) strip loaded slot WG with a 6.5 dB/cm loss [198], and an asymmetric slot WG with an exceptional propagation loss of 2 dB/cm [199]. Slotted WG geometry has been demonstrated to yield a high-quality factor resonators of 27,000 with an estimate low losses of -10 dB/cm which is promising candidate in applications such as chemical and biological sensors and tunable telecommunications filters etc [200]. Horizontal single and multiple slot WG consisting of amorphous Si/SiO_2 layer has been demonstrated with a low propagation loss of 6$\sim$7 dB/cm limited only by the a-Si material absorption [201]. Slot optical WGs have been demonstrated with the ability of high confinement of light even at sharp bends [202]. A polarization-independent directional coupler had been achieved based on slot WG configurations [203]. Slot WG has been utilized as an innovated color-selecting element in color displaying applications operating at visible wavelengths that employs resonant plasmonic and photonic modes in slot WGs [204]. Lasing applications employing resonant cavity in-plane Si electrically-driven LED based on a Si/SiO_2 slot-waveguide microresonator with electroluminescent Er-doped SiO_2 in the slot region has been investigated. It emits light at 1.54 μm with a bias current of only 0.75 nA showing a promising architecture for the fabrication of an electrically-pumped Si laser [205].

A theoretical study is made on the possibilities to achieve nonlinear

frequency conversion in plasmonic slot WGs where the slot core is filled with nonlinear material with high $\chi^{(2)}$. By exploiting the geometrical dispersion of the WG modes, one can obtain a maximized the overlap integral of fundamental and harmonic mode for an enhanced nonlinear application. The flexible geometrical dispersion of the slot WG configurations makes phase matching possible without resorting to other mechanisms like birefringence phase matching or periodic poling of the nonlinear medium [206]. Slot WGs (single and multiple) are ideal structures in exploiting nonlinear effects since they possess high field confinement and flexible dispersion engineering characteristics [207, 208]. Flat and low group velocity dispersion has been investigated in structures like a strip/slot hybrid WG dual slots. Infiltrating the slot with high nonlinear material and through tuning different structural parameters, these WGs can be applied to optimize the nonlinear optical effect such as four wave mixing and broad bandwidth supercontinuum generation etc [209, 210, 185].

Novel high light confinement slot WG opens a new realm for developing highly sensitive sensors such as biochemical sensors and EO based sensors [211, 212]. The first experimental demonstration of a slot WG based biochemical sensor was achieved by Barrios et al for both bulks [213] and surface sensing [214]. These authors employed a vertical (slot/rail interface is normal to the substrate) slot WG ring resonator made of silicon nitride which allows the definition of a wider slot region while maintaining single-mode operation. A sensitivity of 212 nm/RIU had been achieved with the slot based ring resonators.

Si/SiO_2 slot WGs had been investigated as on-chip gas sensor by Robinson et al [215] where a slotted Si/SiO_2 implemented with a micro-ring resonant cavity is designed to detect small changes in the refractive index due to variation in gas composition and pressure acetylene. The refractive index bulk sensitivity of this device was measured to be as high as 490 nm/RIU, evidencing that slot WG is an ideal architecture for highly sensitive sensors design. In addition to micro-ring resonators, other configurations such as passive directional couplers [216, 217] and Fabry-Perot cavities [218] based on slot-waveguides have been demonstrated as biochemical sensors with high sensitivity.

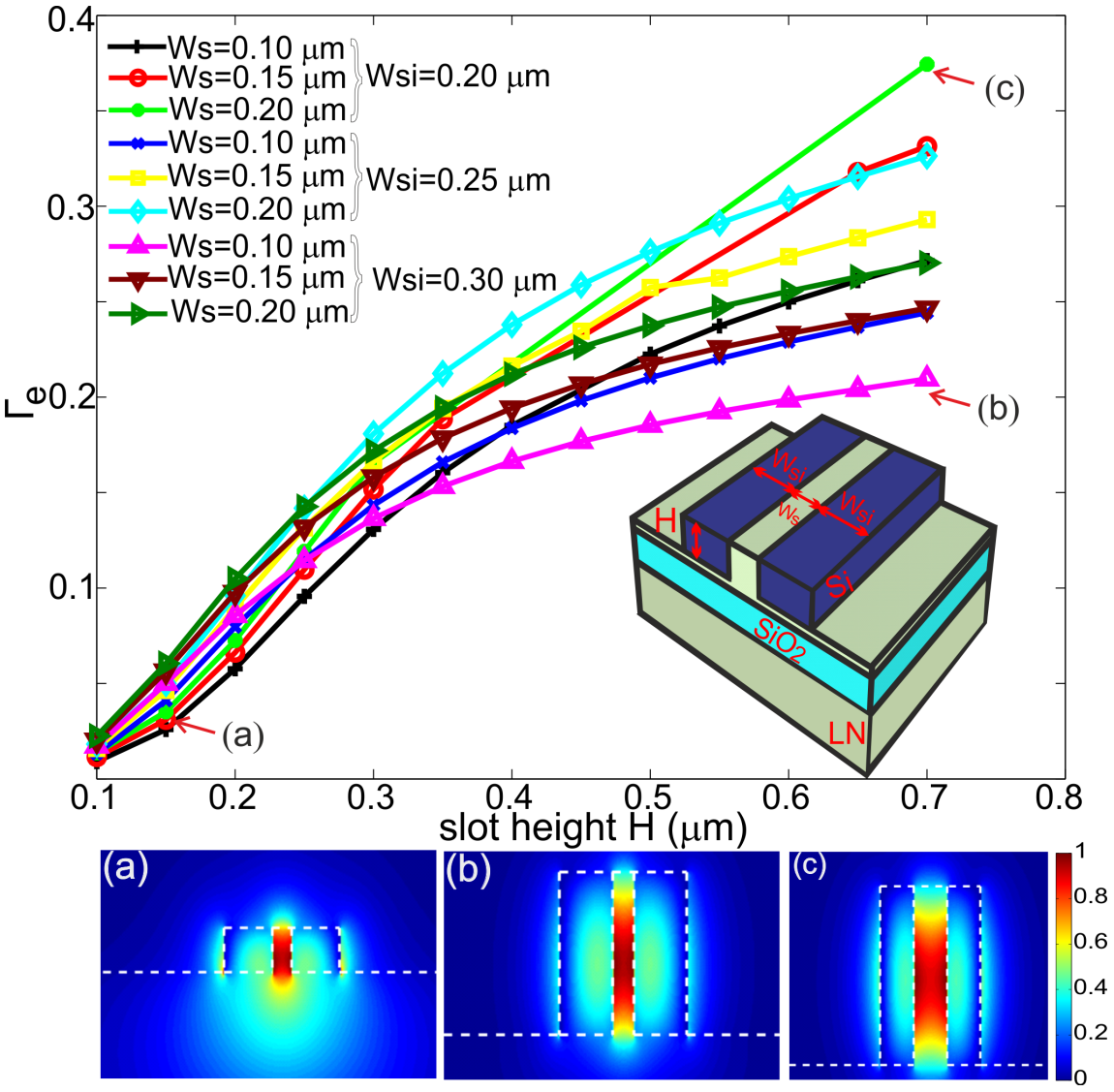

FIGURE 3.12 – Confinement factor Γ_e as a function of the slot height H, different slot widths and silicon widths. Fig. (a), (b) and (c) shown in arrows correspond to different behaviors in the enhancement curves. The geometrical values are (a) Wsi = 0.2 μm, Ws = 0.15 μm, H = 0.15 μm, (b) Wsi = 0.3 μm, Ws = 0.1 μm, H = 0.7 μm, and (c) Wsi = 0.2 μm, Ws = 0.2 μm, H = 0.7 μm.

Slot WG configurations on LN are not investigated as much as that in other material platform like silicon, silicon nitride etc probably due to the fabrication difficulties that is related to the high etching resist nature of LN. Here theoretically investigations are made on LN slot WG configuration together with PhC cavity design to form E-field sensors. In order to confine high intensity of light in LN, we propose to replace the air slot (as shown in Fig. 3.11 (a)) by lithium niobate slot sandwiched between silicon rails architecture (inset of Fig. 3.12)

in order to find out how light can be confined in this hybrid geometry to enhance nonlinear responses within the lithium niobate.

In general, there are vertical and horizontal slot WG (slot/rail interface is parallel to the substrate) configurations. Vertical slot WG which involves dry etching during device fabrication of high-index interfaces may have a large optical scattering losses due to interface roughness. On the other hand, horizontal slot-WG based configurations can be fabricated by using conventional deposition techniques (for instance PECVD) which can be advantageous to control the slot distance and to reduce rail/slot interface roughness.

Vertical slot WG

Limited to the available TFLN sample configurations, systematical simulations are only carried out for vertical slot WGs. In this numerical study, three design parameters will be varied, the LN slot width (W_s), the silicon side walls width (W_{si}) and the height (H) of the structure as shown in the inset of Fig. 3.12.

In order to fulfill the requirement of slot width smaller than the decay length of the evanescent light that exists outside a single WG made by high refractive index material, we have focused on slot widths W_s of 0.1, 0.15, and 0.2 μm. As far as the LN width requirements is concerned, the confinement factor increases as the silicon width decreases. There is however a critical width value W_{si} around 0.1 μm for which, below that value, light is no longer guided in the lithium niobate slot region. From the simulation results in Fig. 3.12, we can see that the confinement factor increases with the height H, but for H values higher than 0.4 μm, Γ_e increases in a much slower pace. With a proper design (which corresponds to H= 700 nm, W_{si}= 200 nm and W_s=100 nm configurations), up to 48 % percentage of the coupled light can be confined in the LN slot. Since the slot region has nanometer dimensions, this confinement implies strong electric field which is extremely interesting for nonlinear optical applications. As an example, zero group velocity and high-order harmonic generation had been already theoretically demonstrated for nonlinear organic materials [210, 219].

In addition to the above perfect vertical LN slot WG with two perfect silicon rails, simulations on configurations of slot WG with silicon height higher than the LN slot height are also performed as schematically shown in Fig. 3.13 (a). Difference in silicon height and LN etching depth is defined as a variable U_{si}. Simulations on slot WG with fixed parameters of W_s= 100 nm, W_{si}= 200 nm and varying H to 500 and 700 nm while U_{si} varies as 50, 100, 150 nm are performed. The confinement factor is tabulated in Table 3.1. Mode profile of a structure with parameters of slot H= 700 nm and U_{si}=50 nm are shown in Fig. 3.13 (b). Part of the light is confined onto the upper 50 nm thick silicon cover and this leads to a confinement factor Γ_e decreasing down to 0.305 while it is 0.37 in the counterpart of perfect slot WG. Table 3.1 summarizes the confinement factor Γ_e varying with different upper silicon height U_{si}. We can conclude that if the upper silicon height is smaller than 100 nm, then most of the light is still confined in the LN slot region with slightly smaller confinement factor. These studies show that slot WG can have some tolerance with different upper silicon height.

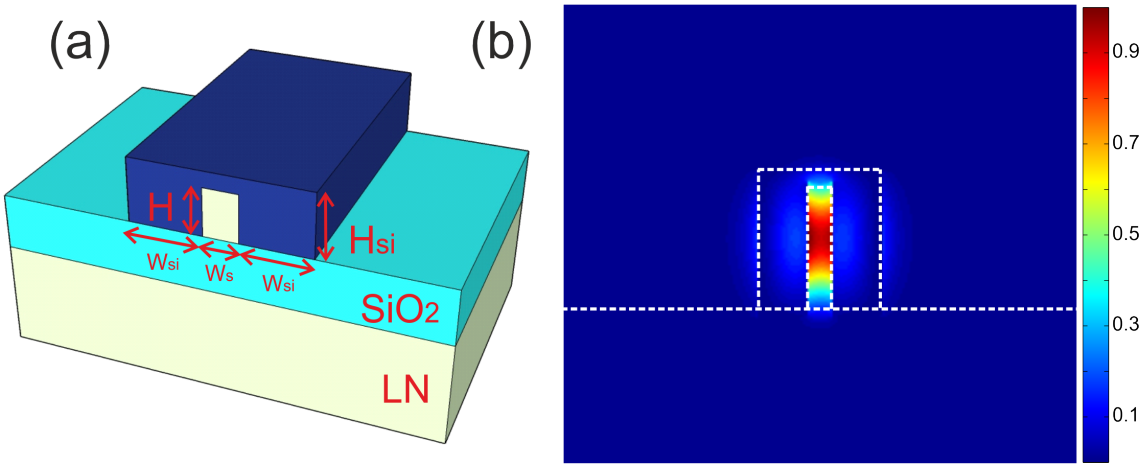

FIGURE 3.13 – (a) Sketch of vertical LN slot WG with silicon cover on top of the slot where H_{si} is the height of silicon and H is the etching depth of LN. (b) Mode profile of LN slot with structure parameters of W_{si}= 200 nm, H_{si}= 750 nm, W_s= 100 nm and H= 700 nm. The white dashed lines show the structure of the WG.

Horizontal slot WG

Horizontal single slot WG on LN self suspended in air as schematically shown in Fig. 3.14 can be realized through the deposition of

TABLE 3.1 – Confinement factor Γ_e of vertical slot WG with different upper Si thickness

WG parameters	H=500 nm	H=700 nm
U_{si}=0 nm	0.275	0.3744
U_{si}=50 nm	0.2506	0.305
U_{si}=100 nm	0.2346	0.2785
U_{si}=150 nm	0.2085	0.24

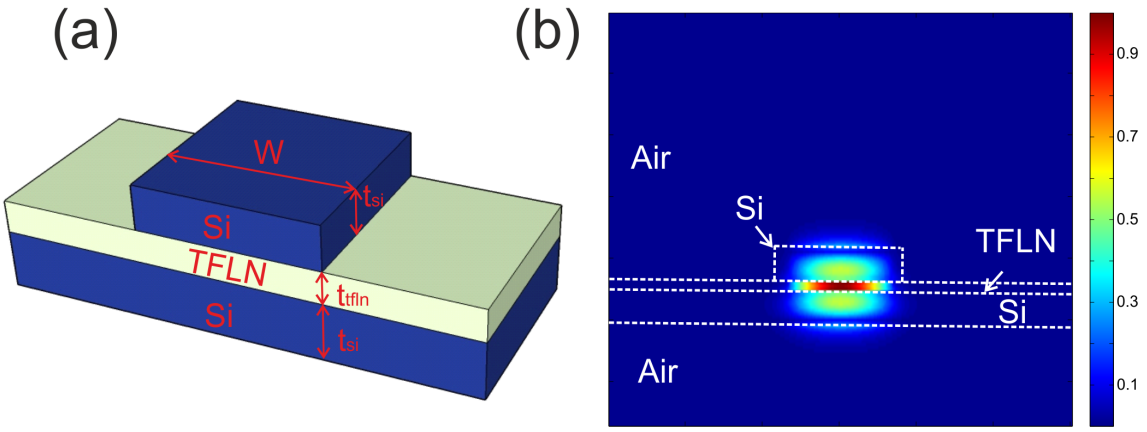

FIGURE 3.14 – (a) Sketch of air suspended horizontal LN slot WG sandwiched by silicon rails. (b) Symmetric horizontal slot WG mode profile with parameters of silicon layer thickness of t_{si}=300 nm, TFLN thickness t_{tfln}=100 nm, upper silicon layer width W=2 μm.

amorphous silicon on top of TFLN on SOI sample. The self suspended structure can be realized through the etching of silicon substrate and silica buffer layer beneath the LN thin film. A typical horizontal LN slot WG mode is shown in Fig. 3.14 (b) with a confinement factor of 30%. Further optimization of the horizontal slot WG is not carried out since for the moment there is no available TFLN on SOI sample for further experimental investigations. However, we believe that fabrication of TFLN bonded onto SOI will succeed with the advancement of thin film technology. Therefore we believe that horizontal LN slot WG is a much more feasible configuration in the viewpoint of fabrication technological difficulty compared to the vertical slot WG.

3.1.4/ DOUBLE SLOT WAVEGUIDE

Double slot WG can be considered as ridge WG with additional two low refractive index slot region and it guides light in the high refractive index material. In order not to confuse it with the names of WG,

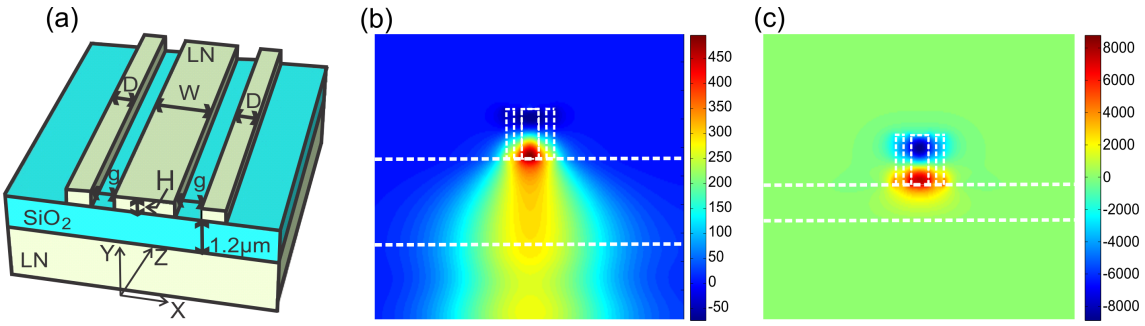

FIGURE 3.15 – (a) Schematic of double slot WG with silica on LN substrate. (b) y component of Poynting vector P_y distribution of double slot with substrate as shown in (a) with parameters of D= 80 nm, g= 80 nm, W= 180 nm, H= 700 nm. The three LN ridges of double slot structure and also the silica layer are outlined with dashed white lines. (c) y component of Poynting vector P_y distribution with double slot WG with the same slot parameters as in (b) but on 500 nm SiO_2 suspended in the air structure. The three LN ridges of double slot structure are outlined with dashed white rectangles, and 500 nm SiO_2 slab layer is also outlined under the double slot structure.

we refer two slot regions where light is guided in high refractive index material as double slot WG. On the other hand, WGs having two slot regions that guide light by the principle of electric field discontinuity in the low refractive index material are referred to as dual slot WG. One might ask the question about the advantage of creating slot region whereas light is guided in the high refractive index material. In fact, double slot WG is much more feasible in the viewpoint of fabrication compared to that of the above studied vertical LN slot WG sandwiched by silicon rails. Fabrication of the vertical slot WG sandwiched by silicon rails not only involves etching LN to nano scale width but also requires the deposition of amorphous silicon attaching on the ridge sidewalls. Notice that silicon and LN are materials with large difference in lattice constant and thermal properties. Attaching such material with high quality would be extremely difficult. Henceforth, fabrication of double slot WG only involving etching of LN seems less challenging. Simulations on double slot WG are started by comparing structures configured with and without substrate as schematically shown in Fig. 3.15 (a) and Fig. 3.16 respectively. Fig 3.15 (b) and (c) show double slot WG Poynting vector P_y component of structures with and without substrate. Figure 3.15 (b) corresponds to the P_y distribution of double slot WG with substrate configurations where a large amount of light leaks into to substrate. Light is not guided as well as the configuration with the

structure suspended in the air as shown in Fig. 3.15 (c). For this reason and also for simplifying our analysis, simulations with double slot structure are only performed on 500 nm SiO_2 suspended in the air as schematically shown in Fig 3.16.

In air suspended double slot WGs as shown in Fig. 3.16, three high index of refraction dielectric walls are separated by two air slots. The side dielectric walls have a width D and the central wall width is W. The air slot width is g and the structure height is H.

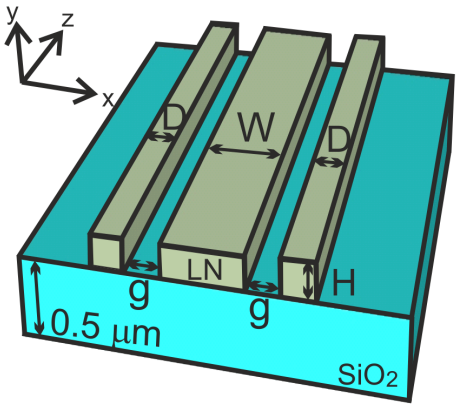

FIGURE 3.16 – Schematic of the double slot waveguide based on three lithium niobate walls set on a 0.5 μm SiO_2 substrate suspended in air.

By controlling the geometry and the air gaps, light can be confined in the central LN region. The WG confinement cross section can be smaller than that in the case of a conventional LN ridge. As for the case of the x-polarized mode, there is a discontinuity of the electric field at the lithium niobate/air interface so light cannot be efficiently guided on the central lithium niobate wall. However, for the y-polarized mode, one can find a set of geometrical parameters for which light can be guided in the central lithium niobate region. Therefore, in this study we will only take into account y-polarized light.

Two cases of different central LN ridge widths will be studied. Figure 3.17 shows the parametric study for a central width of the LN ridge equal to 1 μm. The confinement factor barely changes with the air gap size and has values that are comparable with the ridge WG configuration. However, as it has been mentioned in [186], the presence of air gaps may facilitate the tuning of WG dispersion properties.

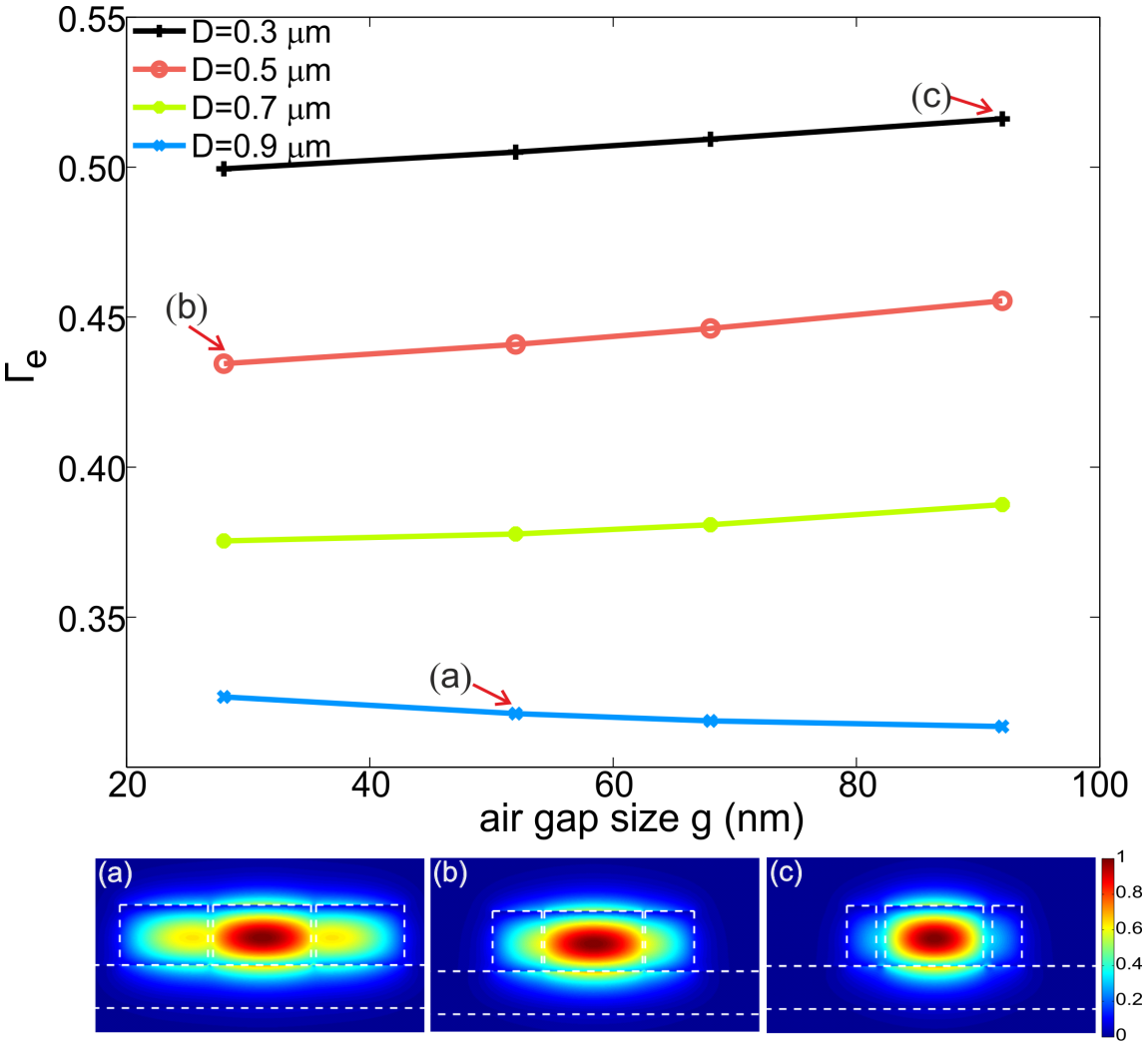

FIGURE 3.17 – Confinement coefficient Γ_e as a function of the air gap slot width g between the side and the central lithium niobate walls for the y-polarized mode. The different curves correspond to different values of the side lithium niobate wall width while the central width is equal to $1\ \mu$m. The three images (a), (b), and (c) are the corresponding mode distribution profiles (amplitude of the main electric field component i.e. $|E_y|$) (a) D = $0.9\ \mu$m and g = $0.052\ \mu$m, (b) D=$0.5\ \mu$m and g =$0.028\ \mu$m, and (c) D = $0.3\ \mu$m, and g =$0.092\ \mu$m.

From the results shown in Fig. 3.18, corresponding to a much smaller central width ($0.3\ \mu$m) we can see that the air gap is more critical when the central wall LN width is small. The side ridges allow guiding light in the central LN even for this small width dimension. Let us note that for the same ridge dimensions y-polarized modes are not supported, as can be seen in Fig. 3.6 where a big blank part (no modal solution) appears in the lower-left portion of the curves.

Finally, Table 3.2 summarizes the best configurations for all the geometries that had been systematically studied above, where S_A is ac-

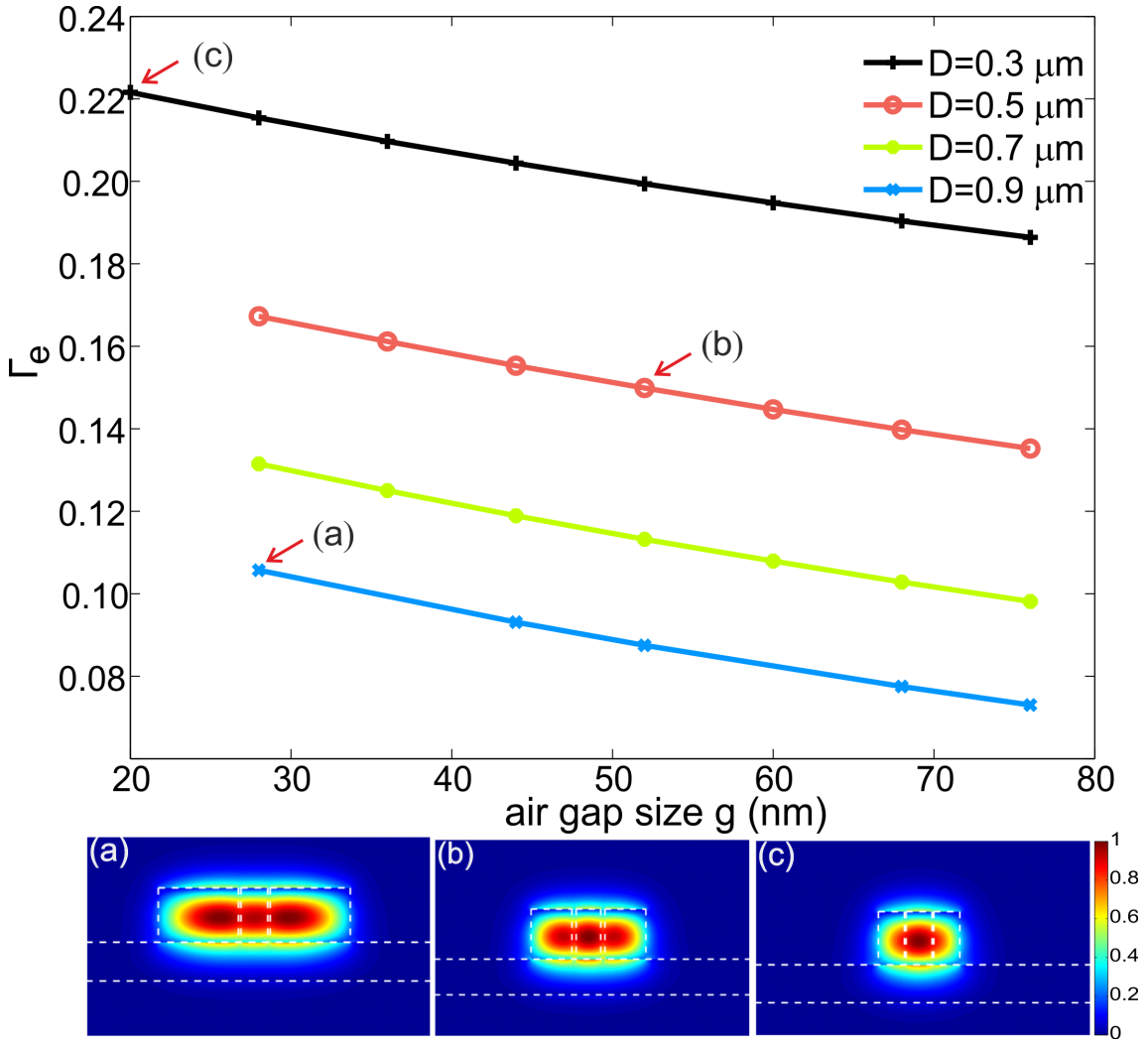

FIGURE 3.18 – Confinement coefficient Γ_e as a function of the air gap g between the side and the central slot for y-polarized mode. The different curves correspond to a central slot width of $0.3\ \mu\ m$. The three images (a), (b), and (c) are the corresponding mode distribution (amplitude of the main electric field component i.e. $|E_y|$) (a) D = $0.9\ \mu$m and g = $0.028\ \mu$m, (b) D=$0.5\ \mu$m and g =$0.052\ \mu$m, and (c) D = $0.3\ \mu$m , and g =$0.02\ \mu$m.

TABLE 3.2 – WGs comparison

waveguide type	S_A (μm^2)	S_G (μm^2)	Neff	Γ_e	$\frac{\Gamma_e}{S_A}$
ridge TE	1.75	1.75	1.9693	0.7658	0.4376
ridge TM	1.75	1.75	1.8989	0.6693	0.3825
strip TE	1.96	1.96	2.0188	0.5888	0.3004
strip TM	1.96	1.96	1.9997	0.5648	0.2882
slot TE	**0.14**	**0.42**	**2.3040**	**0.3744**	**2.6743**
double slot TM	0.70	1.2488	1.8359	0.5163	0.7376

tive guiding cross section and S_G is guiding cross section. Guiding cross section is the physical size of the WG, while the active guiding

cross section is a subsection that includes only the active material in the guiding cross section. As shown in bold in the table, slot WG TE polarized mode outperforms other configurations in terms of Γ_e/S_A, which can be an indication that slot WGs would yield high nonlinear responses. 0.7 μm thin films allow waveguiding for telecommunication wavelength and the compactness depends on the chosen geometry. In the case of ridge WGs, light can be confined for both polarizations but the price to pay is a relative large guiding cross-section. Slot WGs provide the tiniest active area of only 0.14 μm^2 but only TE polarization is allowed and in terms of technological requirements, it is a challenging geometry to fabricate. From the technological point of view strip loaded WG is by far the easiest geometry to fabricate since there is no etching on lithium niobate. Confinement factors are slightly lower than for the ridge geometries but modes are well confined in the thin film. One other important feature of strip loaded WG is its robustness to fabrication imperfections on the loaded layer.

Based on these analysis, slot WG and strip loaded WG are chosen as the host WGs to design PhC cavities to realize the resonance wavelength shift based sensor designs.

3.2/ PHOTONIC CRYSTALS DESIGN ON TFLN WGS AND THEIR SENSING APPLICATIONS

In this section, PhC cavity based F-P configurations on the slot WG and strip loaded WG are presented. Simulations are first performed to construct PhC mirror by designing PhC structure with a large PBG in the interested frequency range (vicinity of 1.55 μm). Cavity is then formed by introducing defect into the PhC mirror design. It is also referred to as Fabry-Perot cavity design where the mirrors are made of PhC. In order to narrow down the parameter search space, calculation methods such as 2D-PWE and 2D-FDTD are applied to first determine a suitable set of parameters to form PhC mirrors. Then by 2D-FDTD and 3D-FDTD transmission investigations, a defect is introduced to the PhC for creating cavity and fine tuning the geometry parameters. Finally, sensitivity analysis of the PhC cavity based device exploited as E-field sensor is carried out through full 3D-FDTD

calculations.

3.2.1/ Bragg grating design in slot WG

From slot WG systematical study in Fig. 3.12, we can see that parameters combining of a silicon rail width of W_{si}= 200 nm and a LN slot width W_{LN}= 100 nm shows superior ability to confine light in LN slot compared with other configurations. Regarding to the slot height H, the larger the height H the better the light confinement of light. Taking into account the difficulty in etching LN material, simulations on slot WG PhC design with the above parameters and different values of slot height H are carried out.

2D PhC design is the most common considered choice in PhC nano patterning due to the fact that it is easier for fabrications and it posses comparable properties to that of 3D PhC structures. Empirically speaking, a filling factor (hole radius to period ratio) of at least about 0.3 is needed to open a PBG in LN air holes PhC structure. For the structure operating at the vicinity of 1.55 μm telecommunication wavelength, the 0.3 filling factor would require a PhC period of about 500 nm which is a large value compared to total width of 500 nm (2*W_{si}+W_{LN}) slot WG. Therefore, a 1D PhC Bragg grating is considered to design on slot WG configurations.

The criteria of how to choose PhC parameters depends on the desired properties required for sensing applications and it is listed as follows :

- Large PBG size ;
- PBG and cavity resonance wavelength centering at wavelength vicinity of 1.55 μm ;
- Compact size of the PhC ;
- High confinement of light in LN material ;

3.2.1.1/ 2D-FDTD simulations of Bragg grating design in slot WG

2D-FDTD methods are employed to investigate transmission properties of Bragg grating design on slot WG due to the fact that it is calculation efficient and it is easy to model the finite size of gratings.

The procedures to design gratings in slot WG are as follows :

— Tuning parameters such as filling factor of the PhC to obtain a large PBG size around wavelength of 1.55 μm and with feasible geometrical size for fabrications as well ;
— Creating PhC defects through investigations on cavity resonance wavelength, transmittance at the resonance peak and the ability of light confinement in LN ;
— Trade off between PhC size, transmittance and light confinement ability in LN ;

Maximizing PBG and tuning PBG at 1.55 μm

The structures considered in 2D-FDTD are schematically shown in Fig. 3.19 (a) and (b) which consist of slot WG top view surrounded by air. Slot WG parameters are fixed with LN slot W_s= 100 nm and silicon rail width of W_{si}= 200 nm. Simulations of maximizing the PBG are studied by fixing the number of air grooves N= 10, period (or pitch) of the grating a= 340 nm, while the width of air grooves W_{air} is varying. Incident signal and detector are put at the entrance and the output of the WG as shown in turquoise and green rectangle in Fig. 3.19 (a) and (b) respectively. In order to efficiently excite the WG mode, the incident signal is taken as a pulse wave with E-field amplitude profile as that of the WG mode profile in Fig. 3.19 (c). The propagating energy flux through the detector is calculated. The normalization of the transmission spectrum is performed by the corresponding energy flux of slot WG simulation as shown in Fig. 3.19 (b). Uniform meshing of the structure is applied with dx= dy= 10 nm. Normalized transmission of structure with parameters of a=340 nm, W_{air}=200 nm is shown in Fig. 3.19 (d). It yields a PBG size of about 250 nm with a gap centered around 1480 nm.

The simulation results of the PBG size by varying air groove width value as 70, 100, 140, 170, 200, 240, 270 nm are summarized in table 3.3. As we can see filling factor *f* (W_{air}/a) between 0.3 and 0.7 yields a PBG size larger than 200 nm which is large enough to host the resonance mode inside. In fact, a large PBG size can be beneficial for the experimental detection in case that it is degraded to a smaller size due to the fabrication defects. However, it is not

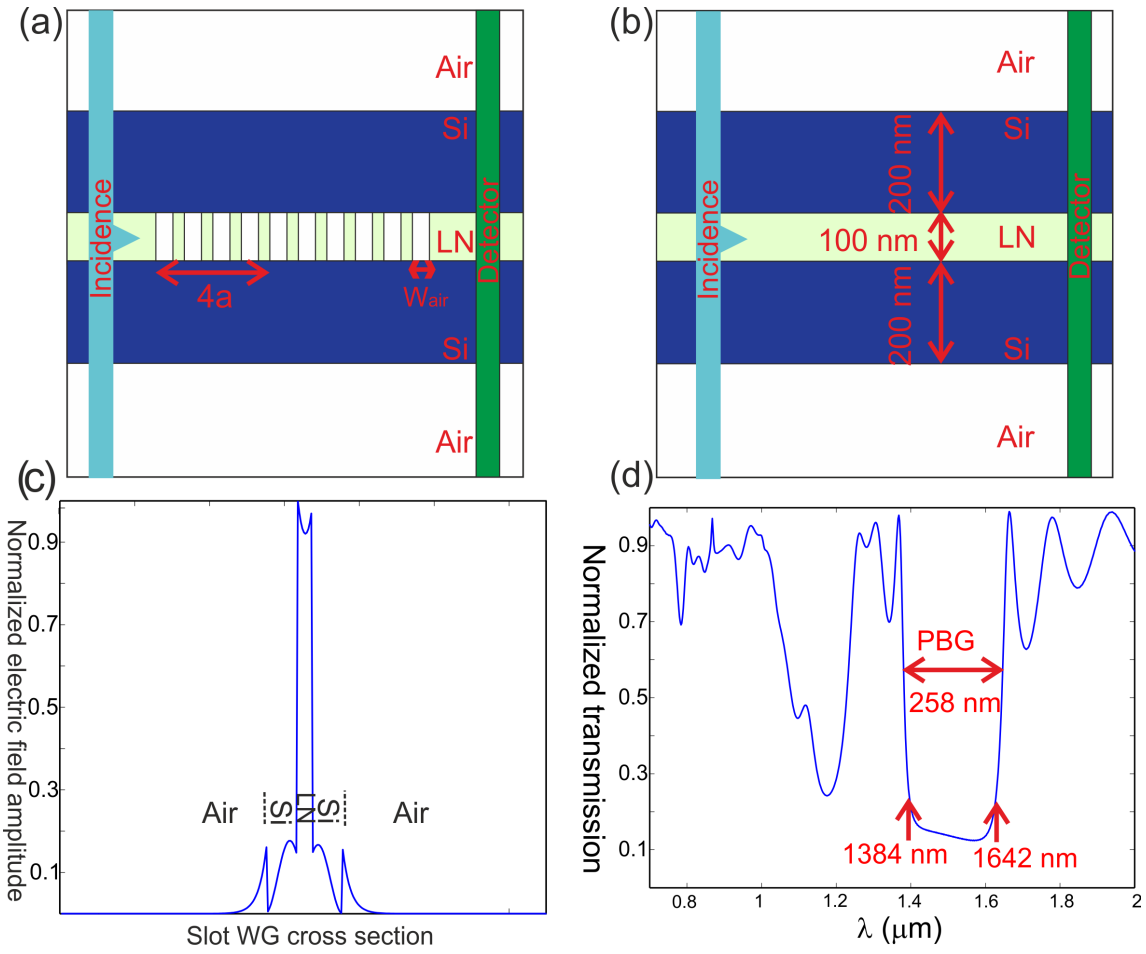

FIGURE 3.19 – (a) Sketch of 2D slot Bragg gating structure considered in the 2D-FDTD simulations. Period of grating a and width of air groove W_{air} is denoted in the figure. (b) Sketch of 2D slot WG considered in the 2D-FDTD simulations. (c) Incident electric field profile in the 2D-FDTD slot Bragg grating simulations. The LN slot, silicon rails and air ambient medium are denoted respectively in the figure. (d) Normalized transmission of 2D slot Bragg grating structure with parameters of a=340 nm, W_{air}=200 nm and number of air grooves N=10.

necessary to choose parameters that yield a maximized PBG size. Taking into account the easiness of fabrication, a larger air groove width is preferable. Henceforth, from the above simulations a filling factor is set to about 0.7.

Simulations of tuning PBG center at wavelength of 1.55 μm are performed with different set of parameters with filling factor *f* fixed to around 0.7. The results are summarized in Table 3.4. As shown in bold , parameters of a= 370 nm and W_{air}=260 nm yield a PBG size of 274 nm centered around 1550 nm. Therefore, parameters of the grating pitch and filling factor *f* had been determined to these va-

TABLE 3.3 – PBG size of 10 air grooves, a= 340 nm and varying W_{air}

W_{air} (nm)	W_{air}/a	PBG size (nm)	PBG center (nm)
70	0.209	154	1639
100	0.294	222	1613
140	0.411	250	1573
170	0.5	232	1542
200	0.588	258	1477
240	0.705	232	1472
270	0.794	190	1441

lues.

TABLE 3.4 – Tuning PBG center by varying a and W_{air}, keeping W_{air}/a around 0.7

a and W_{air} (nm)	W_{air}/a	PBG size (nm)	PBG center (nm)
a=350, W_{air}=240	0.6857	252	1508
a=370, W_{air}=260	**0.7027**	**274**	**1555**
a=390, W_{air}=270	0.69	296	1612
a=400, W_{air}=280	0.7	304	1634
a=440, W_{air}=310	0.7	342	1732

Cavity mode at 1.55 μm

By applying the above determined Bragg grating design as PhC mirror, a F-P cavity consisting of symmetry mirror with different defect size W_d is investigated and the structure is schematically shown in Fig. 3.20 (a). Since we investigate the effects of different W_d, the number of air grooves on each side of the cavity are set to 5 in order to get better light coupling efficiency to the defect mode.

The defect size W_d is varied as the values tabulated in Table 3.5. The normalized transmission curve is shown in Fig. 3.20 (b) corresponding to a 290 nm defect size structure. The resonance cavity with peak wavelength at 1556 nm and a normalized transmittance of about 0.96 is highlighted in red rectangle in Fig. 3.20 (b). The electric field distributions of this resonance at different wavelengths are obtained from CW simulations and they are shown in Fig. 3.21. In Fig. 3.21 (a) which corresponds to CW simulation at resonance peak wavelength of 1556 nm, light is coupled and confined in the cavity region. On the contrary, in Fig. 3.21 (b) corresponding to CW

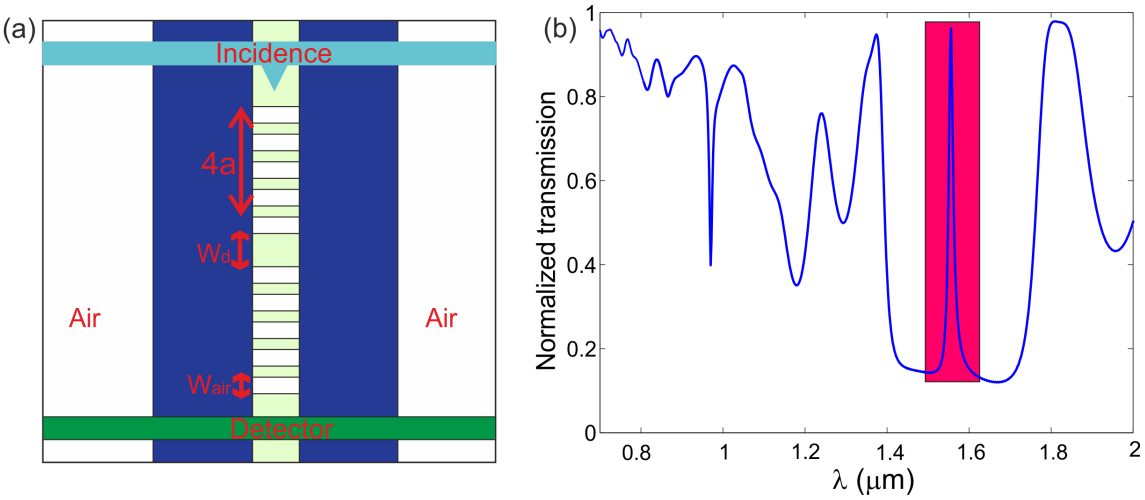

FIGURE 3.20 – (a) Sketch of 2D slot Bragg gating structure with defect size of W_d in the 2D-FDTD simulations. Period of grating a and width of air groove W_{air} is denoted in the figure. (b) Normalized transmission of 2D slot Bragg grating structure symmetry F-P cavity with parameters of a=370 nm, W_{air}=260 nm, W_d=290 nm and number of air grooves on each side of defect N=5.

simulation at resonance valley wavelength of 1650 nm, light is reflected by the PhC mirror. Though most of the light is reflected back at the off resonance wavelength excitation, there is still little portion of light propagates through the PhC region due to the limited reflection coefficient of the PhC mirror. It might also due to this limited reflection coefficient that the transmission (Fig. 3.20(b)) does not go down to zero inside the PBG.

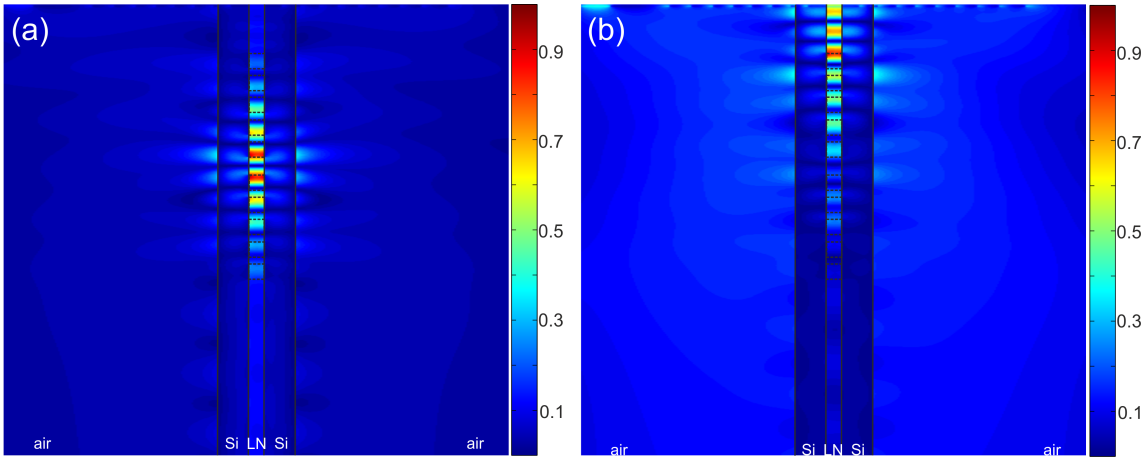

FIGURE 3.21 – Electric field amplitude distribution of Ex component along the Bragg grating structures (the black lines show the contour of the structures) with the same parameters as in Fig. 3.20(b). These results are obtained from CW simulations with excitation wavelength at (a) resonance peak wavelength 1556 nm, (b) off resonance wavelength of 1650 nm.

The criteria of choosing defect size not only depend on the properties of the cavity modes such as the transmittance and resonance wavelength around 1.55 μm, but also requires that the cavity mode have strong light confinement ability.

In previous works [6, 62, 63, 220, 221] by our team, an optical field factor $\overline{f_{opt}}$ estimated as a mean value of the light confinement ability is employed for this light confinement quantification. It is estimated as the ratio of electric field amplitude integration over all the LN region of PhC structure to the same quantity but integration on bulk LN as follows :

$$\overline{f_{opt}} = \frac{\iint_{PhC} |E(x,y)|\, dx\, dy}{\iint_{bulk} |E(x,y)|\, dx\, dy} \tag{3.4}$$

In order to calculate $\overline{f_{opt}}$, two continuous wave calculations with the same illumination conditions, one with PhC structure, and the other with non-patterned LN should be conducted. For the two simulations, the wavelength value is set to the resonance wavelength. $\overline{f_{opt}}$ is then obtained by the ratio of electric field amplitude integration in both calculations. Here, we investigate how the light confinement varies with different defect sizes, henceforth, the integration region is taken only over the defect region with length of W_d shown in Fig. 3.20 (a).

The way resonance properties vary with different defect sizes are summarized in Table 3.5. As shown in bold, Bragg grating with a defect size W_d of 290 nm yields a cavity mode at 1556 nm, 96% of transmittance and a $\overline{f_{opt}}$ of 4.03. A rather high transmittance ($\geq 95\%$) is obtained for all the defect size simulations conducted with parameters listed in the table. This is due to the fact that only 5 air grooves are chosen to form the PhC mirrors, thus yielding a high coupling efficiency of the resonance mode. The defect sizes affect largely the resonance wavelength. A smaller defect size produces a resonance at smaller wavelength values while it shifts to larger values with a larger defect size.

Optical field factor $\overline{f_{opt}}$ reaches maximum value with the configuration of W_d= 290 nm, meaning that a high light confinement can be obtained. Henceforth, the defect size is determined as W_d= 290 nm for next step further optimization.

TABLE 3.5 – Resonance properties versus different defect size

Defect size W_d (nm)	λ_{peak}	transmittance at peak wavelength	$\overline{f_{opt}}$
210	1474	0.955	3.27
260	1524	0.954	3.98
290	**1556**	**0.962**	**4.03**
310	1578	0.961	3.87
360	1630	0.975	3.24
410	1674	0.978	2.53

Trade off between PhC size, transmittance and local field factor $\overline{f_{opt}}$

Different number of air grooves with symmetric gratings configurations are investigated in order to see how they affect the resonance properties. Table 3.6 summarizes the results of these studies. As shown in bold, a structure with 6 air grooves yields the highest $\overline{f_{opt}}$ of 6.31. It resonates at 1554 nm with a transmittance of 91%. We can see that the number of the air grooves does not affect the resonance wavelength position while the transmittance drops dramatically with the increasing of the air grooves number due to the poorer coupling efficiency to the cavity mode and the increasing lateral losses.

TABLE 3.6 – Resonance properties versus different air grooves numbers

Number of air grooves	λ_{peak}	transmittance at peak wavelength	$\overline{f_{opt}}$
4	1556	0.949	2.45
5	1556	0.962	4.03
6	**1554**	**0.913**	**6.31**
7	1554	0.668	5.08
8	1554	0.378	5.74

3.2.1.2/ 3D-FDTD SIMULATIONS OF BRAGG GRATING DESIGN IN SLOT WG

The 2D-FDTD simulation results provide a general rule on how each parameter affects the grating performance. This 2D simulations help to narrow down the structural parameters for 3D-FDTD optimization. For example, 2D-FDTD simulations results imply that varying the defect size of the F-P cavity can largely tune the operation wavelength. The transmittance generally decreases with the increasing

of air grooves number. Henceforth, 3D-FDTD simulations will first start with the optimized parameters determined from 2D modeling. If the resonance phenomenon still exist in the real 3D structure, then the optimization will be performed by following the rules that are concluded from 2D modeling. It will require trial and error simulations in order to find the appropriate set of parameters for the real 3D structure since the parameters employing are determined from 2D approximated structures. Concerning the uncertainty of the etching depth in the TFLN, 3D simulations are performed with different etching depths.

Light couplings and detection are in the form of planes which are put at the entrance and the output of the WG. In order to efficiently excite the WG mode, the incident signal is taken as a pulse wave with E-field amplitude profile of the slot WG mode profile obtained from the mode calculations. Without specifically stated, the specular transmission (also referred to as the zero order transmission) through the detector plane is calculated via Fourier transforming of the time varying EM field signals. The normalization of the transmission spectrum is performed by the corresponding transmission through the 3D slot WG. In order to decrease the calculation burden and also to properly define the fine details of the structure, the meshing is set to be 10 nm in the slot WG cross section while it is set to be 20 nm in the WG propagation direction.

Tuning the number of air grooves

As schematically shown in Fig. 3.22 (a), the 3D real structure is modeled in 3D-FDTD simulations. In 3D simulations, meshing of the structure cannot be as fine as that in 2D case. Henceforth, parameters optimized from 2D simulations are rounded in adaptation to match a coarser meshing in 3D modeling. The zero order transmission results are shown in Fig. 3.22 (b) which are obtained with structure parameters as follows : a= 380 nm, W_{air}=260 nm, W_d=260 nm, H= 500 nm, W_{si}=200 nm, W_s=100 nm and varying number of air grooves on each side of defect N= 6, 7, 8, 9. As the air grooves number is larger than 7, the transmittance decreases dramatically while

the resonance gets slightly narrower. In the red curve case, corresponding to 7 air grooves, a high transmittance of 0.59 at 1489 nm is obtained. Therefore the following further tuning the parameters will start with 7 air grooves.

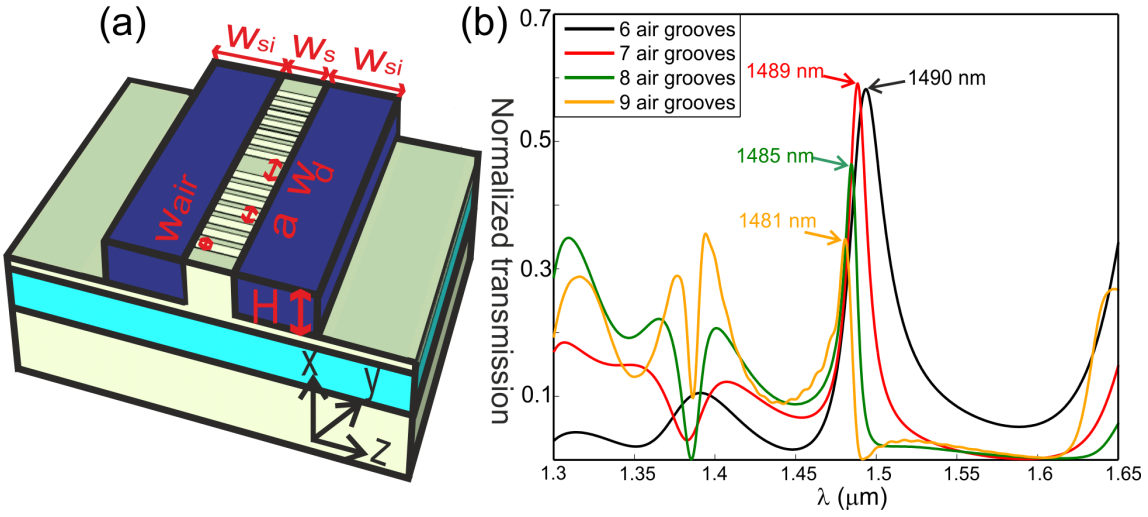

FIGURE 3.22 – (a) Sketch of 3D simulated structure. (b) Zero order normalized transmission of 3D slot Bragg grating structure with different number of air grooves on each side of F-P cavity.

Tuning the defect size

As indicated from 2D simulations, varying the defect size W_d can effectively tune the resonance wavelength. Henceforth in order to tune the operation wavelength at 1.55 μm, simulations with different defect size are carried out and results are shown in Fig. 3.23. Notice that, the defect size not only affects the resonance wavelength, it also plays a role in the transmittance. A high transmittance is obtained with the defect size at the vicinity of 340 nm, while it decreases as the defect sizes depart from this value. Nevertheless, a transmittance higher than 0.9 can yield a good coupling efficiency of the resonance. As shown in the grey curve in Fig. 3.23, defect size of W_d=380 nm yields a resonance at 1554 nm with 0.94 transmittance which is a good candidate for further optimization.

Bragg grating with upper silicon cover

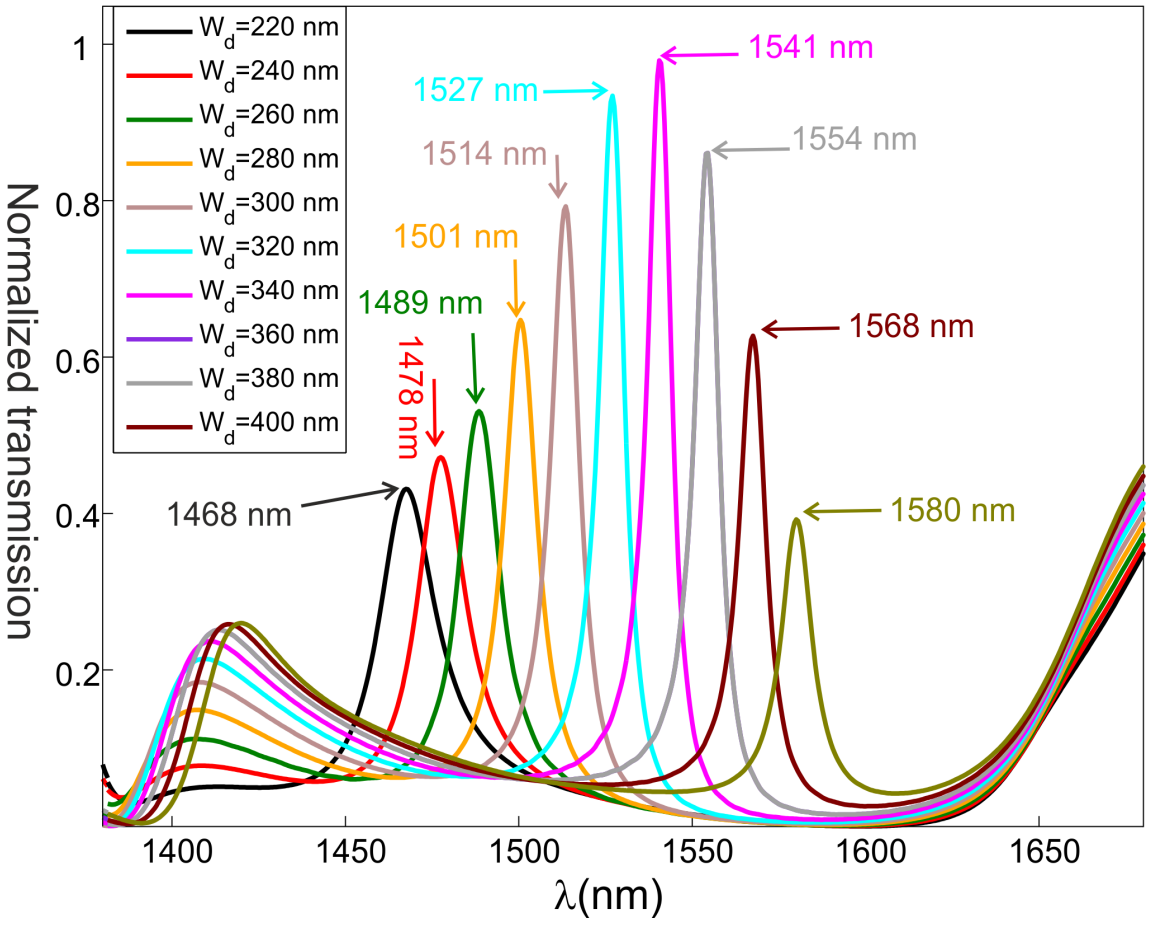

FIGURE 3.23 – 3D-FDTD simulated zero order normalized transmission with structure parameters as : a= 380 nm, W_{air}=260 nm, H= 500 nm, W_{si}=200 nm, W_s=100 nm number of air grooves on each side of defect N= 7 and varying defect size W_d.

A possible fabrication defect on the silicon height (being higher than that of LN etching depth) will degrade the light confinement ability of the structure. Here, grating design on structure with the presence of a thin layer of upper silicon as shown in Fig. 3.24 (a) has been investigated. The air grooves are etched untill the depth of H_{si}. The grating parameters are set as the parameters determined from the above simulations. The upper thin silicon cover thickness is studied by varying it as 40, 60, 80, 100 nm. The results are shown in Fig. 3.24 (b). With the presence of the upper silicon layer, resonance wavelength shifts to larger values along with the decreasing of the transmittance. Nevertheless, this upper silicon layer does not degrade a lot the grating properties if the thickness is less than about 50 nm.

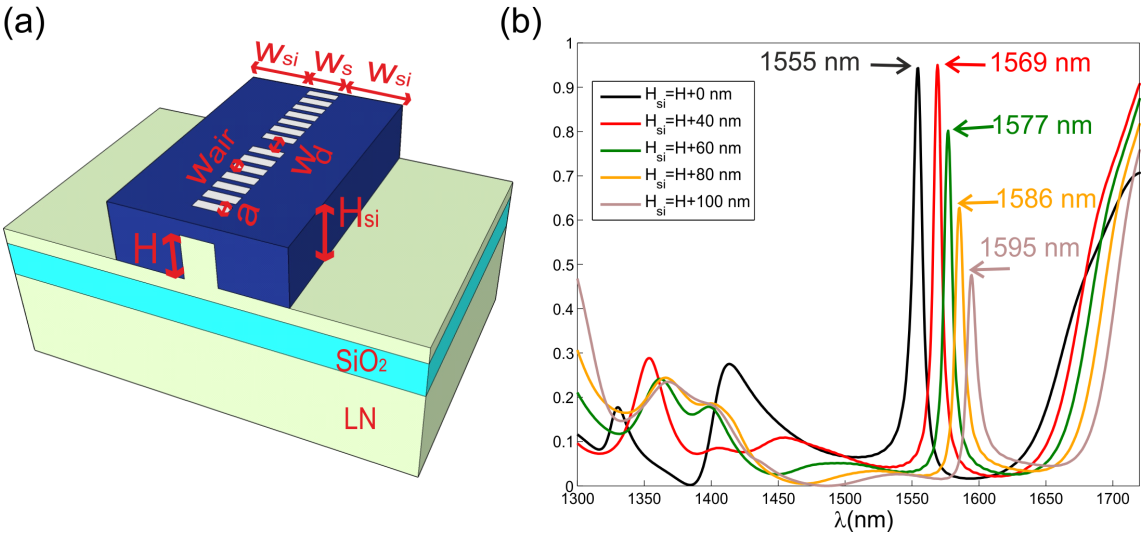

FIGURE 3.24 – (a) Sketch of Bragg grating with silicon height larger than LN slot height. The air grooves etching depth equal to H_{si}. (b) 3D-FDTD simulated zero order normalized transmission with structure parameters as : a= 380 nm, W_{air}=260 nm, H= 500 nm, W_{si}=200 nm, W_s=100 nm, number of air grooves on each side of defect N= 7, W_d=380 nm and varying the silicon height H_{si}.

Tuning the etching depth

The above 3D simulations are all performed with the etching depth of 500 nm. Now we will investigate different LN etching depths in order to see its structural tolerance of the above shown resonance effect on slot Bragg gratings. Etching depth of the slot WG with H= 400 and 700 nm is considered in the simulations. The results are shown in Fig. 3.25 (a) and (b) respectively. The grating parameters employed for these simulations are the same as the above optimized one for slot WG with H= 500 nm while the defect size is varied in order to investigate its effects on the resonance properties. These results show that different defect size can not only shift the resonance wavelength, but also change the transmittance level. A larger defect size yields a higher transmittance. Notice that the defect size has little effects on the size and shape of the PBG. Slot WG with higher etching depth opens up a larger PBG with almost zero transmittance inside the gap zone. However, due to the fact that part of the WG mode lies in the unetched TFLN leading to the poor interaction between WG mode and the grating structure in smaller etching

depth of the WG, only a narrow PBG can be found in this structure as shown in Fig. 3.25 (a). The narrow PBG together with not decreasing down to zero transmittance inside the gap makes the resonance mode difficult to be recognized. Therefore, we can conclude that the etching depth should be at least larger than 500 nm in order to yield a large PBG with an almost zero transmittance inside the gap zone.

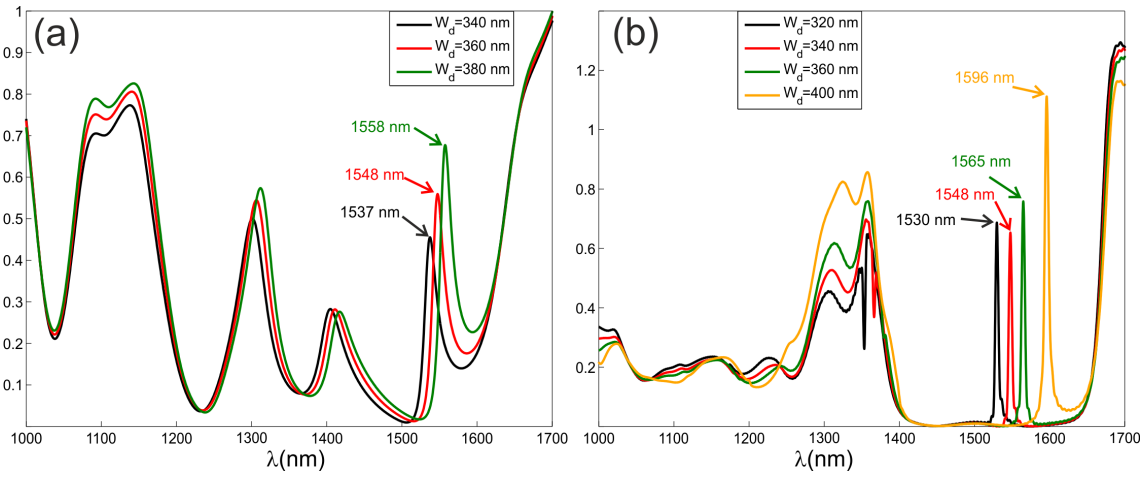

FIGURE 3.25 – 3D-FDTD zero order normalized transmission of slot Bragg grating structure with parameters of a=380 nm, W_{air}=260 nm, W_{si}=200 nm, W_s=100 nm and number of air grooves on each side of defect N=7 (a) Slot etching depth H= 400 nm, varying W_d= 340, 360 and 380 nm. (b) Slot etching depth H= 700 nm, varying W_d= 320, 340, 360, 400 nm.

Transmission calculated with Poynting energy flux

The above presented 3D slot WG Bragg grating design is investigated through zero order (or specular) transmission calculations. These calculations are realized by only recording the mean value of the time varying electromagnetic fields at the output of the structure, thus avoiding the direct Fourier transformation inside the FDTD codes therefore improving the computational efficiency. In the real measurements, the Poynting energy flux through the output facet is oftentimes measured. Henceforth, it is necessary to investigate the transmission property by calculating Poynting energy flux at the output facet of slot Bragg grating structures which is schematically shown in Fig. 3.26 (a). Two sets of parameters are studied ((a=380 nm, W_{air}=260 nm, W_d=360 nm, N= 7 and H= 500 nm) and (a=380

nm, W_{air}=260 nm, W_d=340 nm, N= 7 and H= 700 nm)). The results are shown in Fig. 3.26 (b) and (c) respectively.

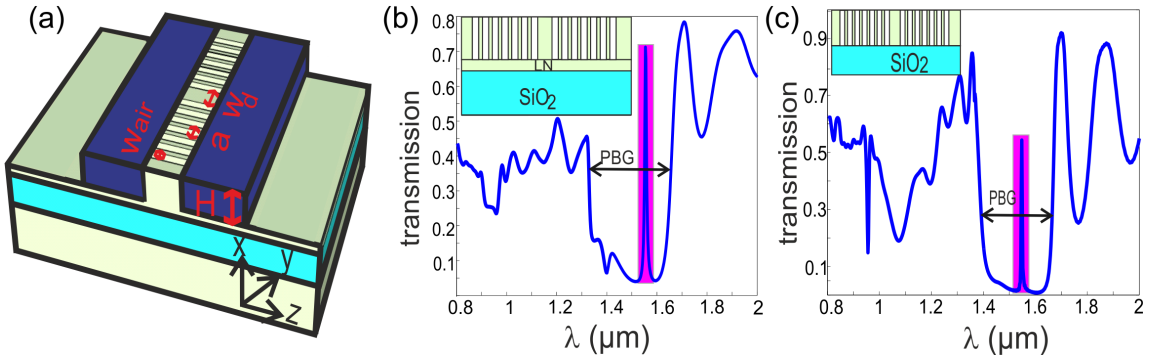

FIGURE 3.26 – (a) A schematic of slot WG with Bragg grating on TFLN with slot height H, Bragg grating pitch a, air groove width W_{air} and defect width W_d denoted in the figure. (b) 3D FDTD normalized transmission calculated by Poynting energy flux at the output of the WG with slot WG height $H = 500$ nm, $a = 380$ nm, $W_{air} = 260$ nm, $W_d = 360$ nm and number of air grooves N=7. The PBG is outlined in the transmission curve, a F-P peak is highlighted out with magenta rectangle. The inset shows the xy cross section in the middle of the slot Bragg grating structure along the propagation direction. (c) 3D FDTD normalized transmission calculated by Poynting energy flux at the output of the WG with slot WG height $H = 700$ nm, $a = 380$ nm, $W_{air} = 260$ nm, $W_d = 340$ nm and number of air grooves N=7. The PBG is outlined in the transmission curve, a F-P peak is highlighted out with magenta rectangle. The inset shows the xy cross section in the middle of the slot Bragg grating structure along the propagation direction.

These transmission results are calculated by the Poynting energy flux ($\mathbf{P} = \mathbf{E} \times \mathbf{H}$) along the the output facet of the structure. The normalization is realized by the same quantity obtained for the WG structure without Bragg gratings. In Fig. 3.26 (b), a transmission peak with 71% normalized power at wavelength 1554 nm is observed. Quality factor of the peak, defined as $Q = \frac{\lambda_{peak}}{\delta\lambda}$, where $\delta\lambda$ is the FWHM (full width at half maximum) with respect to the peak transmission, is equal to 172 in this configuration. The cavity optical field factor $\overline{f_{opt}} = 3.67$. Slot WG with height $H = 700$ nm structure is also carried out with similar Bragg grating design and the results are shown Fig. 3.26 (c). A transmission peak of 54% normalized power at wavelength 1548 nm is observed. The resonance Q factor is 309, and the optical field factor $\overline{f_{opt}} = 6.01$. These simulations confirm the results obtained from zero order calculations though there are differences in the transmission levels due to the fact that all the propagating power is recorded. Notice that a moderate Q value and field factor $\overline{f_{opt}}$ are obtained in this compact slot Bragg grating structure

with an active PhC length smaller than 6 μm. This light enhancement in micro-scale section will be promising for detecting physical variables such as the E-field or temperature through the EO effect of LN material.

3.2.1.3/ SENSITIVITY ANALYSIS OF BRAGG GRATING IN SLOT WG

In this section, sensitivity of the slot Bragg grating structure employing E-field sensors is analyzed. The transmission properties will change with the variation of the resonance mode effective index n_{eff} which is closely relative to the ambient material refractive index. In the presence of E-fields, the refractive index of the LN material will experience a variation Δn that is proportional to the square of optical electric field amplitude. The Δn of LN will then induce a variation in effective index of the resonance mode, thus leading to a shift of the resonance wavelength $\Delta\lambda_{res}$. Henceforth, through the investigation of $\Delta\lambda_{res}$ versus E-field mapping relationship, one can measure the corresponding E-field signal.

Unlike centrosymmetric crystals such as silicon for which linear EO effect is absent, LN belongs to the class of trigonal crystal symmetry and exhibits a large EO effect. Consequently, its optical index variation with respect to the external applied electric field $\vec{E}_{es} = (Ees_x, Ees_y, Ees_z)$ is linked to the EO tensor as following :

$$\begin{vmatrix} \Delta(1/n^2)_1 \\ \Delta(1/n^2)_2 \\ \Delta(1/n^2)_3 \\ \Delta(1/n^2)_4 \\ \Delta(1/n^2)_5 \\ \Delta(1/n^2)_6 \end{vmatrix} = \begin{vmatrix} 0 & -r_{22} & r_{13} \\ 0 & r_{22} & r_{13} \\ 0 & 0 & r_{33} \\ 0 & r_{51} & 0 \\ r_{51} & 0 & 0 \\ -r_{22} & 0 & 0 \end{vmatrix} \begin{vmatrix} Ees_x \\ Ees_y \\ Ees_z \end{vmatrix} \tag{3.5}$$

where r_{ij} are the elements of the EO tensor. For LN material, there are only four distinctive non zero elements and r_{33} ($r_{33} = 30.8$ pm/V at λ = 633 nm) is the largest element among them [64]. In Eq. 3.5 Ees_x, Ees_y, Ees_z are the electric field components to be measured and (x, y, z) is the coordinate system associated to the LN crystalline axis.

In order to exploit the largest EO effect, one must overlap the largest E-field component to be measured with r_{33} which is along the z crystalline direction. By neglecting other small EO element contributions and according to Pockels effect, the EO effect can be simplified as :

$$\Delta n = -\frac{1}{2} n_e^3 r_{33} E_{esz} \tag{3.6}$$

where n_e is the extraordinary refractive index of LN, which is 2.138 at the wavelength of 1550 nm and E_{esz} is the external electric field component along the z-direction.

In slot Bragg grating structure, E_z ((see the coordinate system associated in Fig. 3.26 (a)) is the major electric field, thus the z crystalline direction should be oriented along this direction in order to exploit the largest EO effect. Consequently, X or Y-cut wafers of LN can be considered for the experimental realization. When LN has been designed with high light confinement PhC nano patterned structure, the induced EO effect (and therefore the sensitivity) can be enhanced. Combined with the above introduced optical field factor $\overline{f_{opt}}$ and the proportionality of Δn with the square of optical electric field amplitude in the LN material, the corresponding induced refractive index variation in PhC structure can be quantified as follows :

$$\Delta n = -\frac{1}{2} n_e^3 r_{33} \overline{f_{opt}}^2 \overline{f_{el}} E_{esz} \tag{3.7}$$

Where $\overline{f_{el}}$ is the electro-static field confinement factor which has similar definition as $\overline{f_{opt}}$ and can be quantified as follows :

$$\overline{f_{el}} = \frac{\iiint_{PhcCavity} |E_{es}(i,j,k)| dxdydz}{\iiint_{bulk} |E_{es}(i,j,k)| dxdydz} \tag{3.8}$$

It quantifies the confinement ability of the E-field to be detected due to the nano pattern structure. Electric field distribution in RF domain is modeled by solving Poisson equation with FEM methods in COMSOL where the dielectric constant of silicon is 11.97, LN is 28.7 and SiO_2 is 3.9. Two simulations of electro-static field distribution with and without PhC structure are calculated. The $\overline{f_{el}}$ is then calculated by the ratio of the integration of $|E_{es}|$ in both calculations.

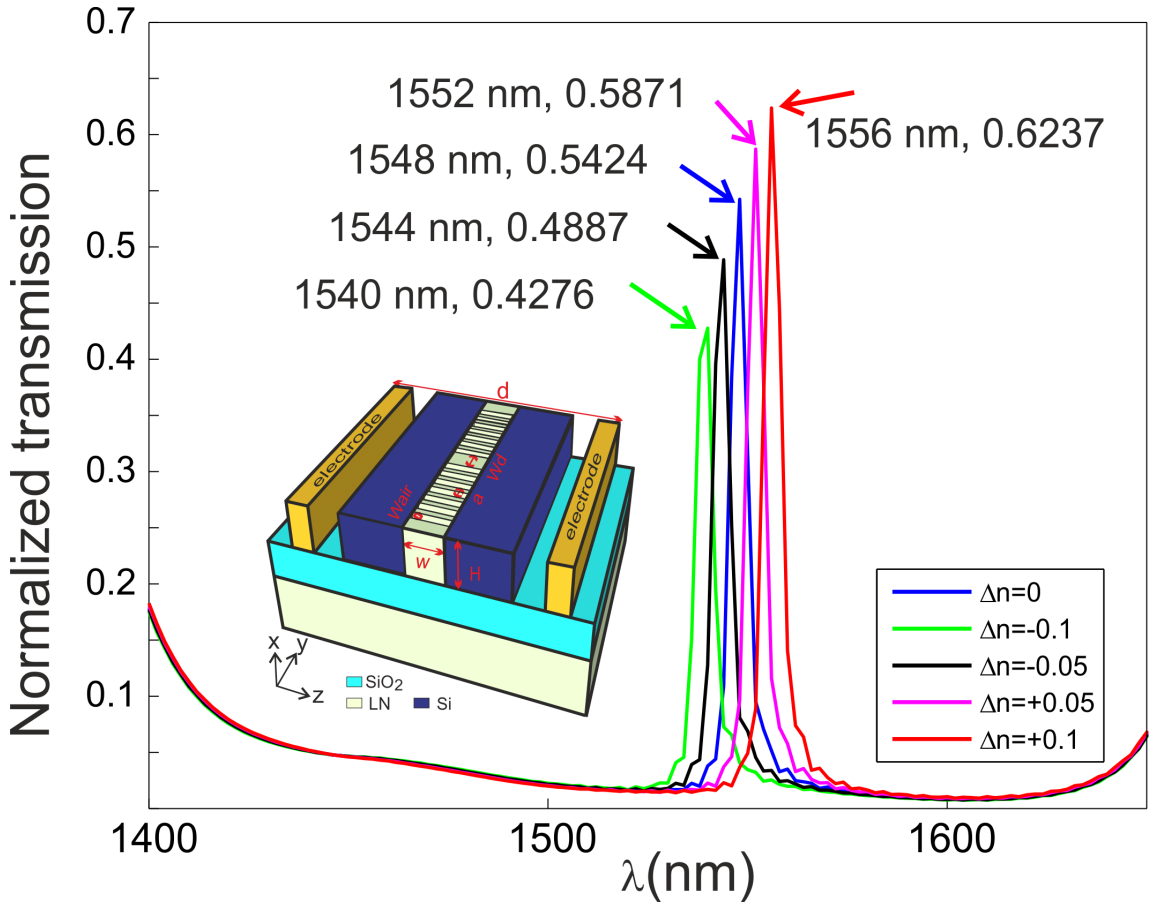

FIGURE 3.27 – 3D FDTD normalized transmission calculated by Poynting energy flux at the output of the WG with slot WG height $H = 700$ nm, $a = 380$ nm, $W_{air} = 260$ nm, $W_d = 340$ nm and number of air grooves N=7 with different Δn values of the LN.

This way of measuring the enhancement had already been experimentally verified by Huihui et al [63]. Electro static field distribution of slot WG Bragg gratings with etching depth of H= 500 and 700 nm are simulated with planar electrodes configuration with 1 μm of separations as schematically shown in the inset of Fig. 3.27 and the calculated $\overline{f_{el}}$ are similar for both two cases which is 1.3. Substituting the value of $\overline{f_{opt}}$ and $\overline{f_{el}}$ into Eq. 3.7, one can map the obtained Δn with different E-field E_{esz}. The mapping relationship of $\Delta\lambda_{res}$ versus E-field E_{esz} is then obtained through 3D-FDTD transmission investigations where the refractive index of LN is modified as the corresponding Δn.

3D-FDTD simulations with different Δn values of slot WG with different etching depths of 500 and 700 nm are performed. The plot of transmission curves shift of slot WG with etching depth H of 700 nm

are shown in Fig. 3.28 with the planar electrodes distance of 1 μm (inset in Fig. 3.27). The increase of refractive index will induce the resonance wavelength λ_{res} shift to a larger wavelength value and a higher transmission level in the resonance while it is the contrary in the case of decreasing the LN refractive index. This shows that the presence of the E-field does not only induce $\Delta\lambda_{res}$ but it also affects the transmission level which is mainly due to the variation of the reflection coefficient of the PhC mirrors and the variation in the lateral losses.

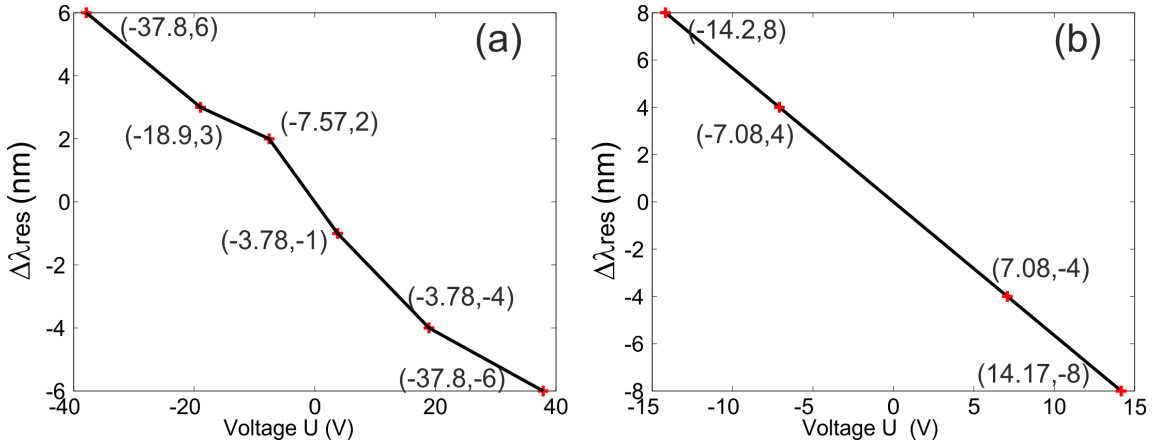

FIGURE 3.28 – $\Delta\lambda_{res}$ versus voltage applied on the 1 μm separation of planar electrodes on slot Bragg gratings with parameters of a = 380 nm, W_{air} =260 nm, W_{si} =200 nm, W_s =100 nm, number of air grooves on each side of defect N=7 (a) W_d= 360 and H=500 nm. (b) W_d= 340 nm and H=700 nm.

The $\Delta\lambda_{res}$ versus different applied voltages U(V) with etching depth H= 500 and 700 nm are shown in Fig. 3.28 respectively. The $\Delta\lambda_{res}$ versus U(V) then can be deduced from the $\Delta\lambda_{res}$ versus Δn mapping relationship (analysis from 3D-FDTD calculations) through Eq. 3.7. In slot grating etching depth H= 500 nm (Fig. 3.28 (a)), the $\Delta\lambda_{res}$ is quasi linearly changed with U while it linearly changes in the case of slot WG of 700 nm etching depth (Fig. 3.28 (b)). This might due to the smaller interaction of WG mode with PhC structure in the slot with etching depth of 500 nm since part of the light lies at the unetched part of TFLN. This difference in the interaction between WG mode and the PhC structure also leads to the sensitivity difference as it can be seen from the different slopes of curves in Fig. 3.28 which represents the sensitivity of $\Delta\lambda_{res}$ versus U(V). In slot Bragg grating structure with 500 nm etching depth, the sensitivity is taken

as the mean value of each piecewise linear slope which is 0.163 nm/V. In slot grating structure with 700 nm etching depth the sensitivity is 0.565 nm/V.

The minimum detectable E-field depends not only on the $\Delta\lambda_{res}$ sensitivity (how $\Delta\lambda_{res}$ changes vs U(V)), but also on the resolution of the detection devices such as the resolution of OSA (optical spectrum analyzer). Assuming a resolution of 0.1 pm OSA devices and unit proportionality of $\Delta\lambda_{res}$ sensitivity, an electric potential of about 600 μV in the slot grating structure with etching depth of 500 nm can shift 0.1 pm, while it is about 200 μV in the slot grating structure with etching depth of 700 nm. The distance of the two electrodes is 1 μm, therefore, the minimum detectable E-field is about 600 μV/m and 200 μV/m in the slot Bragg grating structure with etching depth of 500 nm and 700 nm respectively.

3.2.2/ 2D TRIANGULAR LATTICE PHOTONIC CRYSTALS DESIGN ON STRIP LOADED WG

From TE polarization strip loaded WG systematical study in Fig. 3.8, we can see that parameters combination of Si_3N_4 loaded width W = 2.8 μm, loaded height H= 240 nm is a configuration that yields high light confinement and compact WG size. It yields a WG mode effective index of 2.04. Simulations of PhC design are patterned on this Si_3N_4 loaded parameters combinations. TE polarization is chosen because it allows the overlap of the major electric field with the direction of largest EO coefficient r_{33} in order to exploit the most significant EO effect on x-cut TFLN sample. Strip loaded PhC modeling is guided by the same design rules that have been employed in slot Bragg grating design which is as follows :

— Study of filling factor of the PhC to maximize PBG size ;
— 2D-FDTD simulations to systematically study different PhC configuration and creating cavity modes ;
— 3D-FDTD simulations to fine tune the geometrical parameters that are determined from 2D modelings ;

3.2.2.1/ 2D-FDTD SIMULATIONS OF PHC IN STRIP LOADED WG

Choosing 2D approximated structure

Unlike the slot WG where the top view of the WG cross section can represent all the guiding features, the 2D approximated structure of the strip loaded is not that evident since it guides light in the planar TFLN layer while the WG path is defined by the loaded strip. Henceforth, the vertical geometrical arrangement of the WG is also an important feature for the strip loaded WG. Normally one would be employ the WG effective index to represent the WG core material, while the cladding would be air or the actual cladding material which is LN in the strip loaded WG. However, if the cladding material is chosen as air, then the WG feature is the same as that of ridge WG. Therefore, it is not a proper approximation for the 2D modeling. Since the effective index of the strip loaded WG is smaller than the refractive index of the LN material, the approximation with LN as the cladding cannot even guide light in the guiding core in this 2D approximated structure.

An appropriate idea of the 2D approximation can be inspired by the guiding principle of the strip loaded WG. Light is guided under the loaded strip since the WG effective index under the loaded strip is larger than the effective index of the planar TFLN WG alone. Thus the cladding refractive index is chosen as the effective index of TFLN planar WG which is 1.99. The WG core effective index, corresponding to a loaded width W = 2.8 μm, and a loaded height H= 240 nm, is 2.04.

2D PhC with strip loaded WG

Since the size of the strip loaded WG is large enough to host 2D PhC operating at 1.55 μm, 2D PhC will be chosen to design the PhC mirror and the cavity. In fact if 1D PhC Bragg grating is chosen on the strip loaded WG, it will require a very long Bragg grating as the scale of 100 pitches leading to several hundred micrometers in length in order to open up a large and high extinction ratio PBG. The

lengthy PhC requirement is due to the small refractive index contrast between the WG mode effective index and the effective index of TFLN planar WG which is the case in ref. [222] where the Bragg grating design on $BaTiO_3$ strip loaded WG is 250 μm long. If, on the contrary, a 2D PhC triangular lattice is chosen, a compact size of PhC can already yield a larger PBG.

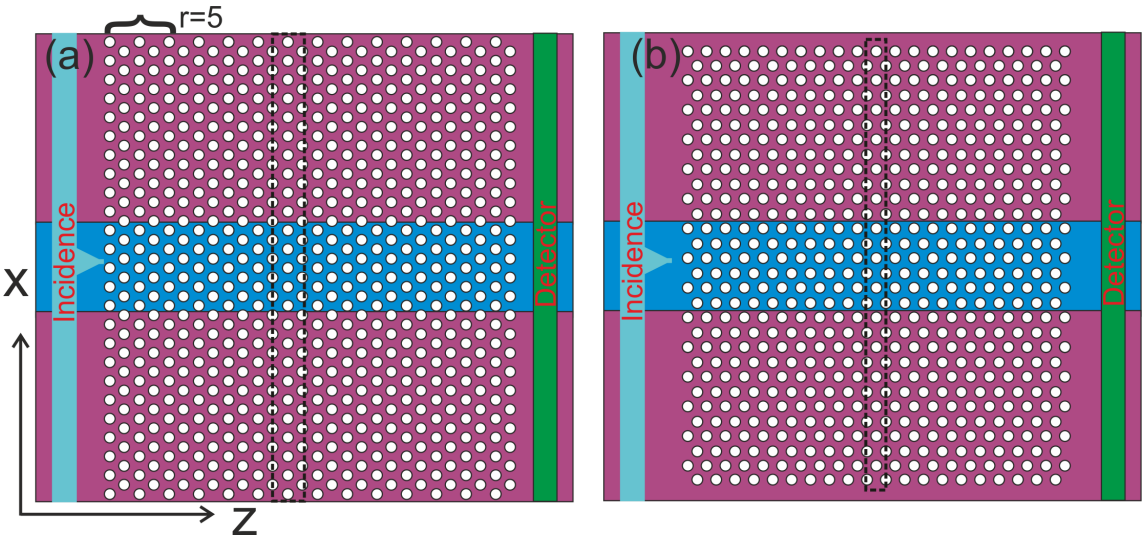

FIGURE 3.29 – Schematic of triangular lattice PhC on strip loaded WG, the dashed rectangle shows the supercell employed in PWE dispersion modeling. (a) The propagation direction is along ΓM direction. (b) The propagation direction is along ΓK direction.

Triangular PhC with propagation directions on both ΓM and ΓK are studied as schematically shown in Fig. 3.29. PWE with supercell technique is employed to model the dispersion relationship where a supercell consists of 25 air holes as shown in the dashed rectangles in Fig. 3.29 (a). The corresponding gap maps are shown in Fig. 3.30 where the largest gap appears for filling factors of around 0.4 for both propagation directions. The gap center for ΓM propagation direction lies at normalized frequency of 0.446, while for the ΓK propagation direction it lies at normalized frequency of 0.467. By centering the gap at 1.55 μm, we obtain the lattice constant for ΓM propagation direction structure which is 692 nm, while it is 725 nm for ΓK propagation direction structure.

2D-FDTD was employed to investigate the transmission properties of the triangular lattice PhC with the parameters determined from PWE calculation. As shown in Fig. 3.29 the incident field was launched at the entrance of the PhC section and a detector is placed at

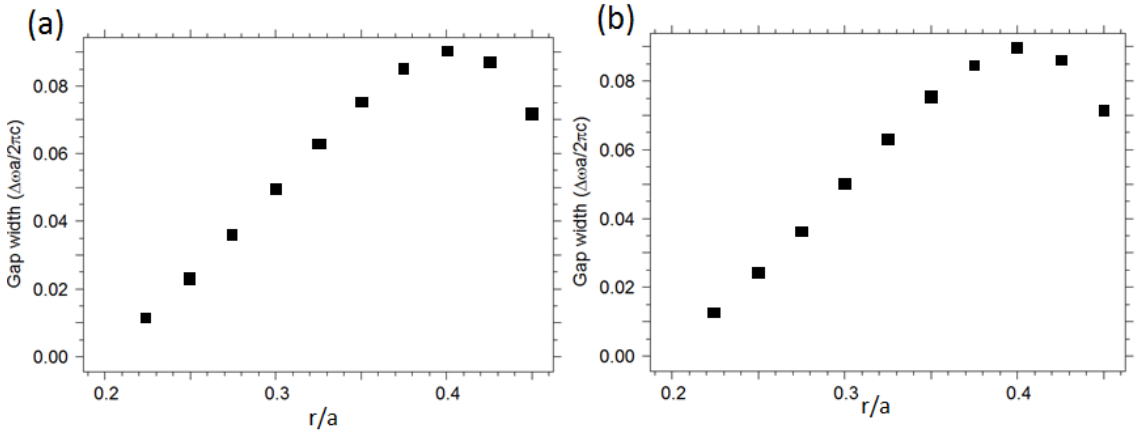

FIGURE 3.30 – Gap map of triangular lattice PhC on strip loaded calculated by PWE methods (a) where the propagation direction is along ΓM direction. (b) where the propagation direction is along ΓK direction.

the end of the PhC section to record the Poynting energy flux. The transmission is normalized by the same calculation condition but in a non-patterned WG structure. The incident field is a pulsed wave with the amplitude profile as that of strip loaded WG mode cross section as shown in Fig.3.31 (a). A uniform meshing of dx= dz= 20 nm is utilized. The rules for choosing the appropriate parameters are similar to that in the slot Bragg grating simulations which are as follows :

— Choosing a compact PhC size with cavity mode operating around 1550 nm ;
— Creating a cavity mode in which light can be easy to couple, large extinction ratio as well as high quality factor ;

2D PhC with ΓK propagation

Simulations are first carried out to investigate how the number of air holes rows *r* affect the PBG. Different values of *r* are varied as 11, 13 and 15 in the simulations and the normalized transmissions for triangular lattice in ΓK propagation are shown in Fig. 3.31. This study shows that the number of rows does not have significant effects on the PBG properties. Henceforth, simulations are performed on small number of rows (*r*=11) configurations which will facilitate the cavity mode excitation.

Different ways of creating defects modes (M1, M2, L1...) on trian-

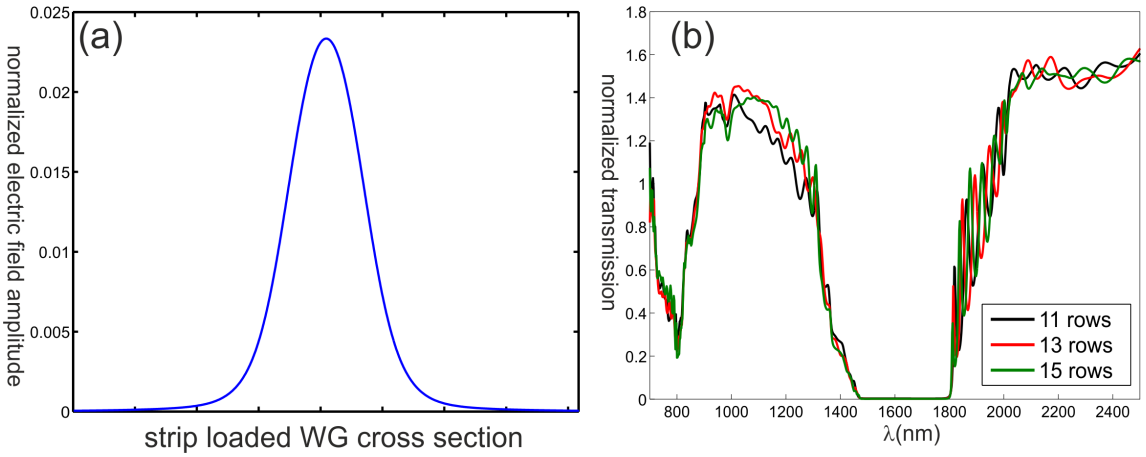

FIGURE 3.31 – (a) Incident field amplitude profile employed in the 2D-FDTD strip loaded PhC simulations. (b) Normalized transmission of triangular PhC propagating along ΓK direction with varying number of rows *r*.

gular PhC propagating along ΓK directions are simulated and the results are shown in Fig. 3.32 and Fig. 3.33 . Due to the large mismatch between the incident field and that of the cavity mode, the defect mode shows small transmittance inside the PBG. Some of the cavity modes are barely recognized. Simulations on the ΓK propagation direction triangular lattice PhC have not been continued due to the difficulty of coupling light to the defect modes.

2D PhC with ΓM propagation

Simulations of triangular lattice PhC propagating along ΓM direction are performed with different numbers of air hole rows and the results are shown in Fig. 3.34 (a). Similar to the ΓK propagation direction configurations, the number of air hole rows does not significantly affect the PBG properties. Cavity modes are created by removing one missing line of air holes (L1) and the simulation results on different number of air hole rows are shown in Fig. 3.34 (b). These results reveal that the smaller the number of air hole rows, the higher the transmittance of the cavity mode along with broader resonance line width. A L1 cavity with 4 rows of air holes PhC mirrors yields a cavity mode at 1586 nm with 91% transmittance. This L1 cavity is multimodal inside PBG since there are some other peaks inside the PBG with smaller transmittance. Without further optimization, this L1 cavity parameters will be chosen to proceed the 3D-FDTD simulations.

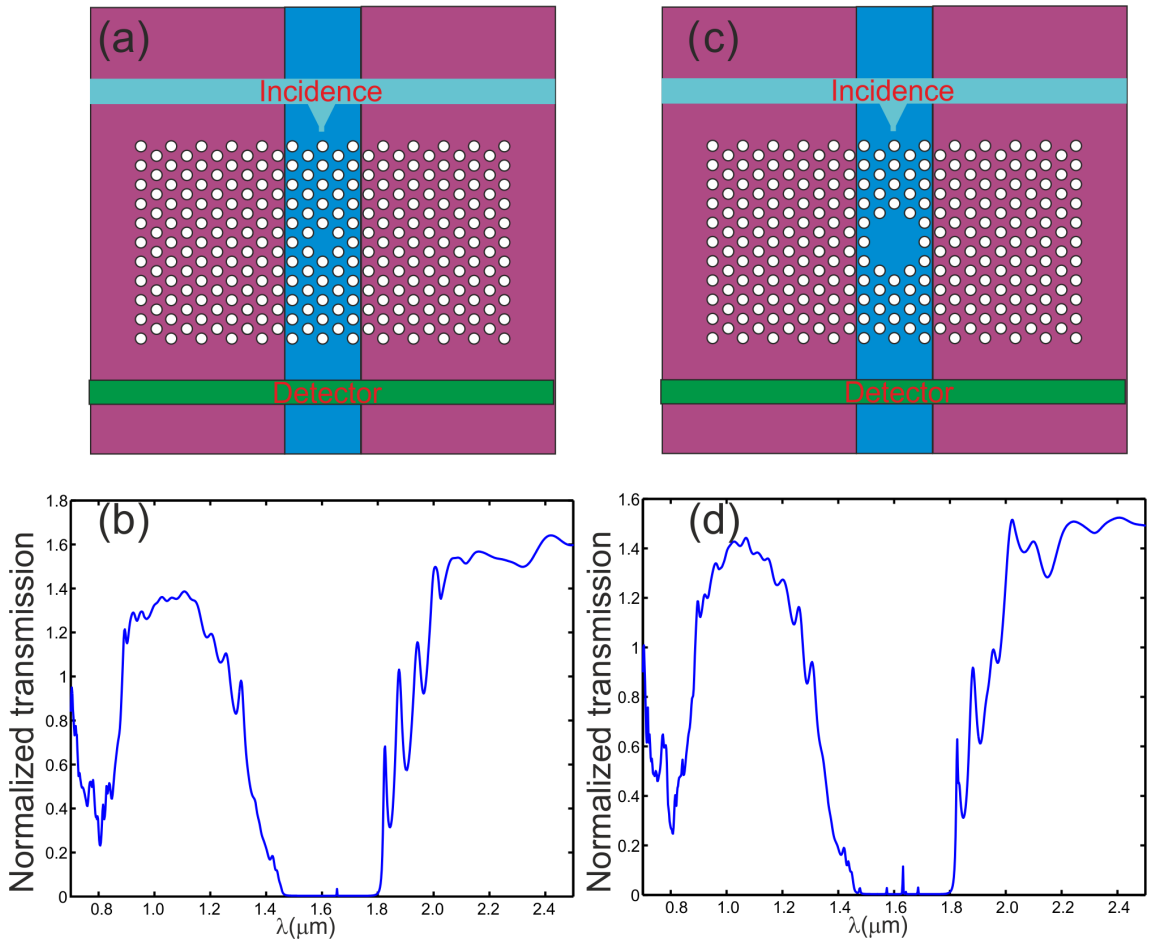

FIGURE 3.32 – (a) Sketch of triangular PhC with one missing hole (M1) cavity. (b) Normalized transmission M1 cavity. (c) Sketch of triangular PhC with two missing holes (M2) cavity. (d) Normalized transmission M2 cavity.

3.2.2.2/ 3D-FDTD SIMULATIONS OF PHC IN STRIP LOADED WG

The 3D structure considered in the simulations is shown in Fig. 3.35 (a) where the air holes penetrates the Si_3N_4 and the TFLN layer. The considered parameters of the structure are as follows : a= 692 nm, r/a= 0.4, 4 rows of air holes on each side of the L1 defect. The normalized transmission is shown in Fig.3.35 (b) where a cavity mode with a broad linewidth lies at 1600 nm with 10.3% of normalized transmission in a small extinction ratio PBG. Compared to 2D simulations, 3D calculations show degraded cavity mode with low transmittance and broad cavity linewidth. The PBG in 3D case has smaller extinction ratio (only about 8% of normalized transmittance) compared to that in 2D simulation. This is mainly due to the fact that there are some portion of light is leaking down to the substrate thus

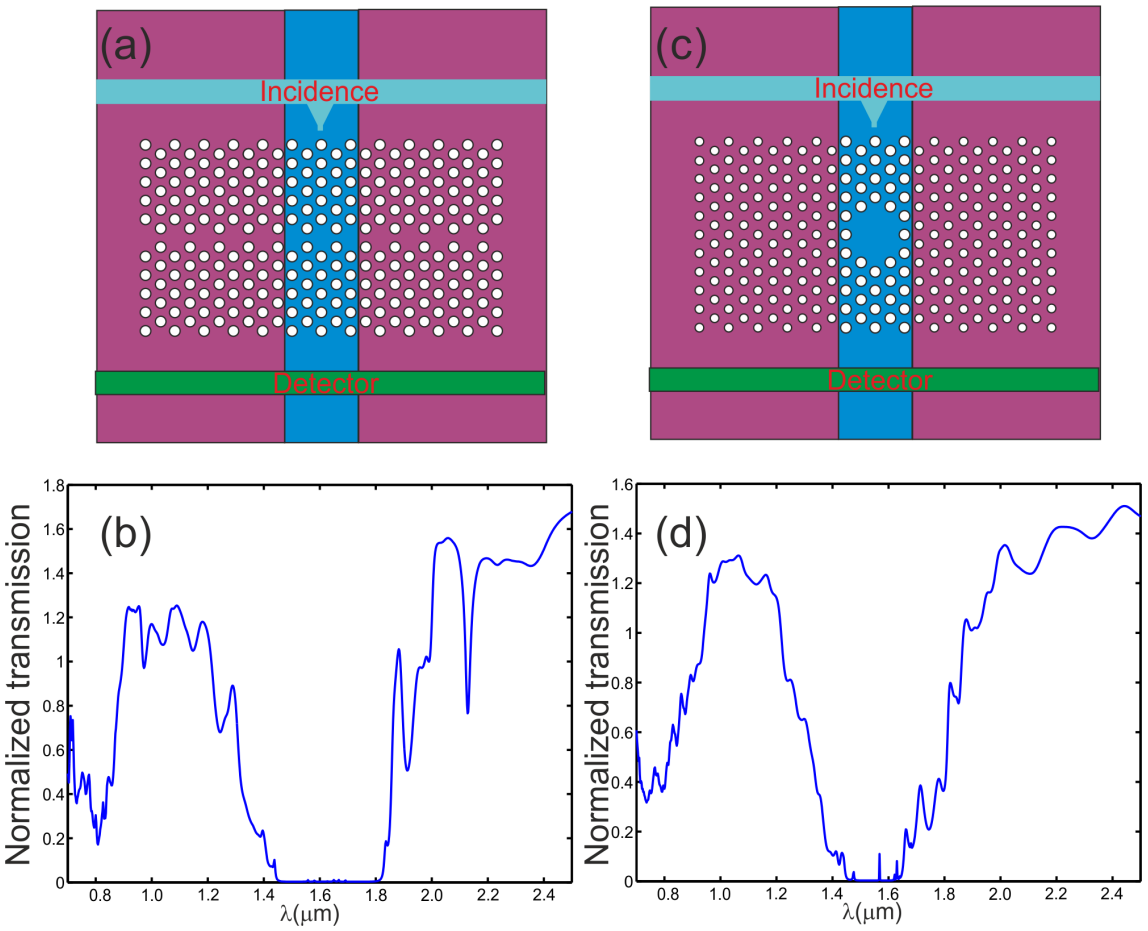

FIGURE 3.33 – (a) Sketch of triangular PhC with one line missing air holes (L1) cavity. (b) Normalized transmission L1 cavity. (c) Sketch of triangular PhC with M2 cavity surrounded by outer PhC barrier formed by smaller air hole radius. (d) Normalized transmission M2 cavity surrounded by PhC barrier.

degrading the performance.

Air membrane structures where the SiO_2 buffer layer under the PhC section is removed away are also considered in 3D simulations as schematically shown in Fig. 3.36 (a). The PhC parameters (PhC lattice constant a, radius of air hole and numbers of the air holes) are the same as the above studied 3D structure. The normalized transmission is shown in Fig. 3.36 (b) where a cavity mode lies at 1572 nm with 22.7% of normalized transmission with a quality factor of 98. The properties of this cavity mode is much improved in terms of the extinction ratio of the PBG and the sharpness of the resonance linewidth thanks to the high index contrast in vertical direction of the WG .

The field distributions at the cavity are shown in Fig. 3.37 which are

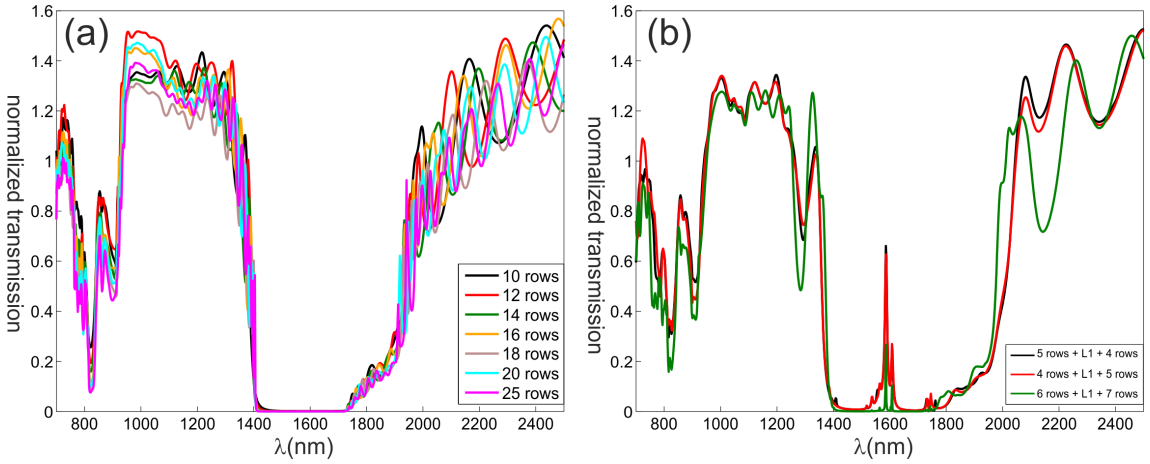

FIGURE 3.34 – Normalized transmission of triangular PhC propagating along ΓM direction (a) with varying number of rows *r*. (b) with L1 cavity modes and varying the number of air hole rows. These curves are configured with asymmetric PhC mirrors on each side of the L1 cavity. The black curve is with 5 rows of holes on the left plus the L1 cavity and 4 rows of holes on the right. The red curve is with 4 rows of holes on the left plus the L1 cavity and 5 rows of holes on the right. The green curve is with 6 rows of holes on the left plus the L1 cavity and 7 rows of holes on the right.

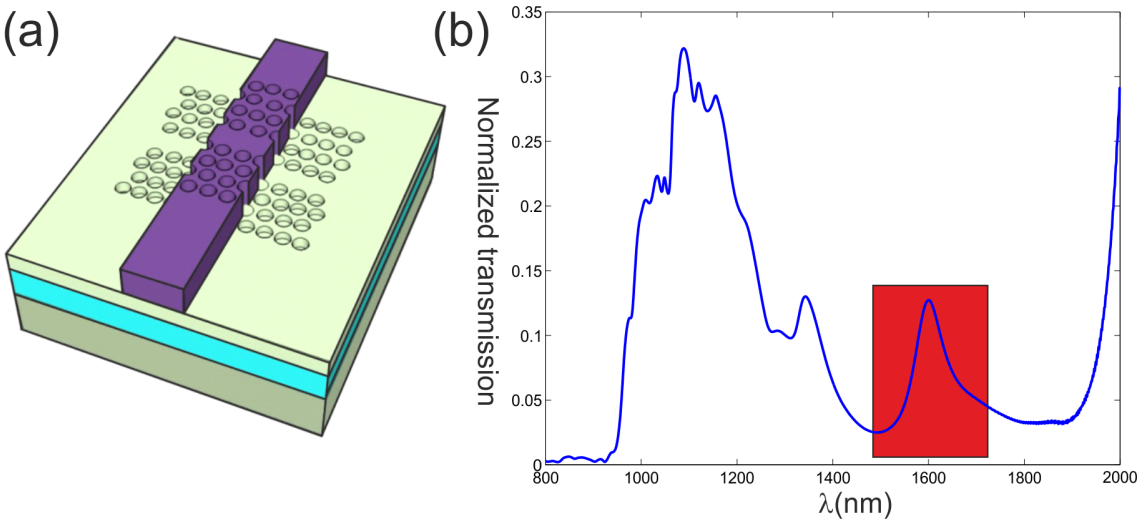

FIGURE 3.35 – (a) Schematic of 3D structure of strip loaded with PhC design. (b) Normalized transmission of triangular PhC propagating along ΓM direction with a resonance mode in the red highlighted rectangle.

obtained by CW calculations at the resonance peak wavelength of 1572 nm. Light is highly confined in the cavity region with an optical field factor $\overline{f_{opt}}$= 3.4.

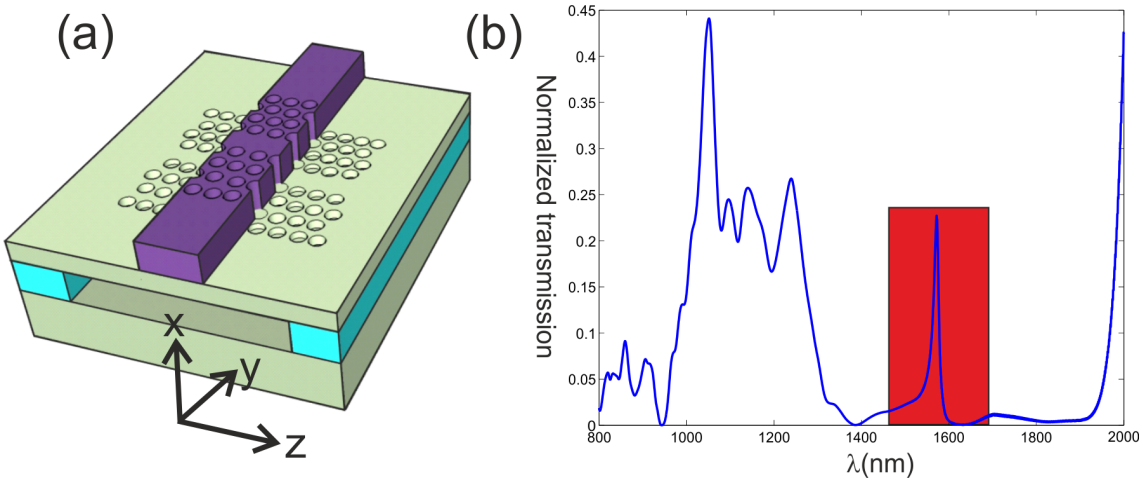

FIGURE 3.36 – (a) Schematic of 3D structure of strip loaded with PhC design on air membrane configurations. (b) Normalized transmission of triangular PhC propagating along ΓM direction on an air membrane configurations with a resonance mode in the red highlighted rectangle.

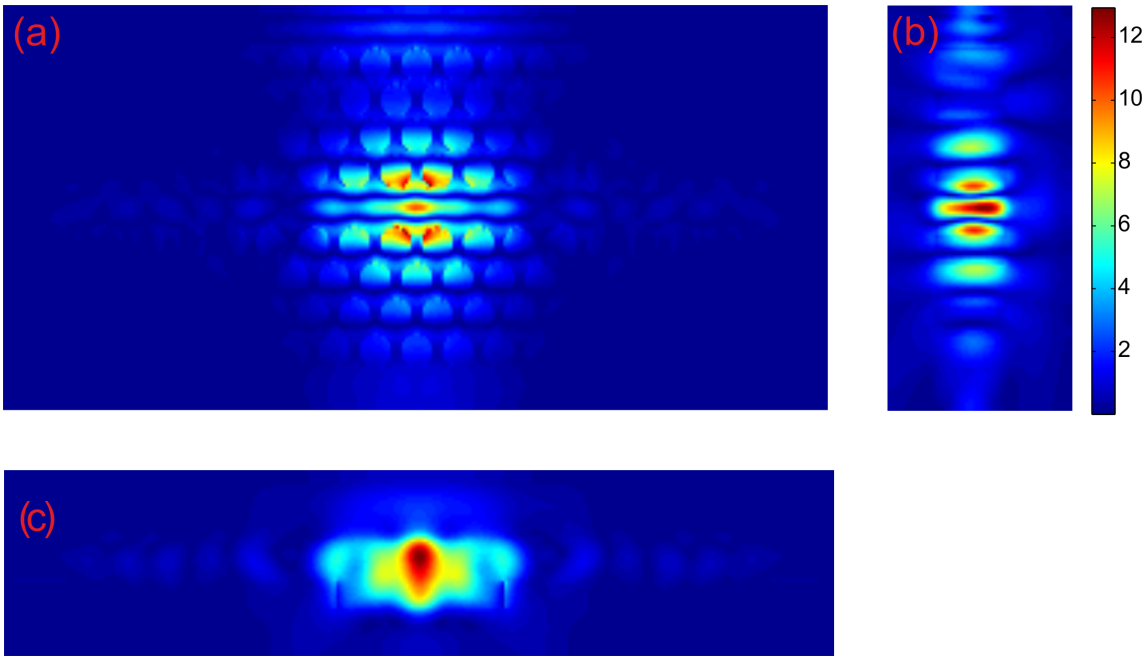

FIGURE 3.37 – (a) Ex amplitude distribution at TFLN middle plane of yz cross section. (b) Ex amplitude distribution of xy cross section at the middle of the strip loaded WG. (c) Ex amplitude distribution of xz cross section at the middle of the cavity.

3.3/ FABRICATION OF STRIP LOADED WG

Strip loaded WG configuration seems a feasible WG structure since it does not need LN etching among all the proposed WG configurations. Therefore, silicon nitride loaded WG fabrication is first tried

and the results are shown here. Figure 3.38 shows the fabrication flow chart. Silicon nitride loaded WG fabrication involves deposition of silicon nitride layer, lithographically defined the WG channel and etching of silicon nitride etc.

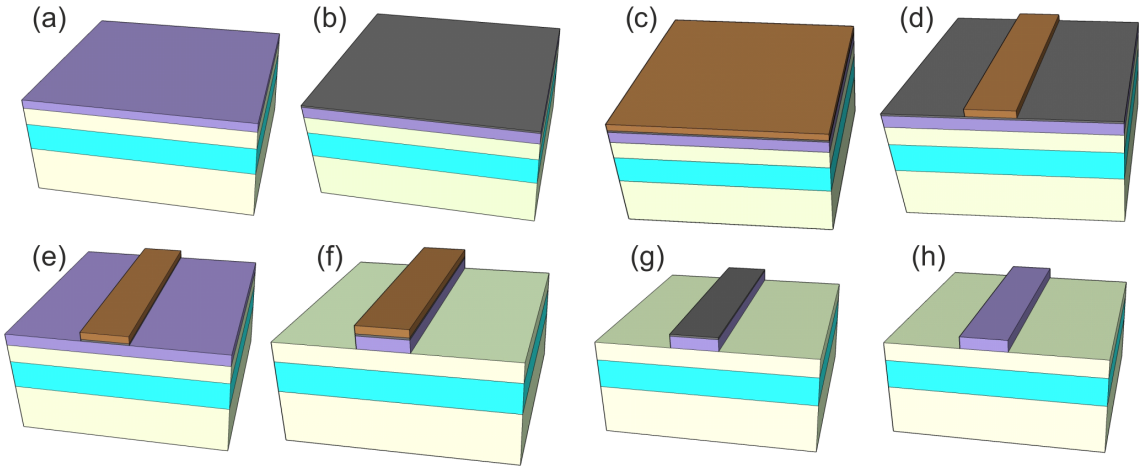

FIGURE 3.38 – (a) Low temperature Si_3N_4 PECVD. (b) Cr sputtering. (c) Spin coating E-beam resist ma-N 2403. (d) E-beam lithography to define WG path. (e) Cr wet etching. (f) Si_3N_4 dry etching with CHF_3 and C_2F_6 mixture. (g) Remove ma-N 2403 resist by O_2 plasma. (h) Cr wet etching and clean the sample.

First, a layer of Si_3N_4 with thickness of about 510 nm was deposited by PECVD (plasma-enhanced chemical vapor deposition) at low temperature of 300^{o}C on an X-cut TFLN sample as shown in Fig. 3.38 (a). This was performed with the clean room facility in LAAS, Toulouse. The following processes were realized with the clean room facility in MIMENTO Besancon. The TFLN sample with Si_3N_4 layer was then cleaned by remover 1165 and then went through a deposition of about 25 nm of Cr by sputtering with the Plassys MP500 (Fig. 3.38 (b)). Figure 3.38 (c) shows that the sample was then coated with E-beam resist of ma-N 2403 with thickness of about 460 nm. Then a hot baking of the resist is performed at 105^{o}C for 1 minute and 15 seconds. E-beam lithography (Raith e-line) was applied to define the WG (Fig. 3.38 (d)) and the parameters are shown in Table 3.7. An SEM image of the WG defined by resist is shown in Fig. 3.39 (a). The WG is well defined with negligible defects.

Before the dry etching of Si_3N_4, the Cr was wet etched away and then rinse it in DI (deionized) water (Fig. 3.38 (e)). Si_3N_4 was etched

TABLE 3.7 – E-beam lithography for Si_3N_4 WG definition

E-beam exposure parameters	development	hot baking of post-exposure
30 KV tension, 30 μm aperture, dosage 250 to 300 $\mu C/cm^2$	MF26A for 1′10, rinse in DI water	100^{o}C for 1′30

by RIE (reactive ion etching) with 10 sccm (standard cubic centimeters per minute) flow of CHF_3 and 5 sccm flow of C_2F_6 mixture at the pressure of 30 μbar and at the power of 120 W for 6 minutes. An SEM image of the loaded WG after 6′ dry etching is shown in Fig. 3.39 (b). The remained resist is about 200 nm and the Si_3N_4 was etched about 510 nm. The etching selectivity is about 1 :2 and the etching speed is about 80 nm/min. The remained ma-N 2403 resist on top of the Si_3N_4 rib was then removed by RIE with 20 sccm O_2 flow at 100 μbar and at a power of 100 W for 10 minutes (Fig. 3.38 (g)). The WG now is with Si_3N_4 and Cr loaded material on top as shown in the SEM image of Fig. 3.39 (c). The loaded WG was finally fabricated with the wet etching of Cr and follow by cleaning the sample (Fig. 3.38 (h)). One of the fabricated WG SEM image is shown in Fig. 3.39 (d) with a Si_3N_4 loaded width of about 2 μm. As we can see it has an almost perfect vertical sidewall with good fabrication quality.

Characterization of the Si_3N_4 loaded WG with a tapered lensed fiber for the injection at the WG entrance was performed. The WG output signal was then collected by a micro objective to a CCD camera. However, the poor quality of the input and output facet of the WG leads to the failure in the detection of the output WG mode. Trials of the optical polishing the facets were made. Probably due to the lattice constant mismatch and the thermal properties difference between different materials, the Si_3N_4 WG was stripped off from the sample during the polishing process.

3.4/ FABRICATION TRIALS OF NANO-METER SCALE WIDTH RIDGE WG

The fabrications of either ridge WG or slot WG require etching of LN material. Here results of fabrication trial on nano-meter scale WG

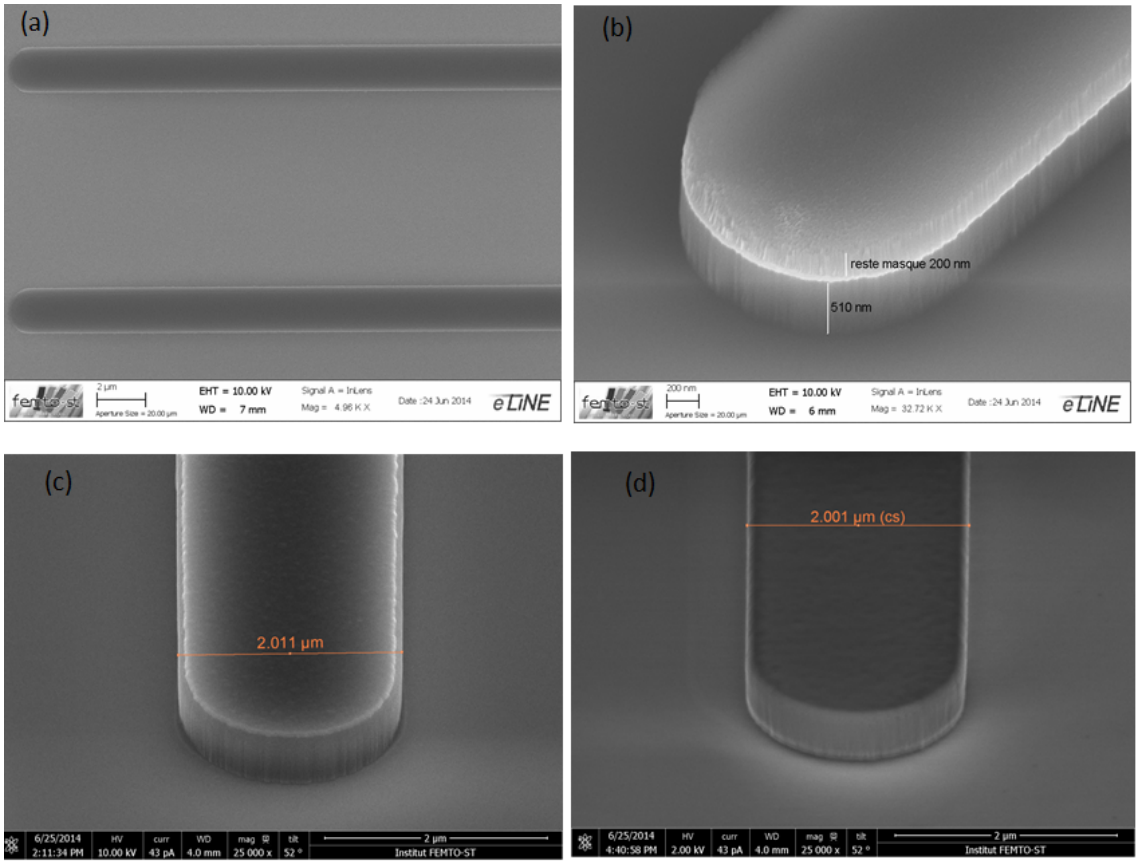

FIGURE 3.39 – (a) WG defined by resist ma-N 2403 after E-beam exposure. (b) Si_3N_4 loaded WG with 510 nm Si_3N_4 height during the dry etching process. (c) Si_3N_4 loaded WG with a top layer of Cr, and the WG width is about 2 μm. (d) Final Si_3N_4 loaded WG with width about 2 μm.

are presented. From these results, discussions about the feasibility of LN slot WG fabrication are made in terms of the current technological constraints.

The fabrication process involves E-beam lithography, deposition of Cr WG and LN ridge etching as shown in the fabrication process flow chart in Fig. 3.40. To begin with, the sample was prepared by O_2 plasma cleaning for surface activation. It was then spin coated with a layer of about 230 nm thick of PMMA resist (Fig. 3.40 (a)). Before the E-beam lithography, a thin layer of Al is deposited by sputtering in order to avoid charge effect during E-beam exposure. E-beam patterning of the WG was performed with parameters shown in Table 3.8. An SEM image of WG with W= 155 nm defined by PMMA is shown in Fig. 3.41 (a) where the WG side wall is rather smooth.

A 150 nm thick Cr layer was then deposited by evaporation (Fig.

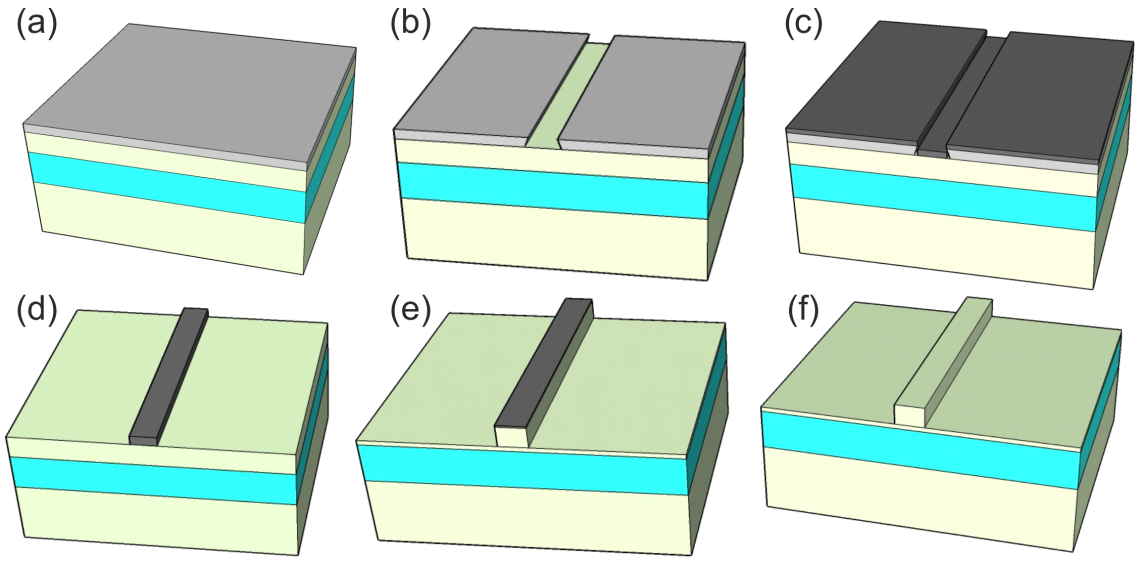

FIGURE 3.40 – (a) Spin coating of a layer about 240 nm thick PMMA E-beam positive resist on top of the TFLN sample. (b) E-beam lithography pattern the WG path. (c) Evaporation of chromium as the hard mask for WG etching. (d) Stripping off Cr and leaving the defined by Cr WG mask. (e) Dry etching of LN WG. (f) Cr wet etching and cleaning the sample.

TABLE 3.8 – E-beam lithography for LN ridge WG definition

E-beam exposure parameters	Development
15 KV tension, 10 μm aperture, dosage 100 to 300 $\mu C/cm^2$	MIBK :IPA with 1 :3 portion for 45″, and then 15″ IPA

3.40(c)) with a speed of 0.9 nm/s in order to form a hard mask for the LN etching. The Cr WG mask was formed by lifting off the resist and the Cr on top of it (Fig. 3.40(d)). This was realized by submerging the sample into Remover 1165 solution with a constant temperature of 60^{o}C. Figure 3.41 (b) shows the SEM image of Cr WG mask with W=150 nm where the Cr WG mask has poor sidewall quality. The Cr WG mask was then applied to a dry etching process to form the LN ridge WG (Fig. 3.40(e)). The recipe for the etching was a mixture of 5 sccm SF_6 and 5 sccm of Ar in 7 μ Torr pressure with coil power of 800 W and platen power of 90 W. The total etching time was 15 minutes and the etched LN depth was 480 nm. This yields an etching rate of 30 nm/min and 1 :3 etching selectivity. An SEM image of the etched LN ridge is shown in Fig. 3.41 (c). Due to the redeposition of LiF, the LN ridge had a really rough sidewalls. This roughness is a detrimental factor for the light confinement in

the nanometer width WG.

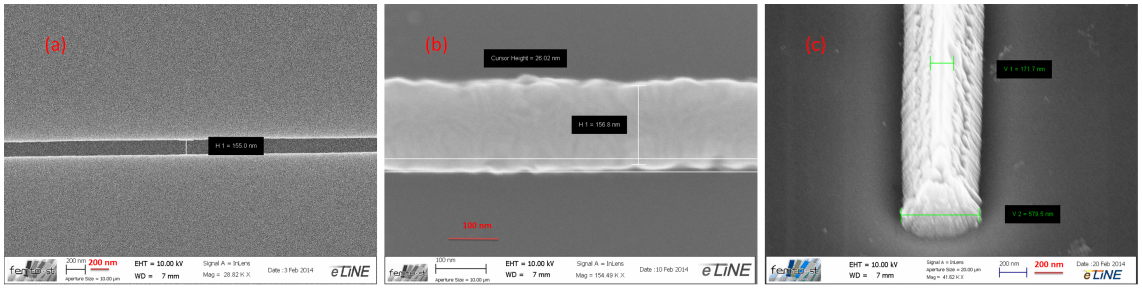

FIGURE 3.41 – (a) E-beam lithography defined PMMA nano meter scale WG path with WG width W about 150 nm, exposure with e-beam dosage of 300 $\mu C/cm^2$. (b) Cr hard mask of WG path with WG with about 150 nm, sidewall roughness on each side of the WG is about 20 nm. (c) LN nano meter ridge WG with top width V_1 about 170 nm and bottom width V_2 about 580 nm.

Though this is only a trial of the nano meter width WG fabrications without any optimization of the process parameters, it can still make clear that the 100 nm LN slot WG is a real challenge for the current fabrication facilities. In addition, another difficulty is the nanometer scale silicon rails that are needed to be deposited and attached to the LN ridge sidewall for the vertical slot WG fabrication. Henceforth, further exploration of the fabrication on vertical slot WG has not been continued. In terms of the technological difficulties, the horizontal slot WG would be a more promising configuration once the TFLN on SOI sample can be attained.

3.5/ CHAPTER SUMMARY

Simulations on WGs with F-P cavity formed by PhC mirrors are presented in order to find suitable configurations for resonance shift based structure to sense E-field. In addition, fabrication trials to realize the proposed structure are also presented. We can conclude that the realization of nano PhC devices especially those concerning LN etching process is really difficult. Oftentimes, the roughness of the WG sidewall or the defect will degrade the expected performance. In terms of the theoretical analysis, F-P cavity formed by PhC mirrors generally have to make compromise between the transmittance and the quality factor of the cavity mode. Thus a cavity with both high transmittance and high Q is difficult to achieve in this kind of

structure. This limitation of compromise between transmittance and quality factor Q in the PhC based F-P cavity makes us to search for another kind of resonance structure that allows both high transmittance and high Q at the same time which will be presented in the next chapter.

4

FANO RESONANCES ON TFLN AND THEIR SENSING APPLICATIONS

4.1/ INTRODUCTION OF FANO RESONANCE

4.1.1/ FANO RESONANCE IN GENERAL AND FANO FORMULA

In the quest of both high Q and good coupling efficiency resonance on TFLN, we are going to focus on guided resonances (GR), which is oftentimes called Fano resonance due to its asymmetric line shape characteristics. Fano resonance, known from atomic physics, can take place in various physical settings. This resonance allows a close coexistence of resonant transmission and resonant reflection and it can be understood as the interaction of a discrete localized state with continuum signals of the background. From the viewpoint of fundamental physics, the Fano resonance may appear in systems characterized by a certain discrete energy state that interacts with the continuum spectrum through an interference effect. Usually, the discrete state is created by a defect that allows (one or several) additional propagation paths of light which can then interact constructively or destructively. Consequently, this interference effect leads to either perfect transmission or perfect reflection, producing a sharp asymmetric profile [10].

The main feature of the Fano resonance is the destructive interference allowing the generation of asymmetric line shapes. In fact, the observation of resonant suppression phenomenon in the transmission line can be dated back to 1902 when Wood observed the spectrum of light resolved by an optical diffraction grating, but it was

not explained properly at that time and it is known as Wood's anomaly [10, 223]. Many other asymmetry transmission line shapes were also observed in various physical settings such as charge transport through quantum dots, plasmon scattering in Josephson-junction networks and matter-wave scattering in ultra-cold atom systems etc [10, 223].

It was Ugo Fano, for the first time, who suggested theoretical explanations for the origin of the sharp asymmetry profiles in various physical settings based on a superposition principle and the physical process can be schematically shown in Fig. 4.1. The complexity of the physical phenomena was encapsulated in a few key parameters and the shape of the resonance profile can be fitted using the following formula [10, 223] :

$$\sigma = \frac{(\epsilon + q)^2}{\epsilon^2 + 1} \tag{4.1}$$

This is the Fano formula, where q is an asymmetry parameter and ϵ is the reduced energy defined as $2(E - E_F)/\Gamma$. E_F is a resonant energy and Γ is the width of the auto-ionized state in the context of quantum-mechanical interaction.

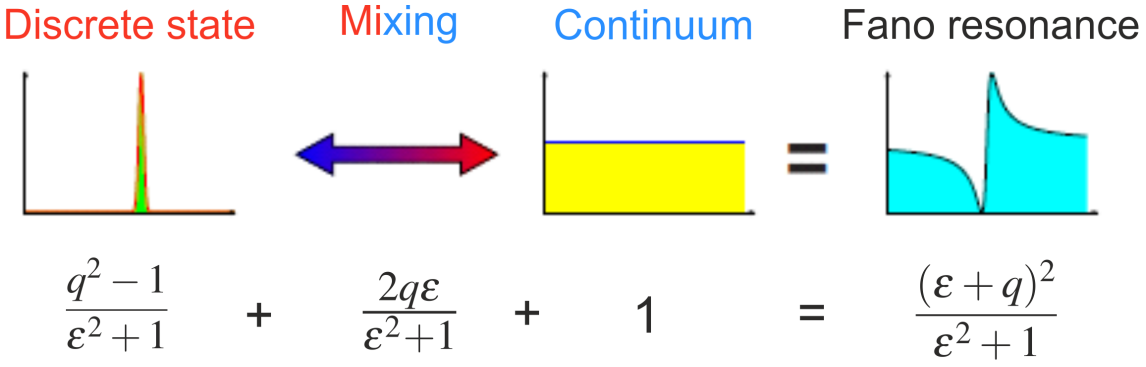

FIGURE 4.1 – Illustration of the Fano formula as a superposition of Lorentzian line shape of the discrete sate with a flat continuous background [10].

Fano introduced the asymmetry parameter q as a ratio of the transition probabilities from the mixed state to the continuum (Fig. 4.1). In the limit $|\, q \,| \to \infty$, the transition to the continuum is very weak, and the line shape is entirely determined by the transition extent of the discrete state exhibiting a standard Lorentzian profile as shown in the dashed black curve in Fig. 4.2. When the asymmetry parameter

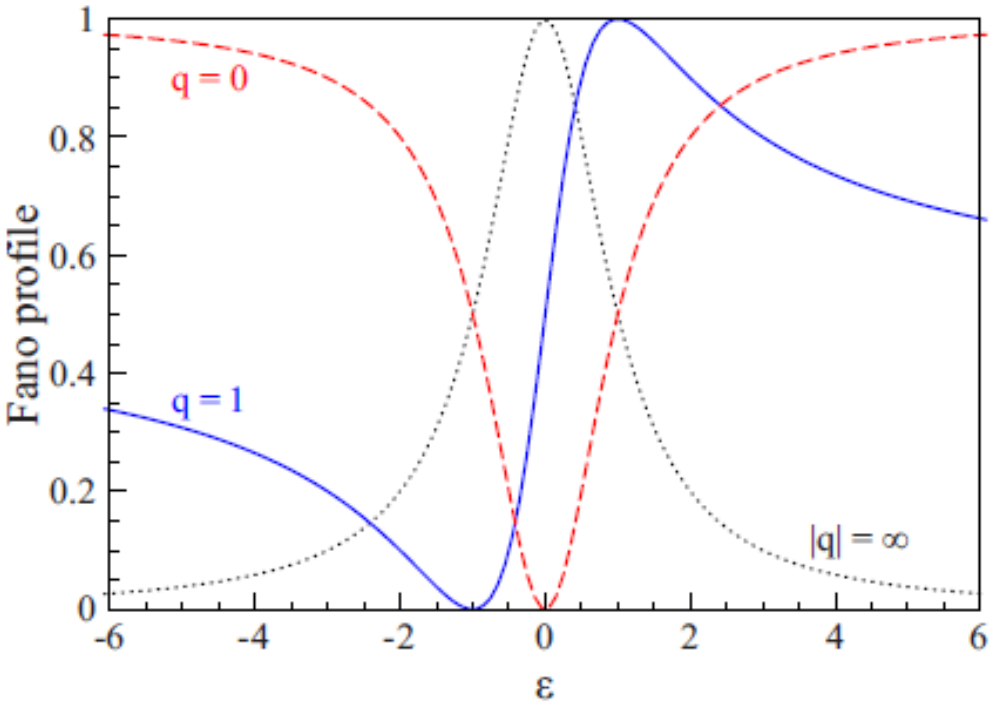

FIGURE 4.2 – Normalized Fano profiles with the prefactor $1/(1+q^2)$ and for various values of the asymmetry parameter q [10].

q is of unity, both the continuum and discrete transitions are of the same strength resulting in an asymmetric profile (solid blue curve in Fig. 4.2) with the maximum value at $E_{max} = E_F + \Gamma/(2q)$ and minimum at $E_{min} = E_F - \Gamma q/2$. The case of zero asymmetry parameter $q = 0$ is unique to the Fano resonance and describes a symmetrical dip, sometimes called an anti-resonance as shown in dashed red curve of Fig. 4.2.

Fano resonances can take place in various physical settings and the resonance line shapes can be fitted with the Fano formula (Eq. 4.1). A broad range of line shapes and quality factors Q can be achieved in the Fano resonance by tuning the asymmetry parameter q as shown in Fig. 4.2 which makes it a suitable choice for various applications.

4.1.2/ FANO RESONANCE IN PHC : GUIDED RESONANCE

In a uniform dielectric slab, guided modes are confined to the slab and are uncoupled to the continuum or radiation modes that exist outside of it. The PhC structure on the slab with the presence of air holes lowers the translational symmetry of the structure changing from a continuous to a discrete one and thereby reducing the degeneracy of the bands supported by the structure. The reduced degeneracy of the mode will then lead to the splitting into singly degenerate states supported by the PhC structures thus enhancing the possibility of generating discrete states that can interact with the continuum.

Fano resonance in PhC is known as a guided resonance from the pioneering work of Fan et al [224]. Fan referred this resonance as a guided resonance due to its similarities with a guided mode in its ability to strongly confine electromagnetic power within the slab. However, a guided resonance distinguishes itself from a guided mode because it can couple to external radiation. Therefore, guided resonances can provide an efficient way to channel light from within the slab to the external environment. In a reduced-zone band diagram, a guided resonance is described as a guided mode that has been folded at the Brillouin zone edge and exists above the light line, hence, coupling to radiation modes. In a transmission spectrum, coupling to a guided resonance results in asymmetry Fano lineshapes which have finite lifetimes described by widely varying Q values.

This kind of resonance, compared with a defect state in PBG, produces theoretically a 100% to 0% transmittance difference within a narrow frequency range due to its intrinsic physical mechanism of generating a π phase shift at a discrete state eigen frequency. In the vicinity of the resonance frequency, a Fano interference occurs allowing incident light to be completely reflected [225]. The resonance frequency and the lifetime of the guided resonance are determined by the PhC structure, which provides great flexibility for engineering different optical properties for various applications. Particularly, the narrow linewidth and steep slope of Fano resonances, when they are exploited in wavelength interrogation sensing applica-

tions, permits that only a small spectral shift is required for detection which, as a consequence, can enhance the sensitivity compared to resonances that have slower slope like Lorentzian line shape resonances. Using guided resonance for sensing is very appealing also because of its easy coupling to externally incident beams.

4.1.3/ STATE OF THE ART ON GUIDED RESONANCE

GR in silicon, silicon nitride and some other semiconductor materials have been extensively studied. The early studies of GR in 2D PhC structures are presented in ref. [226], where the pioneering experimental results of leaky modes supported by a 2D PhC structure on a suspended AlGaAs slab at optical frequencies are shown. Later, P. Paddon et al. developed 2D vector coupled mode theory to illustrate the resonance modes observed in 2D periodic textured structure [227]. Fan et al. studied these resonances by investigating the dispersion diagrams, the modal patterns, transmission and reflection spectra [224]. In ref. [225] a general scheme to analyze a single optical resonance coupled with multiple input and output ports based on temporal coupled mode theory is developed. A great variety of devices have been explored based on GR and have been used for various applications. For example, by tuning the spectral properties of GR, filtering functions such as all-pass transmission or flattop reflection filters have been achieved [228]. Moreover, a displacement sensor is designed through the investigation of transmission and reflection spectra of a pair closely spaced air bridged PhC slabs by varying the spacing between the slabs [138]. A fiber-tip temperature sensor based on silicon PhC is realized by the coupling of two GRs in two PhC slabs exhibiting a two fold increased temperature sensitivity [229]. GR based silicon membrane reflector is integrated in a VCSEL by transfer-printed technique in order to realize efficient silicon based light sources [230]. In ref.[231] Miroshnichenko et al. proposed a novel interferometer configuration by inserting a cavity exhibiting a Fano resonance into a conventional Mach-Zehnder interferometer. An amplitude dependent bistable resonant transmission or reflection based on a linear chain of particles coupled to a single site defect is presented in ref.[232]. GR

have been studied in optical trapping applications and low energy threshold vertical emitting lasers as well as via the investigation of slow Bloch mode (SBM) in the first Brillouin zone center (Γ point) to generate high Q Fano resonances [233, 234].

As we mentioned before, most of the devices on GR are exploited in silicon or some other semiconductor materials. There is however very few works concerning the study of Fano resonance on tunable materials like lithium niobate (LN) [235, 236]. As described before, LN, a nonlinear optical material with high pyro-electric and EO effects [65], is an excellent candidate for EO based temperature or E-field sensor applications. With the recent developments of thin film fabrication techniques, high quality single crystalline LN of a few hundred nanometers thickness remains difficult but attainable [95]. When these TFLN are combined with a Fano resonance possessing high ER (extinction ratio) and high Q design, tunable active devices with different functionalities can be achieved. Numerical studies of GR properties in square lattice air holes on TFLN with an infinite size PhC structure by varying geometrical parameters such as slab thickness, PhC lattice types and radius of holes have been performed by J. Deng et al. [235], where an experimental reflection spectra with poor quality factor of the resonance of a free standing LN passive device has been shown.

In this chapter, GR in Suzuki Phase Lattice (SPL) and a modified rectangular lattice PhC on TFLN have been studied including simulations, fabrication issues and optical characterization for sensing applications. Other types of PhC lattices such as triangular lattice, honeycomb lattice and checker board lattice are also investigated to show the existence of GR in all kinds of PhC lattices.

4.2/ SUZUKI PHASE LATTICE PHC

In this section, guided resonance on SPL PhC on TFLN is investigated both theoretically and experimentally. Experimental tuning of the GR wavelengths with respect to the temperature is demonstrated.

When it comes to the theoretical sensitivity analysis of the device,

the method (employed in Chapter 2 for deducing the sensitivity of slot Bragg grating structure) involving the field factor $\overline{f_{opt}}$ overestimates the sensitivity of GR device. The $\overline{f_{opt}}$ overestimation problem is due to the approximation of the light enhancement by only a single mean value. Henceforth, a modified numerical model for sensitivity analysis that locally calculates the field factor $f_{opt}(x, y, z)$ is presented. It predicts a sensitivity that matches well with the experimental measurements. The newly proposed sensitivity analysis in SPL GR structure also leads to the understanding that except the pyroelectric effect, which is dominant, some other effects such as elastic deformations from thermal expansion and thermal coefficient mismatch between different material layer induced tensor stress might play a role in the temperature tuning of the GR wavelength.

4.2.1/ NUMERICAL MODELING

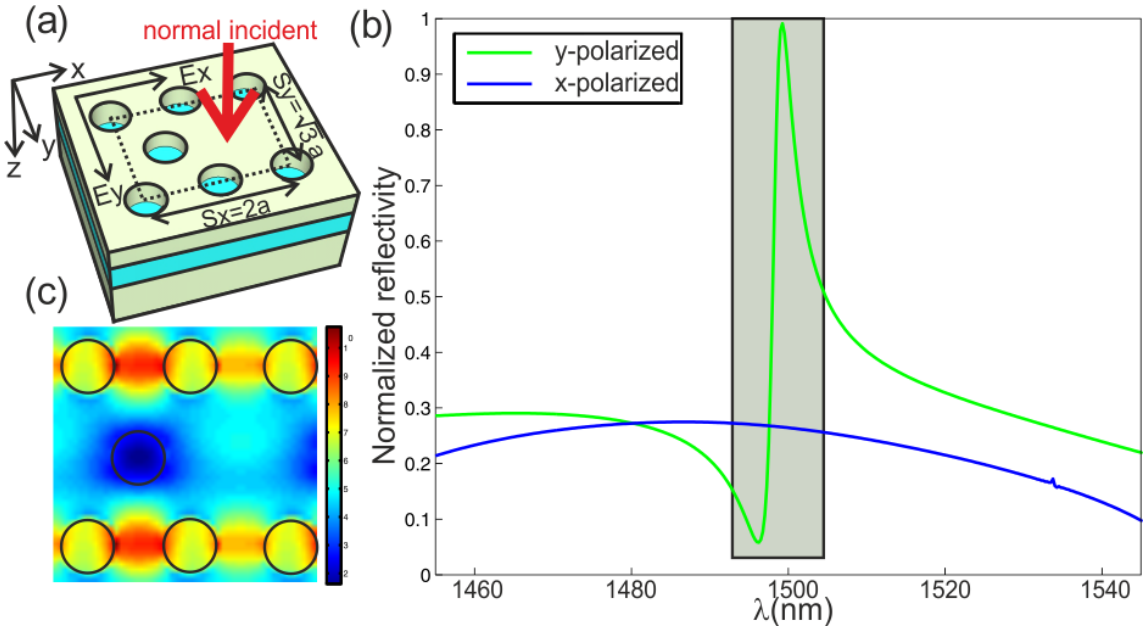

FIGURE 4.3 – (a) Sketch of the SPL PhC on TFLN. The dashed rectangle presents the unit cell considered in the simulations, the red arrow indicates the direction of the incident light. The structure parameters considered here are $a = 500$ nm,$r = 150$ nm. (b) 3D-FDTD simulated normalized zero order reflectivity of the infinite PhC where the highlighted area corresponds to the Fano resonance that is induced under y-polarized incident light with a resonance dip located at 1498 nm. (c) Color map of xOy cross section electric field amplitude distribution of one PhC cell recorded 100 nm below the PhC top surface inside the LN material.

Fig. 4.3(a) shows one unit cell of a SPL as a dashed rectangle.

This lattice was introduced in the context of sound propagation by Caballero *et al* [237, 238] where astonishing sound transmission properties of this rectangular lattice consisting of vacancies embedded in a triangular array of sound scatterers in air were studied. This PhC lattice is named Suzuki phase lattice because of its analogy with the structures discovered by Suzuki in alkali halides [239]. The SPL is obtained by starting with a triangular lattice of holes and removing selected holes to generate a rectangular lattice of H1 cavities (Fig. 4.3(a)). It has different periodicity in the x and y directions : $S_x = 2a$ and $S_y = \sqrt{3}a$ respectively, where a is the lattice constant of the reference triangular lattice. The SPL is chosen to study since the air hole pattern is less dense than the counterpart of triangular lattice which is the most commonly studied. Here we pick the lattice constant $a = 500$ nm and radius of the air holes $r = 150$ nm in order to set the working wavelength in the infrared region. Zero order reflectivity calculations are performed for both incident polarization states along Ox and Oy directions as indicated in Fig. 4.3(a). An infinite PhC is considered and 3D-FDTD simulations have been performed allowing the determination of transmission and reflection coefficients through bi-periodic grating. Infinite size of PhC is realized through one unit cell of PhC combined with Bloch periodic boundary conditions in x and y directions. Sub-grid technique, which generates smooth refractive index change distribution along the two materials interface, is applied to define the air columns more faithfully. The excitation was done with a plane wave propagating along the z direction in air cladding and then through the patterned PhC TFLN as shown with a red arrow in Fig. 4.3(a). Figure 4.3(b) is the normalized zero order reflectivity, where the normalization is done with respect to the incident signal. The reflectivity response in the case of y-polarization exhibits a Fano resonance with almost 100% to 0% peak-dip reflection difference occurring at 1498 nm. This Fano resonance is generated by the superposition of the TFLN guided modes with the background signal. A continuous wave simulation with y-polarized light at resonance dip ($\lambda = 1498$ nm) is performed to obtain the mode field distribution presented in Fig. 4.3(c). Most of the energy is confined in LN material which is favorable for tuning its EO effect.

4.2.2/ STRUCTURE FABRICATION

A PhC size of about $25\ \mu m \times\ 24\ \mu m$ is milled by FIB (Focused Ion Beam) with a Ga^+ liquid metal ion source (acceleration energy = 30 keV). Ions are focused to the lithium niobate thin film with electrostatic lenses with a probe current of 24 pA. In these conditions, the depth of the holes is measured to be the TFLN thickness 600 nm. SEM images of the fabricated structure are shown in Fig. 4.4. The hole radius exhibits a gradual variation along the depth direction as it can be seen from Fig. 4.4(c). Nevertheless, the fabricated structure presents an overall good quality.

4.2.3/ CHARACTERIZATIONS

The optical reflection of the device is characterized using the experimental setup illustrated in Fig. 4.5. The setup is mounted on an Olympus inverted microscope on top of an optical vibration isolation table. The black arrows show the injection optical path and the red arrows show the reflection optical path. For this purpose, a supercontinuum source (LEUKOS SM-20) is first collimated and then it goes through a visible light filter to prevent high light intensity that can induce sample damaging. Since guided resonances are polarization dependent, a polarizer is used to control the polarization of the incident light. The latter passes through a half-wave plate to control the polarization state, and a beam splitter (BS) that allows spatial separation between incident and reflected light. The sample is placed on the supporting stage perpendicular to the reflected light from the beam splitter and is illuminated through a microscope objective ($\times 60, NA = 0.7$). Light is then reflected from the surface of the PhC, back through the objective, the beam splitter and then to a second microscope objective ($\times 40, NA = 0.5$). Finally it is collected by a $SMF - 28e$ optical fiber to the OSA (Optical Spectrum Analyzer). The PhC is placed on the supporting stage upside down, i.e. the focused light from the objective encounters the PhC firstly. Comparing to the configurations in which light is coupled from the substrate, the

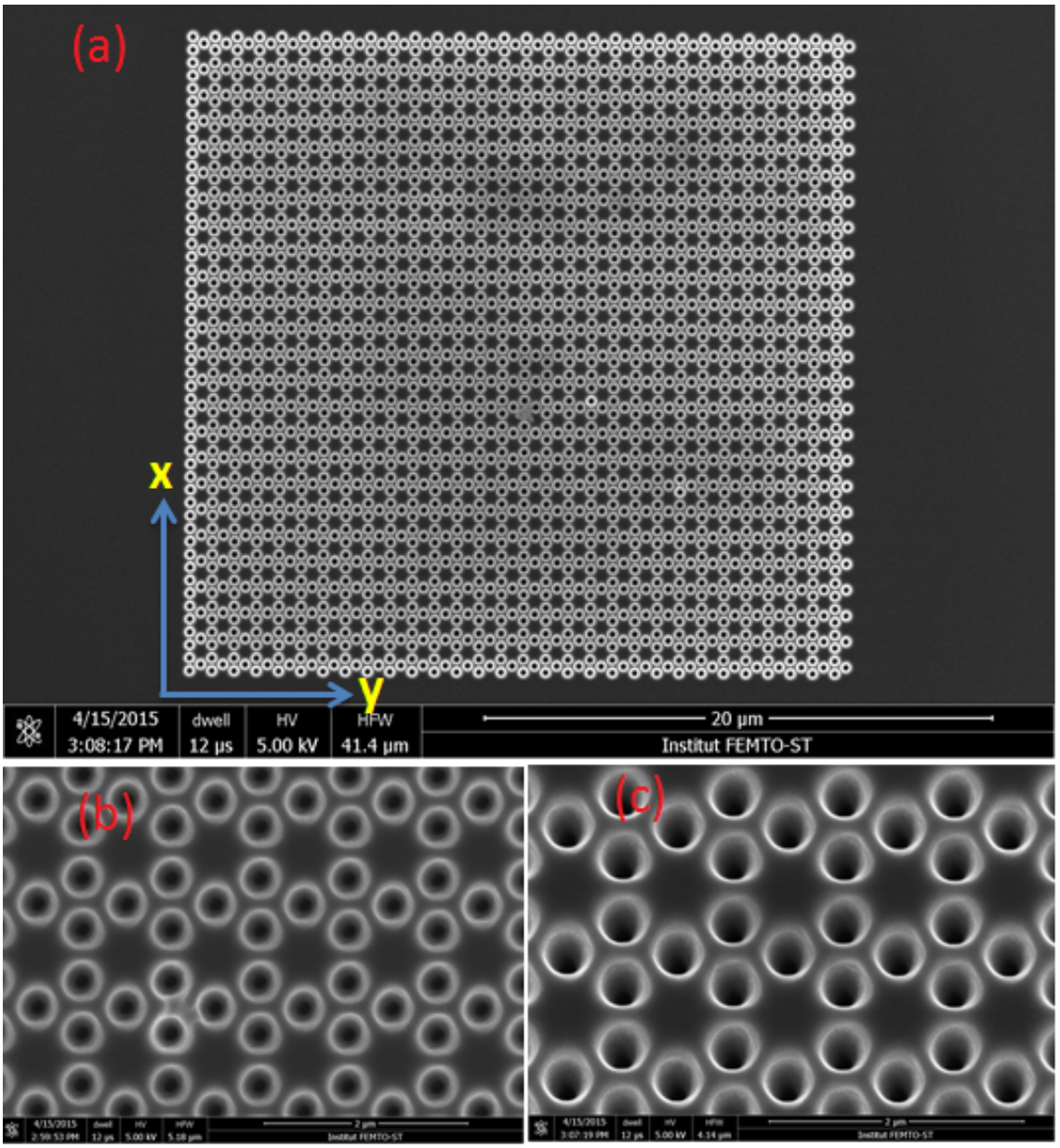

FIGURE 4.4 – (a) SEM image of the whole fabricated structure. (b) Top view zoomed SEM image of the fabricated structure. (b) Zoomed SEM image of the fabricated structure viewed with a tilt angle.

inverted sample benefits from better focus adjustment onto the PhC layer facilitating the measurement of the resonance effect.

The experimental result of the Fano resonance at room temperature is shown in the green curve of Fig. 4.6, where a reflectivity dip is observed in the vicinity of $\lambda = 1500$ nm. The normalization is performed with respect to the reflected signal from a mirror that replaces the sample in the setup. The dip position is in good agreement with nu-

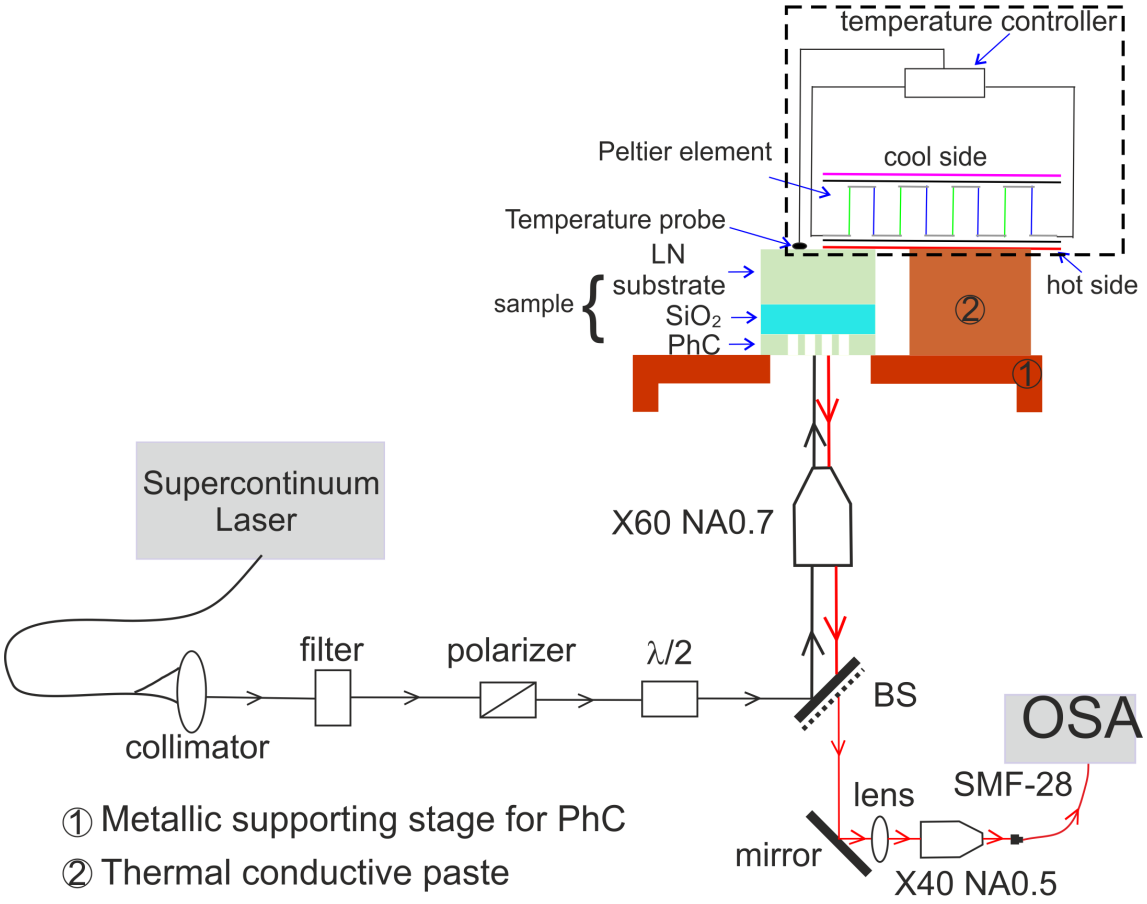

FIGURE 4.5 – Experimental set up for reflectivity measurements.

merical prediction of Fig. 4.3 (b) (only 3 nm difference) while the lineshape of the Fano resonance is different and the peak reflection is not observed experimentally.

The experimental curves are processed through a smooth function in Matlab in order to better determine the resonance dip position as shown in Fig. 4.7 (a). In order to better understand the experimental results, 3D-FDTD finite structure reflectivity calculations approaching the experimental measurement conditions are conducted. Perfectly matched layer boundary conditions are employed to simulate the finite size structure with a uniform meshing of $\Delta x = \Delta y = 50$ nm in both x- and y-directions, while nonuniform meshing is applied in the z direction. Subgriding technique with $\delta x = \delta y = 10$ nm is also applied to faithfully define the refractive index distribution as in the infinite structure case. The total calculation window size in the xOy plane is $31\ \mu$m $\times 30\ \mu$m which is large enough to include the PhC. The structure is illuminated by a Gaussian

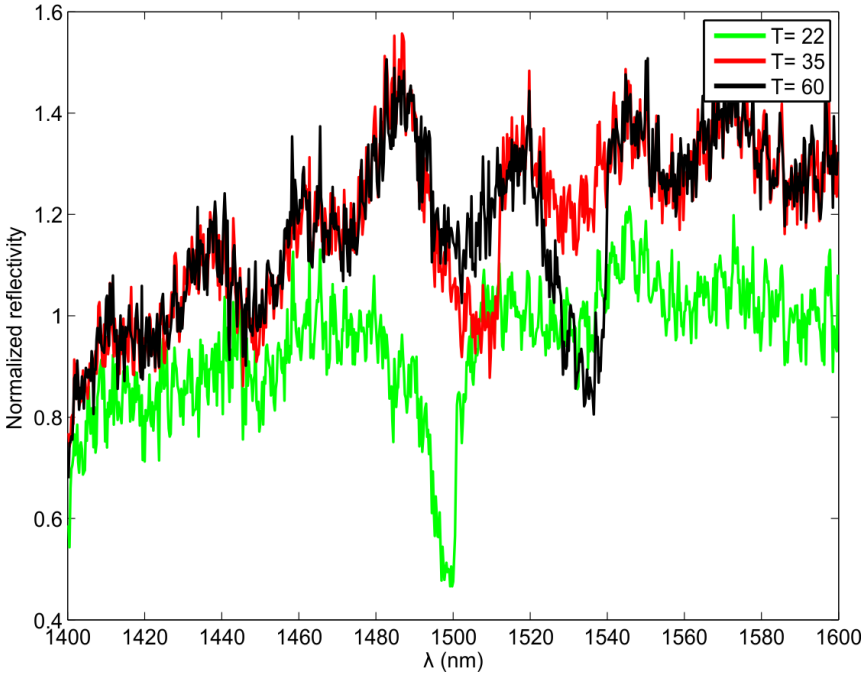

FIGURE 4.6 – Experimental measured normalized reflectivity curves.

beam with beam waist of $15\ \mu$m. The reflection collecting objective of $NA = 0.7$ in the experimental set up means that almost only reflected light inside a cone of half-angle of $44.4°$ is collected. Theoretically, we have considered an angle of $45°$.

The result is shown in Fig. 4.7 (b) where a resonance dip occurs at $\lambda = 1492$ nm. We can see that there is a qualitatively good agreement with the experimental reflectivity of Fig. 4.7 (a). The reflectivity dip position is 2 nm blue-shifted compared to that of infinite PhC (Fig. 4.3 (b)) may be due to the finite size effect. A resonance wavelength difference of 9 nm (0.6% with respect to the resonance wavelength) is observed with respect to the experimental measurements.

The measurement has higher reflectivity level which differs from the simulated results. This might be due to the larger collecting region in the experiment where all the energy traveling through the microscope objective is retrieved by the OSA. Instead, we numerically approximate this condition by recording the Poynting energy flux through a circular area placed in the near-field of the PhC which collects the reflected light inside a cone of $45°$. Another condition that might induce the difference is the normalization signal. In the

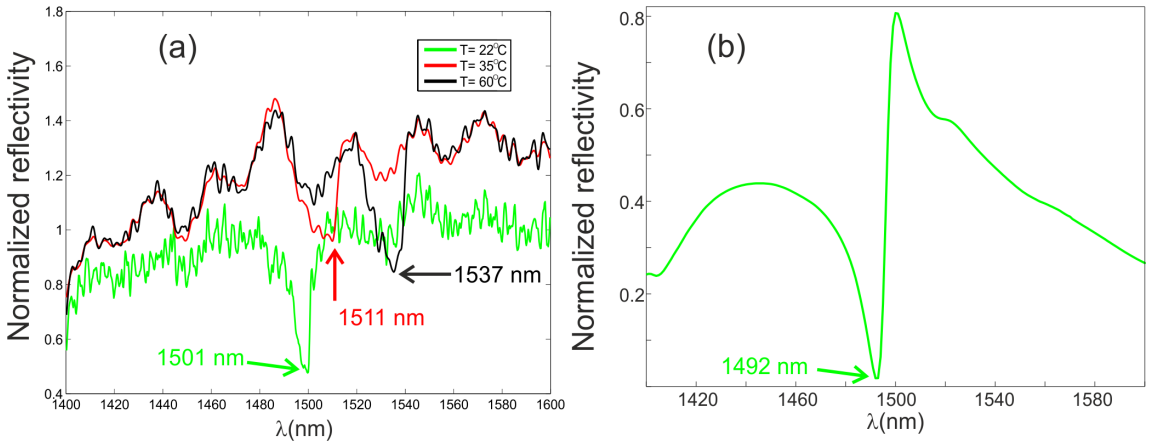

FIGURE 4.7 – (a) Experimental normalized reflectivity of Fano resonance after smooth function processing in y-polarized excitation at different temperatures. (b) 3D-FDTD calculated finite size PhC reflectivity by y-polarized Gaussian beam incidence, with beam size of 15 μm at room temperatures.

experimental measurement the normalization signal is collected by replacing the sample with a mirror of limited reflection coefficient while in the simulations a perfect mirror with total reflection is assumed for the normalization. These differences may contribute to the difference in the reflectivity level. In addition, given the uncertainty of the focused spot size of the illumination, we have performed systematic numerical simulations by decreasing the beam waist in order to point out its effect on the reflectivity level. Figure 4.8 (a) shows that a small incident beam spot size yields a decreased reflectivity level together with a smaller depth of the resonance dip. This also corresponds to the result reported in ref. [240] where the depth of the resonance decreases as the convergence angle of the beam is increased. An illumination spot size of about 10 μm can yield a 0% reflection dip.

4.2.3.1/ TEMPERATURE TUNABILITY

The tunability of the resonance wavelength as a function of temperature is experimentally investigated with a Peltier element as shown in Fig. 4.5. The hot side of the Peltier sits on the metallic support (denoted as ①) through thermal conductive paste (denoted as ②). Part of the Peltier hot side and a temperature probe are directly placed at

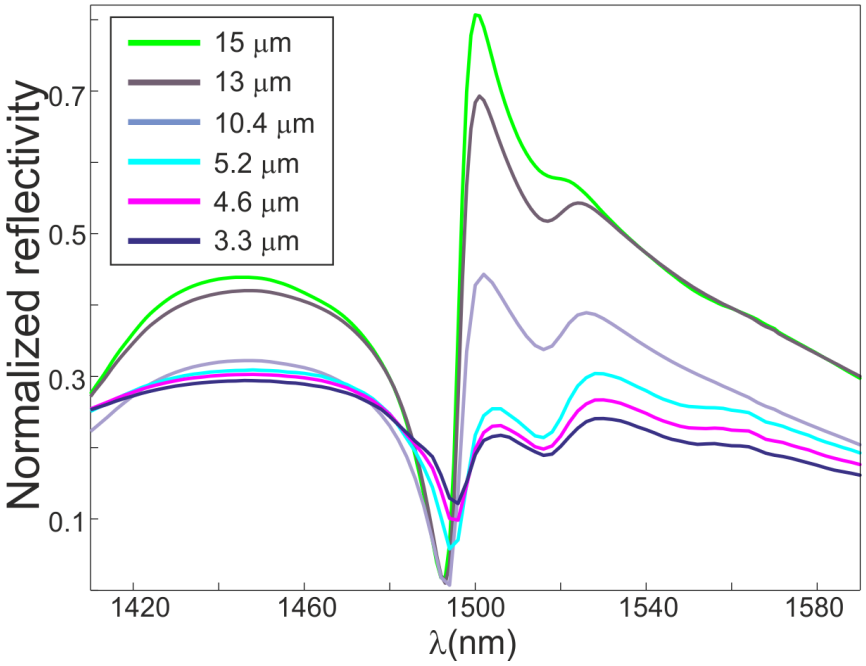

FIGURE 4.8 – 3D-FDTD calculated normalized reflectivity with different beam waist values of the Gaussian beam incidence where the beam waist is given in the legend for each curve.

the bottom surface of the sample and are connected to a temperature controller in order to set the desired temperature. As shown in the red and black curves of Fig. 4.6 (direct measurements) and Fig. 4.7 (a) (measurements after smooth function in Matlab processing), the resonance wavelength shifts towards higher wavelength values as the temperature increases. We have observed that for $T = 35°C$, the Fano resonance dip shifts to 1511 nm, and for $T = 60°C$, it shifts to 1537 nm. We can also notice that the resonance depth gets smaller and the resonance linewidth gets slightly broader as the temperature increases. This indicates that the coupling efficiency of the resonance gets poorer. The resonance lineshape sharpness is degraded at $T = 35°C$ and $60°C$ in red curve and black curve respectively, which is the effect of inhomogeneous refractive index variation therefore leading to lack of periodicity in the structure as it can be described in the following theoretical analysis.

The experimental resonance wavelength shift seems to present a non-linear behavior at higher temperature regime. Indeed, from $T = 22°C$ to $35°C$, a $\Delta\lambda_{res} = 10$ nm red shift of the resonance wavelength is observed while at higher temperature regime a larger shift

of $\Delta\lambda_{res} = 26$ nm is obtained when T increases from $35°C$ to $60°C$. If we assume piecewise linear relationship of resonance wavelength shift versus temperature, then we have a sensitivity of $0.77\ nm/°C$ for $T \in [22, 35]°C$ while a sensitivity of $1\ nm/°C$ for $T \in [35, 60]°C$ is experimentally obtained.

Sensitivity analyzed by $\overline{f_{opt}}$

The observed resonance wavelength shift is mainly due to the pyro-electric effect of LN. A change in temperature ΔT will induce a change of the static electric field generated by the pyro-electric effect, resulting on a variation of the refractive index which, for a PhC geometry, will induce a shift of the resonance wavelength position. In order to exploit the largest EO coefficient in LN, we oriented its crystalline direction along the major electric field direction of the resonance mode. As illustrated in the sensitivity analysis of the slot Bragg gratings in Chapter 3, the refractive index variation is enhanced and proportional to the optical field factor $\overline{f_{opt}}^2$ due to the high light confinement properties of the nano patterned structures. Thus, similar to that of Eq. 3.8 in Chapter 3, a simplified Pockels equation is employed in order to quantify the pyro-electric effect [7] as follows :

$$\Delta n = -\frac{1}{2} {n_e}^3 r_{33} \overline{f_{opt}}^2 E_z, \;\; E_z = -\frac{1}{\epsilon_0 \epsilon_r} p \Delta T \tag{4.2}$$

Where E_z is the electric field generated by the pyro-electric effect, ϵ_0 is the permittivity of vacuum, $\epsilon_r = 28.7$ is the relative permittivity of LN, $p = 6 \times 10^{-5}\ Cm^{-2}K^{-1}$ is the pyro-electric coefficient. $n_e = 2.138$ is the extraordinary refractive index of LN at 1.55 μm. $r_{33} = 30.8$ pm/V is the largest EO coefficient for LN. Optical field factor $\overline{f_{opt}}$ has been introduced in Chapter 3 to quantify the confinement of the light in the PhC which is estimated as an average value over all the PhC volume (see Eq. 3.4).

Notice that, the method of employing optical field factor to quantify the light enhancement induced increase in the effective EO effect in nano patterned LN has already been applied in different PhC geo-

metrical structures with a good matching between the theoretical prediction and experimental measurements.

Band edge modes in the PhC band diagram or creating a defect in the PBG are common ways to benefit from high confinement of light localization for the exploitation of nonlinear effects and strong light matter interactions in PhC. Local field factors are introduced in order to quantify these enhancements. Indeed, in such cases, a generalized local field theory of nonlinear homogeneous media [241] to the case of PhC [242] has been employed to show that nonlinear susceptibilities of the PhC media are enhanced by local field factors in these nonlinear media. For instance, in ref.[243] local field factors were employed to evaluate the third-order nonlinear susceptibility in Kerr and four-wave mixing processes at the band edge of one-dimensional PhC. They present a good agreement with the experimental observations. EO modulation performance on LN with square [62] and triangular lattice [63, 220] was estimated by the local field factor where good agreement with the experimental measurements was achieved. In ref.[7], the sensitivity of a triangular lattice F-P cavity based T-sensor was investigated by integrating local field factor ($\overline{f_{opt}}^3$) into the intrinsic Pockels effect which showed excellent agreement between the theoretical prediction and the experimental measurements. The power of three relationship to the field factor ($\overline{f_{opt}}^3$) was believed due to that the E-field generated by the pyroelectric field that can be confined in the defect regions of nano patterned structures and that it is proportional to $\overline{f_{opt}}$. Combining with the relationship of the intrinsic EO r_{33} proportional to $\overline{f_{opt}}^2$, then $\overline{f_{opt}}^3$ is integrated to quantify the enhanced Pyro-electric effect in F-P cavity.

However, since there is no defect region in GR structure, the structure has no ability to confine the E-field generated by the pyroelectric field. Therefore only $\overline{f_{opt}}^2$ is considered here. The optical field factor is calculated through two 3D-FDTD simulations where one is with the PhC and another is with no PhC-pattern structures with the incident Gaussian beam waist of 5 μm at 1496 nm at room temperature ($T = 22°$C). It yields an $\overline{f_{opt}}$=11.2. Sensitivity simulations in which we modify the LN material refractive index according

to Eq. 4.2 by substituting different ΔT values are carried out. Results are shown in Fig. 4.9 (a). Resonance wavelength variation as a function of the temperature from simulations and experimental measurements are plotted in Fig. 4.9 (b). As we can see, simulations indicate a rather linear resonance wavelength shift relationship with respect with the temperature but there is a clear difference in the slope of the curves between experiments and simulations.

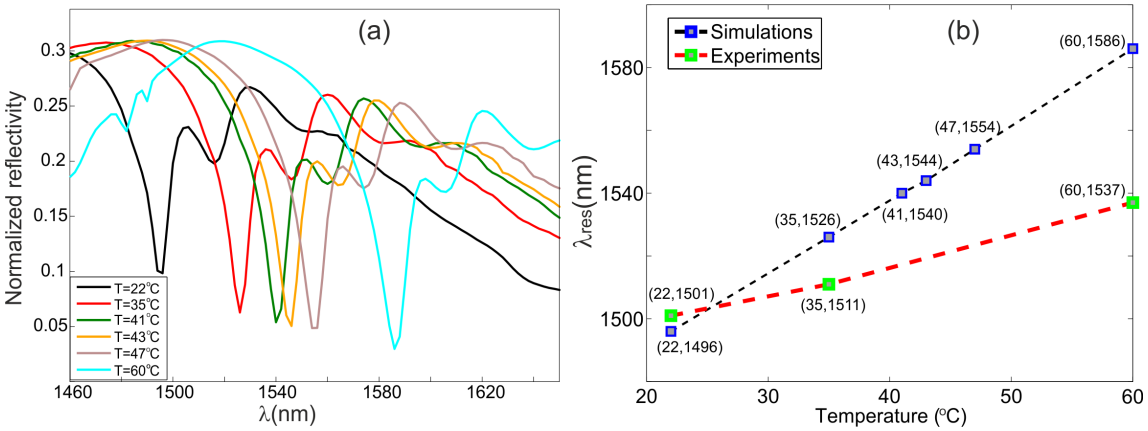

FIGURE 4.9 – (a) 3D-FDTD calculated normalized reflectivity for different temperatures. (b) Numerically calculated (blue squares) and experimental (green squares) results of the resonance wavelength shift as a function of the temperature.

TABLE 4.1 – Resonance dip wavelengths shift with respect to different T calculated by $\overline{f_{opt}}$

T(^{o}C)	22	35	41	43	47	60
ΔT(^{o}C)	0	13	19	21	25	38
λ_{res} (nm)	1496	1526	1540	1544	1554	1586
$\Delta\lambda_{res}$ (nm)		30	44	48	58	90
$\Delta\lambda_{res}/\Delta T$		2.3	2.3	2.28	2.32	2.368

Table 4.1 summarizes the resonance wavelengths and the λ_{res} sensitivity calculated by $\Delta\lambda_{res}/\Delta T$. A sensitivity of about 2.3 nm/^{o}C is obtained. In terms of sensitivity, simulations yield a much larger sensitivity (evident from the difference in the slope of the curves in Fig. 4.9 (b)) than the experimental measurements which is 0.77 nm/^{o}C at $T \in [22, 35]^\circ C$ and 1 nm/^{o}C at $T \in [35, 60]^\circ C$. In terms of the resonance line shapes, the simulated curves present similar resonance line shapes without distortion under the influence of temperature. However, the measurements show degraded and broader line shapes at higher temperatures as in the case of red and black curves in Fig. 4.7 (a).

Sensitivity analyzed by $f_{opt}(x, y, z)$

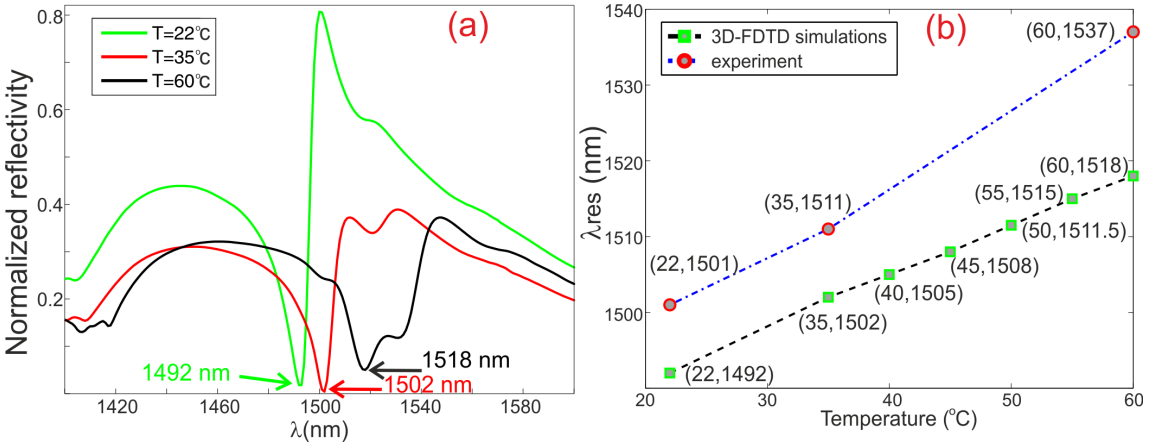

FIGURE 4.10 – (a) 3D-FDTD calculated finite size PhC reflectivity by y-polarized Gaussian beam injection, with beam size of 15 μm at different temperatures. (b) Experimental (circles) and numerically calculated (squares) plots showing the resonance wavelength shift as a function of the temperature.

In order to better understand the discrepancies between the experiments and the theoretical predictions, we have looked for a more accurate way to calculate the optical field factor f_{opt}.

The GR is actually a discrete state of the mode where the local changes of the ambient material properties greatly contribute to the change of the mode effective index and therefore the resonance wavelength. In this case, there is no defect regions, henceforth it is not appropriate to use a mean value $\overline{f_{opt}}$ in order to represent a collective effect contributed by each local refractive index variation elements. Therefore the criteria of the $\overline{f_{opt}}$ estimated by a single mean value is no longer suitable in order to predict a correct sensitivity. We need to take into account each local refractive index variation element. Therefore, a modified model that quantifies the field factor locally for the sensitivity calculation in GR structure is presented. Here, the model is modified by replacing the $\overline{f_{opt}}$ by $f_{opt}(x, y, z)$ which is evaluated cell by cell (in the FDTD algorithm) as the ratio between the electric field amplitude of the nano-patterned structure and the one of the bulk LN. In order to calculate $f_{opt}(x, y, z)$, two 3D-FDTD calculations are performed in the same illumination conditions at the resonance dip wavelength, one with the PhC structure, and the

other with un-patterned LN.

$$\Delta n(x,y,z) = -\frac{1}{2} {n_e}^3 r_{33} f_{opt}^2(x,y,z) E_z, \;\; E_z = -\frac{1}{\epsilon_0 \epsilon_r} p \Delta T \qquad (4.3)$$

Once we have the optical field factor distribution $f_{opt}(x,y,z)$, simulations of the reflectivity for different temperatures at $T = 35°C$ and $60°C$, are conducted by substituting the corresponding ΔT into Eq. 4.3 in order to obtain the refractive index variation distribution $\Delta n(x,y,z)$. The latter is then injected into the FDTD code (new distribution of the index of refraction) to simulate the pyro-electric effect. Fig. 4.10 (a) shows the resonance curves with respect to T. At $T = 35°C$, the resonance dip shifts to 1502 nm, and at $T = 60°C$ it moves to 1518 nm. We can also notice that the resonance depth is only slightly affected by the increase of temperature, while the sharpness of the resonance degrades. Fig. 4.10 (b) shows a comparison between numerical and experimental resonance dip position (λ_{res}) as a function of the temperature. We can see that the numerical modeling sensitivity fulfills a quasi linear relationship with respect to temperature.

In the temperature range of $T \in [22,35]°C$, there is a good agreement between the experimental sensitivity ($0.77\ nm/°C$) and the simulated sensitivity as it can be seen from the same slope of the curves in Fig. 4.10 (b). An experimental sensitivity for $T \in [35,60]°C$ is measured to be $1\ nm/°C$ which is higher than the numerical simulated one of $0.68\ nm/°C$. This denotes that only considering pyro-electric effect is not enough. At higher temperature regime, elastic deformations and mechanical stresses (induced by thermal coefficient mismatch between silica and lithium niobate) of the LN layer are no longer negligible and should be taken into account. Since the silica buffer layer is amorphous, the determination of the deformation properties is difficult, thus we could not include it in the numerical modeling. We can roughly estimate the elastic deformation effect by subtracting the theoretical predicted pyro-electric sensitivity ($0.68\ nm/°C$) from the experimental sensitivity ($1\ nm/°C$) which yields a sensitivity of $0.32\ nm/°C$. Even though this effect plays a positive role in terms of tunability, it adds difficulties on the sensor calibration.

Notice that the refractive index variations $\Delta n(x, y, z)$ are wavelength dependent since $f_{opt}(x, y, z)$ is wavelength dependent. In general, the $f_{opt}(x, y, z, \lambda)$ reaches its maxima at the λ_{res}. Henceforth, the above methods of investigating the $\Delta\lambda_{res}$ sensitivity is in principle only correct for the λ_{res} wavelength position since the $\Delta n(x, y, z, \lambda)$ is modified according to the $f_{opt}(x, y, z, \lambda_{res})$. However, the $\Delta\lambda_{res}$ sensitivity obtained by choosing λ_{res} as operating wavelength yields the highest sensitivity compared to otherwise operating wavelength setting on non λ_{res}. Therefore, the $\Delta\lambda_{res}$ sensitivity can represent the sensitivity of the device. The negative effect of modifying the $\Delta n(x, y, z)$ by only considering the $f_{opt}(x, y, z, \lambda_{res})$ is that it leads to the distortion of transmission curve line shape compared to the experimental measurements as Fig. 4.10 (b). This distortion originates from the fact that the introduced $\Delta n(x, y, z, \lambda)$ is smaller than $\Delta n(x, y, z, \lambda_{res})$ at the resonance wavelength. Intensive simulations with $\Delta n(x, y, z, \lambda)$ modified by $f_{opt}(x, y, z, \lambda)$ at different wavelengths may be applied to more accurately fit the transmission curve. Nevertheless, one can obtain the correct sensitivity with refractive index modified by the $f_{opt}(x, y, z, \lambda_{res})$ regardless the distorted transmission curve line shape.

The above sensitivity analysis with $f_{opt}(x, y, z)$ predicted the sensitivity that can match well with the experiments. In addition, the reflectivity line shape is in well qualitative agreement with experiments. Henceforth, this method is a more appropriate way to model the sensitivity of GR structure. Nevertheless, $\overline{f_{opt}}$ can predict a correct trend of finding the geometric that yields high sensitivity, thus it can be utilized as a visualized method to target the appropriate geometrical parameters range.

The intrinsic pyro-electric induced sensitivity in the SPL structure was evaluated to be $0.02\ nm/°C$ calculated by substituting $f_{opt}(x, y, z) = 1$ in Eq. 4.3 for the 3D-FDTD simulations. Consequently, this SPL PhC temperature sensor yields at least 38 fold enhancement compared to bulk LN. Table 4.2 shows the comparison with state of the art temperature sensors in terms of sensitivity and interaction length. The demonstrated PhC temperature sensor in TFLN has a 7 times higher sensitivity with a smaller interaction length with respect to the double layer Fano resonance on silicon PhC sen-

sor [229].

TABLE 4.2 – Different temperature sensors comparison

Sensor type	Sensitivity (nm/°C)	Interaction length (mm)
Long-period FBG Fiber [39]	0.6	1
Alcohol-filled PCF with loop mirror [244]	6.6	61
Surface Plasmon resonance within selectively coated PCF [245]	0.72	5
Double layer Si PhC [229]	0.108	0.03
Fano resonance in TFLN	**0.77**	**0.025**

As a conclusion, we have demonstrated a compact highly sensitive temperature sensor based on SPL PhC engraved on TFLN. Experimental sensitivity of $0.77\ nm/°C$ with only $25\ \mu m \times 24\ \mu m$ active cross section in TFLN has been achieved. The compact size of the structure offers new perspectives for integrated on-chip sensor components or hand held devices such as on-fiber tip temperature sensor or electric field sensor etc.

4.3/ RECTANGULAR LATTICE PHC ON TFLN

In this section, we have looked for GR on a simpler PhC lattices (square lattice and its variants). Intensive numerical calculations are performed to find suitable structure to be integrated as on fiber end sensors.

4.3.1/ NUMERICAL SIMULATIONS

Numerical simulations on rectangular lattice PhC involve band diagram calculations and 3D-FDTD transmission spectra investigations on both infinite and finite size PhC structures. Detailed theoretical sensitivity analysis of these resonances to exploit them as E-field sensor is analyzed.

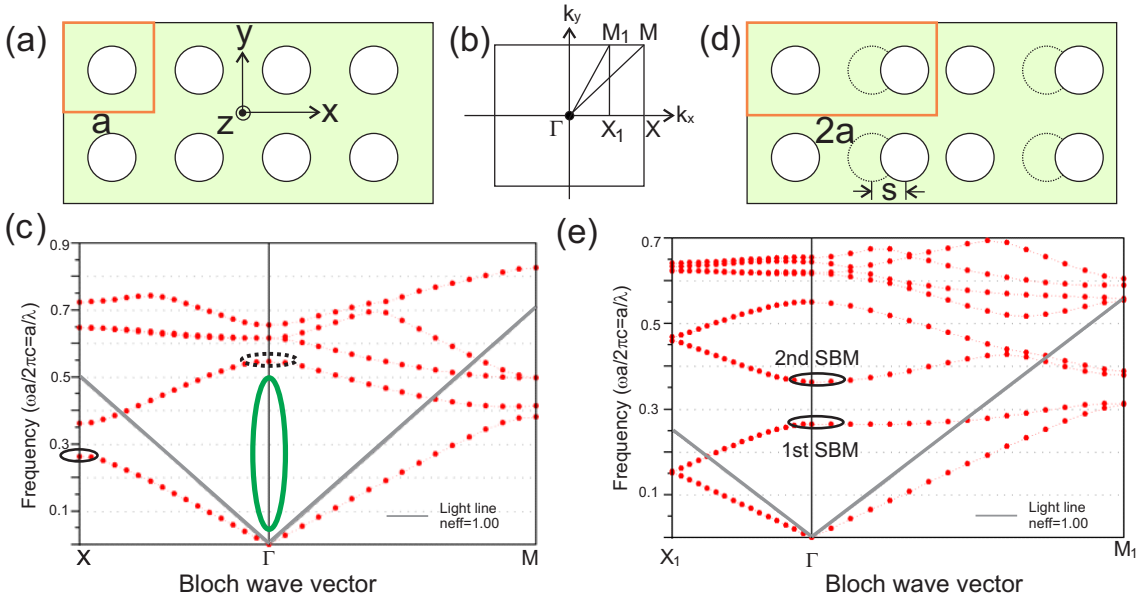

FIGURE 4.11 – (a) Sketch of the studied 2D infinite square lattice of air holes in LN where the orange square displays the unit cell with lattice constant *a*. (b) Reciprocal space associated to the square lattice (Γ, M, X) and rectangular lattice (Γ, M_1, X_1). (c) Band diagram for square lattice structure in (a) with electric field lies in the xy plane and a filling factor *f* of 0.368. The studied SBM in Γ point is black dashed circled out at normalized frequency of 0.545. The band edge black circled mode at symmetry point X lies at normalized frequency of 0.261. (d) Sketch of rectangular lattice air holes in LN formed by shifting holes center positions of *s* value in every two columns. The orange rectangle displays the unit cell with period of 2*a* in x direction. The dashed circles nearby solid line circles is square lattice hole position. (e) Band diagram for rectangular structure in (d) with parameters values *a* = 630 nm, *s* = 30 nm, electric field in xy plane, filling factor *f* of 0.368. The two SBMs in Γ point are black circled out and lie at normalized frequency of 0.265 and 0.363 respectively.

4.3.1.1/ DISPERSION RELATIONSHIP MODELING ON 2D PHC

Flat and low group velocity bands are features of PhC band structures which can be exploited to design resonances with high Q values. Here 2D PWE (RSOFT BANDSOLVE) is first employed to calculate the band diagram in order to determine parameters such as lattice constant *a* and filling factor *f*. We focus only on modes which can be excited by normal incidence illumination. This means that the investigated modes will be located at the Γ-point (the origin of the first Brillouin zone) above the light line. The operation wavelength λ_{res} considered here is in the vicinity of 1.55 μm, which enables the compatibility with most of the telecom devices. Since the lifetime of photons inside the 2D PhC membrane is directly related to the group

velocity Vg, a SBM which posses a low Vg would be a good candidate for a high Q cavity design which will then help to enhance the effective EO coefficient and therefore to increase the E-field probe sensitivity [142]. Consequently, dispersion modeling is performed to determine a filling factor *f* yielding a SBM. Then through the scaling invariant property of Maxwell equations (we only deal with non-dispersive material), a lattice constant *a* can be determined in order to set the operation wavelength at the IR regime.

The studied structure, as shown in Fig. 4.11(a), is a square lattice of air holes milled in LN material in the xy plane, while it is invariant in the z direction. The associated nomenclature of the symmetric points in the irreducible Brillouin zone is shown in Fig. 4.11(b). The corresponding dispersion curve is shown in Fig. 4.11(c). The mode that we are looking for is dashed black circled out in Fig. 4.11(c), which lies in the Γ point above the light line at the normalized frequency $a/\lambda = 0.541$. However, there are some disadvantages in applying this mode for designing compact sensor applications. Firstly, a lattice constant of around 800 nm will be needed in order to set the operation wavelength at 1.55 μm as it is the case in ref.[235] which is not beneficial to scale down the devices. Secondly, the mode lies near high order modes with small frequency separation, which makes the selected mode more prone to interfere with other nearby modes which degrades the resonance visibility in wavelength interrogation based sensing applications. To circumvent these drawbacks, we engineer the band diagram to couple modes in a lower frequency range which is not occupied by any states in the square lattice as it is highlighted in the green ellipse region (Fig. 4.11(c)). To that end, we introduce a shift *s* to the hole position in every two columns of air holes as schematically shown in Fig. 4.11(d). As a result, the period in the x direction becomes $2a$ as shown in orange rectangle unit cell in Fig. 4.11(d). We refer this lattice as biperiodic rectangular PhC structure. Notice that the method of tailoring structural parameters to enable coupling to preferable modes has been investigated in applications for optical tweezer [233] and photonic refractive index sensor for instance [246]. The principle of this method is to 'band fold' the preferable mode so that the mode symmetry has a non-zero convolution with the incident beam [247] thus leading to

the efficient excitation of the modes.

For small values of *s* (*s*<0.1*a*), the band edge mode at the symmetry point X (solid black circled out in Fig.4.11(c)) is folded to the Γ point above the light line. In this case, mode properties such as group velocity can be assumed to be preserved and be the same as for the square lattice case. Henceforth, we first perform square lattice structure band calculations, and determine a filling factor of 0.368, which yields a SBM in the symmetry point X. Keeping the same filling factor, we introduce a *s* = 30 nm to a structure of *a* = 630 nm as shown in Fig. 4.11(d) in order to form the biperiodic rectangular structure and we get the corresponding dispersion curve displayed in Fig. 4.11(e). We can see that two modes (encircled in black) appear at low frequency values in the Γ point above the light line with large frequency separation between other modes (>10% of normalized frequency). The lower frequency mode, which is called first SBM (1st SBM), lies at the normalized frequency a/λ = 0.265, while the second SBM (2nd SBM) lies at the normalized frequency of a/λ = 0.363. By setting λ to 1.55 μm, we obtain the corresponding lattice constant *a* to be 410 nm and 560 nm respectively. Having determined *a* and the filling factor *f*, we can proceed to perform 3D-FDTD simulations to fine tune the design parameters in real 3D structures.

4.3.1.2/ 3D-FDTD TRANSMISSION SPECTRA ANALYSIS

In this section, we present a systematic 3D-FDTD study by investigating the zero order normalized transmission spectra of infinite and finite size PhC structures with the parameters previously determined by PWE calculation.

In the infinite case, the considered structure consists of a TFLN slab milled with a rectangular lattice air holes structure suspended in air as shown in Fig. 4.12 (b). The calculation with parameters determined from PWE for both single square lattice (Fig. 4.12 (a)) and rectangular lattice structure is first conducted. Then the rectangular PhC is studied by varying the lattice constant *a*, the TFLN slab thickness *t*, the hole conicity (angle θ) and the shift value *s* in order to

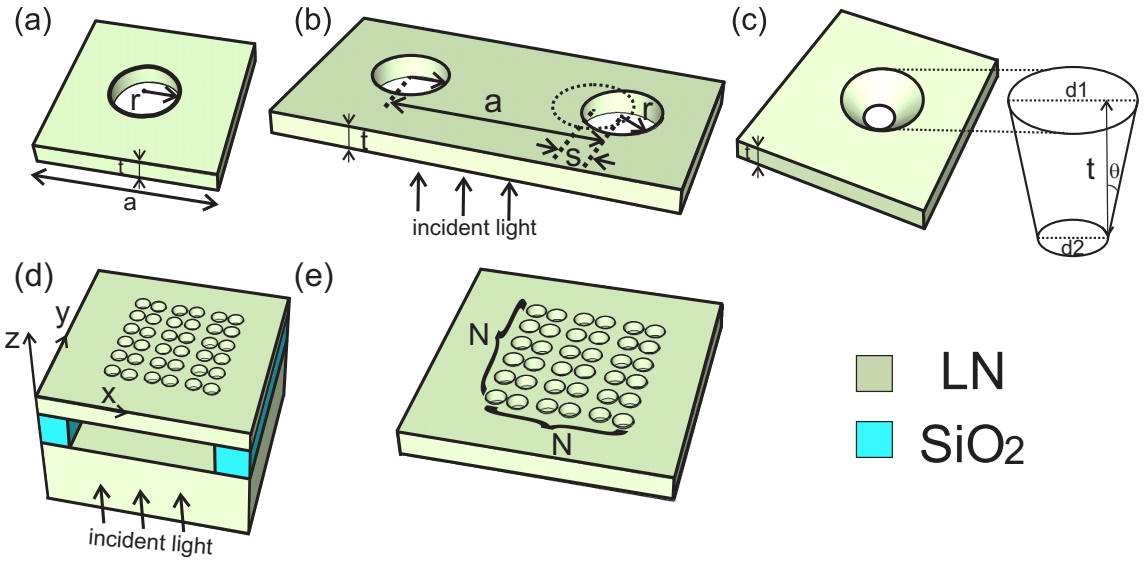

FIGURE 4.12 – (a) Unit cell of square lattice air hole on TFLN of lattice constant *a*, radius *r*, TFLN slab thickness *t*. (b) Unit cell of rectangular lattice structure on TFLN by shifting hole position *s*, the black arrows at the bottom show the illumination direction. (c) Sketch of conical air hole with θ as the conicity angle. (d) Sketch of finite size air membrane type PhC structure, the coordinate shows the direction definition in agreement with that in Fig.4.11 (a). Period along x direction is 2*a*, while along y direction is *a*. (e) $N \times N$ holes of finite size air bridged type PhC structure, with $N = 6$ shown in the sketch.

see the influence of these geometrical parameters on the resonance mode properties such as Q and ER.

In finite PhC size structure case, both the air membrane structure (Fig. 4.12 (d)) and the air bridged structure (Fig. 4.12 (e)) are studied. The starting substrate for a 3D structure is a multi-layer of a 700 nm TFLN bonded onto either a 1.2 μm SiO_2/LN or 1.2 μm SiO_2/Si substrate. The air membrane structure consists of a TFLN slab resting on a square-size air membrane which can be achieved by selectively removing the silica buffer layer on top of the LN substrate. The air bridged structure consists of a thin layer of LN self suspended in air corresponding to a symmetrical structure along the z direction. These finite structure studies are conducted by varying the shift value *s* and the PhC size *N* (number of rows). The optical field factor mean value, ER and resonance Q values are then tabulated in order to compare different geometries. The sensitivity of employing the GR structure as E-field sensor is accurately analyzed by locally calculation of field factor $f_{opt}(x, y, z)$. Details of these studies will be described in the following subsections.

3D-FDTD transmission spectra analysis of infinite PhC structure

The infinite rectangular structure (Fig. 4.12 (b)) for the 3D-FDTD calculations consists of a computational window of $2a \times a$ in the xy plane. The structure is illuminated by a normally incident pulsed plane wave. Bloch periodic boundary condition is applied in x and y direction to realize the infinite structure. In the z direction, PML (perfectly matched layer) is applied to inhibit parasitical reflections on the computational window borders. Specular transmission response in the spectral domain is then calculated by making Fourier transform of the time varying electric field on the detector plane which is placed above the PhC top surface. The normalization is performed with respect to the incident signal. The spatial step size along x and y directions is uniform and it is fixed to $\Delta x = \Delta y = 30$ nm. Along the z direction, nonuniform meshing is employed to better describe the membrane thickness and to reduce the calculation time and computing memory. In order to faithfully describe the cylindrical air holes, a subgriding technique is applied to define the refractive index distribution by considering the mean value of neighboring cells. This generates a gradual change in the refractive index distribution helping to avoid spurious numerical dispersion due to abrupt changes in the index distribution staircase effect.

Transmission simulations on finite thickness start with the parameters determined from PWE calculations on square and rectangular lattice structure. The results are shown in Fig. 4.13 (a). Let us first have a look at the transmission curves corresponding to the square lattice structure (the dashed green, dashed blue and solid red curves in Fig. 4.13 (a)). As expected, there is no resonance mode appearing in the IR wavelength regime in the dashed green and the dashed blue curves cases (corresponding to parameters of a = 410 nm, r = 206 nm, t = 700 nm and a = 560 nm, r = 151 nm, t = 700 nm respectively). When a increases to 900 nm (solid red curve), resonance modes appear in the vicinity of 1.55 μm. Nevertheless, the resonance modes are close to each other with small

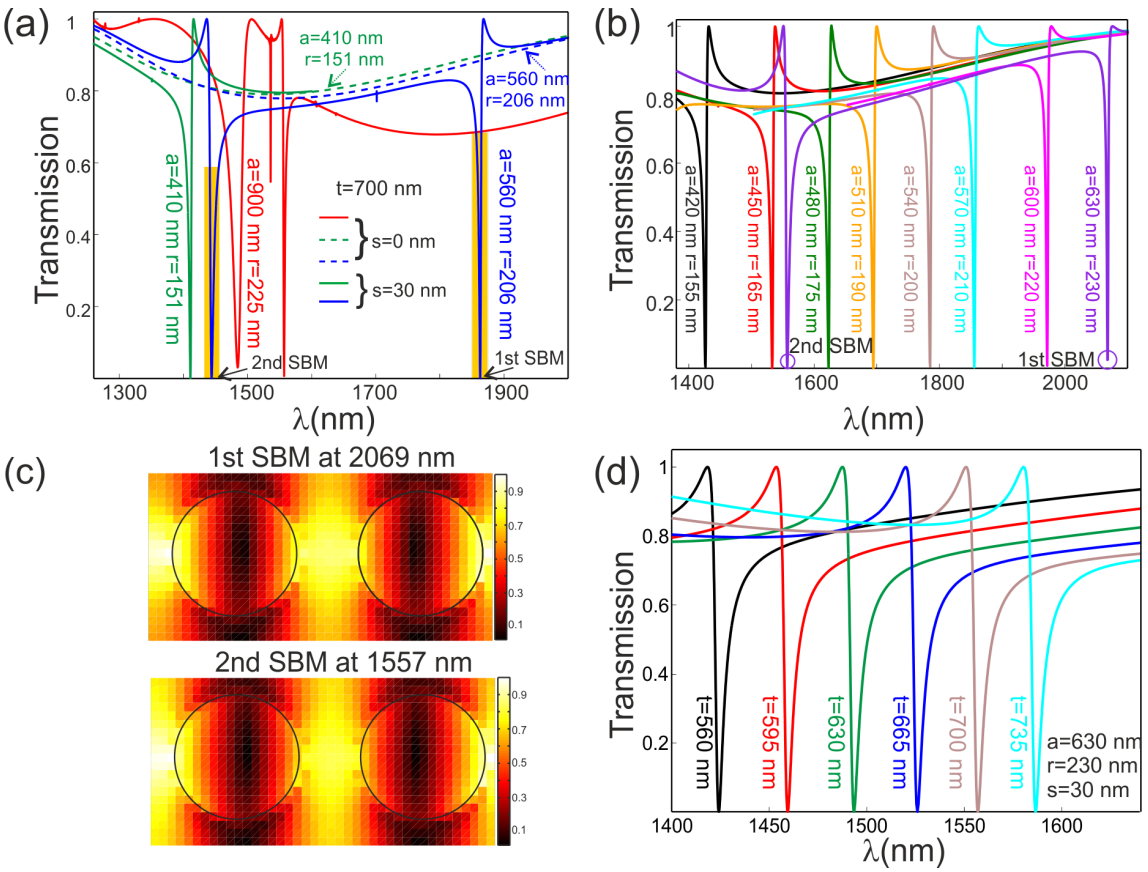

FIGURE 4.13 – (a) Normalized transmission spectra for square and rectangular infinite structures. Dashed blue, green and solid red curves correspond to square lattice structures. Solid blue and green curves correspond to rectangular structures with parameters calculated from PWE prediction to set the two SBMs operating at 1.55 μm. The modes in solid blue curve under highlighted orange rectangles are the folded two SBMs due to the super lattice. (b) Normalized transmission spectra of infinite rectangular structure with s = 30 nm, t = 700 nm, varying lattice constant a and the radius r. (c) Normalized electric field amplitude distribution over one unit cell calculated at 100 nm below the PhC top surface. The upper one corresponds to 1st SBM while the bottom one corresponds to 2nd SBM as indicated in Fig. 4.12(b). (d) Normalized transmission spectra for a = 630 nm, r = 230 nm, s = 30 nm, varying t.

frequency separation (for instance, there is only 21 nm separation in the resonance dip wavelength of the lowest two modes) between each other which is in good agreement with PWE calculations (Fig. 4.11(c)). Now let us investigate the rectangular lattice with s = 30 nm. The results are shown in the solid green and solid blue curves in Fig. 4.13(a), where two resonance dips (highlighted in orange rectangles) with zero to unity transmission and with large inter mode frequency separation appear in the IR zone which is not occupied by any mode in the square lattice case. Due to the finite thickness

of the structure, the λ_{res} shifts to a smaller wavelength value (about 100 nm) with respect to PWE results, making the simulations in 3D essential in order to obtain accurate results that address the experimental constraints.

Simulations varying lattice constant *a* are conducted in order to set λ_{res} into the vicinity of 1.55 μm for a slab thickness of *t* = 700 nm. Results are shown in Fig. 4.13 (b) with lattice constant *a* varying from 420 nm to 630 nm by a step of 30 nm while keeping *f* around 0.368 for a fixed value of *t* = 700 nm and *s* = 30 nm. The radius *r* employed in the simulations is specified in Fig. 4.13 (b). As the lattice constant *a* increases, the resonance wavelength λ_{res} shifts to larger frequency values. We can see that one set of parameters *a* = 450 nm and *r* = 165 nm yield λ_{res} to 1533 nm which corresponds the 1st SBM in Fig. 4.11(e). Parameter values of *a* = 630 nm, *r* = 230 nm yield λ_{res} to 1557 nm which corresponds to the 2nd SBM in Fig. 4.11(e).

The electric field distributions of the two purple encircled SBMs (Fig. 4.13 (b)) are shown in Fig. 4.13 (c). They are obtained by two continuous wave calculations at the transmission dip wavelength of 1557 nm and 2069 nm respectively. The top figure corresponds to the 1st SBM mode at 2069 nm, while bottom figure corresponds to the 2nd SBM mode at 1557 nm. We can clearly see that these two SBMs are dielectric modes for which electric fields are strongly confined in the LN material with a minimum electric field intensity centered on the air holes.

Studies of the robustness of SBMs with respect to fabrication imperfections are also conducted by varying the thickness *t* and the hole conicity θ. Fig. 4.13(d) depicts transmission studies of the structure for parameter values of *a* = 630 nm, *r* = 230 nm, *s* = 30 nm, varying *t* from 560 nm to 735 nm by a step size of 35 nm. As *t* increases, the resonance dip position shifts to larger wavelength values. Fig. 4.14(a) shows the normalized transmission study as a function of the hole angle, where θ is varied from 0° to 2.4°. Conical angle definition is schematically shown in Fig. 4.12 (c). The θ is calculated by $\arctan((0.5(d_1 - d_2)/t$), where the fixed parameters are *t* = 700 nm and $d_1 = 460$ nm. d_2 is varied to define different angle values.

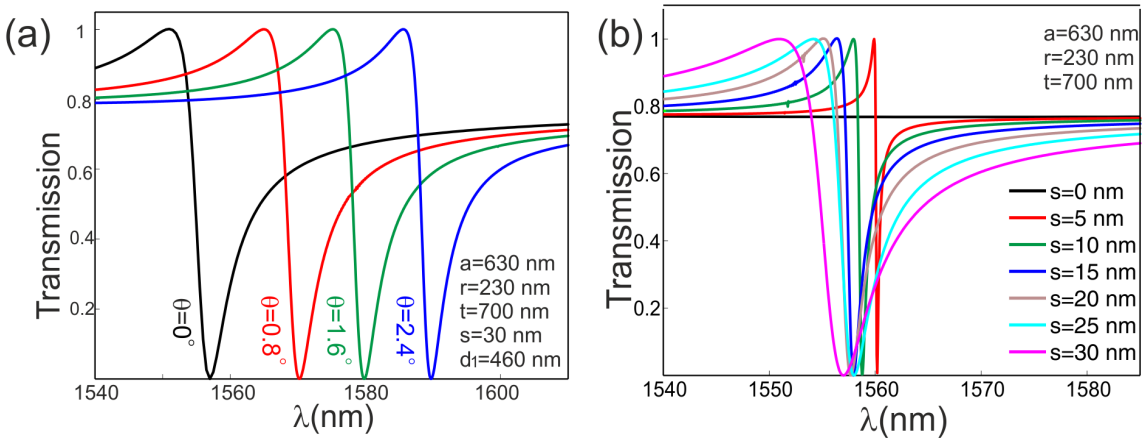

FIGURE 4.14 – (a) Normalized transmission spectra for a = 630 nm, r = 230 nm, s = 30 nm, t = 700 nm, varying θ. (b) Normalized transmission spectra for a = 630 nm, r = 230 nm, t = 700 nm, varying s.

Hole conicity introduces a red shift of the resonance wavelength (1° induces approximately a 10 nm shift) and a slight broadening of the resonance linewidth. Nevertheless, we can conclude that the existence of the resonance is robust under thickness variation and hole conicity which are often unavoidable in fabrication processes.

Studies varying the shift value s were also conducted as shown in Fig. 4.14(b). For s=0, the structure corresponds to that of a square lattice (black curve in Fig. 4.14 (b)), no resonance mode appears in the transmission spectra. The parameter s has negligible effect on the resonance wavelength λ_{res} and ER. As s decreases, the resonance linewidth gets narrower, yielding a higher Q value of the resonance.

3D-FDTD transmission spectra analysis of finite PhC structure

In order to realize the proposed structure, the actual size of the PhC has to be determined (which will be quantified by the number of air hole rows N). Simulations are performed by replacing the Bloch periodic boundary condition in the xy plane in the case of infinite structure by PML as absorbing boundary conditions. The structure is illuminated by a Gaussian beam with beam waist of half the size of the PhC. The near field time varying electromagnetic (EM) field is recorded by putting a detector above the PhC top surface. The EM

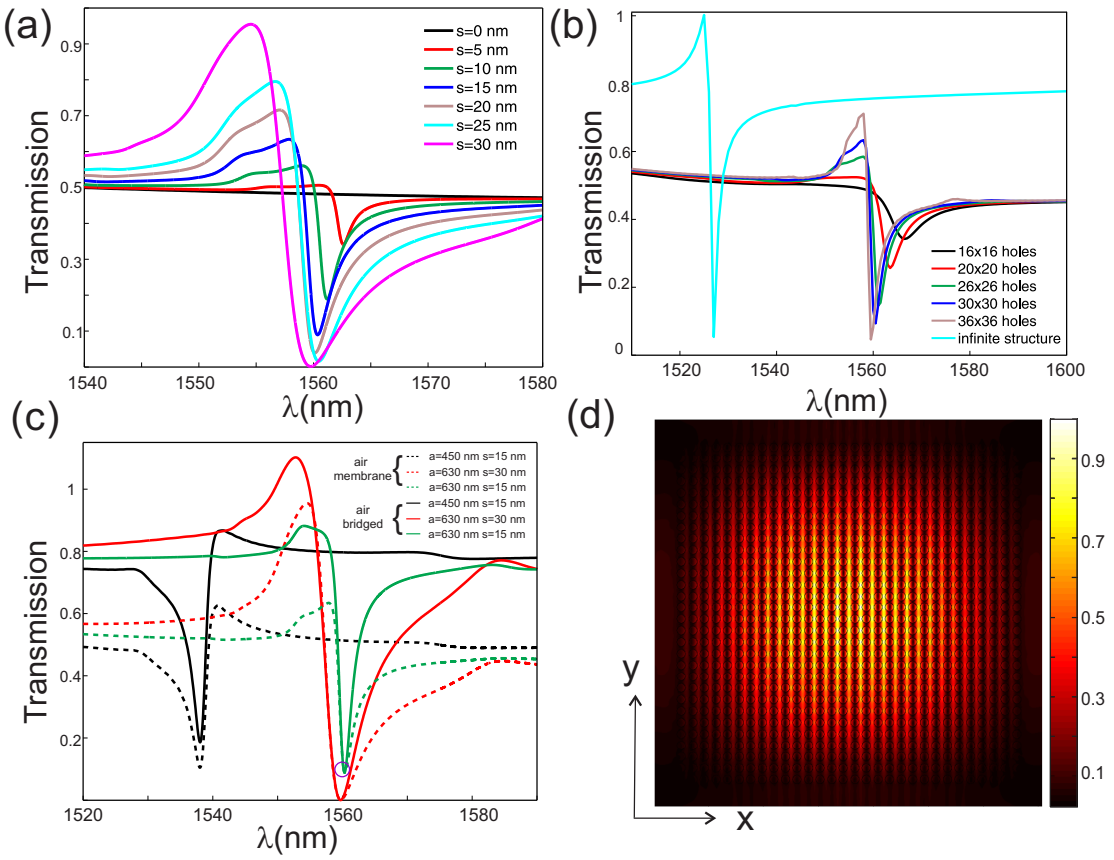

FIGURE 4.15 – (a) Normalized transmission spectra of a finite PhC size air membrane rectangular lattice structure with N = 30, a = 630 nm, r = 230 nm, t = 700 nm as fixed parameters and s being the parameter that varies. (b) Normalized transmission spectra of air membrane rectangular structure of a = 630 nm, r = 230 nm, t = 700 nm, s = 15 nm and varying N. (c) Normalized transmission spectra of air membrane and air bridged structure of N = 30, t = 700 nm for three different configurations (see inset for geometrical parameters). (d) Normalized electric field amplitude distribution of purple circled resonance mode in Fig. 4.15 (c) which corresponds to air bridged structure with a = 630 nm, r = 230 nm, s = 15 nm, N = 30 and t = 700 nm.

field is then processed through Fourier transformation to calculate the specular transmission where the normalization is done by the corresponding incident signal.

Finite size PhC on both air membrane (Fig. 4.12(d)) and air bridged (Fig. 4.12(e)) configurations are studied with 3D-FDTD. The air membrane structure consists of a 700 nm thickness TFLN on 1.2 μm thickness silica buffer layer bonded on LN substrate. The air membrane is formed by opening a square region in silica layer under the PhC region with a side length of 600 nm larger than the size of PhC.

Air membrane structure calculations are conducted by varying the

shift hole position *s* and the number of rows *N*. The thickness of TFLN and buffer layer silica are fixed at 700 nm and 1.2 μm respectively according to the wafer specifications provided by NANOLN [95]. The 3D infinite structure calculations show that two couple of parameters ((a = 450 nm, r = 165 nm) and (a = 630 nm, r = 230 nm)) can set the 1st SBM and 2nd SBM to operate at the vicinity of 1.55 μm respectively. Considering a PhC size *N* of 30 (empirically large enough to excite the resonance modes), then cross section areas of 13 μm $\times$ 13 μm and 19 μm $\times$ 19 μm are required to excite the 1st SBM and the 2nd SBM respectively. Nevertheless, a larger lattice constant *a* yields a larger air hole space which is easier for fabrication. Henceforth, the structure parameters in finite size PhC simulations are mainly performed for lattice constant of a = 630 nm and r = 230 nm configuration.

In Fig. 4.15 (a), the finite air membrane PhC structure with parameters t = 700 nm, N = 30, a = 630 nm, r = 230 nm is studied by varying *s* from 0 (square lattice) to 30 nm by a step size of 5 nm. The λ_{res} corresponding to the 2nd SBM occurs at the same value (around 1560 nm) as for the infinite PhC case. The parameter *s* has a negligible effect on the position of λ_{res} similar to that in infinite structure studies (Fig. 4.14 (b)). Nevertheless the shift parameter *s* can tune the ER and the Q value of the resonance. The ER of the resonance mode degrades as *s* decreases while the resonance line width gets narrower, implying a higher Q value. For sensing applications where high ER and Q value are required, s = 15 nm could be a good compromise. Fig. 4.15 (b) depicts the normalized transmission of the air membrane structure for the parameters t = 700 nm, a = 630 nm, r = 230 nm, s = 15 nm while varying the PhC size (*N*) as 16, 20, 26, 30, 36 and infinite. The smaller the *N*, the smaller the ER and the broader the resonance linewidth. Henceforth, PhC size *N* can also be used to tune the ER and the Q value of the resonance mode. For applications requiring high ER and Q as well as a compact size, N = 30 and s = 15 nm could be a good compromise.

Air membrane structures, compared to air bridged structures, are more amenable for fabrication and manipulation since they only require PhC milling and wet etching processes. On the other hand, TFLN air bridged structures are still difficult but feasible if the LN thin

film is bonded on materials such as silicon that can be easily etched. One can open a square window from the back side of the substrate in order to get a self suspended TFLN air bridged type structure. Henceforth, we conduct simulations on finite size of air bridged PhC and compare them to air membrane structures as shown in Fig. 4.15 (c). The dashed lines correspond to air membrane structures while solid lines correspond to air bridged structures. Black lines correspond to structures with lattice constant a = 450 nm and s = 15 nm, red lines correspond to structures with lattice constant a = 630 nm and s = 30 nm, while green curves correspond to structure with lattice constant a = 630 nm and s = 15 nm. All the curves in Fig. 4.15(c) have been obtained by setting N = 30 , t = 700 nm. As far as the properties of the resonance mode such as ER and Q value are concerned, air bridged structures show superior performance than the same configuration but in air membrane. Concerning the fabrication difficulties, the air membrane structure is more preferable and mechanically more stable because it is bonded on a substrate. Fig. 4.15(d) shows the electric field amplitude distributions for the purple circled resonance mode in Fig. 4.15(c) which is recorded 100 nm below the PhC top surface (inside LN material). The black circles correspond to the air hole positions. We can see nodal planes (zero electric field) formed in the middle of the air holes expelling light out towards the LN material, thus enhancing the light confinement in LN.

4.3.1.3/ SENSITIVITY ANALYSIS

In order to exploit the largest EO effect, the largest electric field component in the optical mode and the largest E-field component to be measured are overlapped with r_{33} which is along the z crystalline direction thus making the sensor exhibiting anisotropic characteristics.

In rectangular GR structure, E_y ((see Fig. 4.15 (d)) is the major electric field of the excited mode, thus the z crystalline direction should be oriented along the y direction in order to exploit the largest EO effect. Consequently, X or Y-cut wafers of LN can be considered for the experimental realization.

As it has been presented in the sensitivity of SPL PhC GR structure, the sensitivity analysis by $\overline{f_{opt}}$ overestimate the sensitivity compared to that of experimental measurements. Nevertheless, the $\overline{f_{opt}}$ can still give a correct trend of sensitivity performance in order to narrow down the parameter search space. Henceforth, the $\overline{f_{opt}}$ is first calculated to see the predicted trend for sensitivity performance with respect to geometrical parameters. The sensitivity is then accurately analyzed with local field factor $f_{opt}(x, y, z)$.

Table 4.3 depicts $\overline{f_{opt}}$ and Q of the resonance in infinite air bridged PhC structure of fixed parameters with *a* = 630 nm, *r* = 230 nm, *t* = 700 nm, varying with *s* from 5 to 30 nm. Notice that in infinite structure case, the ER is from zero to unity as shown in Fig. 4.14(b). Table 4.3 depicts that resonance Q increases as *s* decreases. $\overline{f_{opt}}$ in these infinite structures monotonously increases with a smaller *s* which implies that a smaller *s* might yield a higher sensitivity. Though the field confinement factor $\overline{f_{opt}}$, Q and the ER of the resonance mode will have some penalty in the corresponding finite structure, one can still approach this enhancement by fabricating large structures.

TABLE 4.3 – Resonance Q and $\overline{f_{opt}}$ varies for different *s* quantities

s(nm)	5	10	15	20	25	30
Q	15681	3444	1514	854	546	384
$\overline{f_{opt}}$	42.3	24.2	17.2	13.3	10.9	9.8

As demonstrated in sensitivity analysis of SPL based T-sensor, a more accurate $\Delta\lambda_{res}$ sensitivity is modeled by calculating $f_{opt}(x, y, z)$ of each cell enabling a better description of inhomogeneous field enhancement distribution along the structure.

In order to theoretically analyze the $\Delta\lambda_{res}$ sensitivity with respect to the measurand, $f_{opt}^2(x, y, z)$ is integrated to quantify the light enhancement induced effective EO coefficient r_{33}^{eff}. Consequently, the $r_{33}^{eff}(x, y, z)$ can be quantified as follows :

$$r_{33}^{eff}(x, y, z) = f_{opt}^2(x, y, z) r_{33} \tag{4.4}$$

The corresponding induced local variation of refractive index in PhC structure can be expressed as :

$$\Delta n(x, y, z) = -\frac{1}{2} n_e^3 f_{opt}^2(x, y, z) r_{33} E_z \tag{4.5}$$

The E-field sensor device sensitivity (i.e. the minimum detectable E-field) depends on the $\Delta\lambda_{res}$ sensitivity with respect to the E-field, the resolution of the OSA (Optical Spectrum Analyzer) and the E-field enhancement from the antenna effect (if suitable electrodes are designed)[4, 248]. In the following we theoretically analyze the $\Delta\lambda_{res}$ sensitivity and taking some assumptions into account, the minimum detectable E-field employing the proposed rectangular GR structure as E-field sensor is deduced. The $\Delta\lambda_{res}$ sensitivity is analyzed first by conducting 3D-FDTD CW numerical calculations at resonance dip wavelengths to obtain the $f_{opt}(x, y, z)$ distribution. Next, different E_z values are assumed and substituted into Eq. 4.5 in order to obtain $\Delta n(x, y, z)$. Then 3D-FDTD transmission calculations are performed by including the refractive index variation in the description of the structure in order to estimate the $\Delta\lambda_{res}$.

Let us first investigate the $\Delta\lambda_{res}$ sensitivity of infinite PhC structures. Infinite structure sensitivity results for two couple of configurations that yield λ_{res} near the vicinity of 1.55 μm are shown in Fig. 4.16. Different curves correspond to different *s* values.

We can see that λ_{res} changes quasi linearly with respect to E-field. The $\Delta\lambda_{res}$ sensitivity is analyzed by calculating $\Delta\lambda_{res}/E_z$ between each neighboring data points, then the mean value is taken to represent its sensitivity. We can see that the smaller the *s*, the higher the sensitivity as it can be seen from the steeper slope of the curves where the same trend of how *s* varies with sensitivity has been predicted from the $\overline{f_{opt}}$ calculation in Table. 4.3.

In Fig. 4.16 (a), *s*=5 nm (cyan dashed curve) for *a* = 630 nm configuration yields a sensitivity around 0.4 pm/V, while it decreases down to 0.017 pm/V (green dashed curve) for an *s*=30 nm. The same *s* value with configurations of *a* = 450 nm (corresponds to the 1st SBM) yield a better sensitivity, with 1.2 pm/V for *s*=5 nm and 0.023 pm/V for *s*=30 nm as shown in Fig. 4.16(b). The higher sensitivity achieved with the configuration of the 1st SBM (*a*= 450 nm) than the 2nd SBM is due to its slower group velocity as it can be deduced from the flatter curvatures of Fig. 4.11 (e).

Now let us investigate the $\Delta\lambda_{res}$ sensitivity of finite PhC structures. Due to the heavy computational burden of the finite structure cal-

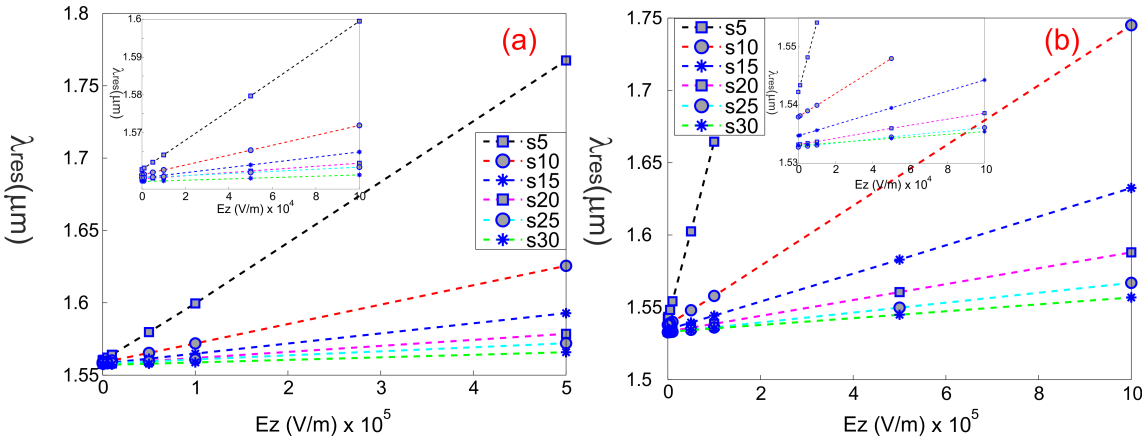

FIGURE 4.16 – Numerically calculated plot showing the λ_{res} as a function of the E-field (the insets show the zoom view of the first few data points) for infinite PhC air bridged structure with parameters of (a) *a* = 630 nm, *r* = 230 nm, *t* = 700 nm and varying *s*. (b) *a* = 450 nm, *r* = 165 nm, *t* = 700 nm and varying *s*.

culations, sensitivity study with respect to different E-field values is only carried out for structures with parameters of *a* = 630 nm, *r* = 230 nm, *s*= 30 nm, *t* = 700 nm and *N* = 30 corresponding to the 2nd SBM. The counterpart of 1st SBM yields a higher GR quality factor Q.

The corresponding $\Delta\lambda_{res}$ sensitivity results are tabulated in Table 4.4. The $\Delta\lambda_{res}$ sensitivity satisfies a quasi-linear relationship with a mean sensitivity value of 0.0028 pm/(V/m). Studies for $E_z = 5 \times 10^3$ V/m are carried out for the same structure parameters with different *s* values of 20 nm and 25 nm. The estimated sensitivity is 0.007 and 0.0045 pm/(V/m) respectively. These results show that a smaller *s* in finite structure case also yield a higher sensitivity. The $\Delta\lambda_{res}$ sensitivity in a finite structure with size of N=30 drops at around 16% of that corresponding to an infinite case.

TABLE 4.4 – Resonance dip wavelengths shift with respect to different E_z

E_z(V/m)	0	5×10^3	1×10^4	5×10^4	1×10^5	5×10^5	1×10^6
λ_{res} (nm)	1559.7	1559.72	1559.735	1559.84	1559.98	1561.1	1562.55
$\Delta\lambda_{res}$ (nm)		0.0100	0.0150	0.1050	0.1400	1.1200	1.4500
$\Delta\lambda_{res}/\Delta$Ez ($\times10^{-5}$ nm/(V/m))		0.250	0.300	0.263	0.280	0.280	0.290

Let us estimate the minimum detectable E-field with the structure parameters *a* = 450 nm, *r* = 165 nm, *t* = 700 nm, *s* = 5 nm and *N*=30. The infinite structure $\Delta\lambda_{res}$ sensitivity is 1.2 pm/(V/m). Considering the above 16% drop of sensitivity in the finite structure case,

a 0.19 pm/(V/m) $\Delta\lambda_{res}$ sensitivity is obtained. The other sensitivity dependent factors such as OSA resolution is assumed to be 0.1 pm (this is feasible in experiments such as stimulated Brillouin scattering based high resolution OSA). If the E-field sensor is designed with electrodes (small enough so that they do not disturb the E-field to be measured), an E-field enhancement from the antenna effect will further enhance the devices sensitivity. For example, assuming a bowtie antenna design as that in ref.[248], a 10^4 field enhancement can be obtained. With this field enhancement, an E-field of about 50 μV/m can generate 0.5 V/m E-field inside the feed gap of the antenna which will induce around 0.1 pm shift in λ_{res} that can be detected by the the high resolution OSA. Consequently, our designed Fano based PhC structure is estimated to be able to detect a minimum E-field as small as 50 μV/m.

In retrospect, band diagram modeling and 3D-FDTD transmission investigations are employed in order to design a Fano resonance based on TFLN rectangular lattice PhC structure. The introduced parameter shift value *s* can add more freedom to tune the resonance Q value, ER and to enable the coupling of high light confinement dielectric modes. With a nodal plane cut through the middle of air columns, highly confined electric field is obtained in LN nonlinear material. This highly confined resonance mode is then combined with EO effect of LN to exploit it as a highly sensitive E-field sensor. The minimum detectable E-field can be in the scale of μV/m when it is combined with sub-picometer scale OSA and high field enhancement factor antenna electrode designs. These systematical studies of designing high Q, ER and steep slope GR on TFLN will pave the way to improve the bulk LN based devices such as filters, optical switches, sensors and modulators etc.

4.4/ GR ON OTHER TYPES OF PHC LATTICE : TRIANGULAR, CHECKERBOARD AND HONEYCOMB LATTICES

In order to demonstrate other possibilities of exciting GR on different kinds of PhC lattices, numerically calculations of triangular lattice, checkerboard lattice and honeycomb lattice on TFLN are presen-

ted. These studies are performed with infinite structures and the geometrical parameters are not optimized.

4.4.1/ GR ON TRIANGULAR LATTICE

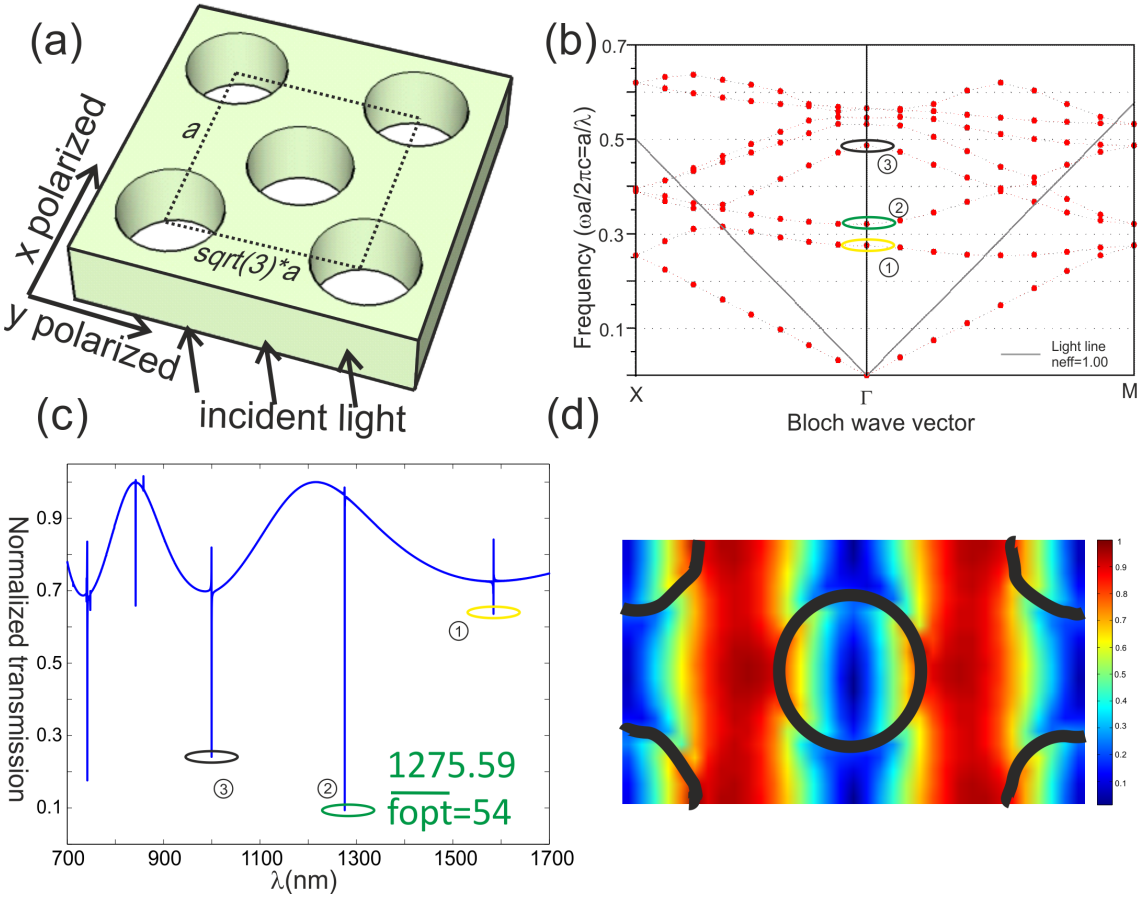

FIGURE 4.17 – (a) Sketch of the triangular lattice PhC on TFLN. The dashed rectangle presents the unit cell considered in the simulation. The black arrow indicates the direction of the incident light. (b) Band diagram for triangular lattice structure in (a) with electric field lies in the xy plane and a filling factor f of 0.3. The interested three lowest order SBMs in Γ point are circled out at normalized frequency of 0.274, 0.3198 and 0.487 respectively. (c) 3D-FDTD simulated normalized zero order transmission of the infinite PhC under y-polarized incident light. The three resonance dips circled out in the transmission curve correspond to the modes that are encircled in the band diagram in (b). (d) Color map of xOy cross section electric field amplitude distribution of one PhC cell recorded at 100 nm below the PhC top surface inside the LN material under CW simulations at 1276 nm. The black contours show the air hole patterns.

An infinite structure of triangular lattice PhC structure, as shown in Fig. 4.17(a), is studied by both PWE dispersion diagram calculations and 3D-FDTD transmission calculations. The 2D PWE calcu-

lation is performed with a unit cell as the dashed rectangle shown in Fig. 4.17(a) with a filling factor of 0.3. The corresponding dispersion curve is shown in Fig. 4.17(b) where the three lowest order modes are circled out in the Γ point above the light line. They lie at the normalized frequency of a/λ = 0.274, 0.3198 and 0.478 respectively. The 3D-FDTD transmission investigations are then performed on a 700 nm thick TFLN with the PhC pattern studied in the band diagram calculations. The result is shown in Fig. 4.17(c) from which we can see that the three lowest order modes in the Brillouin center are efficiently excited and they are visible in the transmission spectra. The CW simulations at λ of 1276 nm, corresponding to the second lowest order mode circled in green ellipse in the transmission curve, are performed. The EM field distribution at 100 nm above the PhC top surface is recorded and shown in Fig. 4.17(d). As we can see, this mode corresponds to a dielectric mode where most of the light is confined in the LN material.

4.4.2/ GR ON CHECKERBOARD LATTICE

A checkerboard lattice PhC structure consists of a similar unit cell as that of a triangular lattice as shown in Fig. 4.18(a). The air hole diameters d_2 in the center is bigger than others while the hole diameter d_1 in the corners is smaller. The PWE dispersion diagram calculation result with the structure parameters of a=1018 nm, d_2= 350 nm and d_2= 450 nm is shown in Fig. 4.18(b). As we can see, the modes (both single degenerated and double degenerated modes) in the Γ point Brillouin zone center are separated with small frequency separations.

The 3D-FDTD transmission investigation is then performed on a 700 nm thick TFLN with the PhC pattern studied in the band diagram calculations. The result is shown in Fig. 4.18(c) from which we can see the same behavior of the modes predicted from PWE calculation in the transmission spectra. The mode field distribution of the lowest order mode which lies at 1704 nm (corresponding to the green circled mode in Fig. 4.18 (b) and (c)) is calculated by CW 3D-FDTD simulation. The recorded EM field distribution at 100 nm above the PhC top surface is shown in Fig. 4.18(d). As we can see this mode

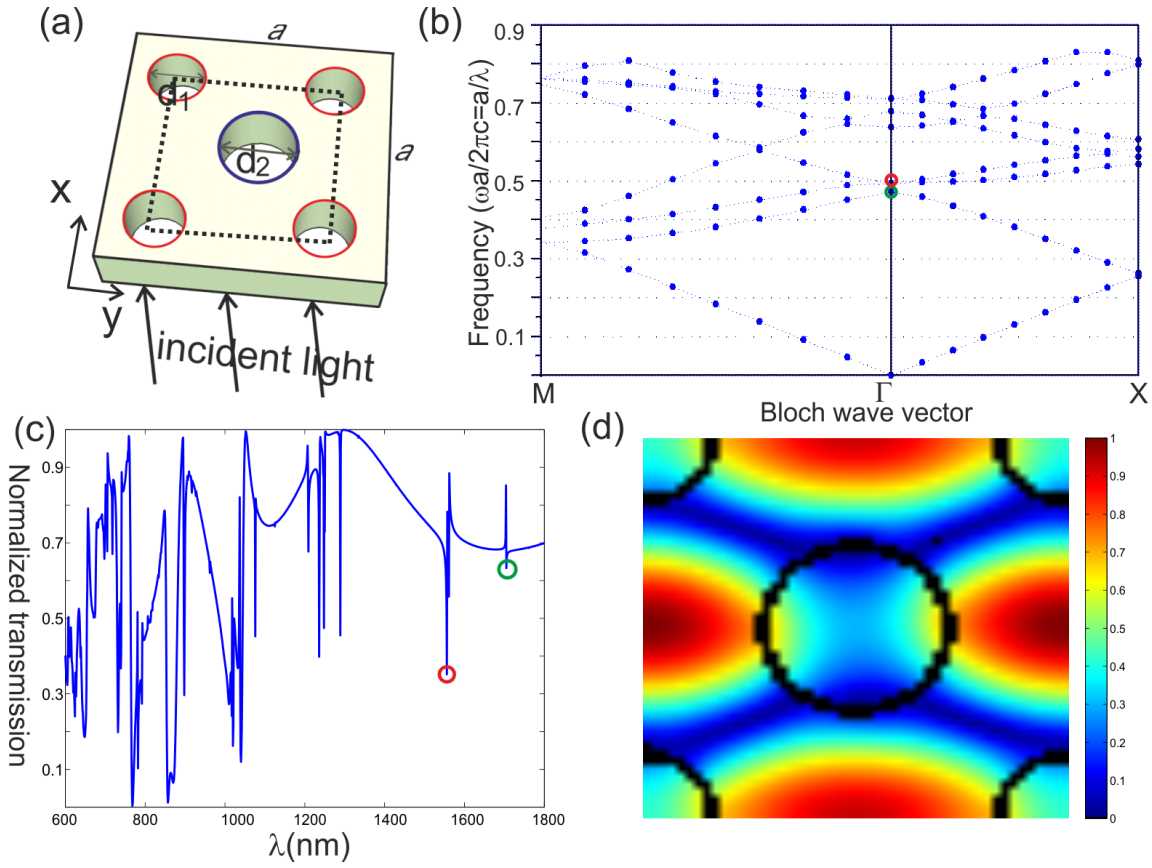

FIGURE 4.18 – (a) Sketch of the checker board lattice PhC on TFLN. The dashed rectangle presents the unit cell considered in the simulations. The black arrow indicates the direction of the incident light. (b) Band diagram for checker board lattice PhC structure in (a) with electric field lies in the xy plane and the structure parameters are a= 1018 nm, d_1= 350 nm, d_2=450 nm. The interested two lowest order SBMs in Γ point are circled out at normalized frequency of 0.4715 and 0.494 respectively. (c) 3D-FDTD simulated normalized zero order transmission of the infinite PhC under y-polarized incident light. Two resonance dips circled out in the transmission curve correspond to the modes that are encircled in the band diagram in (b). (d) Color map of xOy cross section electric field amplitude x component distribution of one PhC cell recorded at 100 nm below the PhC top surface inside the LN material under CW simulations at 1704 nm. The black contours show the air hole patterns.

corresponds to a dielectric mode where light is confined in the LN material.

4.4.3/ GR ON HONEYCOMB LATTICE

A honeycomb lattice PhC structure as shown in Fig. 4.19(a) is also studied by PWE and 3D-FDTD transmission calculations. The unit cell considered in the calculations is shown in the dashed rectangle

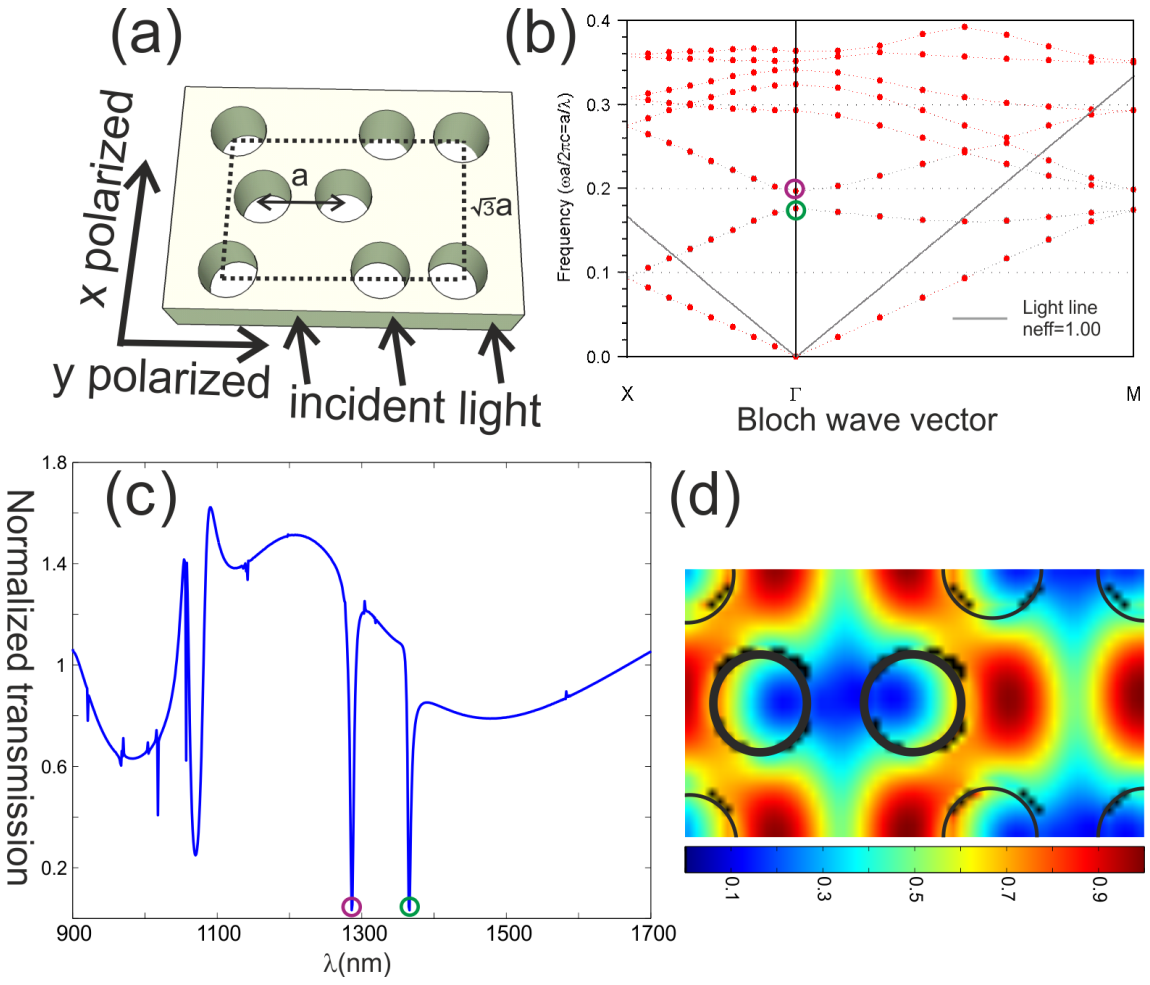

FIGURE 4.19 – (a) Sketch of the honeycomb lattice PhC on TFLN. The dashed rectangle presents the unit cell considered in the simulations. The black arrow indicates the direction of the incident light. (b) Band diagram for honeycomb lattice structure in (a) with electric field lies in the xy plane and a filling factor *f* of 0.34. The interested two lowest order SBMs in Γ point are circled out at normalized frequency of 0.176 and 0.1973 respectively. (c) 3D-FDTD simulated normalized zero order transmission of the infinite PhC under y-polarized incident light. Two resonance dips circled in the transmission curve correspond to the modes that are encircled in the band diagram in (b). (d) Color map of xOy cross section electric field amplitude distribution of one PhC cell recorded at 100 nm below the PhC top surface inside the LN material under CW simulations at 1276 nm.

in Fig. 4.19(a) with air hole filling factor of 0.34. The PWE dispersion diagram result is shown in Fig. 4.19(b) where the two lowest order mode are circled out in the Γ point of Brillouin zone center. The corresponding 3D-FDTD transmission spectra with a 700 nm thick TFLN is shown in Fig. 4.19(c) from which we can see the same behavior of the modes predicted from PWE calculation in the transmission spectra. Two resonance dips highlighted in the transmission curve correspond to the the two modes encircled in the band

diagram.

The mode field distribution of the second lowest order mode lies at 1276 nm (corresponding to the purple circled out mode in Fig. 4.19 (b) and (c)) is calculated by CW 3D-FDTD simulations. The recorded EM field distribution at 100 nm above the PhC top surface are shown in Fig. 4.19(d). As we can see that this mode corresponds to a dielectric mode where light is confined in the LN material.

4.5/ CHAPTER SUMMARY

Guided resonances (GR) characterizing with both high Q and high ER are studied on TFLN with different PhC lattices. The design is carried out by 2D PWE band diagram engineering and transmission investigations implemented by home-made 3D-FDTD algorithms.

A SPL GR based temperature sensor is experimentally and theoretically demonstrated presenting 38 fold enhancement of EO effect in a compact size of 25μm $\times$ 24μm cross section. A local field factor that is calculated locally in each FDTD cell is for the first time proposed to accurately analyze the sensitivity of the structure with the essential idea of replacing a single averaged field factor to local field factor distributions in order to better describe the ensemble effect where each local refractive index variation element contribution is taken into account. Good agreement between experimental measurements and the numerical prediction is achieved.

Detailed numerical investigations on rectangular lattice PhC with a shift value *s* of the neighboring air hole position have been demonstrated to be able to tune the resonance Q value, ER and to enable the coupling of high light confinement dielectric modes. When the rectangular lattice GR is associated with sub-picometer optical spectrum analyzer and high field enhancement antenna design, an E-field probe with a sensitivity of 50 μV/m could be achieved.

Finally the widely existence of GR effect in all kinds of PhC lattice are demonstrated from the simulations on triangular lattice, checkerboard lattice and honeycomb lattice.

5

Conclusion and Outlook

Conclusion

Theoretical analysis by numerical simulations, fabrication and optical characterization of PhC devices on thin film lithium niobate have been studied in this thesis. The PhC structures are designed to yield resonances in the transmission or reflection spectra at the vicinity of 1.55 μm. These resonances are then employed for sensing applications by combining the EO effect of LN material through wavelength interrogations of the resonance wavelength. In order to have high sensitivity, high Q and high extinction ratio resonance properties are desired. Two types of structures are studied in this thesis : on-chip sensors and on fiber end sensors. In the study of on-chip sensors, the main results are summarized as follows :

— Different nanometric WG configurations (ridge WG, strip loaded WG, slot WG and double slot WG) are systematic studied by evaluating their light confinement factor. Slot WG yields the highest light confinement ability among all the studied WG configurations. Strip loaded WG, where LN does not need to be etched, is an easier WG geometry for structure realizations considering the constrains of current nano fabrication technology in this material.

— Slot WGs are designed with 1-D PhC structure Bragg gratings with an ultra compact size (0.5 μm $\times$ 0.7 μm $\times$ 6μm). A moderate Q (about 300) of the F-P like cavity where the mirrors are made of PhC is achieved with ER about 70%.

— Strip loaded WG are designed with 2-D PhC of triangular air holes pattern. These PhCs are designed to yield a resonance

in the transmission spectra by creating a line defect in the PhC pattern. A low Q (about 100) resonance has been achieved in the configurations of air membrane PhC cavity.
— Fabrication trials of nano-metric WG are made. However, the sidewall roughness is still a limiting factor of waveguiding in this nanometric WG.
— Fabrication of high quality Si_3N_4 strip loaded WG are presented. However, due to the attachment stability of the deposited Si_3N_4 onto the TFLN, the dicing and polishing of the input and output facets of the WG was not succeed without lifting off the Si_3N_4.

In terms of on-fiber end sensors structure study, the results are summarized as follows :

— SPL PhC has been studied and demonstrated as a temperature sensor with a sensitivity of 0.77 nm/^{o}C and a size of only 25 μm $\times$ 24 μm by the exploitation of a guided resonance.
— Guided resonances in rectangular lattice PhC, a promising structure that can be integrated onto the fiber end face, have been systematically studied through band diagram calculations, 2D and 3D-FDTD simulations. Accurate theoretical sensitivity analysis for a rectangular lattice guided resonance as an E-field sensor is carried out by a newly proposed local field factor $f_{opt}(x, y, z)$ method which is calculated cell by cell in 3D-FDTD algorithm. An E-field sensitivity of about 50 μV/m can be achieved in rectangular lattice structure.

OUTLOOK

Look back around all the modeled and fabricated devices on TFLN present in this thesis, the realizations of nano-metrical devices according to the state of the art clean room technologies proved to be challenging and difficult for lithium niobate material. However, among the many structures modeled and fabrications attempts in this thesis, at this point, I would like to outline several structures that might be relatively feasible for realization in the near future :

— Slot WG yields the highest confinement factor among all the

WGs studied. Horizontal slot WG without the need of etching nanometrical LN material, seems a more feasible configuration for realization.

— Strip loaded WG with Si_3N_4 loaded material fabrication have been demonstrated in this thesis. The failure of experimental characterization of the WG is only because polishing problem of the WG input and output facets. Further trials on the parameters of Si_3N_4 deposition condition and the polishing condition might help to solve the problem and allow the detection of light guiding in strip loaded WG.

— Even though guided resonance structures are studied with the aim of having high Q and high ER properties, the versatility of the guided resonance can also be exploited in applications such as flat-top filters and lasing operations etc.

— Further fabrication and experimental exploitation on TFLN configured with the proposed GR PhC structures, air bridge PhC and on-fiber end devices could be realized.

BIBLIOGRAPHIE

[1] M. Kanda and K.D. Masterson. Optically sensed EM-field probes for pulsed fields. *Proceedings of the IEEE*, 80(1) :209–215, January 1992.

[2] Kyoung Yang, Linda PB Katehi, and J. F. Whitaker. Electric field mapping system using an optical-fiber-based electrooptic probe. *Microwave and wireless Components Letters, IEEE*, 11(4) :164–166, 2001.

[3] M Tabib-Azar, B Sutapun, T Srikhirin, J Lando, and G Adamovsky. Fiber optic electric field sensors using polymer-dispersed liquid crystal coatings and evanescent field interactions. *Sensors and Actuators A : Physical*, 84(12) :134–139, 2000.

[4] V.m.n. Passaro and F. De Leonardis. Modeling and design of a novel high-sensitivity electric field silicon-on-insulator sensor based on a whispering-gallery-mode resonator. *IEEE Journal of Selected Topics in Quantum Electronics*, 12(1) :124–133, January 2006.

[5] I W Jung, B Park, J Provine, R T Howe, and O Solgaard. Highly Sensitive Monolithic Silicon Photonic Crystal Fiber Tip Sensor for Simultaneous Measurement of Refractive Index and Temperature. *Journal of Lightwave Technology*, 29(9) :1367–1374, May 2011.

[6] Matthieu Roussey, Fadi I. Baida, and Maria-Pilar Bernal. Experimental and theoretical observations of the slow-light effect on a tunable photonic crystal. *JOSA B*, 24(6) :1416–1422, 2007.

[7] Huihui Lu, Benattou Sadani, Gwenn Ulliac, Clement Guyot, Nadge Courjal, Manuel Collet, Fadi Issam Baida, and Maria-Pilar Bernal. Integrated temperature sensor based on an enhanced pyroelectric photonic crystal. *Optics Express*, 21(14) :16311, July 2013.

[8] Pao Tai Lin, Fei Yi, Seng-Tiong Ho, and Bruce W. Wessels. Two-Dimensional Ferroelectric Photonic Crystal Waveguides : Simulation, Fabrication, and Optical Characterization. *J. Lightwave Technol.*, 27(19) :4330–4337, October 2009.

[9] L. Arizmendi. Photonic applications of lithium niobate crystals. *physica status solidi (a)*, 201(2) :253–283, January 2004.

[10] Andrey E. Miroshnichenko, Sergej Flach, and Yuri S. Kivshar. Fano resonances in nanoscale structures. *Reviews of Modern Physics*, 82(3) :2257–2298, August 2010.

[11] G. P Agrawal. *Fiber-optic communication systems*. Wiley-Interscience, New York, 2002.

[12] Pollock Clifford R. and Lipson Michal. *Integrated Photonics*. 2003.

[13] J.D. Meindl. Interconnect opportunities for gigascale integration. *IEEE Micro*, 23(3) :28–35, 2003.

[14] Lorenzo Pavesi, editor. *Silicon photonics*. Number 94 in Topics in applied physics. Springer, Berlin, 2004.

[15] Ian A. Young, Edris Mohammed, Jason T. S. Liao, Alexandra M. Kern, Samuel Palermo, Bruce A. Block, Miriam R. Reshotko, and Peter L.D. Chang. Optical i/o technology for tera-scale computing. *IEEE Journal of Solid-State Circuits*, 45(1) :235–248, January 2010.

[16] M. A. Green. Solar cells : operating principles, technology, and system applications. January 1982.

[17] Wendy U. Huynh, Janke J. Dittmer, and A. Paul Alivisatos. Hybrid nanorod-polymer solar cells. *Science*, 295(5564) :2425–2427, March 2002.

[18] Doo-Hyun Ko, John R. Tumbleston, Lei Zhang, Stuart Williams, Joseph M. DeSimone, Rene Lopez, and Edward T. Samulski. Absorption enhancement using photonic crystals for silicon thin film solar cells. *Nano Letters*, 9(7) :2742–2746, July 2009.

[19] Eberhart Zrenner. Artificial vision : solar cells for the blind. *Nature Photonics*, 6(6) :344–345, 2012.

[20] Ulrich W. Paetzold, Stephan Lehnen, Karsten Bittkau, Uwe Rau, and Reinhard Carius. Nanoscale Observation of Waveguide Modes Enhancing the Efficiency of Solar Cells. *Nano Letters*, 14(11) :6599–6605, November 2014.

[21] V.M.N. Passaro, F. Dell'Olio, and F. De Leonardis. Electromagnetic field photonic sensors. *Progress in Quantum Electronics*, 30(2-3) :45–73, January 2006.

[22] D. Runde, S. Brunken, C.E. Ruter, and D. Kip. Integrated optical electric field sensor based on a Bragg grating in lithium niobate. *Applied Physics B*, 86(1) :91–95, November 2006.

[23] Giancarlo C. Righini, Antonella Tajani, and Antonello Cutolo, editors. *An introduction to optoelectronic sensors*. Number v. 7 in Series in optics and photonics. World Scientific, Hackensack, NJ, 2009.

[24] Li Chen and Ronald M. Reano. Compact electric field sensors based on indirect bonding of lithium niobate to silicon microrings. *Opt Express*, 20(4) :4032–4038, February 2012.

[25] Rong Zeng, Bo Wang, Ben Niu, and Zhanqing Yu. Development and Application of Integrated Optical Sensors for Intense E-Field Measurement. *Sensors*, 12(8) :11406–11434, August 2012.

[26] F. Klotz. EMC test specification for integrated circuits. In *18th International Zurich Symposium on Electromagnetic Compatibility, 2007. EMC Zurich 2007*, pages 73–78, September 2007.

[27] S. Ben Dhia and A. Boyer. Long-term Electro-Magnetic Robustness of Integrated Circuits : EMRIC research project. *Microelectronics Reliability*, 53(911) :1266–1272, September 2013.

[28] Hiroyoshi Togo. Metal-free electric-field probe based on photonics and its EMC applications. *2014 International Symposium on Electromagnetic Compatibility, Tokyo*, page 662, January 2014.

[29] Kimihiro TAJIMA, Ryuichi KOBAYASHI, Nobuo KUWABARA, and Masamitsu TOKUDA. Development of Optical Isotropic E-Field Sensor Operating More than 10 GHz Using Mach-Zehnder Interferometers(Special Issue on Optical Fibers and

Devices). *IEICE transactions on electronics*, 85(4) :961–968, 2002.

[30] J B Rosolem, C F Barbosa, C Floridia, and E W Bezerra. A passive opto-electronic lightning sensor based on electromagnetic field detection for utilities applications. *Measurement Science and Technology*, 21(9) :094032, September 2010.

[31] T. Klepsch, T.d. Lindel, W. Hoffmann, H. Botterweck, B. Ittermann, and F. Seifert. Calibration of fibre-optic RF E/H-field probes using a magnetic resonance (MR) compatible TEM cell and dedicated MR measurement techniques. *Biomedizinische Technik*, 57(57) :119–122, September 2012.

[32] M. S. Fernandes, J. H. Correia, and P. M. Mendes. Electro-optic acquisition system for ECG wearable sensor applications. *Sensors and Actuators A : Physical*, 203 :316–323, December 2013.

[33] Celso Gutierrez-Martinez, Joel Santos-Aguilar, and Adolfo Morales-Diaz. On the Design of Video-Bandwidth Electric Field Sensing Systems Using Dielectric LiNbO3 Electro-Optic Sensors and Optical Delays as Signal Carriers. *IEEE Sensors Journal*, 13(11) :4196, November 2013.

[34] Fen Miao, Yayu Cheng, Yi He, Qingyun He, and Ye Li. A Wearable Context-Aware ECG Monitoring System Integrated with Built-in Kinematic Sensors of the Smartphone. *Sensors*, 15(5) :11465–11484, May 2015.

[35] Jaakko O. Nieminen, Lari M. Koponen, and Risto J. Ilmoniemi. Transcranial Magnetic Stimulation (TMS) : Experimental Characterization of the Electric Field Distribution Induced by TMS Devices. *Brain Stimulation*, 8 :582–589, May 2015.

[36] G. Meltz, W_W Morey, and W. H. Glenn. Formation of Bragg gratings in optical fibers by a transverse holographic method. *Optics letters*, 14(15) :823–825, 1989.

[37] T. Erdogan, V. Mizrahi, P. J. Lemaire, and D. Monroe. Decay of ultraviolet-induced fiber Bragg gratings. *Journal of Applied Physics*, 76(1) :73–80, 1994.

[38] Jun-long Kou, Sun-jie Qiu, Fei Xu, and Yan-qing Lu. Demonstration of a compact temperature sensor based on first-order Bragg grating in a tapered fiber probe. *Optics express*, 19(19) :18452–18457, 2011.

[39] Miroslav Chomát, Jiři Čtyrokýa, Daniela Berkováa, Vlastimil Matějeca, Jiří Kaňkaa, Jana Skokánkováa, Filip Todorov, Alexandr Jančárekc, and Petr Bittner. Temperature sensitivity of long-period gratings inscribed with a CO2 laser in optical fiber with graded-index cladding. *Sensors and Actuators B : Chemical*, 119(2) :642–650, December 2006.

[40] S. Wakana, Takuya Ohara, M. Abe, Etsushi Yamazaki, M. Kishi, and M. Tsuchiya. Fiber-edge electrooptic/magnetooptic probe for spectral-domain analysis of electromagnetic field. *IEEE Transactions on Microwave Theory and Techniques*, 48(12) :2611–2616, December 2000.

[41] J. W. Doane, A. Golemme, J. L. West, J. B. Whitehead Jr, and B.-G. Wu. Polymer Dispersed Liquid Crystals for Display Application. *Molecular Crystals and Liquid Crystals Incorporating Nonlinear Optics*, 165(1) :511–532, 1988.

[42] Simoni Francesco. *Nonlinear Optical Properties of Liquid Crystals and Polymer Dispersed Liquid Crystals*. World Scientific Pub Co Inc, October 1997.

[43] Sergei Bronnikov, Sergei Kostromin, and Vjacheslav Zuev. Polymer-Dispersed Liquid Crystals : Progress in Preparation, Investigation, and Application. *Journal of Macromolecular Science, Part B*, 52(12) :1718–1735, December 2013.

[44] C. Fernandez-Valdivielso, I. R. Matias, M. Gorraiz, F. J. Arregui, C. Bariain, and M. Lopez-Amo. Low cost electric field optical fiber detector. In *Optical Fiber Sensors Conference Technical Digest, 2002. Ofs 2002, 15th*, pages 499–502 vol.1, May 2002.

[45] J. Kee P. Koo and G. H. Sigel. An Electric Field Sensor Utilizing a Piezoelectric Polyvinylidene Fluoride (PVF/sub 2/) Film in a Single-Mode Fiber Interferometer. *IEEE Transactions on Microwave Theory and Techniques*, 30(4) :516–521, April 1982.

[46] K. Kawano, M. Kohtoku, M. Ueki, T. Ito, S. Kondoh, Y. Noguchi, and Y. Hasumi. Polarisation-insensitive travelling-wave

electrode electroabsorption (TW-EA) modulator with bandwidth over 50 GHz and driving voltage less than 2 V. *Electronics Letters*, 33(18) :1580–1581, August 1997.

[47] R. Heinzelmann, A. Stohr, M. Groz, D. Kalinowski, T. Alder, M. Schmidt, and D. Idger. Optically powered remote optical field sensor system using an electroabsorption-modulator. In *Microwave Symposium Digest, 1998 IEEE MTT-S International*, volume 3, pages 1225–1228 vol.3, June 1998.

[48] S. Wakana, T. Ohara, M. Abe, E. Yamazaki, M. Kishi, and M. Tsuchiya. Novel electromagnetic field probe using electro/magneto-optical crystals mounted on optical fiber facets for microwave circuit diagnosis. In *Microwave Symposium Digest. 2000 IEEE MTT-S International*, volume 3, pages 1615–1618 vol.3, June 2000.

[49] W. Mann and K. Petermann. VCSEL-based miniaturised E-field probe with high sensitivity and optical power supply. *Electronics Letters*, 38(10) :455–456, May 2002.

[50] P. R. N. Childs, J. R. Greenwood, and C. A. Long. Review of temperature measurement. *Review of scientific instruments*, 71(8) :2959–2978, 2000.

[51] L. Michalski, K. Eckersdorf, and J. Kucharski. Temperature Measurement , 2nd Edition, 1991.

[52] D. McGee Thomas. Wiley : Principles and Methods of Temperature Measurement - D. McGee, 1998.

[53] M. McSherry, C. Fitzpatrick, and E. Lewis. Review of luminescent based fibre optic temperature sensors. *Sensor Review*, 25(1) :56–62, March 2005.

[54] R. M. Measures. Structural Monitoring with Fiber Optic Technology, 1st Edition | Raymond Measures | ISBN 9780080518046, 2001.

[55] Cusano A., Cutolo A., Arregui F.J., and Giordano M. *Optochemical Nanosensors*. CRC Press, Boca Raton, FL, 1 edition edition, November 2012.

[56] Andrea Cusano, Antonello Cutolo, and Jacques Albert, editors. *Fiber Bragg Grating Sensors : Recent Advancements,*

Industrial Applications and Market Exploitation. BENTHAM SCIENCE PUBLISHERS, March 2012.

[57] A. Ricciardi, M. Consales, G. Quero, A. Crescitelli, E. Esposito, and A. Cusano. Lab-on-Fiber devices as an all around platform for sensing. *Optical Fiber Technology*, 19(6) :772–784, December 2013.

[58] A. Yariv. Coupled-mode theory for guided-wave optics. *IEEE Journal of Quantum Electronics*, 9(9) :919–933, September 1973.

[59] Turan Erdogan. Fiber grating spectra. *Lightwave Technology, Journal of*, 15(8) :1277–1294, 1997.

[60] Yange Liu, Bo Liu, Xinhuan Feng, Weigang Zhang, Guang Zhou, Shuzhong Yuan, Guiyun Kai, and Xiaoyi Dong. High-birefringence fiber loop mirrors and their applications as sensors. *Applied Optics*, 44(12) :2382–2390, 2005.

[61] Yong Zhao and Peng Gao. High-sensitive temperature sensor based on an alcohol-filled HiBi photonic crystal fiber loop mirror. *Microwave & Optical Technology Letters*, 56(6) :1334–1337, 2014.

[62] M. Roussey, M.-P. Bernal, N. Courjal, D. Van Labeke, F. I. Baida, and R. Salut. Electro-optic effect exaltation on lithium niobate photonic crystals due to slow photons. *Applied Physics Letters*, 89(24) :241110, 2006.

[63] H. Lu, B. Sadani, G. Ulliac, N. Courjal, C. Guyot, J. M. Merolla, M. Collet, F. I. Baida, and M.-P. Bernal. 6-micron interaction length electro-optic modulation based on lithium niobate photonic crystal cavity. *Opt. Express*, 20(19) :20884–20893, September 2012.

[64] Amnon Yariv and Pochi Yeh. *Optical Waves in Crystals : Propagation and Control of Laser Radiation*. Wiley-Blackwell, reprint edition, 2002.

[65] Wong K.K. *Properties of Lithium Niobate*. The Institution of Engineering and Technology, London, December 2002.

[66] Payam Rabiei, Jichi Ma, Saeed Khan, Jeff Chiles, and Sasan Fathpour. Heterogeneous lithium niobate photonics on silicon substrates. *Optics Express*, 21(21) :25573, October 2013.

[67] Rajratan Basu. Effects of graphene on electro-optic switching and spontaneous polarization of a ferroelectric liquid crystal. *Applied Physics Letters*, 105(11) :1–5, September 2014.

[68] Susbhan Das, Alessandro Salandrino, Judy Z. Wu, and Rongqing Hui. Near-infrared electro-optic modulator based on plasmonic graphene. *Optics Letters*, 40(7) :1516, April 2015.

[69] Christopher T. Phare, Yoon-Ho Daniel Lee, Jaime Cardenas, and Michal Lipson. Graphene electro-optic modulator with 30 GHz bandwidth. *Nature Photonics*, 9(8) :511–514, July 2015.

[70] Tazawa, Ying-Hao Kuo, Dunayevskiy, Jingdong Luo, Jen, Fetterman, and Steier. Ring resonator-based electrooptic polymer traveling-wave modulator. *Journal of Lightwave Technology*, 24(9) :3514–3519, September 2006.

[71] C. Koos, P. Vorreau, T. Vallaitis, P. Dumon, W. Bogaerts, R. Baets, B. Esembeson, I. Biaggio, T. Michinobu, F. Diederich, W. Freude, and J. Leuthold. All-optical high-speed signal processing with siliconorganic hybrid slot waveguides. *Nat Photon*, 3(4) :216–219, 2009.

[72] Feng Qiu, Andrew M. Spring, Feng Yu, Isao Aoki, Akira Otomo, and Shiyoshi Yokoyama. Thin TiO2 core and electro-optic polymer cladding waveguide modulators. *Applied Physics Letters*, 102(23) :233504, June 2013.

[73] R. Palmer, S. Koeber, D.l. Elder, M. Woessner, W. Heni, D. Korn, M. Lauermann, W. Bogaerts, L. Dalton, W. Freude, J. Leuthold, and C. Koos. High-speed, Low Drive-voltage Silicon-organic Hybrid Modulator Based on a Binary-chromophore Electro-optic Material. *Journal of Lightwave Technology*, 32(16) :2726–2734, 2014.

[74] Feng Qiu, Andrew M. Spring, Daisuke Maeda, Masa-aki Ozawa, Keisuke Odoi, Akira Otomo, Isao Aoki, and Shiyoshi Yokoyama. A hybrid electro-optic polymer and TiO2 double-slot waveguide modulator. *Sci. Rep.*, 5, 2015.

[75] D. M. Gill, C. W. Conrad, G. Ford, B. W. Wessels, and S. T. Ho. Thin-film channel waveguide electro-optic modulator in epitaxial BaTiO3. *Applied physics letters*, 71(13) :1783–1785, 1997.

[76] Stefan Abel, Thilo Stoferle, Chiara Marchiori, Christophe Rossel, Marta D. Rossell, Rolf Erni, Daniele Caimi, Marilyne Sousa, Alexei Chelnokov, Bert J. Offrein, and Jean Fompeyrine. A strong electro-optically active lead-free ferroelectric integrated on silicon. *Nat Commun*, 4 :1671, 2013.

[77] Stefan Abel, Thilo Stoferle, T.ferle, Chiara Marchiori, Daniele Caimi, Lukas Czornomaz, Christophe Rossel, Marta Rossell, Rolf Erni, Marilyne Sousa, Heinz Siegwart, Jens Hofrichter, Michael Stuckelberger, Alexei Chelnokov, Bert J. Offrein, and Jean Fompeyrine. Electro-Optical Active Barium Titanate Thin Films in Silicon Photonics Devices. page IW4A.5. OSA, 2013.

[78] Chi Xiong, Wolfram H. P. Pernice, Joseph H. Ngai, James W. Reiner, Divine Kumah, Frederick J. Walker, Charles H. Ahn, and Hong X. Tang. Active Silicon Integrated Nanophotonics : Ferroelectric BaTiO3 Devices. *Nano Lett.*, 14(3) :1419–1425, March 2014.

[79] Xuan Hu, Sbastien Cueff, Pedro Rojo Romeo, and Rgis Orobtchouk. Modeling the anisotropic electro-optic interaction in hybrid silicon-ferroelectric optical modulator. *Opt. Express*, 23(2) :1699–1714, January 2015.

[80] I. P. Kaminow. Lithium niobate ridge waveguide modulator. *Applied Physics Letters*, 24(12) :622, 1974.

[81] J. Sochtig, H. Schutz, R. Widmer, R. Corsini, D. Hiller, C. Carmannini, G. Consonni, S. Bosso, and L. Gobbi. Monolithically integrated DBR waveguide laser and intensity modulator in erbium doped LiNbO3. *Electronics Letters*, 32(10) :899–900, 1996.

[82] E.l. Wooten, K.m. Kissa, A. Yi-Yan, E.j. Murphy, D.a. Lafaw, P.f. Hallemeier, D. Maack, D.v. Attanasio, D.j. Fritz, G.j. McBrien, and D.e. Bossi. A review of lithium niobate modulators for fiber-optic communications systems. *IEEE Journal of Selected Topics in Quantum Electronics*, 6(1) :69–82, January 2000.

[83] R. Kim, J. Zhang, O. Eknoyan, H. F. Taylor, and T. L. Smith. Distributed Bragg feedback intensity modulator in Ti : LiNbO3. *Electronics Letters*, 41(18) :1028–1030, 2005.

[84] Yi Liao, Huijuan Zhou, and Zhou Meng. Modulation efficiency of a LiNbO_3 waveguide electro-optic intensity modulator operating at high microwave frequency. *Optics Letters*, 34(12) :1822, June 2009.

[85] R. Geiss, S. Diziain, M. Steinert, F. Schrempel, E.-B. Kley, A. Tunnermann, and T. Pertsch. Photonic crystals in lithium niobate by combining focussed ion beam writing and ion-beam enhanced etching. *Physica Status Solidi A - Applications and Materials Science*, 211(10) :2421–2425, October 2014.

[86] R. S. Weis and T. K. Gaylord. Lithium niobate : summary of physical properties and crystal structure. *Applied Physics A*, 37(4) :191–203, 1985.

[87] A. W. Warner, M. Onoe, and G. A. Coquin. Determination of Elastic and Piezoelectric Constants for Crystals in Class (3m). *The Journal of the Acoustical Society of America*, 42(6) :1223–1231, December 1967.

[88] Tomoaki Yamada, Nobukazu Niizeki, and Hiroo Toyoda. Piezoelectric and Elastic Properties of Lithium Niobate Single Crystals. *Japanese Journal of Applied Physics*, 6(2) :151–155, February 1967.

[89] R. T. Smith. Temperature Dependence of the Elastic, Piezoelectric, and Dielectric Constants of Lithium Tantalate and Lithium Niobate. *Journal of Applied Physics*, 42(6) :2219, 1971.

[90] Izumi Tomeno and Sadao Matsumura. Elastic and Dielectric Properties of LiNbO3. *J. Phys. Soc. Jpn.*, 56(1) :163–177, January 1987.

[91] J. R. Teague, R. R. Rice, and R. Gerson. High-frequency dielectric measurements on electro-optic single crystals. *Journal of Applied Physics*, 46(7) :2864, 1975.

[92] Yoshiro Ohmachi, Ken'ichi Sawamoto, and Hiroo Toyoda. Dielectric Properties of LiNbO $_3$ Single Crystal up to 9 Gc. *Japanese Journal of Applied Physics*, 6(12) :1467–1468, December 1967.

[93] A. S. Barker and R. Loudon. Dielectric Properties and Optical Phonons in LiNbO3. *Physical Review*, 158 :433–445, June 1967.

[94] I. P. Kaminow and W. D. Johnston Jr. Quantitative Determination of Sources of the Electro-Optic Effect in LiNb O 3 and LiTa O 3. *Physical Review*, 160(3) :519, 1967.

[95] nanoln.com.

[96] M. Levy, R. M. Osgood, R. Liu, L. E. Cross, G. S. Cargill, A. Kumar, and H. Bakhru. Fabrication of single-crystal lithium niobate films by crystal ion slicing. *Applied Physics Letters*, 73(16) :2293, 1998.

[97] G. Poberaj, H. Hu, W. Sohler, and P. Gnter. Lithium niobate on insulator (LNOI) for micro-photonic devices. *Laser & Photonics Reviews*, 6(4) :488–503, July 2012.

[98] Yukio Sakashita and Hideo Segawa. Preparation and characterization of LiNbO3 thin films produced by chemical-vapor deposition. *Journal of Applied Physics*, 77(11) :5995, 1995.

[99] X. Lansiaux, E. Dogheche, D. Remiens, M. Guilloux-viry, A. Perrin, and P. Ruterana. LiNbO[sub 3] thick films grown on sapphire by using a multistep sputtering process. *Journal of Applied Physics*, 90(10) :5274, 2001.

[100] F Gitmans, Z Sitar, and P Gnter. Growth of tantalum oxide and lithium tantalate thin films by molecular beam epitaxy. *Vacuum*, 46(810) :939–942, 1995.

[101] Jong-Gul Yoon and Kun Kim. Growth of highly textured LiNbO3 thin film on Si with MgO buffer layer through the sol-gel process. *Applied Physics Letters*, 68(18) :2523, 1996.

[102] Y. Nakata, S. Gunji, T. Okada, and M. Maeda. Fabrication of LiNbO3 thin films by pulsed laser deposition and investigation of nonlinear properties. *Applied Physics A*, 79(4-6), September 2004.

[103] Timothy A. Rost, He Lin, Thomas A. Rabson, Robert C. Baumann, and Daniel L. Callahan. Deposition and analysis of lithium niobate and other lithium niobium oxides by rf magnetron sputtering. *Journal of Applied Physics*, 72(9) :4336, 1992.

[104] G. Griffel, S. Ruschin, and N. Croitoru. Linear electro-optic effect in sputtered polycrystalline LiNbO3 films. *Applied Physics Letters*, 54(15) :1385, 1989.

[105] Michel Bruel. The History, Physics, and Applications of the Smart-Cut Process. *MRS Bulletin*, 23(12) :35–39, 1998.

[106] G. K. Celler and Sorin Cristoloveanu. Frontiers of silicon-on-insulator. *Journal of Applied Physics*, 93(9) :4955, 2003.

[107] M. Bruel. Silicon on insulator material technology. *Electronics Letters*, 31(14) :1201–1202, 1995.

[108] Andrea Guarino, Gorazd Poberaj, Daniele Rezzonico, Riccardo Degl'Innocenti, and Peter Gnter. Electrooptically tunable microring resonators in lithium niobate. *Nature Photonics*, 1(7) :407–410, July 2007.

[109] Gorazd Poberaj, Manuel Koechlin, Frederik Sulser, Andrea Guarino, Jaroslav Hajfler, and Peter Gnter. Ion-sliced lithium niobate thin films for active photonic devices. *Optical Materials*, 31(7) :1054–1058, 2009.

[110] A. M. Radojevic, M. Levy, R. M. Osgood, A. Kumar, H. Bakhru, C. Tian, and C. Evans. Large etch-selectivity enhancement in the epitaxial liftoff of single-crystal LiNbO[sub 3] films. *Applied Physics Letters*, 74(21) :3197, 1999.

[111] I. Szafraniak, I. Radu, R. Scholz, M. Alexe, and U. Gsele. Single-Crystalline Ferroelectric Thin Films by Ion Implantation and Direct Wafer Bonding. *Integrated Ferroelectrics*, 55(1) :983–990, May 2003.

[112] Marin Alexe, Ulrich Gsele, Robert Hull, R. M. Osgood, Jrgen Parisi, and Hans Warlimont, editors. *Wafer Bonding*, volume 75 of *Springer Series in MATERIALS SCIENCE*. Springer Berlin Heidelberg, Berlin, Heidelberg, 2004.

[113] T. Izuhara, R. Roth, R. M. Osgood Jr, S. Bakhru, and H. Bakhru. Low-voltage tunable TE/TM converter on ion-sliced lithium niobate thin film. *Electronics Letters*, 39(15) :1118–1119, 2003.

[114] A. M. Radojevic, M. Levy, H. Kwak, and R. M. Osgood. Strong nonlinear optical response in epitaxial liftoff single-crystal LiNbO[sub 3] films. *Applied Physics Letters*, 75(19) :2888, 1999.

[115] Payam Rabiei and William H. Steier. Lithium niobate ridge waveguides and modulators fabricated using smart guide. *Applied Physics Letters*, 86(16) :161115, 2005.

[116] Djordje Djukic, Guiem Cerda-Pons, Ryan M. Roth, Richard M. Osgood, Sasha Bakhru, and Hassaram Bakhru. Electro-optically tunable second-harmonic-generation gratings in ion-exfoliated thin films of periodically poled lithium niobate. *Applied Physics Letters*, 90(17) :171116, 2007.

[117] Payam Rabiei and Peter Gunter. Optical and electro-optical properties of submicrometer lithium niobate slab waveguides prepared by crystal ion slicing and wafer bonding. *Applied Physics Letters*, 85(20) :4603–4605, November 2004.

[118] Huangpu Han, Lutong Cai, and Hui Hu. Optical and structural properties of single-crystal lithium niobate thin film. *Optical Materials*, 42 :47–51, 2015.

[119] Eli Yablonovitch. Inhibited spontaneous emission in solid-state physics and electronics. *Physical review letters*, 58(20) :2059, 1987.

[120] Sajeev John. Strong localization of photons in certain disordered dielectric superlattices. *Phys. Rev. Lett.*, 58(23) :2486–2489, 1987.

[121] John D. Joannopoulos, Steven G. Johnson, Joshua N. Winn, and Robert D. Meade. *Photonic crystals : molding the flow of light*. Princeton university press, 2011.

[122] K. M. Ho, C. T. Chan, and C. M. Soukoulis. Existence of a photonic gap in periodic dielectric structures. *Phys. Rev. Lett.*, 65(25) :3152–3155, 1990.

[123] E. Yablonovitch, T. J. Gmitter, and K. M. Leung. Photonic band structure : The face-centered-cubic case employing nonspherical atoms. *Phys. Rev. Lett.*, 67(17) :2295–2298, October 1991.

[124] R. D. Meade, A. M. Rappe, K. D. Brommer, and J. D. Joannopoulos. Nature of the photonic band gap : some insights from a field analysis. *JOSA B*, 10(2) :328–332, 1993.

[125] Steven G. Johnson, Pierre R. Villeneuve, Shanhui Fan, and J. D. Joannopoulos. Linear waveguides in photonic-crystal slabs. *Physical Review B*, 62(12) :8212, 2000.

[126] A. V. Krasavin and A. V. Zayats. Three-dimensional numerical modeling of photonic integration with dielectric-loaded SPP waveguides. *Physical Review B*, 78(4), July 2008.

[127] Min Qiu and Bozena Jaskorzynska. Design of a channel drop filter in a two-dimensional triangular photonic crystal. *Applied Physics Letters*, 83(6) :1074, 2003.

[128] Adam Mock and Ling Lu. *Two-Dimensional Photonic Crystal Micro-Cavities for Chip-Scale Laser Applications.* INTECH Open Access Publisher, 2010.

[129] Masahiro Imada, Susumu Noda, Alongkarn Chutinan, Takashi Tokuda, Michio Murata, and Goro Sasaki. Coherent two-dimensional lasing action in surface-emitting laser with triangular-lattice photonic crystal structure. *Applied Physics Letters*, 75(3) :316, 1999.

[130] C. Monat, C. Seassal, X. Letartre, P. Regreny, P. Rojo-Romeo, P. Viktorovitch, M. Le Vassor dYerville, D. Cassagne, J. P. Albert, E. Jalaguier, S. Pocas, and B. Aspar. InP-based two-dimensional photonic crystal on silicon : In-plane Bloch mode laser. *Applied Physics Letters*, 81(27) :5102–5104, December 2002.

[131] C. Monat, C. Seassal, X. Letartre, P. Regreny, M. Gendry, P. Rojo Romeo, P. Viktorovitch, M. Le Vassor dYerville, D. Cassagne, J. P. Albert, E. Jalaguier, S. Pocas, and B. Aspar. Two-dimensional hexagonal-shaped microcavities formed in a two-dimensional photonic crystal on an InP membrane. *Journal of Applied Physics*, 93(1) :23–31, January 2003.

[132] Kartik Srinivasan, Paul E. Barclay, Oskar Painter, Jianxin Chen, Alfred Y. Cho, and Claire Gmachl. Experimental demonstration of a high quality factor photonic crystal microcavity. *Applied Physics Letters*, 83(10) :1915, 2003.

[133] Brett Maune, Jeremy Witzens, Thomas Baehr-Jones, Michael Kolodrubetz, Harry Atwater, Axel Scherer, Rainer Hagen, and Yueming Qiu. Optically triggered Q-switched photonic crystal laser. *Optics express*, 13(12) :4699–4707, 2005.

[134] Hideki Watanabe and Toshihiko Baba. High-efficiency photonic crystal microlaser integrated with a passive waveguide. *Optics express*, 16(4) :2694–2698, 2008.

[135] B. Ben Bakir, Ch. Seassal, X. Letartre, P. Viktorovitch, M. Zussy, L. Di Cioccio, and J. M. Fedeli. Surface-emitting microlaser combining two-dimensional photonic crystal membrane and vertical Bragg mirror. *Applied Physics Letters*, 88(8) :081113, 2006.

[136] A. Jugessur, P. Pottier, and R. De La Rue. Engineering the filter response of photonic crystal microcavity filters. *Optics Express*, 12(7) :1304–1312, 2004.

[137] Kerry J. Vahala. Optical microcavities. *Nature*, 424(6950) :839–846, 2003.

[138] Wonjoo Suh, M. F. Yanik, Olav Solgaard, and Shanhui Fan. Displacement-sensitive photonic crystal structures based on guided resonance in photonic crystal slabs. *Applied Physics Letters*, 82(13) :1999, 2003.

[139] O. Painter, T. Vuckovic, and A. Scherer. Defect modes of a two-dimensional photonic crystal in an optically thin dielectric slab. *Journal of the Optical Society of America B (Optical Physics)*, 16(2) :275–285, 1999.

[140] Han-Youl Ryu, Soon-Hong Kwon, Yong-Jae Lee, Yong-Hee Lee, and Jeong-Soo Kim. Very-low-threshold photonic band-edge lasers from free-standing triangular photonic crystal slabs. *Applied Physics Letters*, 80(19) :3476–3478, May 2002.

[141] Xavier Letartre, Christelle Monat, Christian Seassal, and Pierre Viktorovitch. Analytical modeling and an experimental investigation of two-dimensional photonic crystal microlasers : defect state (microcavity) versus band-edge state (distributed feedback) structures. *J. Opt. Soc. Am. B*, 22(12) :2581–2595, 2005.

[142] Marin Soljacic, Steven G. Johnson, Shanhui Fan, Mihai Ibanescu, Erich Ippen, and J. D. Joannopoulos. Photonic-crystal slow-light enhancement of nonlinear phase sensitivity. *JOSA B*, 19(9) :2052–2059, 2002.

[143] Mohamed El Beheiry, Victor Liu, Shanhui Fan, and Ofer Levi. Sensitivity enhancement in photonic crystal slab biosensors. *Optics express*, 18(22) :22702–22714, 2010.

[144] Max Born, Emil Wolf, A. B. Bhatia, P. C. Clemmow, D. Gabor, A. R. Stokes, A. M. Taylor, P. A. Wayman, and W. L. Wilcock. *Principles of Optics : Electromagnetic Theory of Propagation, Interference and Diffraction of Light*. Cambridge University Press, 7 edition, October 1999.

[145] L. D. Landau, L. P. Pitaevskii, and E.M. Lifshitz. *Electrodynamics of Continuous Media, Second Edition : Volume 8*. Butterworth-Heinemann, 2 edition edition, January 1984.

[146] J. D. Jackson. *Classical Electrodynamics Third Edition*. Wiley, 3 edition edition, August 1998.

[147] Bloembergen. Maxwell's equations in nonlinear media. In *Nonlinear Optics*, pages 62–73. WORLD SCIENTIFIC, 4 edition, January 1996.

[148] A. W. McDavid and C. D. McMullen. Generalizing cross products and maxwell's equations to universal extra dimensions. *arXiv :hep-ph/0609260*, September 2006. arXiv : hep-ph/0609260.

[149] Kane S. Yee. Numerical solution of initial boundary value problems involving Maxwells equations in isotropic media. *IEEE Trans. Antennas and Propagation*, pages 302–307, 1966.

[150] Taflove Allen and Hagness Susan C. *Computational Electrodynamics : The Finite-Difference Time-Domain Method, Third Edition*. Artech House, Boston, 3 edition edition, May 2005.

[151] R. T. Ling. A finite-difference frequency-domain (fdfd) approach to electromagnetic scattering problems. *Journal of Electromagnetic Waves and Applications*, 3(2) :107–128, January 1989.

[152] P. Clauberg and P. von Allmen. Vectorial beam-propagation method for integrated optics. *Electronics Letters*, 27(8) :654–655, April 1991.

[153] C. T. Chan, Q. L. Yu, and K. M. Ho. Order-N spectral method for electromagnetic waves. *Physical Review B*, 51(23) :16635, 1995.

[154] C.M. Rappaport and B.J. McCartin. Fdfd analysis of electromagnetic scattering in anisotropic media using unconstrained

triangular meshes. *IEEE Transactions on Antennas and Propagation*, 39(3) :345–349, March 1991.

[155] Yen-Chung Chiang, Yih-Peng Chiou, and Hung-Chun Chang. Improved full-vectorial finite-difference mode solver for optical waveguides with step-index profiles. *Journal of Lightwave Technology*, 20(8) :1609–1618, August 2002.

[156] Zhaoming Zhu and Thomas Brown. Full-vectorial finite-difference analysis of microstructured optical fibers. *Optics Express*, 10(17) :853–864, 2002.

[157] Wonseok Shin. *FINITE-DIFFERENC FREQUENCY-DOMAI METHOD FOR PLASMONICS AND NANOPHOTONICS*. PhD thesis, Stanford University, 2013.

[158] Jiunn-Nan Hwang. A compact 2-d fdfd method for modeling microstrip structures with nonuniform grids and perfectly matched layer. *IEEE Transactions on Microwave Theory and Techniques*, 53(2) :653–659, 2005.

[159] Robert Scarmozzino and R. M. Osgood. Comparison of finite-difference and Fourier-transform solutions of the parabolic wave equation with emphasis on integrated-optics applications. *JOSA A*, 8(5) :724–731, 1991.

[160] W.-P. Huang and C.L. Xu. Simulation of three-dimensional optical waveguides by a full-vector beam propagation method. *IEEE Journal of Quantum Electronics*, 29(10) :2639–2649, October 1993.

[161] S. Jungling and J.C. Chen. A study and optimization of eigenmode calculations using the imaginary-distance beam-propagation method. *IEEE Journal of Quantum Electronics*, 30(9) :2098–2105, September 1994.

[162] T. Ando, H. Nakayama, S. Numata, J. Yamauchi, and H. Nakano. Eigenmode analysis of optical waveguides by a Yee-mesh-based imaginary-distance propagation method for an arbitrary dielectric interface. *Journal of Lightwave Technology*, 20(8) :1627–1634, August 2002.

[163] Junji Yamauchi, Gen Takahashi, and Hisamatsu Nakano. Full-vectorial beam-propagation method based on the mckee-

mitchell scheme with improved finite-difference formulas. *Lightwave Technology, Journal of*, 16(12) :2458–2464, 1998.

[164] G. Ronald Hadley. Wide-angle beam propagation using Padé approximant operators. *Optics letters*, 17(20) :1426–1428, 1992.

[165] J. C. Chen and S. Jüngling. Computation of higher-order waveguide modes by imaginary-distance beam propagation method. *optical and quantum electronics*, 26(3) :S199–S205, 1994.

[166] R. D. Meade, A. M. Rappe, K. D. Brommer, J. D. Joannopoulos, and O. L. Alerhand. Accurate theoretical analysis of photonic band-gap materials. *Phys. Rev. B*, 48(11) :8434–8437, September 1993.

[167] Min Qiu, Tekniska hgskolan i Stockholm, and sensorer och system Institutionen fr signaler. *Computational methods for the analysis and design of photonic bandgap structures*. PhD thesis, Tekniska hgsk., Stockholm, 2000.

[168] Steven G. Johnson, Attila Mekis, Shanhui Fan, and John D. Joannopoulos. Molding the flow of light. *Computing in Science & Engineering*, 3(6) :38–47, 2001.

[169] Steven Johnson and John Joannopoulos. Block-iterative frequency-domain methods for Maxwell's equations in a plane-wave basis. *Optics Express*, 8(3) :173–190, 2001.

[170] Shangping Guo and Sacharia Albin. Simple plane wave implementation for photonic crystal calculations. *Optics Express*, 11(2) :167–175, 2003.

[171] Shouyuan Shi, Caihua Chen, and Dennis W. Prather. Plane-wave expansion method for calculating band structure of photonic crystal slabs with perfectly matched layers. *JOSA A*, 21(9) :1769–1775, 2004.

[172] E. Ghahramani and J. E. Sipe. Transfer-matrix method for the complex band structure of superlattices. *Physical Review B*, 40(2) :1102, 1989.

[173] Min Qiu and Sailing He. A nonorthogonal finite-difference time-domain method for computing the band structure of a two-dimensional photonic crystal with dielectric and metallic inclusions. *Journal of Applied Physics*, 87(12) :8268, 2000.

[174] Min Qiu and Sailing He. FDTD algorithm for computing the off-plane band structure in a two-dimensional photonic crystal with dielectric or metallic inclusions. *Physics Letters A*, 278(6) :348–354, January 2001.

[175] F.I. Baida, D. Van Labeke, G. Granet, A. Moreau, and A. Belkhir. Origin of the super-enhanced light transmission through a 2-D metallic annular aperture array : a study of photonic bands. *Applied Physics B : Lasers and Optics*, 79(1) :1–8, July 2004.

[176] Waldemar Axmann and Peter Kuchment. An Efficient Finite Element Method for Computing Spectra of Photonic and Acoustic Band-Gap Materials : I. Scalar Case. *Journal of Computational Physics*, 150(2) :468–481, 1999.

[177] David C Dobson. An Efficient Method for Band Structure Calculations in 2d Photonic Crystals. *Journal of Computational Physics*, 149(2) :363–376, March 1999.

[178] David C. Dobson, Jayadeep Gopalakrishnan, and Joseph E. Pasciak. An Efficient Method for Band Structure Calculations in 3d Photonic Crystals. *J. Comput. Phys.*, 161(2) :668–679, 2000.

[179] Joannopoulos John D, Johnson Steven G, Winn Joshua N, and Meade Robert D. *Photonic Crystals : Molding the Flow of Light*. Princeton University Press, Princeton, second edition edition, March 2008.

[180] Charles Kittel. *Introduction to Solid State Physics*. John Wiley & Sons, 8th edition edition, November 2004.

[181] Jean-Pierre Berenger. A perfectly matched layer for the absorption of electromagnetic waves. *Journal of Computational Physics*, 114(2) :185–200, October 1994.

[182] P. Pepeljugoski, J. Kash, F. Doany, D. Kuchta, L. Schares, C. Schow, M. Taubenblatt, B.J. Offrein, and A. Benner. Low power and high density optical interconnects for future supercomputers. In *Optical Fiber Communication (OFC), collocated National Fiber Optic Engineers Conference, 2010 Conference on (OFC/NFOEC)*, pages 1–3, March 2010.

[183] M. Lipson. Guiding, modulating, and emitting light on silicon challenges and opportunities. *Journal of Lightwave Technology*, 23(12) :4222–4238, Dec 2005.

[184] Thomas Edward Murphy, Jeffrey Todd Hastings, and Henry I. Smith. Fabrication and characterization of narrow-band bragg-reflection filters in silicon-on-insulator ridge waveguides. *Journal of lightwave technology*, 19(12) :1938, 2001.

[185] Ming Zhu, Hongjun Liu, Xuefeng Li, Nan Huang, Qibing Sun, Jin Wen, and Zhaolu Wang. Ultrabroadband flat dispersion tailoring of dual-slot silicon waveguides. *Optics express*, 20(14) :15899–15907, 2012.

[186] Jun-long Kou, Qin Wang, Zi-yan Yu, Fei Xu, and Yan-qing Lu. Broadband and highly efficient quadratic interactions in double-slot lithium niobate waveguides through phase matching. *Optics Letters*, 36(13) :2533, July 2011.

[187] E.L. Wooten, K.M. Kissa, A. Yi-Yan, E.J. Murpley, D.A. Lafaw, P.F. Hallemeier, D. Maack, D.V. Attanasio, D.J. Fritz, G.J. McBrien, and D.E. Bossi. A review of lithium niobate modulators for fiber-optic communication systems. *IEEE J. Se. Top Quantum Electron*, 6 :69, 2000.

[188] G. D. Miller, R. G. Batchko, W. M. Tulloch, D. R. Weise, M. M. Fejer, and R. L. Byer. 42%-efficient single-pass cw second-harmonic generation in periodically poled lithium niobate. *Opt. Lett.*, 22(24) :1834–1836, Dec 1997.

[189] S. Tanzilli, H.D. Riedmatten, W. Tittle, H. Zbindend, P. Baldi, M. D. Micheli, D.B. Ostrowsky, and N. Gisin. Highly efficient photon-pair source using periodically poled lithium niobate waveguide. *Electron. Lett*, 37 :26, 2001.

[190] F. Lacour, N. Courjal, M. P. Bernal, A. Sabac, C. Bainier, and M. Spajer. Nanostructuring lithium niobate substrates by focused ion beam milling. *Optical Materials*, 27(8) :1421–1425, May 2005.

[191] M. Soljacic and J.D. Joannopoulos. Enhancement of nonlinear effects using photonic crystals. *Nature Materials*, 3 :211–219, 2004.

[192] Keijiro Suzuki, Kazuhiko Ogusu, and Makoto Minakata. Single-mode ag-as2se3 strip-loaded waveguides for applications to all-optical devices. *Opt. Express*, 13(21) :8634–8641, Oct 2005.

[193] Pingsheng Tang, D. J. Towner, A. L. Meier, and B. W. Wessels. Low-voltage, polarization-insensitive, electro-optic modulator based on a polydomain barium titanate thin film. *Applied Physics Letters*, 85(20) :4615–4617, 2004.

[194] Zhifu Liu, Pao-Tai Lin, Bruce W. Wessels, Fei Yi, and Seng-Tiong Ho. Nonlinear photonic crystal waveguide structures based on barium titanate thin films and their optical properties. *Applied Physics Letters*, 90(20) :–, 2007.

[195] Vilson R. Almeida, Qianfan Xu, Carlos A. Barrios, and Michal Lipson. Guiding and confining light in void nanostructure. *Opt. Lett.*, 29(11) :1209–1211, Jun 2004.

[196] Tom Baehr-Jones, Boyan Penkov, Jingqing Huang, Phil Sullivan, Joshua Davies, Jocelyn Takayesu, Jingdong Luo, Tae-Dong Kim, Larry Dalton, Alex Jen, Michael Hochberg, and Axel Scherer. Nonlinear polymer-clad silicon slot waveguide modulator with a half wave voltage of 0.25 V. *Applied Physics Letters*, 92(16) :163303, 2008.

[197] Guangxi Wang, Tom Baehr-Jones, Michael Hochberg, and Axel Scherer. Design and fabrication of segmented, slotted waveguides for electro-optic modulation. *Applied Physics Letters*, 91(14) :143109, 2007.

[198] Ran Ding, Tom Baehr-Jones, Woo-Joong Kim, Xugang Xiong, Richard Bojko, Jean-Marc Fedeli, Maryse Fournier, and Michael Hochberg. Low-loss strip-loaded slot waveguides in silicon-on-insulator. *Optics express*, 18(24) :25061–25067, 2010.

[199] Ran Ding, T. Baehr-Jones, Woo-Joong Kim, B. Boyko, R. Bojko, A. Spott, A. Pomerene, C. Hill, W. Reinhardt, and M. Hochberg. Asymmetric strip-loaded slot waveguides and its applications in silicon-polymer hybrid electro-optic modulators. IEEE Photonics Soc. Photonics Soc., January 2011.

[200] Tom Baehr-Jones, Michael Hochberg, Chris Walker, and Axel Scherer. High-Q optical resonators in silicon-on-insulator-based slot waveguides. *Applied Physics Letters*, 86(8) :081101, 2005.

[201] Rong Sun, Po Dong, Ning-ning Feng, Ching-yin Hong, Jurgen Michel, Michal Lipson, and Lionel Kimerling. Horizontal single and multiple slot waveguides : optical transmission at = 1550 nm. *Optics express*, 15(26) :17967–17972, 2007.

[202] P. Andrew Anderson, Bradley S. Schmidt, and Michal Lipson. High confinement in silicon slot waveguides with sharp bends. *Optics Express*, 14(20) :9197–9202, 2006.

[203] Takeshi Fujisawa and Masanori Koshiba. Polarization-independent optical directional coupler based on slot waveguides. *Optics letters*, 31(1) :56–58, 2006.

[204] Kenneth A. Diest, Jennifer A. Dionne, Harry A. Atwater, and Henri Lezec. Slot waveguide for color display, April 2011. U.S. Classification 385/1, 385/8, 385/129 ; International Classification G02F1/01 ; Cooperative Classification G02F2203/34, G02F2203/10, G02F2202/42, G02F2202/20, G02F1/035, G02F2203/055, G02F2001/213, G02F1/133516 ; European Classification G02F1/035.

[205] Carlos Angulo Barrios and Michal Lipson. Electrically driven silicon resonant light emitting device based on slot-waveguide. *Optics express*, 13(25) :10092–10101, 2005.

[206] Shakeeb Bin Hasan, Carsten Rockstuhl, Thomas Pertsch, and Falk Lederer. Second-order nonlinear frequency conversion processes in plasmonic slot waveguides. *Journal of the Optical Society of America B*, 29(7) :1606, July 2012.

[207] Lin Zhang, Yang Yue, Yinying Xiao-Li, Jian Wang, Raymond G. Beausoleil, and Alan E. Willner. Flat and low dispersion in highly nonlinear slot waveguides. *Optics Express*, 18(12) :13187, June 2010.

[208] R. Spano, J. V. Galan, P. Sanchis, A. Martinez, J. Mart, and L. Pavesi. Group velocity dispersion in horizontal slot waveguides filled by Si nanocrystals. In *2008 5th IEEE International Conference on Group IV Photonics*, 2008.

[209] Lin Zhang, Qiang Lin, Yang Yue, Yan Yan, Raymond G. Beausoleil, and Alan E. Willner. Silicon waveguide with four zero-dispersion wavelengths and its application in on-chip octave-spanning supercontinuum generation. *Optics express*, 20(2) :1685–1690, 2012.

[210] Peter W. Nolte, Christian Bohley, and Jrg Schilling. Tuning of zero group velocity dispersion in infiltrated vertical silicon slot waveguides. *Optics Express*, 21(2) :1741, January 2013.

[211] Francesco Dell'Olio and Vittorio M. Passaro. Optical sensing by optimized silicon slot waveguides. *Optics Express*, 15(8) :4977–4993, 2007.

[212] Carlos Angulo Barrios. Optical Slot-Waveguide Based Biochemical Sensors. *Sensors*, 9(6) :4751–4765, June 2009.

[213] Carlos A. Barrios, Kristinn B. Gylfason, Benito Snchez, Amadeu Griol, Hans Sohlstrm, Miquel Holgado, and Raphael Casquel. Slot-waveguide biochemical sensor. *Optics letters*, 32(21) :3080–3082, 2007.

[214] Carlos A. Barrios, Mara Jos Bauls, Victoria Gonzlez-Pedro, Kristinn B. Gylfason, Benito Snchez, Amadeu Griol, Angel Maquieira, Hans Sohlstrm, Miquel Holgado, and R. Casquel. Label-free optical biosensing with slot-waveguides. *Optics Letters*, 33(7) :708–710, 2008.

[215] Jacob T. Robinson, Long Chen, and Michal Lipson. On-chip gas detection in silicon optical microcavities. *Optics Express*, 16(6) :4296–4301, 2008.

[216] Vittorio M. N. Passaro, Francesco DellOlio, Caterina Ciminelli, and Mario N. Armenise. Efficient Chemical Sensing by Coupled Slot SOI Waveguides. *Sensors*, 9(2) :1012–1032, February 2009.

[217] Xiaoguang Tu, Xuejun Xu, Shaowu Chen, Jinzhong Yu, and Qiming Wang. Simulation Demonstration and Experimental Fabrication of a Multiple-Slot Waveguide. *IEEE Photonics Technology Letters*, 20(5) :333–335, 2008.

[218] Carlos Angulo Barrios, B. Sanchez, Kristinn Bjrgvin Gylfason, Amadeu Griol, H. Sohlstr, Miquel Holgado, Raphael Cas-

quel, and others. Demonstration of slot-waveguide structures on silicon nitride/silicon oxide platform. *Optics express*, 15(11) :6846–6856, 2007.

[219] Linliang An, Hongjun Liu, Qibing Sun, Nan Huang, and Zhaolu Wang. Wavelength conversion in highly nonlinear silicon-organic hybrid slot waveguides. *Applied Optics*, 53(22) :4886, August 2014.

[220] H. Lu, B. Sadani, N. Courjal, G. Ulliac, N. Smith, V. Stenger, M. Collet, F. I. Baida, and M.-P. Bernal. Enhanced electro-optical lithium niobate photonic crystal wire waveguide on a smart-cut thin film. *Optics express*, 20(3) :2974–2981, 2012.

[221] Philippe Delaye, Magali Astic, Robert Frey, and Grald Roosen. Transfer-matrix modeling of four-wave mixing at the band edge of a one-dimensional photonic crystal. *JOSA B*, 22(11) :2494–2504, 2005.

[222] Zhifu Liu, Pao-Tai Lin, Bruce W. Wessels, Fei Yi, and Seng-Tiong Ho. Nonlinear photonic crystal waveguide structures based on barium titanate thin films and their optical properties. *Applied Physics Letters*, 90(20) :201104, 2007.

[223] U. Fano. Effects of Configuration Interaction on Intensities and Phase Shifts. *Phys. Rev.*, 124(6) :1866–1878, 1961.

[224] Shanhui Fan and J. D. Joannopoulos. Analysis of guided resonances in photonic crystal slabs. *Phys. Rev. B*, 65(23) :235112, 2002.

[225] Shanhui Fan, Wonjoo Suh, and J. D. Joannopoulos. Temporal coupled-mode theory for the Fano resonance in optical resonators. *Journal of the Optical Society of America A*, 20(3) :569, 2003.

[226] M. Kanskar, P. Paddon, V. Pacradouni, R. Morin, A. Busch, Jeff F. Young, S. R. Johnson, Jim MacKenzie, and T. Tiedje. Observation of leaky slab modes in an air-bridged semiconductor waveguide with a two-dimensional photonic lattice. *Applied Physics Letters*, 70(11) :1438, 1997.

[227] P. Paddon and Jeff F. Young. Two-dimensional vector-coupled-mode theory for textured planar waveguides. *Physical Review B*, 61(3) :2090, 2000.

[228] Wonjoo Suh and Shanhui Fan. All-pass transmission or flattop reflection filters using a single photonic crystal slab. *Applied Physics Letters*, 84(24) :4905, 2004.

[229] Bryan Park, Il Woong Jung, J. Provine, Antonio Gellineau, Joe Landry, Roger T. Howe, and Olav Solgaard. Double-layer silicon photonic crystal fiber-tip temperature sensors. *IEEE Photonics Technology Letters*, 26(9) :900–903, May 2014.

[230] Hongjun Yang, Deyin Zhao, Santhad Chuwongin, Jung-Hun Seo, Weiquan Yang, Yichen Shuai, Jesper Berggren, Mattias Hammar, Zhenqiang Ma, and Weidong Zhou. Transfer-printed stacked nanomembrane lasers on silicon. *Nature Photonics*, 6(9) :617–622, July 2012.

[231] Andrey E. Miroshnichenko and Yuri S. Kivshar. Mach zehnder fano interferometer. *Applied Physics Letters*, 95(12) :121109, 2009.

[232] Andrey E. Miroshnichenko, Sergei F. Mingaleev, Sergej Flach, and Yuri S. Kivshar. Nonlinear fano resonance and bistable wave transmission. *Phys. Rev. E*, 71(3), 2005.

[233] T. Benyattou, E. Gerelli, L. Milord, C. Jamois, A. Harouri, C. Chevalier, Christian Seassal, A. Belarouci, Xavier Letartre, and P. Viktorovitch. Slow bloch mode cavity for optical trapping. In *Transparent Optical Networks (ICTON), 2013 15th International Conference on*, pages 1–5. IEEE, 2013.

[234] L. Ferrier, P. Rojo-Romeo, E. Drouard, X. Letatre, and P. Viktorovitch. Slow Bloch mode confinement in 2d photonic crystals for surface operating devices. *Optics express*, 16(5) :3136–3145, 2008.

[235] Jun Deng, Sajid Hussain, Vanga Sudheer Kumar, Wei Jia, Ching Eng Png, Lim Soon Thor, Andrew A. Bettiol, and Aaron J. Danner. Modeling and experimental investigations of Fano resonances in free-standing LiNbO3 photonic crystal slabs. *Opt Express*, 21(3) :3243–3252, February 2013.

[236] Yingbo Zhang, Xiaoyong Hu, Yulan Fu, Hong Yang, and Qihuang Gong. Ultrafast all-optical tunable Fano resonance in nonlinear ferroelectric photonic crystals. *Applied Physics Letters*, 100(3) :031106, 2012.

[237] D. Caballero, J. Snchez-Dehesa, R. Martnez-Sala, C. Rubio, J. V. Snchez-Prez, L. Sanchis, and F. Meseguer. Suzuki phase in two-dimensional sonic crystals. *Physical Review B*, 64(6), July 2001.

[238] Alfonso R. Alija, Luis J. Martnez, Pablo A. Postigo, Jose Snchez-Dehesa, Matteo Galli, Alberto Politi, Maddalena Patrini, Lucio C. Andreani, Christian Seassal, and Pierre Viktorovitch. Theoretical and experimental study of the Suzuki-phase photonic crystal lattice by angle-resolved photoluminescence spectroscopy. *Opt. Express*, 15(2) :704–713, January 2007.

[239] Kazuo Suzuki. X-ray Studies on Precipitation of Metastable Centers in Mixed Crystals NaCl-CdCl2. *J. Phys. Soc. Jpn.*, 16(1) :67–78, January 1961.

[240] K. B. Crozier, Virginie Lousse, Onur Kilic, Sora Kim, Shanhui Fan, and Olav Solgaard. Air-bridged photonic crystal slabs at visible and near-infrared wavelengths. *Phys. Rev. B*, 73(11) :115126, March 2006.

[241] Y. R. Shen. *The Principles of Nonlinear Optics*. Wiley-Blackwell, reprint edition, December 2002.

[242] DELALANDE Claude RIGNEAULT Herv, LOURTIOZ Jean-Michel and LEVENSON Ariel. *La nanophotonique*. HERMES SCIENCE PUBLICATIONS / LAVOISIER, july 2005.

[243] Luca Razzari, Denis Tr¨ ager, Magali Astic, Philippe Delaye, Robert Frey, Gérald Roosen, and Régis André. Kerr and four-wave mixing spectroscopy at the band edge of one-dimensional photonic crystals. *Applied Physics Letters*, 86(23) :231106, 2005.

[244] Wenwen Qian, Chun-Liu Zhao, Shaoling He, Xinyong Dong, Shuqin Zhang, Zaixuan Zhang, Shangzhong Jin, Jiangtao Guo, and Huifeng Wei. High-sensitivity temperature sensor based on an alcohol-filled photonic crystal fiber loop mirror. *Optics Letters*, 36(9) :1548, May 2011.

[245] Yang Peng, Jing Hou, Zhihe Huang, and Qisheng Lu. Temperature sensor based on surface plasmon resonance within selectively coated photonic crystal fiber. *Applied Optics*, 2012.

[246] Costa Nicolaou, Wah Tung Lau, Raanan Gad, Hooman Akhavan, Ryan Schilling, and Ofer Levi. Enhanced detection limit by dark mode perturbation in 2d photonic crystal slab refractive index sensors. *Opt. Express*, 21(25) :31698–31712, 2013.

[247] Onur Kilic, Michel Digonnet, Gordon Kino, and Olav Solgaard. Controlling uncoupled resonances in photonic crystals through breaking the mirror symmetry. *Optics express*, 16(17) :13090–13103, 2008.

[248] Xingyu Zhang, Amir Hosseini, Harish Subbaraman, Shiyi Wang, Qiwen Zhan, Jingdong Luo, Alex K.-Y. Jen, and Ray T. Chen. Integrated Photonic Electromagnetic Field Sensor Based on Broadband Bowtie Antenna Coupled Silicon Organic Hybrid Modulator. *Journal of Lightwave Technology*, 32(20) :3774–3784, October 2014.

Document réalisé avec LaTeX et :
le style LaTeX pour Thèse de Doctorat créé par S. Galland — http://www.multiagent.fr/ThesisStyle
la collection de paquets `tex-upmethodology` — http://www.arakhne.org/tex-upmethodology/

Abstract :

Light is incredibly versatile for measuring all kinds of physical quantities : temperature, electric field (E-field), displacement and strain etc. Photonic sensors are promising candidates for the new generation of sensors developments due to their virtues of high sensitivity, large dynamic range and compact size etc. Integrated and on-fiber end photonic sensors on thin film lithium niobate (TFLN) exploring the electro-optic (EO) and pyro-electric effects are studied in this thesis in order to design E-field sensors and temperature sensors (T-sensors). These studies aim to develop sensors with high sensitivity and compact size. To achieve that aim, sensors that are made of photonic crystals (PhC) cavities are studied by sensing the measurand through the resonance wavelength interrogation method.

In integrated sensor studies, intensive numerical calculations by PWE method, mode solving technique and FDTD methods are carried out for the design of high light confinement waveguiding structures on TFLN and suitable PhC configurations. Four types of waveguide (WG) structures (ridge WG, strip loaded WG, slot WG and double slot WG) are studied with a large range of geometrical parameters. Among them, slot WG yields the highest confinement factor while strip loaded WG is an easier option for realizations. Bragg grating is designed in slot WG with an ultra compact size (about 0.5μm $\times$0.7μm $\times$6μm) and is employed to design PhC cavity. A moderate resonance Q of about 300 in F-P like cavity where the mirrors are made of PhC is achieved with ER of about 70% of the transmission. Theoretical minimum E-field sensitivity of this slot Bragg grating structure can be as low as 200 μV/m. On the other hand, Si_3N_4 strip loaded WG is designed with 2D PhC structure and a low resonance Q of about 100 is achieved. Fabrications of nano-metrical WG such as ridge WG Si_3N_4 strip loaded are demonstrated. However, the realization of nanometric components on LN presents a big challenge.

In the on-fiber end sensor studies, guided resonance, oftentimes referred to as Fano resonance due to its asymmetric lineshape, is studied with different PhC lattice types. A Suzuki phase lattice (SPL) PhC presenting a Fano resonance at the vicinity of 1500 nm has been studied and demonstrated as temperature sensor with sensitivity of 0.77 nm/^{o}C with a size of only 25 μm $\times$ 24 μm. In addition, guided resonances on rectangular lattice PhC have been systematically studied through band diagram calculations, 2D-FDTD and 3D-FDTD simulations. Accurate theoretical sensitivity analysis of employing the rectangular lattice guided resonance as an E-field sensor are carried out by a newly proposed local field factor $f_{opt}(x, y, z)$ calculated cell by cell in 3D-FDTD algorithm, yielding an E-field sensitivity of about 50 μV/m. Other types of PhC lattices (triangular lattice, checkerboard lattice and honeycomb lattice) are